Vlakke antennesystemen
voor toepassingen binnen het 'Internet der Dingen'

Low-Profile Antenna Systems
for the Next-Generation Internet of Things Applications

Sam Lemey

Promotoren: prof. dr. ir. H. Rogier, prof. dr. ir. J. Vanfleteren
Proefschrift ingediend tot het behalen van de graad van
Doctor in de ingenieurswetenschappen: elektrotechniek

Vakgroep Informatietechnologie
Voorzitter: prof. dr. ir. D. De Zutter

Vakgroep Elektronica en Informatiesystemen
Voorzitter: prof. dr. ir. R. Van de Walle

Faculteit Ingenieurswetenschappen en Architectuur
Academiejaar 2015 - 2016

UNIVERSITEIT
GENT

ISBN 978-90-8578-916-1
NUR 959
Wettelijk depot: D/2016/10.500/47

Low-Profile Antenna Systems for the Next-Generation Internet of Things Applications

Sam Lemey

Dissertation submitted to obtain the academic degree of
Doctor of Electrical Engineering

Publicly defended at Ghent University on August 11th, 2016

Supervisor:
prof. dr. ir. H. Rogier
Electromagnetics group
Department of Information Technology
Faculty of Engineering and Architecture
Ghent University
Technologiepark-Zwijnaarde 15
B-9052 Ghent, Belgium
http://emweb.intec.ugent.be

Supervisor:
prof. dr. ir. J. Vanfleteren
Centre for Microsystems Technology
Department of Electronics and Information Systems
Faculty of Engineering and Architecture
Ghent University
Technologiepark - Zwijnaarde 15
B-9052 Ghent, Belgium

Members of the examining board:

prof. dr. ir. R. Van de Walle (chairman)	Ghent University, Belgium
prof. dr. ir. J. Bauwelinck (secretary)	Ghent University, Belgium
prof. dr. ir. H. Rogier (supervisor)	Ghent University, Belgium
prof. dr. ir. J. Vanfleteren (supervisor)	Ghent University, Belgium
prof. dr. ir. C. Craeye	Université Catholique de Louvain, Belgium
prof. dr. ir. M. Bozzi	Università degli Studi di Pavia, Italy
prof. dr. ir. L. Van Langenhove	Ghent University, Belgium
prof. dr. ir. E. De Poorter	Ghent University, Belgium

Dankwoord

Dit 160-tal bladzijden tellend werk vormt het sluitstuk van een boeiende periode waarin ik zelfstandig, maar met deskundige begeleiding, de wondere wereld der elektromagnetisme mocht exploreren. Doorheen deze vier jaar waren er heel wat mensen die elk op hun eigen manier hebben bijgedragen tot het welslagen van deze uitdagende onderneming. Zonder hun hulp zou mijn doctoraatsonderzoek nooit hetzelfde niveau gehaald hebben. Ik wil hier dan ook graag van de gelegenheid gebruik maken om deze mensen uitdrukkelijk te bedanken voor hun hulp, inbreng, steun en inspiratie.

Eerst en vooral wens ik mijn beide promotoren, prof. Hendrik Rogier en prof. Jan Vanfleteren, te bedanken. Ik ben prof. Hendrik Rogier niet enkel bijzonder dankbaar omwille van de geboden kans om mijn doctoraatsstudie aan te vatten, maar ook omwille van het grote vertrouwen dat ik doorheen de jaren heb mogen ervaren. Verder kan ik hem niet genoeg bedanken om altijd paraat te staan bij het analyseren van problemen, voor de grote bereidheid om ieder stukje tekst zorgvuldig na te lezen en natuurlijk ook voor de constructieve feedback en kritische vragen die me in staat stelden dit proefschrift naar een hoger niveau te tillen. Zijn inbreng was bepalend voor het succes van dit werk. Ook prof. Jan Vanfleteren ben ik heel dankbaar voor de constructieve samenwerking en de vele mogelijkheden en faciliteiten die hij me aanbood om mijn prototypes daadwerkelijk te realiseren. Ik beschouw het als een groot privilege om hen als promotoren te hebben gehad. Het stelde me in staat om als mens en als onderzoeker enorm te evolueren.

Verder wil ik prof. Daniël De Zutter, hoofd van de vakgroep Informatietechnologie, en prof. Rik Van de Walle, hoofd van de vakgroep Elektronica en Informatiesystemen, bedanken om mij de mogelijkheid te geven mezelf als onderzoeker te ontwikkelen in deze leerrijke omgeving. Hun niet-aflatende inzet laat toe om op hoog niveau onderzoek te doen. Ook prof. Dries Vande Ginste ben ik zeer erkentelijk. Hij stond steeds klaar om zijn expertise op het vlak van EMC en "microwave engineering" met me te delen. Daarnaast wil ik ook de leden van de lees- en examencommissie die hierboven nog niet werden vernoemd, bedanken voor het minutieus nalezen van dit werk, de doelgerichte vragen en de constructieve feedback: prof. Johan Bauwelinck, prof. Christophe Craeye, prof. Maurizio Bozzi, prof. Lieva Van Langenhove, en prof. Eli De Poorter.

Dit doctoraatsonderzoek kon enkel tot stand komen door de vruchtbare samenwerking tussen verschillende vakgroepen. Binnen de vakgroep Informatietechnologie wens ik Frederick Declercq uitdrukkelijk te bedanken om me onder zijn vleugels te nemen bij de aanvang van mijn doctoraat en me zo een vliegende start te geven. Ook Patrick Van Torre ben ik oprecht dankbaar. Naast de vele aangename

gesprekken in de koffiehoek, ben ik sterk onder de indruk van zijn inzicht in en kennis over de technische materie. Verder wil ik ook mijn appreciatie uitdrukken voor mijn vegetarische voornaamgenoot, Sam Agneessens. Ik beschouw het als een grote eer om de voorbije vier jaar met hem te hebben mogen samenwerken. Zowel op menselijk als op professioneel vlak heb ik veel van hem opgestoken. De samenwerking was altijd heel erg aangenaam. De wisselwerking van ideeën in combinatie met zijn kritische blik leidden tot innovatieve concepten. Ook de samenwerking met Luigi Vallozzi was een positieve ervaring. Hij stond steeds met de glimlach klaar om anderen te helpen. Binnen de vakgroep Elektronica en Informatiesystemen wil ik Thomas Vervust, Björn Vandecasteele en Jindrich Windels bedanken voor de hulp bij het vervaardigen van elektronische systemen op flexibele substraten en het ter beschikking stellen van de benodigde meetapparatuur. Tevens wil ik ook Samira Khelifi en Aimi Abass van het Solar cells Lab binnen de vakgroep Elektronica en Informatiesystemen bedanken voor hun hulp bij het opmeten van de verschillende fotovoltaïsche modules. Ook Kurt Van Houtte van de vakgroep Toegepaste Materiaalwetenschappen wens ik te bedanken voor zijn bereidwilligheid inzake het lasersnijden van textielantenneprototypes.

Verder wil ik ook graag het administratief personeel danken en in het bijzonder Isabelle Van der Elstraeten. Dankzij haar vakkundige ondersteuning werd de tijd die ik aan administratieve rompslop moest spenderen steeds tot een minimum herleid. Ook Peter Guns wens ik te bedanken om allerhande praktische problemen zo snel mogelijk en op een deskundige manier op te lossen.

Een doctoraat wordt in vele gevallen door de buitenwereld aanschouwd als een eenzame bezigheid. Echter, niets is minder waar. Doorheen de voorbije jaren heb ik de wandelgangen mogen delen met zoveel interessante en boeiende personen die middels gesprek of lach de werksfeer aangenaam hebben beïnvloed en voor de nodige “verstrooiing” zorgden. Vandaar een specifiek dankwoord aan alle (ex)-collega’s. Eerst en vooral richt ik me tot mijn bureaugenoten van de -T verdieping van het technicum: Arne, Wouter, Sam, Marina, Niels, Arnaut, Thomas Deckmyn en Thomas Cuyckens. De vele gesprekken met deze intelligente en interessante mensen hadden een sterke bijdrage in de kwaliteit van dit werk. Ik ben ook blij de bureau te hebben mogen delen met Thomas, Dries, bureausheriff en “Buchnikan”-ster Niels, Joren, Irven, Robbe, Olivier en Thijs op de 11de verdieping van de iGent toren. In het bijzonder wens ik de loftrompet te steken over Thijs Castel. Sinds de aanvang van onze hogere studies, 8 jaar geleden, zijn onze wegen sterk gelijkaardig ontwikkeld. Het was altijd zeer aangenaam om met hem samen te werken. Hij was altijd bereid om zijn technische kennis ter beschikking te stellen wanneer nodig en ook als proefpersoon in de meetkamer was hij een grote hulp. Samen zijn we erin geslaagd om de nodige doctoral schools te doorzwemmen en ook buiten de werkuren kan ik het opperbest met hem vinden. Quad Industries heeft naar mijn mening zijn beste transfer gerealiseerd door hem een contract aan te bieden. Eveneens wens ik alle andere EM collega’s en oud-collega’s die de gang in het Technicum en de iGent toren bevolkten te bedanken voor de collegiale sfeer en de toffe babbels: Gert-Jan, Martijn, Michiel, Steven, Giorgos, Zdravko, Marco,

Simon, Paolo, Bart, Freek, Karel, Sofian, Marijn, Véronique, Eline, Katia, Abdul, Peter, Alessandro en Mykola.

Wie zeker niet mag ontbreken in dit dankwoord is mijn familie. Een hechte familieband is voor mij van zeer groot belang en is een belangrijke bouwsteen van mijn carrière. In het bijzonder wil ik mijn ouders bedanken. Doorheen de jaren zijn ze me onvoorwaardelijk blijven steunen en hebben ze me altijd alle kansen gegeven. Ik ben hen hiervoor heel erg dankbaar en vandaar een dikke en welgemeende merci !!! Ook mijn beide zussen, Griet en Mieke, mijn beide broers, Kevin en Robin, en mijn schoonbroers, Laurens, Stéphane en Lieven, wil ik hier graag bedanken, net als mijn nichtjes en neefjes, Silke, Zjoske, Jitske, Lévi, Thibo, Louise en mijn petekind Simon. Ik heb altijd genoten van de familiebijeenkomsten en onze reisjes naar de Ardennen. Naast familie, beschouw ik hen als zéér goede vrienden. Specifiek gerelateerd aan dit doctoraat wil ik Laurens bedanken om mij de nodige materialen aan te leveren om de integratie van antennesystemen in meubilair te onderzoeken (Hoofdstuk 2 en 3 in dit proefschrift).

Verder wil ik zeker ook Willem en Marianne, mijn toekomstige schoonouders, bedanken voor de steun en appreciatie die ik heb mogen ervaren sinds ik samen ben met Judith. Het is altijd fijn om langs te komen in hun mooie en uitgestrekte tuin voor een babbel en een drankje. Ook Judiths broer, Simon, en zijn vriendin Julie wens ik hier te bedanken voor de immer aangename samenkomsten.

Naast mijn familie wil ik ook mijn vrienden bedanken voor de vele ontspanningsmomenten, wat toch wel héél belangrijk is om af en toe het hoofd te kunnen leegmaken. Eerst en vooral de MRA-vrienden voor de onvergetelijke avonden in Gent en Ardooie, en natuurlijk ook om in te staan voor de uitbreiding van mijn muzikale kennis. Ook de vriendengroep die zich centraliseert rond Ardooie, maar uitstrekkingen kent tot Heule, Tielt, Roeselare, Koolskamp, en Meulebeke, mag hier zeker niet ontbreken. De meesten onder ons kennen elkaar al meer dan 10 jaar, wat niet enkel tot een grote bende leidt, maar ook tot een unieke groep waarin iedereen elkaar onvoorwaardelijk helpt en steunt. Ik wil hen echter niet enkel daarvoor bedanken, maar ook voor de leuke weekendjes weg, de bierproefavonden in de OPCD en d'Oude Maalderij, de supportersavonden voor de Rode Duivels in Ardooie en Chimay, de quizzen, de frequente BBQ's met bijhorende Kubb-challenge, en zoveel meer. Ook Jonathan David wil ik hier bedanken. Ondanks zijn drukke carrière, waarin hij vaak meerdere weken vertoeft in landen zoals Zuid-Korea en de Verenigde Arabische Emiraten, maakt hij altijd tijd om te blijven afspreken. Het is steeds een leuk weerzien waarin heel wat herinneringen over onze studies in Kortrijk en onze master thesis in Gent worden opgehaald. Ten slotte wil ik ook nog de vrienden van de badminton danken voor alle leuke en spannende badmintonmatchen en voor alle daarmee gerelateerde activiteiten, zoals de verschillende nationale en internationale toernooien, de kaarting, de BBQ, ...

De laatste paragraaf heb ik bewaard voor de belangrijkste persoon in mijn leven: mijn verloofde Judith Brandt. Niettegenstaande ik meteen verkocht was, zijn we doorheen de jaren nóg meer naar elkaar toegegroeid. Gaande van onze eerste ont-

moeting tijdens het badmintontoernooi van BC Tielt, onze eerste date in de Backdoor, onze eerste gezamenlijke concert van de wereldvermaarde groep “Muzze en Vantorre”, naar de aanschaf en verbouwing van ons eigen huisje met tuin, de roadtrips doorheen Europa en nu finaal een spetterend huwelijksfeest. Ik besef elke dag hoeveel geluk ik heb door jou te hebben mogen ontmoeten en bij je te mogen zijn. Je hebt zoveel eigenschappen en talenten waar ik naar opkijk: je ziet altijd meteen het goede in een persoon, je optimisme, je creativiteit, en vooral je vermogen om met mij samen te leven. Jij bent DE reden van ons succes.

Emelgem, Juli 2016
Sam Lemey

The great accomplishments of man have resulted from the transmission of ideas and enthusiasm.

THOMAS J. WATSON

Inhoudsopgave

Samenvatting

In de nabije toekomst zal het 'Internet der Dingen' (Engels: 'Internet of Things', 'IoT') de manier waarop we leven en werken compleet veranderen. Gestimuleerd door de ontwikkeling van verschillende baanbrekende technologieën worden binnen deze visie alledaagse objecten, machines en zelfs kledij voorzien van extra functionaliteit, zoals waarnemen via sensoren, dataverwerking, lokalisatie en draadloze communicatie. Dit laat hen toe om hun omgeving en de context te begrijpen en gepast te reageren. Door vervolgens deze intelligente objecten te verbinden met het internet, zal er een constante stroom data en kennis aangeleverd worden die ons helpt betere beslissingen te nemen in alle aspecten van ons leven. Het zal zorgen voor meer bewustzijn over onze omgeving en onze eigen fysieke toestand. Meer nog, het zal ons in staat stellen om onze omgeving te controleren en te beïnvloeden op manieren die we ons nu nog niet volledig kunnen voorstellen.

Intelligente oppervlakte technologie (Engels: 'Smart Surface Technology'), en meer bepaald intelligente textielsystemen, spelen een belangrijke rol bij de ontwikkeling van het 'Internet der Dingen'. Binnen deze tak van draagbare systemen wordt de functionaliteit van alledaagse kledij uitgebreid door sensoren, elektronica en draadloze communicatiesystemen rechtstreeks in het textiel zelf te implementeren met als doel de fysieke toestand van de gebruiker en zijn interactie met de omgeving nauwgezet op te volgen. Het is duidelijk dat deze technologie interessante nieuwe opportuniteiten opent om de mogelijkheden van de gebruiker beduidend te verhogen in een breed scala aan toepassingsgebieden, en dit zonder hem/haar te overladen met extra apparatuur. Het uitrusten van reddingswerkers met dergelijke intelligente kledij laat toe om hun vitale parameters en locatie op te volgen vanuit een centrale commandopost en in te grijpen indien nodig. Het uitrollen van zulke systemen tijdens interventies draagt bij tot het beter en veiliger uitvoeren van hun hoofdtaak, namelijk het redden van levens. In de gezondheidszorg kunnen intelligente textielsystemen een drastische verbetering betekenen voor de levenskwaliteit van zowel patiënten als ouderen, door thuiszorg en zelfstandig leven te ondersteunen. Dit helpt tevens om de kost voor de samenleving in te perken. Verder werden recent ook andere, nieuwe concepten ontwikkeld die gebruik maken van intelligente oppervlakte technologie om de interactie met de omringende infrastructuur zo onopvallend mogelijk te maken, zoals intelligente vloeren, intelligent behangpapier en intelligente plafonds.

In dit proefschrift concentreren we ons op twee fundamentele technologische uitdagingen die gerelateerd zijn met het ontwerp van antennesystemen voor toepassing binnen het IoT concept. Het eerste deel van dit werk is voornamelijk gewijd aan het ontwerp van robuuste antennesystemen die een onzichtbare integratie toelaten in een intelligente vloer, plafond of bureau. Hierbij wordt extra aandacht

besteed om een betrouwbare en snelle draadloze communicatielink op te zetten over een zeer kleine afstand binnen een beperkte, afgebakende ruimte.

In Hoofdstuk 2 gaan we de uitdaging aan met de strenge ontwerpvereisten die verbonden zijn aan de realisatie van onzichtbaar geïntegreerde antennesystemen die geschikt zijn om de datasnelheden te ondersteunen die gepaard gaan met de volgende generatie multimediatoepassingen. Hiervoor combineren we de substraatgeïntegreerde golfgeleiderimplementatietechnologie (Engels: 'Substrate Integrated Waveguide technology' of 'SIW technology') met de welgekende sleuf-antennemet-achterliggende-caviteit (Engels: 'cavity-backed slot antenna', 'CBSA') topologie. Op die manier worden de voordelen van de CBSA topologie, namelijk een hoge stralingsefficiëntie en een hoge isolatie tussen antenne en integratieplatform, gecombineerd met de voordelen van planaire antennetechnologie, namelijk een laag profiel, een lage fabricagekost en eenvoudige integratie met andere elektronicacomponenten. Verder worden twee hybride modes geëxciteerd en samengevoegd om de impedantiebandbreedte te verhogen, terwijl de symmetrie van deze hybride modes uitgebuit wordt om het ontwerp te miniaturizeren. Twee nieuwe antenne(rooster)s worden voorgesteld om het potentieel van deze ontwerpstrategie aan te tonen. Eerst introduceren we een compact antennerooster dat bestaat uit drie antenne-elementen. Hierbij wordt de anders ongebruikte oppervlakte binnen meubels aangewend om onzichtbare integratie mogelijk te maken. Daarna stellen we een geminiaturizeerde antenne voor die gebruik maakt van het beschikbare materiaal in kurk vloer- en wandtegels om onzichtbare integratie in een intelligente vloer of wand te bekomen. Metingen tonen aan dat beide ontwerpen een hoge antennewinst en stralingsefficiëntie vertonen over een zeer hoge bandbreedte in een realistische IoT omgeving. Dit onderstreept de sterkte van deze ontwerpmethode.

Hoofdstuk 3 gaat dieper in op het antennerooster dat ontworpen is in Hoofdstuk 2. We stellen richtlijnen op om dat antennerooster te integreren in een bureau, om zo een stabiele, zeer snelle 3 x 3 MIMO (Engels: 'multiple-input multiple-output') draadloze communicatie verbinding op te zetten met een mobiele gebruiker die op de desbetreffende bureau is geplaatst. Het uiteindelijke doel van deze onderzoeksinspanning is om een zeer hoge datasnelheid aan te bieden aan elke deelnemer van een vergadering of om een gebruiksvriendelijker alternatief aan te bieden voor bedrade basisstations in een intelligente thuisomgeving. Metingen uitgevoerd in een realistische opstelling hebben aangetoond dat er een hoge multiplexeringswinst wordt behaald over een zeer hoge bandbreedte, en dit voor verschillende posities en oriëntaties van de mobiele gebruiker. Deze winst kan enerzijds gebruikt worden om het zendvermogen te reduceren of om de datasnelheid te verhogen. Bovendien is er, dankzij het specifieke ontwerp van het antennerooster, geen kennis over het kanaal nodig bij de verzender. Dit vermindert de complexiteit van het signaalverwerkingsalgoritme en de responstijd, aangezien er geen terugkoppeling meer nodig is.

Het tweede deel van dit werk is gewijd aan een holistische ontwerpstrategie om een nieuwe generatie van autonome, betrouwbare en onopvallende intelligente

textielsystemen te implementeren. Deze actieve antennes zijn in staat om een draadloze communicatieverbinding op te zetten en in stand te houden in een uitdagende, en soms vijandige, IoT omgeving, zonder hierbij telkens de batterij te moeten herladen.

In Hoofdstuk 4 wenden we de inzichten die verkregen zijn in Hoofdstuk 2 aan om een draagbare, ultra-breedbandige (Engels: 'Ultra-wideband', 'UWB') textielantenne te onwikkelen die werkzaam is in de [3.4-4.8] GHz UWB band. Ons ontwerp is gebaseerd op koperen zeilringen en textielmaterialen om een flexibele, lichte en vlakke UWB antenne te verkrijgen die onopvallende integratie in kledij toelaat, zonder de gebruiker te hinderen. Metingen bewijzen niet enkel een zeer hoge isolatie tussen de antenne en het menselijke lichaam, maar ook zeer stabiele werking wanneer de antenne gebogen wordt, zoals in realistische situaties.

In het daaropvolgende hoofdstuk bieden we een oplossing voor twee hoofdbekommernissen van ontwerpers van intelligente textielsystemen: betrouwbaarheid en autonomie. Daarvoor combineren we het potentieel van energie-oogstsystemen (Engels: 'energy-harvesting systems') met een betrouwbare, energie-efficiënte draadloze communicatieverbinding die opgezet wordt door een zorgvuldig ontworpen textiel antennesysteem. In het bijzonder ontwerpen we een draagbare textielantenne die zowel werkt in de 2.45 GHz ISM band als in de 4G-LTE-band-7. Op dit antenneplatform wordt een systeem geïntegreerd dat in staat is om zonne-energie te winnen. Het tweebandige karakter van het ontwerp reduceert de probabiliteit op het verliezen van de draadloze verbinding in de heterogene IoT omgeving, en verbetert zo niet enkel de betrouwbaarheid maar ook de gebruiksvriendelijkheid. Door middel van een aangepaste ontwerpstrategie hergebruiken we vervolgens de antenne-oppervlakte voor het opwekken van DC vermogen. Hiervoor wordt een flexibel vermogensbeheer- en energieopslagsysteem geïntegreerd op de achterkant van de antenne en een flexibele zonnecel op de voorkant van de antenne. Door de specifieke antennetopologie wordt het aantal benodigde DC-verbindingsdraden geminimaliseerd evenals hun lengte, zonder hierbij in te boeten aan stralingsperformantie. Dit wordt gevalideerd door antennewinst- en reflectiecoefficiëntmetingen in de vrije ruimte te vergelijken vóór en na integratie van deze extra hardware. De prestatie van de volledige module wordt vervolgens gevalideerd in realistische omstandigheden door enerzijds op te meten hoeveel zonne-energie we kunnen oogsten in een buitenomgeving en door anderzijds het stralingspatroon en de reflectiecoefficiënt op te meten wanneer de module geplaatst is op het menselijke lichaam.

Hoofdstuk 5 beschreef reeds een belangrijke stap in de richting van een hogere betrouwbaarheid en grotere systeemautonomie. Het is echter duidelijk dat wanneer energie slechts gewonnen wordt van één energiebron, er gevaarlijke situaties kunnen ontstaan als deze niet langer beschikbaar is. Denk aan een reddingswerker die vertrouwt op zonne-energie om het systeem dat zijn vitale parameters opvolgt te voorzien van stroom tijdens een interventie in een ondergrondse parkeergarage. Het is duidelijk dat een hybride energie-oogstproces, waarbij gelijktijdig energie

gecollecteerd wordt van verschillende energiebronnen, noodzakelijk is om dergelijke situaties te vermijden. Daarom gaan we in Hoofdstuk 6 dieper in op de mogelijkheid om textielantennes te gebruiken als een platform voor hardware die meerdere energievormen gelijktijdig omzet in elektrische energie en deze vervolgens op een intelligente manier beheert. Als startpunt bespreken we de vier primaire energiebronnen en de bouwstenen die nodig zijn om energie te oogsten van deze bronnen. Dan bestuderen we draagbare antennetopologieën die de integratieprocedure ondersteunen of vereenvoudigen. Bovendien wordt een stappenplan opgesteld om te voorkomen dat de integratie van deze extra hardware invloed heeft op de prestaties van de antenne. Uiteindelijk wordt er een antenne/hybride energie-oogstsysteem co-ontwerpprocedure voorgesteld die in staat is om de voordelen van beide technologieën te combineren, zonder wederzijdse negatieve beïnvloeding. De kracht en voordelen van deze aanpak worden dan aangetoond door de realisatie van een compact intelligent textielsysteem, waarbij een flexibel hybride energie-oogstsysteem wordt geïntegreerd op een draagbare SIW CBS textielantenne. Drie verschillende actuatortechnieken worden aangewend om energie te oogsten en te combineren van zonlicht, artificieel licht en de lichaamswarmte van de gebruiker. Deze ontwerpstrategie is gevalideerd door antenneparameters te vergelijken vóór en na integratie van deze extra hardware. Verder wordt het potentieel van het hybride energie-oogstsysteem geverifieerd in realistische binnen- en buitenomstandigheden. Hiermee wordt aangetoond dat het geïntegreerde hybride energie-oogstsysteem toelaat om energie ter beschikking te bestellen in de meeste situaties, zowel binnen als buiten. Het is echter belangrijk te melden dat optimale energiewinning slechts verkregen kan worden als de energiebronnen gekozen worden in functie van de toepassing en wanneer het achterliggende energiebeheersysteem afgestemd wordt op zowel het vermogenprofiel van het intelligente textielsysteem als van de geselecteerde energie-omzetters.

Daarom gebruiken we in het laatste hoofdstuk van dit proefschrift de co-ontwerpprocedure voorgesteld in Hoofdstukken 5 en 6 als de basis voor een nieuwe holistische ontwerpmethode voor autonome, intelligente textielsystemen, waarin de textielantenne de sleutelcomponent vormt om optimale prestaties te bewerkstelligen. Verder worden de energiebronnen waarvan energie wordt geoogst, gekozen als functie van de toepassing en is het vermogenbeheersysteem op maat gemaakt om het energieverbruik van de draadloze communicatiemodule af te stemmen op de energiewinning. Vervolgens wordt deze nieuwe strategie toegepast om een volledig nieuwe autonome en draagbare RFID tag te ontwikkelen die werkzaam is in de 2.45-GHz RFID SHF band. Het ontwerp is gebaseerd op een circulaire patchantenne vervaardigd uit textiel, waarbij zeilogen gebruikt worden om het stralingspatroon op maat te maken voor optimale prestaties in het concept van een intelligente vloer of plafond. De eigenschappen van dit toepassingsspecifieke antenne-ontwerp worden dan uitgebuit om sensoren, microcontroller en transceiver te integreren, evenals de hardware die nodig is om energie te winnen uit de omringende energiebronnen, en dit met een minimum aan fragiele en verlieshebbende verbindingsdraden. Kort samengevat levert deze nieuwe aanpak een

RFID tag die gekenmerkt wordt door een uitstekend comfort voor de gebruiker, een zeer hoog uitleesbereik, flexibele interfacing met verschillende analoge en digitale sensoren, uitgebreide functionaliteit, en een zeer hoge operationele autonomie.

Summary

In the near future, the 'Internet of Things' will bring a massive change to the way we live and work nowadays. Fueled by the adaption of novel key-enabling technologies, common objects, tools, machinery, and even garments, will be augmented with sensing, processing, and wireless communication capabilities, allowing them to understand and respond to their context and environment. By integrating these smart objects into the internet, billions of everyday objects surrounding us will provide a constant dataflow, helping us to take better decisions in all aspects of our lives. It will improve our awareness of our surroundings and of our physical condition. Moreover, it will enable us to control our surroundings in ways that we cannot fully imagine today.

Smart surface technology, and more in particular smart-fabric interactive-textile (SFIT) systems, play an important role within the vision of the Internet of Things. These body-centric systems, in which the functionality of traditional garments is extended by seamless integration of sensing, actuating and computing functionalities, leverage pervasive quantification of the wearer's physical conditions and his/her interaction with the environment. This technology offers exciting new opportunities to improve the wearer's capabilities in a plethora of application areas, without overburdening the wearer with additional pieces of equipment that have to be carried around. For instance, in critical professional applications, SFIT systems facilitate vital sign monitoring, localization and remote coordination of first responders or firefighters during their intervention. It helps to safe-guard their lives and, hence, also the lives of the persons in distress. Using SFIT systems in healthcare improves quality of life of patients and elderly people by facilitating home care and independent living, in the meantime reducing healthcare costs for the society. Recently, other smart surface related concepts, such as smart floors, smart wall papers, and smart ceilings, were developed, making the interaction between man and infrastructure even more seamless to the user.

The work presented in this dissertation focuses on two fundamental technological challenges related to antenna system design for the Internet of Things. The first part of this thesis is primarily concerned with antenna system design for invisible and robust integration within smart floors, ceilings and desk configurations. Special attention was devoted to establishing reliable, high data rate ultra-short-range wireless communication.

In Chapter 2, we face the challenging set of design requirements related to the practical realization of invisibly integrated (multi-)antenna systems, capable of supporting the data speed levels required by the next-generation multimedia applications. Therefore, the substrate integrated waveguide (SIW) implementation

technology is combined with the cavity-backed slot antenna topology. In doing so, the advantages of the latter, being excellent radiation efficiency and a high antenna-to-integration-platform isolation, are combined with the benefits of planar antenna technology, being low-profile, low cost and easy integration with planar circuitry. Then, two hybrid modes are excited and merged to enhance bandwidth, whereas miniaturization is obtained by relying on the symmetry of both hybrid modes. Two novel antenna (array) designs are introduced to demonstrate the potential of this design approach: a compact, ultra-wideband three-element antenna array for invisible integration into furniture, exploiting the otherwise unused area, and a miniaturized ultra-wideband single element antenna design that exploits the readily available material of cork floor and wall tiles to enable invisible integration in a smart floor or wall. Measurements demonstrate a high gain and large radiation efficiency over an ultra-wide bandwidth in a realistic IoT environment, underlining the strength of this design approach.

Chapter 3 elaborates on the three-element antenna array designed in Chapter 2. More in particular, we provide guidelines to embed the antenna array into a desk to set up a stable, high data-rate ultra-short-range 3 x 3 MIMO wireless communication link with a mobile user (MU) on top of that worktop. The main idea consists of offering a high data-rate wireless connection to each participant of a meeting or providing a user-friendly alternative for wired docking stations in a smart home environment. Measurements in a realistic environment have revealed a high multiplexing gain over a wide bandwidth for different relative orientations and positions of the MU. This gain can be exploited to reduce power consumption and/or to increase the data rate. In addition, it was shown that an ultra-short-range MIMO channel implemented by our three-element array does not require channel knowledge at the transmitter. This reduces latency and signal processing complexity, since no feedback is required.

Part two of this dissertation focuses on the need for a holistic design approach to develop a new generation of autonomous, reliable and unobtrusive SFIT systems, which are capable of establishing and maintaining wireless communication in the harsh and hostile IoT environment without the burden of frequent battery recharging.

In Chapter 4, we exploit the insights gained in Chapter 2 to design a wearable ultra-wideband (UWB) textile antenna for operation in the low-duty cycle restricted [3.4-4.8] GHz UWB band. Our design relies on copper tubular eyelets and textile materials to realize a conformal, light-weight and low-profile UWB cavity-backed slot antenna. Experimental validation shows a very high antenna-to-human-body isolation and stable performance under realistic bending conditions.

In the next chapter, we address two key concerns of SFIT system designers: reliability and autonomy. Therefore, we combine the potential of harvesting energy with setting up a reliable, energy-efficient wireless communication link, implemented in a well-designed textile antenna system. In particular, a wearable textile antenna with integrated solar energy harvester is presented for operation

in the 2.45-GHz-ISM band and the 4G-LTE-band-7. The design relies on a textile dual-band SIW cavity-backed slot antenna to reduce the probability of being disconnected in the highly heterogeneous IoT environment, hence, enhancing reliability and user friendliness. By means of a dedicated design strategy, the surface required by the antenna is then reused for DC-power generation by embedding a power management module and an energy-storage device in the antenna feed plane and a flexible photovoltaic module in the antenna slot plane. In addition, the SIW cavity-backed slot antenna topology minimizes the amount and the length of DC wires, without affecting radiation performance. The latter was validated by comparing free-space gain and reflection coefficient measurements of the antenna with and without energy-harvesting hardware. Performance of the solar wearable textile antenna was validated in realistic conditions by carrying out on-body gain pattern measurements, on-body return loss measurements and by measuring the solar harvesting potential in a realistic environment.

Chapter 6 described already an important step along the long road towards a higher reliability and extended system autonomy. Yet, it is clear that harvesting energy from only one ambient energy source could lead to dangerous situations when this source is no longer available. Just think of a first responder relying on solar energy to power his vital sign monitoring system during an intervention in an underground parking lot. Indeed, a hybrid energy harvesting approach, in which energy is simultaneously scavenged from different energy sources, is necessary to avoid such events. Therefore, Chapter 7 elaborates on the exploitation of the textile antenna as a platform for hybrid-energy-harvesting and power-management hardware. As a starting point, the four primary energy sources are discussed in a body-centric context and the building blocks required to harvest from these sources are outlined. Then, wearable antenna topologies that facilitate the integration procedure are reviewed and an action plan to avoid reduction in antenna performance due to the additional hardware is proposed. Finally, an antenna/hybrid-harvester co-design paradigm is proposed that combines the advantages of both key-enabling technologies without reciprocal detrimental effects. The merits and strength of this paradigm are demonstrated through the realization of a compact and highly-integrated SFIT system, in which a flexible hybrid energy-scavenging system is embedded on a wearable SIW cavity-backed textile slot antenna. Three different actuation techniques are exploited to combine the energy from natural solar light, artificial light and the wearer's body heat. Comparison of the antenna parameters before and after integration of this additional hardware reveals no significant performance degradation, validating this design approach. Furthermore, the energy-harvesting potential was verified in realistic indoor and outdoor conditions. It is shown that the embedded hybrid-energy harvester enables scavenging in most indoor and outdoor situations. Yet, it is important to mention that optimal energy-harvesting only can be obtained when the diverse energy sources are chosen as a function of the application and when the power management system is tailored to the power profile of both the SFIT module and the selected energy-harvesting transducers.

Therefore, in the last chapter of this dissertation, the antenna/harvester co-design paradigm is used as the base for a novel holistic microwave system design paradigm, in which the antenna forms the central component to obtain peak performance. The ambient energy source(s) is(are) selected based on the application. The power management system is tailored to fit the power consumption profile of the wireless communication module on the power generation profile of the energy-harvesting transducer(s). This novel paradigm was applied to realize a novel autonomous wearable radio-frequency identification (RFID) tag for operation in the 2.45-GHz RFID super high frequency (SHF) band. The tag relies on a textile circular patch antenna with tubular eyelets that tailor its radiation pattern for application in a smart floor/ceiling concept. The characteristics of the antenna topology are then exploited to embed sensing, computing, transceiver, and energy-harvesting hardware, without fragile and lossy interconnections. In summary, the holistic design approach leveraged a RFID tag that features excellent wearability, very high read range, enhanced functionality, interfacing with diverse analog or digital sensors, and extended system autonomy.

List of Abbreviations

AC	Alternating Current
ADC	Analog to Digital Converter
AP	Access Point
a-Si:H	Hydrogenated amorphous Silicon
AWGN	Additive White Gaussian Noise
BCI	Boost Converter Input
BELSPO	BELgian Science Policy Office
BESTCOM	BElgian network on STochastic modelling, analysis, design and optimization of COMmunication systems
CBS	Cavity-Backed Slot
CFC	ChloroFluoroCarbon
CNC	Computer Numerically Controlled
COST	COoperation in Science and Technology
CPMS	Central Power Management System
CST	Computer Simulation Technology
DC	Direct Current
ECC	Envelope Correlation Coefficient
ECG	ElectroCardioGraphy
EEG	ElectroEncephaloGraphy
EH	Energy Harvesting
FBW	Fractional BandWidth
FCB	Flexible Circuit Board
FCC	Federal Communications Commission
FLCB	Flexible printed circuit Lithium Ceramic Battery
FOC	Fractional Open Circuit
FTBR	Front-To-Back Ratio
GCPW	Grounded CoPlanar Waveguide
GPS	Global Positioning System
GSM	Global System for Mobile communications
HCFC	HydroChloroFluoroCarbon
HMSIW	Half-Mode Substrate Integrated Waveguide
HPL	High Pressure Laminate
IAP	Inter-university Attraction Poles program
IC	Integrated Circuit
ICNIRP	International Commission on Non-Ionizing Radiation Protection
I^2C	Inter-Integrated Circuit
IoT	Internet of Things

IR-UWB	Impulse Radio Ultra-WideBand
ISM	Industrial Scientific and Medical
LDO	Low-DropOut
LHI	Linear Harvesting Input
LoS	Line-of-Sight
LPS	Low Power System
LTE	Long Term Evolution
MEC	MicroEnergy Cell
MEG	Mean Effective Gain
MIMO	Multiple-Input Multiple-Output
MOSFET	Metal-Oxide-Semiconductor Field-Effect Transistor
MPP	Maximum Power Point
MPPT	Maximum Power Point Tracking
MU	Mobile User
MUX	MUltipleXing
NLoS	Non Line-of-Sight
PCB	Printed Circuit Board
PFM	Pulse-Frequency Modulation
PIFA	Planar Inverted-F Antenna
PKCP	Protected Output of Pack
PMS	Power Management System
PSPICE	Personal computer Simulation Program with Integrated Circuit Emphasis
PV	PhotoVoltaic
RF	Radio-Frequency
RFID	Radio-Frequency IDentification
RTI	Rectenna Topology Indicator
RX	Reception (telegraph abbreviation)
SC	Solar Cell
SFIT	Smart-Fabric Interactive-Textile
SHF	Super High Frequency
SHS	Solar Harvesting System
SIW	Substrate Integrated Waveguide
SMA	SubMiniature version A
SNR	Signal-to-Noise Ratio
SPI	Serial Peripheral Interface
SPICE	Simulation Program with Integrated Circuit Emphasis
TARC	Total Active Reflection Coefficient
TEC	ThermoElectric Cooler
TEG	ThermoElectric Generator
UHF	Ultra-High-Frequency
U-NII	Unlicensed National Information Infrastructure
UTCP	Ultra Thin Chip Package
UVLO	UnderVoltage-LockOut
UWB	Ultra-WideBand

WBAN	Wireless Body Area Network
WLAN	Wireless Local Area Network
WMAN	Wireless Metropolitan Area Network
WPT	Wireless Power Transfer
WSN	Wireless Sensor Network

List of Symbols

$\lvert\cdot\rvert$	Magnitude of a complex or real number
$\cdot^*$	Complex conjugate
$\cdot^H$	Hermetian conjugate
ϵ	Permittivity of a medium
ϵ_r	Relative permittivity
η_{rad}	Radiation efficiency
θ	Elevation angle
λ	Wavelength[1]
σ	Electrical conductivity
φ	Azimuth angle
f	Frequency
$\mathbf{S}$	Scattering matrix
S	Scattering parameters
$tan\ \delta$	Loss tangent
λ	Eigenvalue[2]
C	Channel capacity
E_S	Total average energy over a symbol period at the transmitter
$\mathbf{H}$	Channel matrix
h	Channel coefficients[1]
$\log_2(\gamma_k)$	Ellipticity
$\mathbf{n}$	Additive White Gaussian Noise vector
N_0	Noise power
N_R	Number of receive antennas
N_T	Number of transmit antennas
r	Rank of the singular matrix
$\mathbf{s}$	Transmitted signal vector
$\mathbf{y}$	Received signal vector
α	Seebeck coefficient of all thermocouples
ΔT	Thermal gradient
η	Efficiency
h	heat transfer coefficient[2]
λ	Thermal conductivity[3]
ρ	Electrical resistivity
N_{th}	Number of thermoelectric couples
P	Power

R_G	Electrical resistance of all thermocouples
R_L	Electrical load resistance
R_{th}	Thermal resistance
T_c	Temperature of the cold side of a peltier module
T_h	Temperature of the hot side of a peltier module
V_{oc}	Open circuit voltage
$Z\bar{T}$	Figure of merit for TEG semiconductor materials

List of Publications

Contributions published in International Journals

- G.-J. Stockman, S. Lemey, H. Rogier, and D. Vande Ginste,"Full-Wave Modeling of Interacting Multiport Devices with Arbitrary Relative Positions and Orientations for Efficient EMI Assessment," *IEEE Transactions on Electromagnetic Compatability*, vol. 58, no. 4, pp. 1322–1330, 2016.
- T. Castel, S. Lemey, P. Van Torre, C. Oestges, and H. Rogier, "Four-Element Ultra-Wideband Textile Cross Array for Dual Spatial and Dual Polarization Diversity," *IEEE Antennas and Wireless Propagation Letters*, Accepted 2016.
- S. Lemey, S. Agneessens, P. Van Torre, K. Baes, J. Vanfleteren, and H. Rogier, "Wearable, Flexible, Light-Weight Modular RFID Tag with Integrated Energy Harvester," *IEEE Transactions on Microwave Theory and Techniques*, vol. 64, no. 7, pp. 2304–2314, 2016.
- S. Lemey, T. Castel, P. Van Torre, T. Vervust, J. Vanfleteren, P. Demeester, D. Vande Ginste, and H. Rogier, "Threefold Rotationally Symmetric SIW Antenna Array for Ultra-Short-Range MIMO Communication," *IEEE Transactions on Antennas and Propagation*, vol. 64, no. 5, pp. 1689–1699, 2016.
- T. Castel, P. Van Torre, L. Vallozzi, M. Marinova, S. Lemey, W. Joseph, C. Oestges, and H. Rogier, "Capacity of Broadband Body-to-Body Channels between Firefighters Wearing Textile SIW Antennas," *IEEE Transactions on Antennas and Propagation*, vol. 64, no. 5, pp. 1918–1931, 2016.
- O. Caytan, S. Lemey, S. Agneessens, and H. Rogier, "SIW Antennas as Hybrid Energy Harvesting and Power Management Platforms for the Internet of Things," *International Journal of Microwave and Wireless Technologies*, pp. 1–9, Apr. 2016.
- O. Caytan, S. Lemey, S. Agneessens, D. Vande ginste, P. Demeester, C. Loss, R. Salvado, and H. Rogier, "Half-Mode Substrate-Integrated-Waveguide Cavity-Backed Slot Antenna on Cork Substrate," *IEEE Antennas and Wireless Propagation Letters*, vol. 15, pp. 162-165, 2016.
- S. Agneessens, S. Lemey, T. Vervust, and H. Rogier, "Wearable, Small, and Robust: the Circular Quarter-Mode Textile Antenna," *IEEE Antennas and Wireless Propagation Letters*, vol. 14, pp. 1482–1485, 2015.

- S. Lemey, F. Declercq, and H. Rogier, "Textile Antennas as Hybrid Energy-Harvesting Platforms," *Proceedings of the IEEE*, vol. 102, no. 11, pp. 1833–1857, Nov. 2014.
- S. Lemey, F. Declercq, and H. Rogier, "Dual-Band Substrate Integrated Waveguide Textile Antenna with Integrated Solar Harvester," *IEEE Antennas and Wireless Propagation Letters*, vol. 13, pp. 269–272, 2014.

Articles published in Conference Proceedings

- S. Lemey, O. Caytan, D. Vande Ginste, P. Demeester, H. Rogier, and M. Bozzi, "SIW Cavity-Backed Slot (Multi-)Antenna Systems for the Next-Generation IoT Applications," in *2016 IEEE Topical Conference on Wireless Sensors and Sensor Networks (WiSNet)*, Austin, TX, USA, 24-27 Jan. 2016, pp. 75–77.
- T. Castel, S. Lemey, P. Van Torre, C. Oestges, and H. Rogier, "LTE as a Potential Standard for Public Safety Indoor Body-to-Body Networks," in *22nd IEEE Symposium on Communications and Vehicular Technology in the Benelux*, Luxembourg City, Luxembourg, 24 Nov. 2015, pp. 1–6.
- T. Castel, S. Lemey, S. Agneessens, P. Van Torre, H. Rogier, and C. Oestges, "Reliable Communication between Rescuers During Interventions using Textile Antenna Systems," in *20th IEEE International Workshop on Computer Aided Modelling and Design of Communication Links and Networks*, Guildford, United Kingdom, 7-9 Sept. 2015, pp. 135–139.
- O. Caytan, S. Agneessens, S. Lemey, D. Vande ginste, P. Demeester, and H. Rogier, "Ultra-Wideband Cork Substrate-Integrated-Waveguide Cavity-Backed Slot Antenna," in *2015 International Conference on Electromagnetics in Advanced Applications (ICEAA)*, Turin, Italy, 7-11 Sept. 2015, pp. 1104–1107.
- S. Lemey, S. Agneessens, and H. Rogier,"Textile SIW Antennas as Hybrid Energy Harvesting and Power Management Platforms," in *2015 European Microwave Conference (EuMC)*, Paris, France, 6-11 Sept. 2015, pp. 20–23.
- S. Agneessens, S. Lemey, H. Rogier, T. Vervust, and J. Vanfleteren, "Applying QMSIW Technique in Textile for Compact Wearable Design and High Body-Antenna Isolation," in *2015 IEEE International Symposium on Antennas and Propagation & USNC/URSI National Radio Science Meeting*, Vancouver, Canada, 19-24 Jul. 2015, pp. 1205–1206.
- H. Rogier, S. Agneessens, T. Cuyckens, S. Lemey, P. Vanveerdeghem, L. Vallozzi, and P. Van Torre,"Wireless Power Transfer in a Body-Centric Setup: Recent Advances and Remaining Challenges," in *2015 1st URSI Atlantic Radio Science Conference*, Gran Canaria, Spain, 16-24 May 2015, pp. 1.

- S. Lemey, and H. Rogier,“ Substrate Integrated Waveguide Textile Antennas as Energy Harvesting Platforms,” in *2015 International Workshop on Antenna Technology (iWAT)*, Seoul, Republic of Korea, 4-6 Mar. 2015, pp. 23–26.
- H. Rogier, S. Agneessens, T. Castel, S. Lemey, F. Declercq, P. Vanveerdeghem, P. Van Torre, L. Vallozzi, W. Joseph, “Novel Wearable Antenna Systems for High Datarate Mobile Communication in Healthcare,” in *2014 EAI 4th International conference on Wireless Mobile Communication and Healthcare (Mobihealth)*, Athens, Greece, 3-5 Nov. 2014, pp. 188–191.
- S. Lemey, and H. Rogier, “SIW Textile Antennas as a Novel Technology for UWB RFID tags,” in *2014 IEEE RFID Technology and Applications Conference (RFID-TA)*, Tampere, Finland, 8-9 Sept. 2014, pp. 256–260.
- S. Agneessens, S. Lemey, R. Moro, M. Bozzi, and H. Rogier,“ The Next-Generation Textile Antennas Based on Substrate Integrated Waveguide Technology,” in *Proc. of the XXXIth General Assembly and Scientific Symposium of the International Union of Radio Science*, Beijing, China, 16-23 Aug. 2014, pp. 1–4.

Future Book chapter

- S. Agneessens, S. Lemey, R. Moro, M. Bozzi and H. Rogier, “Textile Substrate Integrated Waveguide Technology for the Next-Generation Wearable Microwave Systems,” in Q. H. Abbasi, M. Ur Rehman and A. Alomainy (Eds.), *State-of-the-art in Body-Centric Wireless Communications and Associated Applications*, IET Press, Expected date of publication: 2016.

Awards

- Best Paper Award at the Topical Conference on Wireless Sensors and Sensor Networks (WiSNet) at Radio Wireless Week (RWW) 2016 (Austin, TX, USA) for the work entitled, *"SIW Cavity-Backed Slot (Multi-)Antenna Systems for the Next Generation IoT Applications"*.
- Co-recipient of the Best Student Paper Award at the 22nd IEEE Symposium on Communications and Vehicular Technology in the Benelux (Luxembourg City, Luxembourg) for the work entitled, *"LTE as a Potential Standard for Public Safety Indoor Body-to-Body Networks"*.

Low-Profile Antenna Systems for the Next-Generation Internet of Things Applications

1 Introduction

1.1 Context

The invention of the transistor by the end of the 1950s and, thereafter, the development of integrated circuits, were the herald of a new era in which the influence of computers and the internet on society has exponentially grown. Whereas, in the 1990s, people sent their first emails and browsed their first web pages by means of a keyboard, a mouse and a lot of patience, most people nowadays are continuously carrying around a multifunctional device, which, by simply touching a screen, allows them to stay in touch with anyone, anywhere on the world at any time of the day, and provides them with fast access to an information source more complete than all of the world's libraries combined.

In the near future, it is expected that the internet will evolve to a true 'Internet of Things' ('IoT'), in which nearly all everyday objects surrounding us will be connected to the internet. By embedding sensors in common objects and combining the potential of the internet with emerging technologies, such as real-time localization [1], radio-frequency identification (RFID) [2], and wireless communication [3], those everyday objects are transformed into smart devices, which are able to understand and respond to their context and environment. In doing so, the IoT offers great potential to revolutionize many aspects of everyone's daily life by giving us unprecedented control over our surroundings, and by enabling us to interact intelligently with those surroundings in ways we cannot even fully imagine today. As a matter of fact, the Internet of Things will bring as massive a change to society as the first internet has done and it is already shaping today, illustrated by the ongoing massive increase in number of internet-connected devices [4].

In this evolution towards an immersively connected world, in which man and machine are in perfect symbiosis, smart surface technology [5], and, more in particular, smart-fabric interactive-textile (SFIT) systems [6], [7], will play a vital

role. Whereas the former facilitates seamless interaction between man and infrastructure by enabling the realization of novel concepts, such as smart floors [8], [9], smart wall papers [10], and smart ceilings [11], the latter offers great potential in increasing quality-of-life of users in their day-to-day activities, owing to a well-balanced combination of seamless integration of functionality within their garments, enhancing the wearer's capabilities, and sufficient comfort to the user for the device to be worn all day long. Numerous application areas can be figured out that may benefit from smart surface and SFIT technology. For instance, in health-care applications, these technologies enable wireless monitoring of vital signs of patients in hospitals or in home-care scenarios [12]–[16], rehabilitation and geriatric care [17]–[19], and epidemiologic studies [20]–[22]. Furthermore, in critical professional applications, SFIT systems leverage monitoring, localization and coordination of first responders during emergencies [23]–[25], allowing to significantly reduce the number of casualties. Leisure activities, such as sports & fitness monitoring [26]–[28], and industrial processes [29] can also be substantially augmented by exploiting the potential of both technologies.

1.2 Motivation

To accelerate the pervasive deployment of the IoT, and to fully unlock its enormous potential, a large number of multidisciplinary challenges still need to be tackled [30]. This dissertation focuses on reconciling the conflicting demands posed by the last three topics of the following four well-known features, considered to be the pillars of IoT systems:

- Data acquisition and processing;
- Wireless communication;
- Energy autonomy;
- Compatibility with objects.

First, the emergence of the IoT will be accompanied, and enabled, by the ongoing massive increase in the number of interconnected objects and persons. Experts estimate that the IoT will consist of almost 24 billion 'things' by 2020 [4]. As a result, huge volumes of data are being generated and each of these 'things' should have the capability to migrate gathered information to the best location, in the meantime providing the highest scalability. In addition, the call for higher-speed wireless connections, driven by various types of future emerging wireless multimedia applications [30], is getting louder and louder. Furthermore, as IoT systems are to be deployed in critical application areas, such as patient monitoring and rescue operations, their reliability is a key requirement, as it could mean the difference between life and death [7], [23]. Obviously, the evolution of the IoT will

be inextricably entwined with an increasing demand for wireless communication systems that are capable of setting up stable, reliable, high-speed wireless communication links, even under harsh environmental conditions in a challenging IoT environment.

Second, efficient use of energy and low power consumption form additional key requirements to accelerate the evolution of the IoT. It stands to reason that the massive increase in number of internet-connected devices will push global energy consumption to unprecedented levels [31]. Moreover, with those billions of 'things' come billions of batteries that must be purchased, maintained, and disposed of. In addition, in critical applications, batteries running out of power, when immediate battery replacement or recharging is impossible, may lead to life-threatening situations [32], [33]. Hence, a two-fold approach is required, in which, on the one hand, low and efficient power consumption is pursued, whereas, on the other hand, the opportunities related to energy-harvesting techniques should be examined to enhance operational autonomy or, in the ideal case, to avoid battery usage at all.

Last, but certainly not least, a smart environment needs to be seamless to the user, imposing the need for a noninvasive integration of intelligence [11], [30]. This does not only encompasses the esthetical point of view, but also requires a shift towards environmentally friendly systems, such that technological progress does not impact on the equilibrium of the natural environment [34]. Moreover, in body-centric systems, seamless integration is even more vital [35]. The wearer should be able to take advantage of the additional functionality, without having to pay the price of reduced comfort.

In summary, a comprehensive approach is essential to reconcile the conflicting demands imposed by these three pillars. Yet, the large diversity in an IoT environment also demands for an application-specific solution, in which the design strategy is tailored to the specific needs and demands of the application. Therefore, in this thesis, we focus on two important research fields within the IoT concept that require such an approach: antenna system design for seamless integration within smart floors, ceilings and desk configurations enabling reliable, very high data rate ultra-short-range wireless communications, on the one hand, and SFIT system design, on the other hand.

1.3 Current state of the art

Given the huge potential of the IoT, and the corresponding economic opportunities, many researchers, from diverse domains in academia and in industry, have contributed to speed up the development of the IoT paradigm. This section summarizes the main research efforts and major progress within both research fields discussed in Section 1.2.

The ever-increasing demand for higher and higher data-rates over wireless con-

nections has led to an increased interest in multiple-input multiple-output (MIMO) wireless communication. It is a cost-effective technology that exploits multiple antennas at transmitter and receiver side to substantially increase channel capacity and/or reliability without increasing transmit power or bandwidth [36], [37]. Aiming at improved channel capacity, originally multipath propagation was exploited to transmit independent information streams over a number of parallel spatial radio propagation channels [38]. Promising results quickly led to the introduction of MIMO techniques in the IEEE 802.11n standard [39], supporting up to four parallel spatial channels, and further elaboration in the subsequent IEEE 802.11ac standard [40], supporting up to eight transmit and eight receiving antennas and beamforming techniques. In addition, they were successfully adopted in an IoT environment to increase data rate [23], to improve reliability [41], [42] or to reduce power consumption [42] in smart textile applications. Only recently, MIMO has been applied in short range or near-field wireless systems [3], [43]–[45]. It was demonstrated that the near-field/short range MIMO scheme features a channel capacity, exceeding the one obtained when multipath propagation is exploited [45]. These new insights offer exciting new opportunities to establish an ultra-short-range, very-high data rate wireless communication link between an access point (AP) integrated into a common object and a mobile user (MU) in its close proximity. Yet, to this moment, no practical designs can be found in literature that fully unlock the potential of this opportunity in a real-life application and environment. On the one hand, this is caused by the stringent demands that are put forward by the IoT paradigm on antenna system design [11], [30]. On the other hand, the near-field MIMO scheme also imposes far-reaching requirements [43], [45], making the design even more challenging.

In the field of SFIT systems, great progress has been made since the first 'all textile' antenna was reported in 2003 [46]. Whereas the first textile antennas typically exhibited single narrow band operation, nowadays, many designs exist that exhibit multiband [47], [48], or ultra-wideband [49], [50] behavior. In the meantime, single linear polarized, dual linear polarized [41], [51], and circularly polarized [25], [52], [53] on-body designs have been proposed in recent years. Most of these designs have been implemented in microstrip line or coplanar waveguide technology. Yet, since recently, a lot of designs exploit the substrate integrated waveguide (SIW) implementation technology [35], [54]–[56] to enhance antenna-human body isolation. The area of textile antenna design has also significantly broadened, covering more and more aspects of SFIT design. Different studies have focused on external influences that might degrade antenna operation, such as the proximity of the human body [57], movements of the wearer [58], [59], washing [60], [61], varying environmental conditions [52], [62], and fabrication tolerances [63]. Dedicated material characterization techniques have been developed [64], [65] and strategies to embed active electronics onto the textile antenna have been researched [7], [66]. To this moment, the major operational constraint of SFIT systems is related to its limited system autonomy [67]. To maximize battery life, the primary solution of current generation SFIT systems consists of using energy in

an intelligent manner and avoiding unnecessary power dissipation. [68] demonstrated that a carefully designed textile antenna system can substantially reduce power consumption, whereas [42] shows that multiple of such highly-efficient textile antennas could be deployed onto the user's body to increase autonomy even more. Operational autonomy can be extended even further by extracting energy from ambient sources, such as solar [69]–[71] and RF energy [72], [73], or from the user's activities, generating body heat [74]–[76], breathing [77], or walking [78], [79]. This energy scavenging can be performed at the place where the smart textile is worn by the user. Preferably, energy is harvested from multiple different energy sources to increase the amount of collected energy and to guarantee a higher continuity in the energy flow. Various attempts have been made to prolong operational autonomy with energy-harvesting techniques. Yet, the key challenge appears to be the co-design of antenna system and energy-harvesting hardware in order to embed the required additional energy-harvesting transducers and power management system, without affecting antenna performance and the end user's comfort.

1.4 Own contributions

The research efforts in this work are aimed at tackling two fundamental technological challenges. First, we focus on the demand for seamlessly integrated wireless communication systems that are capable of setting up a reliable, energy-efficient, high-speed wireless communication link to bring information exchange between backbone infrastructure and mobile users to the next level. Second, we focus on the main deficiency of the current generation SFIT systems, being their limited operational autonomy, and more in general, on the pursuit of autonomous, reliable and unobtrusive SFIT systems, that are capable of establishing and maintaining wireless communication in a harsh environment.

The first part of this dissertation focuses on the first of both technological challenges and describes two critical aspects. First, a new generation of ultra-wideband, high-performance, low-cost (multi-)antenna designs is proposed that facilitate seamless and robust integration within the smart floor, ceiling and furniture concept. Therefore, the advantages of the conventional cavity-backed slot antenna topology, being a large radiation efficiency and an excellent isolation from its environment at out-of-band frequencies and in unwanted directions, are combined with the advantages of planar antenna technology, being low profile, low fabrication cost, and easy integration with planar circuitry. This is done by adopting the SIW technology to implement the cavity backing the radiating slot. In addition, the opportunity to reuse the object's materials to implement the SIW structure is exploited, leveraging a significant cost reduction and a maximum compatibility with the object acting as integration platform. Furthermore, multiple hybrid modes are excited to enhance bandwidth, whereas antenna miniaturization is obtained by relying on the symmetry of these modes, yielding a compact, yet broadband, de-

sign. The merits and potential of this approach are demonstrated by the practical realization of two novel antenna designs. First, a compact, three-element ultra-wideband antenna array is proposed with very low mutual coupling, enabling integration into furniture by adopting a closed-cell expanded rubber as a substrate. Second, a miniaturized, yet ultra-wideband, half-mode SIW antenna is presented for seamless integration in cork floors and walls, adopting the readily available cork as antenna substrate. Both designs were realized and validated in free space and after integration into the actual application environment, proving their excellent performance and huge potential to intertwine technology even more with our everyday lives. The second aspect encompasses the effective integration procedure of the three-element antenna array within a desk to establish a stable, high data rate ultra-short-range 3 x 3 MIMO wireless communication link with a MU positioned on top of that worktop. For the first time in literature, wideband MIMO performance is investigated for separations over distances ranging from only a fraction of the operating wavelength to several wavelengths, and for different relative orientations and positions of the MU, in a realistic scenario in which integration aspects are fully taken into account. In fact, the multiplexing gain offered by the ultra-short-range 3 x 3 MIMO channel, implemented with our novel arrays, allows a significant reduction in transmit power, in the meantime guaranteeing data rates that are comparable to those established by ethernet-connected devices (100 Mbps for 100base-T, 1 Gbps for 1000base-T, and 10 Gbps for 10 Gbase-T).

The second part of this thesis presents our research efforts devoted to the major operational constraint of the current generation SFIT systems, being the limited system autonomy and the corresponding burden of frequent recharging or battery replacement. Our approach is twofold. On the one hand, a vast amount of attention is devoted to the textile antenna component within the SFIT, as inappropriate design of this critical component will inadvertently lead to bad signal quality, short range, low data rates, high power consumption (and quickly drained batteries), and discomfort to the user. On the other hand, the potential of exploiting energy-harvesting techniques to increase system autonomy is examined. To this end, the four primary energy-harvesting sources are reviewed and their potential in a body-centric context is analyzed. Furthermore, the key building blocks to convert and combine the small and highly-fluctuating levels of ambient energy into a form that is useful for empowering SFIT systems are identified. Although garments provide sufficient space to integrate a textile (multi-)antenna system, a carefully considered integration strategy is required to add energy-harvesting hardware, in order to harvest sufficient amounts of energy, on the one hand, and to maintain the user's comfort, on the other hand, without affecting antenna performance. Therefore, we introduce a novel antenna/harvester co-design paradigm that combines the advantages of both key-enabling technologies without reciprocal detrimental effects. It relies on reusing the surface required by the textile (multi-)antenna system as power management and energy-harvesting platform. In a first step, an ultra-wideband textile antenna was designed that boasts excellent on-body performance. In a second step, this design was slightly modified and the novel an-

tenna/harvester co-design procedure was applied to design a 2.45-GHz-ISM/4G-LTE-band-7 dual-band wearable textile antenna with integrated solar harvester. The dual-band character, maximizing compatibility and user flexibility within the highly heterogeneous IoT environment, in combination with the compact embedded solar harvester to enhance system autonomy, provides a huge step forward in guaranteeing sufficient robustness, comfort and autonomy for reliable deployment in critical applications. In a subsequent design, operational autonomy was taken to an even higher level by the integration of a hybrid energy harvesting architecture. For the first time in literature, a compact and highly-integrated SFIT module was presented that is not only able to set up a reliable and energy-efficient wireless communication link, but also to simultaneously harvest energy from up to three different energy sources. In particular, measurements in five well-chosen indoor and outdoor scenarios demonstrate that our system is capable of combining the energy scavenged from artificial light in an indoor environment, from solar light in an outdoor environment and from the heat emanated by the user's body. Obviously, such a hybrid energy harvesting approach reduces the time during which no energy is harvested and increases the overall amount of harvested energy. Finally, our antenna/harvester co-design strategy was combined with an already existing active textile antenna co-design procedure to form a holistic microwave system design paradigm, in which antenna design is taken into consideration from the very early stages and the power generation profile of the energy harvester is tailored to the power consumption profile of the wireless communication module, and vice versa. This novel paradigm leverages a novel autonomous wearable RFID tag for operation in the 2.45-GHz RFID super high frequency (SHF) band, with an unprecedented combination of excellent wearability, very high read range, enhanced functionality, flexible interfacing with diverse low-power sensors, and extended system autonomy. The RFID tag allows pervasive quantification of the user's interaction with his/her environment, by wirelessly migrating physical information about the wearer and his/her nearby environment to the internet via a question-and-reply protocol, without the discomfort of carrying heavy equipment. Moreover, frequent recharging or replacing batteries is avoided.

1.5 Overview of the manuscript

This dissertation focuses on two main aspects related to antenna system design for the Internet of Things. First, innovations are proposed in antenna system design for seamless integration within smart floors, ceilings and desk configurations. These antenna configurations enable reliable, high data rate ultra-short-range wireless communication. Second, autonomous SFIT systems are realized with textile antennas as key enablers for high performance operation.

Part one of the work identifies SIW cavity-backed slot antenna topologies as promising candidates to address the specific antenna design challenges posed by the IoT. Special attention was devoted to reconcile conflicting demands: ultra-wideband

behavior, high performance, compactness, recyclability, and high antenna-to-integration-platform isolation. Furthermore, these features were exploited to satisfy the need for wireless communication systems that are invisibly integrated inside smart floors, ceilings and desk configurations. In these settings, they are able to provide very high data rates in only a particular area of a room.

In Chapter 2, their potential is demonstrated by discussing two novel designs on two different, application-specific, innovative substrate materials. First, a compact, ultra-wideband three-element array with very low mutual coupling is presented for integration into furniture. In the second design, the half-mode SIW technique is applied to obtain a miniaturized ultra-wideband design, enabling invisible integration into cork floor and wall tiles. Measurements have been performed and demonstrate excellent performance in free-space and in a realistic IoT environment, proving the strength of our approach for IoT applications.

In Chapter 3, multiple scenarios are proposed and analyzed to integrate the three-element antenna array, presented in Chapter 2, inside or underneath the worktop of a desk. At that location, the array sets up a stable, high data-rate ultra-short-range 3 x 3 MIMO wireless communication link with a mobile user positioned on top of that worktop. Special care was taken to maximally exploit the multiplexing capabilities of the ultra-short-range 3 x 3 MIMO channel over a wide bandwidth. In addition, guidelines are provided to guarantee a channel capacity that is less dependent on the relative orientation of the mobile user. Measurements in a realistic operating scenario have revealed a high and stable multiplexing gain, which can be used to reduce power consumption and/or to increase the data rate, making the array an ideal candidate to provide an ultra-high data-rate wireless connection at each seat in a meeting room, or, as a more seamless and user-friendly alternative for wired docking stations.

Part two of this thesis focuses on two key concerns related to current generation SFIT systems, being autonomy and reliability. To this end, an innovative holistic microwave system design paradigm for SFIT systems is pursued, in which antenna design is taken into consideration from the very early stages. Our design approach relies on augmenting the functionality of a carefully designed textile antenna, by reusing its surface as an integration platform for the other key building blocks of an SFIT, with a special focus on energy-harvesting and power management hardware. In this way, a robust, compact, highly-integrated and unobtrusive wearable textile antenna system is obtained, which is capable of establishing a reliable and energy-efficient wireless body-centric communication link, empowered by energy harvested from ambient sources at the location where the SFIT is worn by the user.

As a first step, Chapter 4 exploits the expertise acquired in Chapter 2 to design a compact, yet ultra-wideband, textile antenna. Measurements demonstrate high, and stable, performance when deployed on different human body parts and under realistic bending conditions.

Chapter 5 describes our novel antenna/harvester co-design procedure and leverages the first 2.45-GHz ISM/4G-LTE-band-7 dual-band wearable textile antenna

with integrated solar harvester in literature. This design represents a huge leap forward in guaranteeing sufficient reliability, comfort and autonomy for usage in critical applications. Whereas the dual-band character reduces the probability of being disconnected in life-threatening situations, the integrated solar harvester (including power management and energy storage) provides a regulated output for adequately powering the SFIT system based on energy extracted from ambient light, thereby enhancing system autonomy. In addition, the novel antenna-harvester co-design procedure minimizes the amount and length of fragile interconnections, bringing more comfort to the user and yielding a higher robustness.

Given the huge potential of energy-harvesting techniques in body-worn applications, Chapter 6 discusses more in depth the opportunities related to the exploitation of a textile antenna system as an integration platform for energy-harvesting and power management hardware. Besides presenting the four primary energy-harvesting sources in a body-centric context, suitable antenna topologies that facilitate integration of energy-harvesting hardware are identified, and measures that should be taken to avoid a reduction in antenna performance are outlined. In addition, the necessity of hybrid energy harvesting, in which energy is scavenged simultaneously from different energy sources, is stressed. Finally, the integration of a flexible hybrid energy-scavenging system onto a wearable SIW cavity-backed textile slot antenna is described. This was the first compact and highly integrated wearable textile antenna system that is capable of simultaneous harvesting of energy from three different ambient energy sources. In particular, by combining the energy scavenged by a photovoltaic (PV) module from artificial light in an indoor environment and the energy scavenged by a thermoelectric generator from the heat emanated by the user's body, energy harvesting is enabled in most indoor situations. Moreover, by including a second PV module, significant amounts of solar power can be scavenged in outdoor environments. Measurements, conducted in realistic indoor and outdoor conditions, prove that the selected textile antenna is indeed suitable as an integration platform, and that the hybrid energy-harvesting approach leads to a higher amount of scavenged energy in a more continuous way.

Chapter 7 presents a novel autonomous wearable RFID tag with sensing, processing, and decision-taking capability for operation in the 2.45-GHz RFID super high frequency band. The base of the proposed active RFID tag now consists of a dedicated textile shorted circular patch antenna with tailored radiation pattern for communication with a smart floor/ceiling. Based on the insights gained in Chapters 5 and 6, the textile antenna's functionality is substantially augmented by reusing its surface as an integration platform for light-energy-harvesting, sensing, processing, and transceiver hardware, without sacrificing antenna performance or the wearer's comfort. The unprecedented combination of excellent wearability, very high read range, enhanced functionality, flexible interfacing with diverse low-power sensors, and extended system autonomy, leverages pervasive quantification of the wearer's interaction with his/her environment, by wirelessly communicating physical information about the wearer and his/her nearby environment to the internet via a

question-and-reply protocol, without the burden of frequent recharging or replacing batteries.

References

[1] C.-H. Lim, Y. Wan, N. Boon-Poh, and C.-M. See, "A Real-Time Indoor WiFi Localization System Utilizing Smart Antennas", *IEEE Trans. Consumer Electron.*, vol. 53, no. 2, pp. 618–622, 2007.

[2] E. Welbourne, L. Battle, G. Cole, K. Gould, K. Rector, S. Raymer, M. Balazinska, and G. Borriello, "Building the Internet of Things Using RFID: The RFID Ecosystem Experience", *IEEE Internet Comput.*, vol. 13, no. 3, pp. 48–55, May 2009.

[3] K. Nishimori, N. Honma, T. Seki, and K. Hiraga, "On the Transmission Method for Short-Range MIMO Communication", *IEEE Trans. Veh. Technol.*, vol. 60, no. 3, pp. 1247–1251, Mar. 2011.

[4] J. Gubbi, R. Buyya, S. Marusic, and M. Palaniswami, "Internet of Things (IoT): A vision, architectural elements, and future directions", *Future Gener. Comp. Sy.*, vol. 29, no. 7, pp. 1645–1660, Sep. 2013.

[5] L. Roselli, N. Borges Carvalho, F. Alimenti, P. Mezzanotte, G. Orecchini, M. Virili, C. Mariotti, R. Goncalves, and P. Pinho, "Smart Surfaces: Large Area Electronics Systems for Internet of Things Enabled by Energy Harvesting", *Proc. IEEE*, vol. 102, no. 11, pp. 1723–1746, 2014.

[6] J. Cheng, P. Lukowicz, N. Henze, A. Schmidt, O. Amft, G. A. Salvatore, and G. Troster, "Smart Textiles: From Niche to Mainstream", *IEEE Pervasive Computing*, vol. 12, no. 3, pp. 81–84, 2013.

[7] A. Dierck, S. Agneessens, F. Declercq, B. Spinnewyn, G.-J. Stockman, P. Van Torre, L. Vallozzi, D. Vande Ginste, J. Vanfleteren, T. Vervust, and H. Rogier, "Active Textile Antennas in Professional Garments for Sensing, Localisation and Communication", *International Journal of Microwave and Wireless Technologies*, vol. 6, no. 3-4, pp. 331–341, 2014.

[8] S. Chang, S. Ham, S. Kim, D. Suh, and H. Kim, "Ubi-Floor: Design and Pilot Implementation of an Interactive Floor System", in *Proc. 2nd Int. Conf. Intell.Human-Mach. Syst. and Cybern.*, Nanjing, China, 26-28 Aug. 2010, pp. 290–293.

[9] R. Goncalves, J. Reis, E. Santana, N. B. Carvalho, P. Pinho, and L. Roselli, "Smart floor: Indoor navigation based on RFID", in *Proc. IEEE Wireless Power Transfer*, May 2013, pp. 103–106.

[10] M. Shur, "Giant area and flexible electronics", in *Proc. IEEE Nanotechnol. Mater. Devices Conf.*, vol. 1, Oct. 2006, pp. 264–265.

[11] O. Caytan, S. Lemey, S. Agneessens, D. Vande Ginste, P. Demeester, C. Loss, R. Salvado, and H. Rogier, "Half-mode substrate-integrated-waveguide cavity-backed slot antenna on cork substrate", *Antennas Wirel. Propag. Lett.*, vol. 15, no. 99, pp. 162–165, May 2015.

[12] A. Fanelli, M. Ferrario, L. Piccini, G. Andreoni, G. Matrone, G Magenes, and M. Signorini, "Prototype of a wearable system for remote fetal monitoring during pregnancy", in *Engineering in Medicine and Biology Society (EMBC), 2010 Annual International Conference of the IEEE*, IEEE, 2010, pp. 5815–5818.

[13] M. Di Rienzo, F. Rizzo, G. Parati, G. Brambilla, M. Ferratini, and P. Castiglioni, "MagIC system: A new textile-based wearable device for biological signal monitoring. Applicability in daily life and clinical setting.", in *27th Annual International Conference of Engineering in Medicine and Biology Society, 2005.*, 2005, pp. 7167–7169.

[14] Y. Hao and R. Foster, "Wireless body sensor networks for health-monitoring applications", *Physiol. Meas.*, vol. 29, no. 11, pp. 27–56, 2008.

[15] A. Pantelopoulos and N. Bourbakis, "A Survey on Wearable Sensor-Based Systems for Health Monitoring and Prognosis", *IEEE Transactions on Systems, Man, and Cybernetics, Part C: Applications and Reviews*, vol. 40, no. 1, pp. 1–12, Jan. 2010.

[16] N. Oliver and F. Flores-Mangas, "HealthGear: A real-time wearable system for monitoring and analyzing physiological signals", in *International Workshop on Wearable and Implantable Body Sensor Networks, 2006.*, Cambridge, MA, USA, 3-5 Apr. 2006, pp. 4–64.

[17] S. Patel, H. Park, P. Bonato, L. Chan, and M. Rodgers, "A review of wearable sensors and systems with application in rehabilitation", *Journal of neuroengineering and rehabilitation*, vol. 9, no. 1, pp. 9–21, 2012.

[18] T. Faetti and R. Paradiso, "A novel wearable system for elderly monitoring", *Advances in Science and Technology*, vol. 85, pp. 17–22, Sept. 2012.

[19] S. Amendola, R. Lodato, S. Manzari, C. Occhiuzzi, and G. Marrocco, "RFID Technology for IoT-Based Personal Healthcare in Smart Spaces", *IEEE Internet Things J.*, vol. 1, no. 2, pp. 144–152, Apr 2014.

[20] A. Thielens, H. De Clercq, S. Agneessens, J. Lecoutere, L. Verloock, F. Declercq, G. Vermeeren, E. Tanghe, H. Rogier, R. Puers, *et al.*, "Personal distributed exposimeter for radio frequency exposure assessment in real environments", *Bioelectromagnetics*, vol. 34, no. 7, pp. 563–567, 2013.

[21] A. Thielens, P. Vanveerdeghem, S. Agneessens, G. Vermeeren, H. Rogier, L. Martens, and W. Joseph, "Whole-Body Averaged Specific Absorption Rate Estimation using a Personal, Distributed Exposimeter", *IEEE Antenn. Wireless Propag. Lett.*, vol. 14, pp. 1534–1537, 2014.

[22] P. Vanveerdeghem, P. Van Torre, A. Thielens, J. Knockaert, W. Joseph, and H. Rogier, "Compact Personal Distributed Wearable Exposimeter", *IEEE Sensors Journal*, vol. 15, no. 8, pp. 4393–4401, Aug. 2015.

[23] T. Castel, P. Van Torre, L. Vallozzi, M. Marinova, S. Lemey, W. Joseph, C. Oestges, and H. Rogier, "Capacity of Broadband Body-to-Body Channels between Firefighters wearing Textile SIW Antennas", *IEEE Trans. Antennas Propagat.*, vol. PP, no. 99, pp. 1–10, 2016.

[24] S. Agneessens, P. Van Torre, F. Declercq, B. Spinnewyn, G.-J. Stockman, H. Rogier, and D. Vande Ginste, "Design of a wearable, low-cost, through-wall doppler radar system", *Int. J Antennas Propag*, vol. 2012, pp. 1–9, 2012.

[25] A. Dierck, H. Rogier, and F. Declercq, "A Wearable Active Antenna for Global Positioning System and Satellite Phone", *IEEE Trans. Antennas Propag.*, vol. 61, no. 2, pp. 532–538, Feb. 2013.

[26] C. Katsis, Y Goletsis, G Rigas, and D. Fotiadis, "A wearable system for the affective monitoring of car racing drivers during simulated conditions", *Transportation research part C: Emerging technologies*, vol. 19, no. 3, pp. 541–551, 2011.

[27] J. Chardonnens, J. Favre, B. Le Callennec, F. Cuendet, G. Gremion, and K. Aminian, "Automatic measurement of key ski jumping phases and temporal events with a wearable system", *Journal of sports sciences*, vol. 30, no. 1, pp. 53–61, 2012.

[28] C.-N. Lee, L. Chan, C.-Y. Yang, G.-Y. Lee, and C.-R. Ciou, "The design and implementation of the E-BIKE physiological monitoring prototype system for cyclists", in *IEEE iWEM2011*, Taipei, Taiwan, 8-10 Aug. 2011, pp. 161–165.

[29] H. Ramamurthy, B. S. Prabhu, R. Gadh, and A. M. Madni, "Wireless Industrial Monitoring and Control Using a Smart Sensor Platform", *IEEE Sensors Journal*, vol. 7, no. 5, pp. 611–618, May 2007.

[30] H. Sundmaeker, P. Guillemin, P. Friess, and S. Woelffle, Eds., *Vision and challenges for realising the internet of things.* Luxembourg: Publications Office of the European Union, 2010.

[31] V. Kardeby, U. Jennehag, and M. Gidlund, "Power consumption for global information dissemination in the Internet of Things", in *2015 IEEE Tenth International Conference on Intelligent Sensors, Sensor Networks and Information Processing (ISSNIP)*, Singapore, 7-9 Apr. 2015, pp. 1–6.

[32] S. Lemey, F. Declercq, and H. Rogier, "Dual-band substrate integrated waveguide textile antenna with integrated solar harvester", *IEEE Antenn. Wireless Propag. Lett.*, vol. 13, no. 1, pp. 269–272, 2014.

[33] ——, "Textile antennas as hybrid energy-harvesting platforms", *Proc. IEEE*, vol. 102, no. 11, pp. 1833–1857, Nov. 2014.

[34] M. Bozzi and R. Moro, "Low-cost fabrication, eco-friendly materials, and easy integration: the new technological paradigm for the future wireless sensor networks", in *European Microwave Conference (EuMC)*, Nuremberg, Germany, Oct. 6-10, 2013, pp. 858–861.

[35] S. Agneessens, S. Lemey, T. Vervust, and H. Rogier, "Wearable, small, and robust: the circular quarter-mode textile antenna", *IEEE Antenn. Wireless Propag. Lett.*, vol. 14, pp. 1482–1485, 2015.

[36] Y. Karasawa, "Innovative Antennas and Propagation Studies for MIMO Systems", *IEICE Transactions on Communications*, vol. E90-B, no. 9, pp. 2194–2202, Sep. 2007.

[37] B. Clerckx, C. Craeye, D. Vanhoenacker-Janvier, and C. Oestges, "Impact of Antenna Coupling on 2 x 2 MIMO Communications", *IEEE Trans. Veh. Technol.*, vol. 56, no. 3, pp. 1009–1018, 2007.

[38] M. Jensen and J. Wallace, "A Review of Antennas and Propagation for MIMO Wireless Communications", *IEEE Trans. Antennas Propagat.*, vol. 52, no. 11, pp. 2810–2824, 2004.

[39] "802.11n", IEEE Standard for Information technology - Local and metropolitan area networks - Specific requirements - Part 11: Wireless LAN Medium Access Control (MAC) and Physical Layer (PHY) Specifications - Amendment 5: Enhancements for Higher Througput, Tech. Rep., 2009.

[40] "802.11ac", IEEE Standard for Information technology - Telecommunications and information exchange between systems - Local and metropolitan area networks - Specific requirements - Part 11: Wireless LAN Medium Access Control (MAC) and Physical Layer (PHY) Specifications - Amendment 4: Enhancements for Very High Throughput for Operation in Bands below 6 GHz, Tech. Rep., 2013.

[41] P. Van Torre, L. Vallozzi, C. Hertleer, H. Rogier, M. Moeneclaey, and J. Verhaevert, "Indoor Off-Body Wireless MIMO Communication With Dual Polarized Textile Antennas", *IEEE Trans. Antennas Propag.*, vol. 59, no. 2, pp. 631–642, Feb 2011.

[42] P. Van Torre, L. Vallozzi, A. Dierck, H. Rogier, and M. Moeneclaey, "Power-efficient Body-centric Communications", in *URSI Benelux Forum*, 14 Sept. 2012, pp. 8–10.

[43] J.-S. Jiang and M. Ingram, "Spherical-wave model for short-range MIMO", *IEEE Transactions on Communications*, vol. 53, no. 9, pp. 1534–1541, Sep. 2005.

[44] F. Bohagen, P. Orten, and G. Oien, "Construction and capacity analysis of high-rank line-of-sight MIMO channels", in *Wireless Communications and Networking Conference, 2005 IEEE*, vol. 1, New Orleans, LA, USA, 13-17 March 2005, pp. 432–437.

[45] N. Honma, K. Nishimori, T. Seki, and M. Mizoguchi, "Short range MIMO communication", in *Proc. of the 3th European Conference on Antennas and Propagation (EUCAP)*, Berlin, Germany, 23-27 March 2009, pp. 1763–1767.

[46] P. Salonen and L Hurme, "A novel fabric WLAN antenna for wearable applications", in *IEEE Antennas and Propagation Society International Symposium, 2003.*, vol. 2, Columbus, OH, USA, 22-27 Jun. 2003, pp. 700–703.

[47] P. Soh, G. Vandenbosch, S. Ooi, and M. Husna, "Wearable dual-band Sierpinski fractal PIFA using conductive fabric", *Electronics Letters*, vol. 47, no. 6, pp. 365–367, 2011.

[48] S. Z. Zhu and R. Langley, "Dual-Band Wearable Textile Antenna on an EBG Substrate", *IEEE Trans. Antennas Propagat.*, vol. 57, no. 4, pp. 926–935, Apr. 2009.

[49] P. Samal, P. Soh, and G. Vandenbosch, "UWB All-Textile Antenna With Full Ground Plane for Off-Body WBAN Communications", *IEEE Trans. Antennas Propagat.*, vol. 62, no. 1, pp. 102–108, 2014.

[50] M. Klemm and G. Troester, "Textile UWB antennas for wireless body area networks", *IEEE Trans. Antennas Propagat.*, vol. 54, no. 11, pp. 3192–3197, Nov. 2006.

[51] L. Vallozzi, P. Van Torre, C. Hertleer, H. Rogier, M. Moeneclaey, and J. Verhaevert, "Wireless communication for firefighters using dual-polarized textile antennas integrated in their garment", *IEEE Trans. Antennas Propag.*, vol. 58, no. 4, pp. 1357–1368, Apr. 2010.

[52] C. Hertleer, H. Rogier, L. Vallozzi, and L. Van Langenhove, "A Textile Antenna for Off-Body Communication Integrated Into Protective Clothing for Firefighters", *IEEE Trans. Antennas Propagat.*, vol. 57, no. 4, pp. 919–925, 2009.

[53] M. Klemm, I. Locher, and G. Troster, "A novel circularly polarized textile antenna for wearable applications", in *Proc. 7th Eur. Conf. Wirel. Tech.*, Amsterdam, The Netherlands, 11-12 Oct. 2004, pp. 285–288.

[54] R. Moro, S. Agneessens, H. Rogier, and M. Bozzi, "Wearable textile antenna in substrate integrated waveguide technology", *IET Electron. Lett.*, vol. 48, no. 16, pp. 985–987, Aug. 2012.

[55] R. Moro, S. Agneessens, H. Rogier, A. Dierck, and M. Bozzi, "Textile Microwave Components in Substrate Integrated Waveguide Technology", *IEEE Transactions on Microwave Theory and Techniques*, vol. 63, no. 2, pp. 422–432, 2015.

[56] S. Agneessens and H. Rogier, "Compact Half Diamond Dual-Band Textile HMSIW On-Body Antenna", *IEEE Trans. Antennas Propagat.*, vol. 62, no. 5, pp. 2374–2381, 2014.

[57] P. Salonen, Y. Rahmat-Samii, and M. Kivikoski, "Wearable antennas in the vicinity of human body", in *IEEE Antennas and Propagation Society International Symposium, 2004.*, IEEE, vol. 1, 2004, pp. 467–470.

[58] F. Boeykens, L. Vallozzi, and H. Rogier, "Cylindrical Bending of Deformable Textile Rectangular Patch Antennas", *International Journal of Antennas and Propagation*, p. 170 420, 2012.

[59] F. Boeykens, H. Rogier, and L. Vallozzi, "An efficient technique based on polynomial chaos to model the uncertainty in the resonance frequency of textile antennas due to bending", *IEEE Trans. Antennas Propagat.*, vol. 62, no. 3, pp. 1253–1260, 2014.

[60] T. Kellomäki, J. Virkki, S. Merilampi, and L. Ukkonen, "Towards washable wearable antennas: A comparison of coating materials for screen-printed textile-based UHF RFID tags", *International Journal of Antennas and Propagation*, vol. 2012, 2012.

[61] M. L. Scarpello, I. Kazani, C. Hertleer, H. Rogier, and D. Vande Ginste, "Stability and efficiency of screen-printed wearable and washable antennas", *IEEE Antenn. Wireless Propag. Lett.*, vol. 11, pp. 838–841, 2012.

[62] M. Scarpello, D. Vande Ginste, and H. Rogier, "Design of a low-cost steerable textile antenna array operating in varying relative humidity conditions.", *Microw. Opt. Technol. Lett.*, vol. 54, no. 1, pp. 40–44, Jan. 2012.

[63] M. Rossi, A. Dierck, H. Rogier, and D. Vande Ginste, "A Stochastic Framework for the Variability Analysis of Textile Antennas", *IEEE Trans. Antennas Propagat.*, vol. 62, no. 12, pp. 6510–6514, Dec. 2014.

[64] F. Declercq, H. Rogier, and C. Hertleer, "Permittivity and loss tangent characterization for garment antennas based on a new matrix-pencil two-line method", *IEEE Trans. Antennas Propagat.*, vol. 56, no. 8, pp. 2548–2554, Aug. 2008.

[65] F. Declercq, I. Couckuyt, H. Rogier, and T. Dhaene, "Environmental High Frequency Characterization of Fabrics Based on a Novel Surrogate Modelling Antenna Technique", *IEEE Trans. Antennas Propagat.*, vol. 61, no. 10, pp. 5200–5213, Oct. 2013.

[66] P. Vanveerdeghem, H. Rogier, J. Knockaert, P. Van Torre, and C. Stevens, "Flexible dual-diversity wearable wireless node integrated on a dual-polarised textile patch antenna", *IET Science, Measurement & Technology*, vol. 8, no. 6, pp. 452–458, Nov. 2014.

[67] M. A. Hanson, "Body Area Sensor Networks: Challenges and Opportunities", *Computer*, vol. 42, no. 1, pp. 58–65, 2009.

[68] P. Vanveerdeghem, B. Jooris, P. Becue, P. Van Torre, H. Rogier, I. Moerman, and J. Knockaert, "Reducing power consumption in body-centric zigbee communication links by means of wearable textile antennas", in *Proc. 2nd Int. Workshop Meas.-Based Exp. Res. Methodol. Tools*, vol. 4, Dublin, Ireland, 7 May 2013, pp. 1–5.

[69] B Markus and H Jurgen, "Flexible solar cells for clothing", *Mater. Today*, vol. 9, no. 6, pp. 42–50, 2006.

[70] K. Sangani, "Power solar: the sun in your pocket", *Eng. Technol.*, vol. 2, no. 8, pp. 36–38, Aug. 2007.

[71] F. Declercq, A. Georgiadis, and H. Rogier, "Wearable Aperture-Coupled Shorted Solar Patch Antenna for Remote Tracking and Monitoring Applications", in *Proc. 5th Eur. Conf. Antennas Propag. (EUCAP)*, Rome, Italy, 11-15 Apr. 2011, pp. 2992–2996.

[72] G. Andia Vera, A. Georgiadis, A. Collado, and S. Via, "Design of a 2.45 GHz rectenna for electromagnetic (EM) energy scavenging", in *Proc. Radio Wireless Symp.*, New Orleans, LA, USA, 10-14 Jan. 2010, pp. 61–64.

[73] A. Nimo, D. Grgic, and L. M. Reindl, "Optimization of passive low power wireless electromagnetic energy harvesters", *Sensors*, vol. 12, no. 10, pp. 13 636–13 663, 2012.

[74] L. Mateu, C. Codrea, N. Lucas, M. Pollak, and P. Spies, "Human body energy harvesting thermogenerator for sensing applications", in *Proc. Int. Conf. Sensor Technol. Appl.*, Valencia, Spain, 14-20 Oct. 2007, pp. 366–372.

[75] L Francioso, C De Pascali, I Farella, C Martucci, P Creti, P Siciliano, and A Perrone, "Flexible Thermoelectric Generator for Wearable Biometric Sensors", in *Proc. IEEE Sensors*, Kona, HI, USA, 1-4 Nov. 2010, pp. 747–750.

[76] M. Lossec, B. Multon, H. Ahmed, and C. Goupil, "Thermoelectric generator placed on the human body: system modeling and energy conversion improvements", *Eur. Phys. J.*, vol. 52, no. 1, pp. 1–10, 2010.

[77] T. Starner, "Human-powered wearable computing", *IBM Syst. J.*, vol. 35, no. 3, pp. 618–629, 1996.

[78] G. Orecchini, L. Yang, M Tentzeris, and L. Roselli, "Smart Shoe: An autonomous inkjet-printed RFID system scavenging walking energy", in *Proc. IEEE Int. Symp. Antennas and Propagation (APSURSI)*, Spokane, WA, USA, 3-8 Jul. 2011, pp. 1417–1420.

[79] Y Minami and E Nakamachi, "Development of enhanced piezoelectric energy harvester induced by human motion", in *Proc. Annu. Int. Conf. IEEE Eng. Med. Biol. Soc.*, San Diego, CA, USA, 28 Aug. - 1 Sept. 2012, pp. 1627–1630.

Part I

Antenna Systems for Integration in Smart Floors, Ceilings and Desk Configurations

In the vision of the Internet of Things, there is a strong need for wireless communication systems that may be seamlessly and invisibly integrated inside common objects and that support very high data rates to cope with the huge volumes of data generated by the ever-increasing amount of interconnected smart objects. This far-reaching integration, the ever increasing demand for higher data rates and the challenging IoT environment make antenna design for IoT applications more challenging. In Chapter 2, we propose a new class of high-performance low-cost ultra-wideband antenna designs that facilitate robust and invisible integration. Their potential is proven by the realization and validation of two novel designs that envision application in a smart floor, ceiling and desk configuration, guaranteeing seamless interaction between a person/object and the back bone infrastructure. In Chapter 3, the features of this novel class of antennas are exploited to invisibly integrate an antenna array within a desk. The module sets up a stable, high-speed ultra-short-range MIMO wireless communication link with a mobile user, such as a laptop or tablet, positioned on top of that desk.

2

SIW Cavity-Backed Slot (Multi-)Antenna Systems for the Next-Generation IoT Applications

Sam Lemey, Olivier Caytan, Dries Vande Ginste, Piet Demeester, Hendrik Rogier, and Maurizio Bozzi

Published in the proceedings of the 2016 IEEE Topical Conference on Wireless Sensors and Sensor Networks (WiSNet)

★ ★ ★

Substrate integrated waveguide (SIW) cavity-backed slot antenna topologies are promising candidates to adress the specific design challenges posed by the Internet of Things (IoT). In this contribution, we demonstrate their potential by discussing two designs on two different, application-specific, innovative substrate materials. First, a compact, ultra-wideband three-element array with very low mutual coupling is presented for integration into furniture. In the second design, the half-mode SIW technique is applied to obtain a miniaturized ultra-wideband design, enabling invisible integration into cork floor and wall tiles. The compactness, integrability, and stable, high performance of both designs in different operating conditions, make them ideal candidates for IoT applications.

2.1 Introduction

The emergence of the Internet of Things (IoT) in the last few years has led to an increasing demand for wireless communication systems that are invisibly integrated inside common objects and that support very high data rates to meet the requirements of various types of future emerging wireless applications [1]. This far-reaching integration and ever increasing demand for higher data rates make antenna design for IoT applications more challenging.

First, an antenna topology that guarantees a stable and high radiation efficiency, when deployed in different environments, and that minimizes detuning, due to varying environmental conditions, is of major importance. Second, a low-cost and low-profile design is essential to facilitate invisible integration into a common object without significantly increasing cost. Furthermore, wideband performance is necessary to meet the stringent requirements of the current and next generation wireless applications. Finally, as multiple-input multiple-output (MIMO) wireless communication is supported by more and more wireless standards, an antenna topology that allows a compact array design with low mutual coupling is preferable.

Cavity-backed slot (CBS) antennas have the potential to meet these requirements, as they exhibit an excellent suppression of radiation leakage in unwanted directions. In addition, they allow significant size reduction through miniaturization techniques, by relying on the symmetry of the field distribution in the cavity [2]. Moreover, stable and efficient radiation over an ultra-wide bandwidth can be obtained by relying on the excitation of multiple modes [3], whereas the use of substrate integrated waveguide (SIW) technology [4] yields a low-cost and low-profile design. Therefore, in this paper, the CBS antenna topology is combined with SIW technology to realize a new generation of high-performance low-cost antenna designs, facilitating invisible integration inside common objects.

2.2 SIW technology: benefits and realization

SIW technology exhibits very attractive features for IoT applications. Both active and passive components can be implemented on a single substrate by means of a low-cost production process [4], paving the way for a low-profile and cost-effective realization of a complete circuit.

Furthermore, the SIW technology may be combined with innovative substrate materials to obtain a green, stable and high-performance broadband design [2]–[4]. For IoT applications, the object's materials can be reused to implement the SIW structure, provided that a dedicated material characterization technique indicates that they possess the appropriate RF characteristics, such as low moisture regain, low losses, and consistent batch-to-batch dielectric permittivity. Such an approach yields a significant cost and area reduction, as the readily available material and area of the object itself are exploited to construct the complete circuit.

Finally, undesired radiation and surface waves are minimized by confining the fields inside the SIW structure through rows of vias that act as effective electric walls. This enables a compact array design with low mutual coupling and significantly improves efficiency, as power is only radiated in the desired directions.

SIW components may be implemented in unconventional materials by means of thin wires in combination with a conductive epoxy sealant or by using tubelets to provide a good electrical contact between the conductive layers on each side of the substrate. The latter method, in combination with copper-plated taffeta as conductive layers (sheet resistance of 0.18 Ω/sq), is used in this work.

2.3 SIW CBS antennas for IoT applications

Two different (multi-)antenna designs, implemented on different substrate materials suitable for IoT applications, and relying on a cavity-backed slot antenna topology, are presented. Both are designed for the [5.15 - 5.85] GHz frequency band, referred as the 5 GHz Wi-Fi band in the remainder. The first design is a ultra-wideband three-element array, designed for integration into furniture, constructed out of particle board on which a high pressure laminate (HPL) is thermally bonded. The second is a half-mode SIW design optimized for excellent performance when integrated into cork floor and wall tiles, in combination with small dimensions. The remainder of this section describes the operating principles and the design-specific details related to both designs.

2.3.1 Three-element SIW CBS antenna array for integration into furniture

Particle board, on which HPL is thermally bonded, is a commonly used material to manufacture furniture, such as desks, closets, tables, ... Yet, particle board is not an ideal candidate to be used as the antenna's substrate. Instead, a 3.94-mm-thick closed-cell expanded-rubber by Javaux is adopted as antenna substrate. This material possesses the appropriate charracteristics to obtain a high-performance, broadband design, robust for varying relative humidity levels, and allowing recycling. Its electrical parameters are determined by means of the dedicated material characterization technique described in [5]. It is found that 1.495 and 0.017 are a good estimation for its dielectric permittivity (ϵ_r) and loss tangent ($\tan\delta$) at 5.5 GHz, respectively. Invisible integration is then obtained by deploying the proposed array inside a recess, milled in the particle board, directly underneath the HPL layer, as shown in Fig. 2.1 (b).

A prototype of the presented three-element array is depicted in Fig. 2.1. The array consists of three identical coaxial-fed linearly-polarized SIW CBS antenna elements, each consisting of a rectangular cavity that is split into two subcavities (A and B) by means of a non-resonant rectangular slot. They are arranged in such a way that the array exhibits 3-fold rotational symmetry. This geometry was carefully

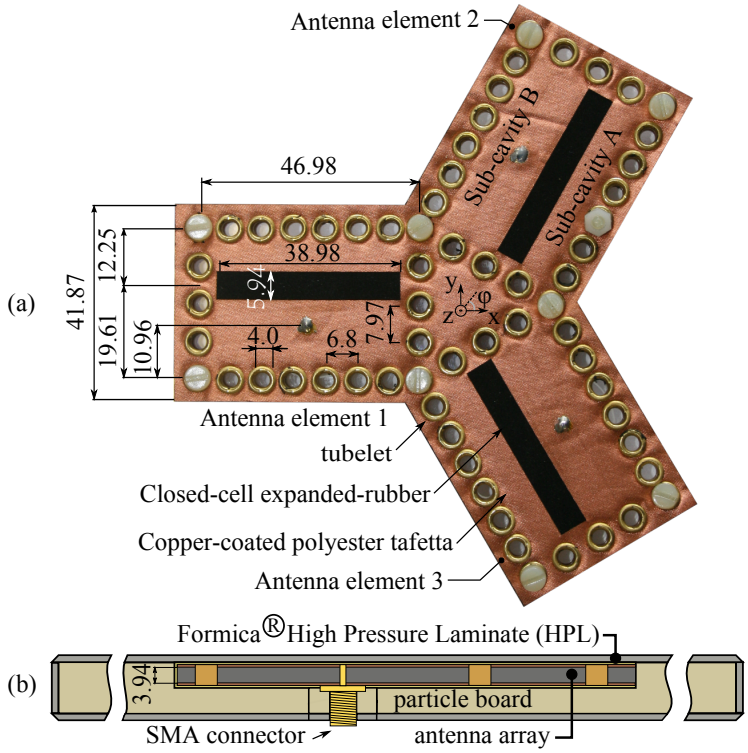

Figure 2.1: Three-element SIW cavity-backed slot antenna array for integration into furniture, with annotated dimensions [mm]. (a) Top view of a prototype; (b) Cross-sectional view after integration inside a commonly used board material to manufacture furniture.

selected to exploit both spatial and polarization diversity. Each individual antenna element is designed to exhibit a return loss larger than 10 dB within the complete 5 GHz Wi-Fi band, with 250 MHz margins. Furthermore, mutual coupling remain lower than -25 dB over the [5.15 - 5.85] GHz-band to minimize correlation between received signals. To meet the impedance matching bandwidth criterion, the bandwidth enhancement technique presented in [6], was applied. This means that two different hybrid mode combinations at two neighbouring frequencies are excited and merged, by carefully selecting the dimensions of the slot and cavity. More specifically, the hybrid mode at the lowest frequency is a combination of a weak TE_{110} and a strong TE_{120} mode. This specific combination leads to a dominant field in subcavity B (Fig. 2.1(a)) that is out-of-phase with the fields in subcavity A (Fig. 2.1(a)). At the highest frequency, the hybrid mode is a combination of a strong TE_{110} and a weak TE_{120} mode, yielding a dominant field in subcavity A that is in-phase with the fields in subcavity B. Both specific combinations lead to a large E-field across the slot, causing it to radiate. For the optimized dimensions in Fig. 2.1, the two hybrid modes resonate at 5.23 and 5.92 GHz, with mode profiles shown in Fig. 2.2(a) and (b), respectively.

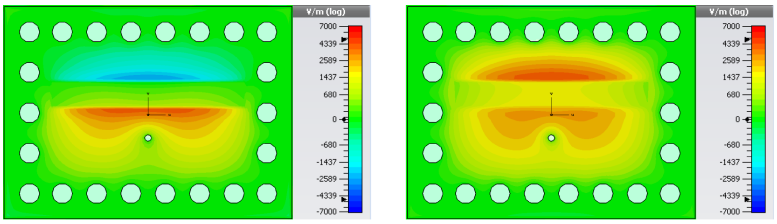

Figure 2.2: Simulated hybrid mode profiles of a stand-alone antenna element of the three-element array: z-component of the electric field [V/m]. (a) 5.23 GHz; (b) 5.92 GHz.

The performance of the array was validated in an anechoic chamber by means of Agilent's N5242A PNA-X network analyzer by measuring its S-parameters from 4.0 GHz to 7.0 GHz and its radiation pattern at 5.5 GHz, before and after integrating the array according to Fig. 2.1(b). Fig. 2.3 shows that the measured stand-alone return loss and mutual coupling are in good agreement with the simulated curves. Fig. 2.3 also demonstrates that both imposed S-parameter requirements remain satisfied after integration of the array. Radiation pattern measurements at 5.5 GHz show that the integration of the array only causes a slight decrease in measured maximum gain (from 5.94 dBi to 5.80 dBi) and a neglible decrease in front-to-back ratio (FTBR) (from 15.90 dB to 15.70 dB). In addition, the radiation efficiency equals 78 % when the array is integrated according to Fig. 2.1(b). Hence, the measurements have proven that the presented array guarantees excellent performance, even after integration.

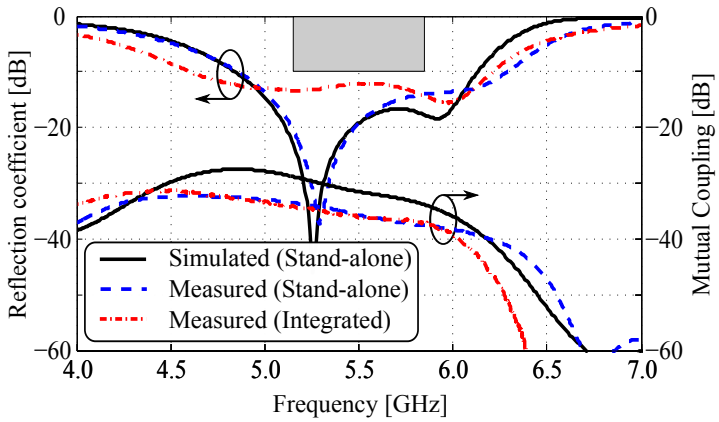

Figure 2.3: Reflection coefficient and mutual coupling of the three-element SIW CBS antenna array in free-space conditions.

2.3.2 Half-mode SIW CBS antenna on cork substrate

The second design [2] is implemented on a 3-mm-thick cork substrate, by Amorim Cork Composites S.A., making it suitable for integration into cork floors or walls. The material exhibits a characterized ϵ_r of 1.22 and tanδ of 0.036 at 5.5 GHz. Invisible integration in a cork tile is obtained by covering the antenna with a similar cork sheet.

The antenna is based on the same multi-moded CBS antenna topology as described in Section 2.3.1. Now, however, the half-mode SIW (HMSIW) technique is applied to reduce the cavity size by half to obtain an even more compact design. Indeed, since both hybrid modes in the initial cavity exhibit a virtual magnetic wall (Fig. 2.4), the cavity may be cut in half, removing the part for $x < 0$ (indicated by dotted lines). Then, the antenna dimensions and feed location are optimized by means of full-wave simulation in CST Microwave studio to obtain a return loss exceeding 10 dB within the 5 GHz Wi-Fi band with 300 MHz margins. Furthermore, the length of the ground plane L_{gp} is extended to 15.0 mm to maximize the FTBR. In this case, the two hybrid modes resonate at 5.26 and 5.85 GHz, with mode profiles shown in Fig. 2.5(a) and (b), respectively.

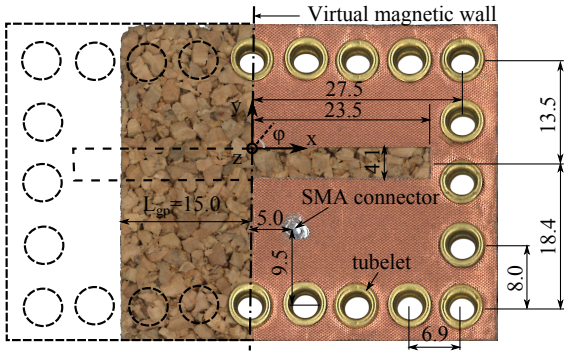

Figure 2.4: Prototype of the cork half-mode SIW antenna, with annotated dimensions [mm].

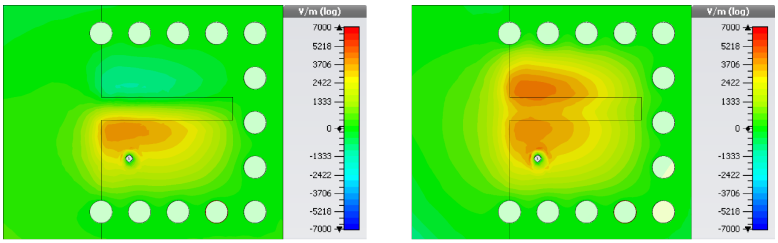

(a) (b)

Figure 2.5: Simulated half-mode hybrid mode profiles: z-component of the electric field [V/m]. (a) 5.26 GHz; (b) 5.85 GHz.

The HMSIW CBS antenna's performance was then validated in free-space condtions by measuring the antenna's stand-alone reflection coefficient and radiation pattern, and when covered by a 3-mm thick cork sheet (identical to the antenna's substrate). Fig. 2.6 demonstrates a shift to lower frequencies for the measured reflection coefficients, due to variations in the cork parameters. Covering the antenna by the cork sheet, results in a broader impedance bandwidth because of a downward shift of the lowest hybrid mode. Measuring the radiation pattern at 5.5 GHz, shows a comparable maximum gain (from 4.3 dBi to 4.2 dBi), an increase in FTBR (from 15 dB to 16.8 dB) and a decrease in radiation efficiency (from 85% to 80%), when covering the antenna with the cork sheet. In general, we can conclude that an excellent impedance matching and radiation performance is obtained for both setups.

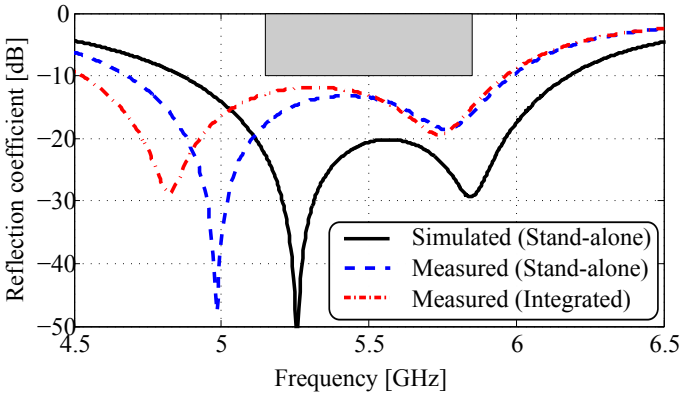

Figure 2.6: Reflection coefficient of the cork half-mode SIW CBS antenna in free-space conditions.

2.4 Conclusion

In this work, the SIW technology is combined with innovative materials to implement two different high performance, ultra-wideband cavity-backed slot antenna designs to enable invisible integration in an IoT environment, in the mean time guaranteeing stable, high performance. More specifically, two designs were discussed to demonstrate the merits and potential of this design approach: a compact, three-element antenna array with very low mutual coupling for integration into furniture and a miniaturized HMSIW antenna for seamless integration in cork floors and walls. Measurements have been performed and demonstrate excellent performance in free-space and after integration, proving the potential of our approach for IoT applications.

Acknowledgment

This work was supported in part by the iMinds IoT research program.

References

[1] H. Sundmaeker, P. Guillemin, P. Friess, and S. Woelffle, Eds., *Vision and challenges for realising the internet of things.* Luxembourg: Publications Office of the European Union, 2010.

[2] O. Caytan, S. Lemey, S. Agneessens, D. Vande Ginste, P. Demeester, C. Loss, R. Salvado, and H. Rogier, "Half-mode substrate-integrated-waveguide cavity-backed slot antenna on cork substrate", *Antennas Wirel. Propag. Lett.*, vol. 15, no. 99, pp. 162–165, May 2015.

[3] S. Lemey and H. Rogier, "SIW textile antennas as a novel technology for UWB RFID tags", in *2014 IEEE RFID-TA*, Tampere, Finland, Sept. 8-9, 2014, pp. 256–260.

[4] M. Bozzi and R. Moro, "Low-cost fabrication, eco-friendly materials, and easy integration: the new technological paradigm for the future wireless sensor networks", in *European Microwave Conference (EuMC)*, Nuremberg, Germany, Oct. 6-10, 2013, pp. 858–861.

[5] F. Declercq, H. Rogier, and C. Hertleer, "Permittivity and loss tangent characterization for garment antennas based on a new matrix-pencil two-line method", *IEEE Trans. Antennas Propagat.*, vol. 56, no. 8, pp. 2548–2554, Aug. 2008.

[6] G. Q. Luo, Z. F. Hu, W. J. Li, X. H. Zhang, L. L. Sun, and J. F. Zheng, "Bandwidth-Enhanced Low-Profile Cavity-Backed Slot Antenna by Using Hybrid SIW Cavity Modes", *IEEE Trans. Antennas Propagat.*, vol. 60, no. 4, pp. 1698–1704, Apr. 2012.

3

Threefold Rotationally Symmetric SIW Antenna Array for Ultra-Short-Range MIMO Communication

Sam Lemey, Thijs Castel, Patrick Van Torre, Thomas Vervust, Jan Vanfleteren, Piet Demeester, Dries Vande Ginste, and Hendrik Rogier

Published in the IEEE Transactions on Antennas and Propagation

★ ★ ★

A high performance, three-element substrate integrated waveguide (SIW) cavity-backed slot antenna array that covers the [5.15 - 5.85] GHz band is designed for integration inside or underneath the worktop of a desk, to set up a stable, high data rate ultra-short-range 3 x 3 multiple-input multiple-output (MIMO) wireless communication link with a mobile user (MU) positioned on top of that worktop. The antenna topology and array geometry are carefully selected to maximally exploit the multiplexing capabilities of the ultra-short-range 3 x 3 MIMO channel over a wide bandwidth, yielding an increased channel capacity and/or reduced power consumption. In addition, special care was taken to guarantee a channel capacity that is less dependent on the relative orientation of the MU. Furthermore, the SIW implementation technology is combined with innovative antenna materials to guarantee a low-profile, low-cost, stable and high-performance broadband array design that maintains its excellent performance after integration. A prototype of the antenna array was fabricated, integrated according to two different integration scenarios, and validated. Measurements prove that the antenna array allows integration into a worktop with only a minor influence on its return loss and mutual coupling, guaranteeing a bandwidth of at least 1.078 GHz and a minimum isolation between antenna elements of 30 dB within the entire [5.15 - 5.85] GHz band.

3.1 Introduction

In the past few years, the Internet of Things (IoT) has become a widespread term to emphasize the vision of a global infrastructure of interconnected everyday devices, augmented with sensing, processing, and wireless communication capabilities [1]. By embedding sensors in common objects and combining the potential of the internet with emerging technologies, such as real-time localization [2] and wireless communication [3], those everyday objects are transformed into smart devices, which are able to understand and respond to their context and environment. However, the emergence of the IoT is inextricably linked to an increasing demand for wireless communication systems that are invisibly integrated inside common objects [4] and able to support very high data rates [5] to meet the requirements of various types of future emerging wireless multimedia applications.

Exploiting multiple antennas at transmitter and receiver, also known as multiple-input multiple-output (MIMO) wireless communication, is a cost-effective technology that may substantially increase channel capacity without increasing transmit power or bandwidth [6]–[8]. As the demand for high data rate connections is often limited to a particular area in a room [9], applying MIMO in short-range [10], [11] or near-field systems [3], [9] has received increasing interest. The latter technique could be exploited to set up an ultra-short-range, high data rate wireless communication link between an access point (AP), integrated into a common object, and a mobile user (MU) in its close proximity. However, antenna systems

for IoT applications are subject to stringent design requirements [4]. First, they should be low-cost and low-profile, enabling invisible integration into common objects, without significantly increasing cost. Therefore, innovative antenna materials and fabrication technologies need to be explored [12]–[16]. Furthermore, an antenna topology that guarantees stable and high performance, when deployed in different environments, is required. Moreover, wideband performance is necessary to fulfill the demanding requirements of the current and next generation wireless applications [4].

In this chapter, a high performance three-element antenna array that covers the [5.15 - 5.85] GHz frequency band is designed for integration inside or underneath the worktop of a desk, to set up a stable, high data rate ultra-short-range 3 by 3 MIMO wireless communication link with a MU positioned on top of that worktop. This frequency band covers all Unlicensed National Information Infrastructure (U-NII) radio bands [17] and is referred to as the 5 GHz Wi-Fi band in the remainder. Covering this band makes the array suitable for Wi-Fi APs, such as 802.11ac stations. To exploit both spatial and polarization diversity, the antenna array consists of three identical linearly-polarized substrate integrated waveguide (SIW) cavity-backed slot antenna elements that are arranged such that the array exhibits 3-fold rotational symmetry. A high multiplexing gain is achieved in proximity of a designated working area, by separating the ultra-short-range MIMO link into three crosstalk-free virtual data transmission links. Moreover, the diverse polarizations provide a high and stable channel capacity that is less dependent on the relative orientation of the MU. A cavity-backed slot antenna topology was selected, as [18] demonstrated that such a topology exhibits a high supression of unwanted surface waves and excellent isolation from its environment at out-of-band frequencies and in unwanted directions. Positioning such antenna elements in a compact array configuration results in an antenna system with low mutual coupling [19] and stable performance when integrated into a multitude of everyday devices [12]. Furthermore, the cavity, backing each antenna element, was implemented in SIW technology to obtain a simple, low-profile and cost-effective single substrate realization [19]. By combining the SIW technology with innovative antenna materials, a recyclable, low-cost, stable and high-performance broadband array design is obtained [20].

To the authors' best knowledge, this is the first paper that describes the design and performance analysis of an array for integration inside or underneath the worktop of a desk, exploiting both spatial and polarization diversity to implement a stable, wideband and high data rate ultra-short-range MIMO link between the AP and MU array. The wideband MIMO performance of the array is investigated for separations over distances ranging from only a fraction of the intended wavelength to several wavelengths, and for different relative orientations and positions of the MU. In prior work, unipolarized spatial array configurations were used to investigate short range [10] and near-field MIMO [3] systems at a single frequency. In [10], MIMO performance was analyzed for diverse relative orientations between both arrays indicating a minimum channel capacity when TX and RX arrays are orthogonal to

each other. In [3], inter-antenna element spacing was optimized for a fixed distance and relative orientation between both arrays to maximize channel capacity. Yet, neither integration aspects nor wideband MIMO performance were discussed. In [21], measurements of a 2 x 2 near-field ultra-wideband (UWB) MIMO channel, in which each link-end consists of an orthogonally polarized antenna pair, were analyzed. The authors demonstrated wideband MIMO performance. However, measurements were only conducted for fixed relative orientations between both arrays. Again, no integration aspects were discussed.

The paper is organized as follows. In Section 3.2, the antenna topology and array geometry are outlined as well as the fabrication procedure. Furthermore, two integration scenarios are described. Section 3.3 discusses the system model and channel capacity for ultra-short-range MIMO communication. The antenna array and its MIMO performance are validated in Section 3.4 by measurements carried out in free-space and in realistic operating conditions, respectively.

3.2 Antenna design and array topology

3.2.1 Design considerations

A high performance, three-element antenna array that covers the [5.15 - 5.85] GHz frequency band is designed for integration inside or underneath the worktop of a desk, to set up a stable, high data rate ultra-short-range 3 x 3 MIMO wireless communication link, with a mobile user positioned on top of that worktop, as depicted in Fig. 3.1. Such an approach may be exploited in a meeting room, to provide an ultra-high data-rate wireless connection at each seat, or to replace wired docking stations. The antenna topology and array geometry are selected with the greatest care to maximally exploit the multiplexing capabilities of the ultra-short-range channel, yielding a high multiplexing gain, thereby reducing power consumption and/or increasing data rate. Moreover, this multiplexing gain should be robust against varying relative orientations of the MU and should be maintained after integration inside or underneath the worktop. Therefore, each individual array element must meet the impedance matching criterion of $|S_{11}| <$ -10 dB, with respect to 50 Ω, both stand-alone and after integration, in the entire [5.15 - 5.85] GHz-band. Furthermore, mutual coupling between array elements should be lower than -25 dB to minimize correlation between received signals and to allow for a high multiplexing gain. In addition, the total active reflection coefficient (TARC) [22], characterizing the entire array's impedance bandwidth, should remain lower than -10 dB within the entire band. Finally, an eco-friendly and cost-efficient implementation is pursued by carefully selecting antenna materials [20].

3.2.2 Antenna element

The antenna element forming the basis of our proposed antenna array is depicted in Fig. 3.2. A SIW cavity-backed slot antenna topology was selected as such a

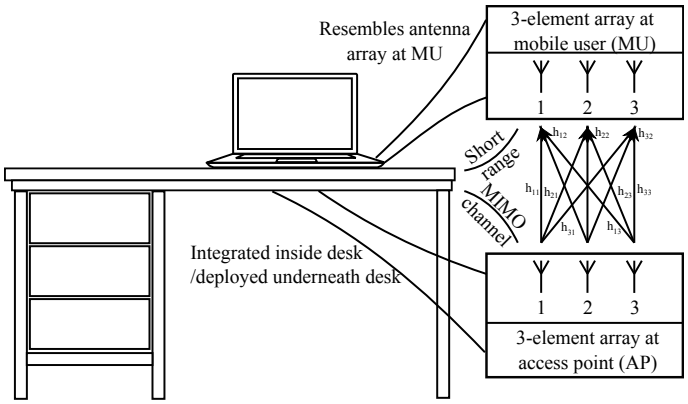

Figure 3.1: System concept of a smart desk, enabling a high-speed and low power wireless communication link by exploiting ultra-short-range 3 x 3 MIMO.

topology combines the advantages of a conventional solid cavity-backed antenna, namely a large front-to-back ratio (FTBR) and a high isolation from its environment, with the advantages of planar antennas, being low profile, low fabrication cost, and easy integration with planar circuitry [18],[19]. Given their very high isolation from their environment and high suppression of unwanted surface waves, such cavity-backed SIW slot antennas are excellent building blocks for compact antenna arrays with low mutual coupling and stable characteristics when installed in different desk configurations. In addition, by integrating the antenna in the desk in such a way that the slot is oriented upwards, the antenna mainly radiates in the upward direction with a very high FTBR. Hence, a safer and more power-efficient design with less interference is obtained.

A bandwidth enhancement technique [23] is applied to the narrowband cavity-backed slot antenna topology of [18] to achieve the imposed -10 dB impedance bandwidth, corresponding to a fractional bandwidth (FBW) of 12.8%. Therefore, the rectangular SIW cavity is subdivided into two subcavities (cavity A and B) by a non-resonant rectangular slot. The specific materials applied in the antenna construction are discussed in Section 3.2.4. Then, the transient solver of CST Microwave Studio is applied to determine the dimensions of both subcavities and the slot, such that two hybrid modes are excited at two frequencies chosen such that coverage of the entire 5 GHz band is obtained. The hybrid mode at the lowest resonance frequency combines a weak TE_{110} and a strong TE_{120} mode, whereas the hybrid mode at the highest resonance frequency consists of a strong TE_{110} mode in combination with a weak TE_{120} mode. These specific combinations lead to electrical fields in both subcavities that are out-of-phase at the lowest resonance frequency and in-phase, but with a large difference in magnitude, at the highest resonant frequency. Hence, at both neighbouring frequencies, a large electric field occurs across the non-resonant slot, enabling strong radiation in the hemisphere along the positive z-direction (Fig. 3.2). Unlike [18], [23] and [24], where a

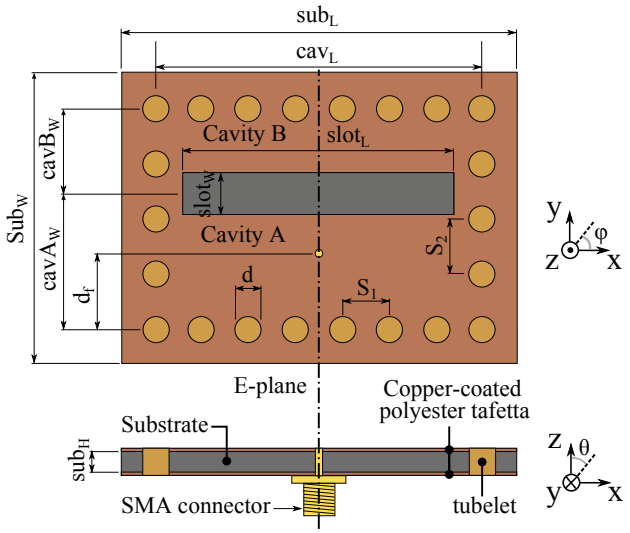

Figure 3.2: SIW cavity-backed slot antenna element. Optimized dimensions: $sub_H = 3.94$ mm, $sub_W = 41.87$ mm, $sub_L = 56.98$ mm, $cav_L = 46.98$ mm, $cavA_W = 19.61$ mm, $cavB_W = 12.25$ mm, $d = 4.0$ mm, $S_1 = 6.8$ mm, $S_2 = 7.97$ mm, $slot_L = 38.98$ mm, $slot_W = 5.94$ mm, and $d_f = 10.96$ mm. Substrate parameters at 5.5 GHz: $\epsilon_r = 1.495$, $\tan\delta = 0.016$.

50 Ω grounded coplanar waveguide (GCPW) is used to effectively excite the required modes, our design exploits a coaxial feed to minimize backside radiation even further. This feed, of which the inner and outer conductors are connected to the antenna's top and bottom plane, respectively, is located in subcavity A. By optimizing the feed position, a loop is created that injects energy into the cavity by coupling to the magnetic fields of the cavity modes. Because of the better shielding, the coaxial feed offers a higher robustness against mismatch when integrated in different desk configurations compared to a GCPW feed.

By means of an extensive computer-aided optimization process, the antenna dimensions are determined to obtain maximum bandwidth, in the meantime taking care that the return loss exceeds 13 dB in the region where both hybrid modes merge, to account for fabrication inaccuracies and frequency detuning due to integration. The final antenna dimensions are given in the caption of Fig. 3.2. CST Microwave Studio's transient solver demonstrates excellent impedance matching to $Z_0 = 50\ \Omega$ from 4.835 GHz to 6.125 GHz (see further in Section 3.4, Fig. 3.6), corresponding to an impedance bandwidth of 1.290 GHz, or an FBW of 23.5%. In the far-field, the total antenna efficiency exceeds 90% over the entire band, indicating very low losses. The far-field radiation pattern remains very stable over the entire 5 GHz Wi-Fi band and exhibits strong and stable radiation in the hemisphere along the positive z-direction, whereas backside radiation is minimal. Specifically, the far-field gain along the z-direction and the far-field FTBR only vary between 6.20 dBi and 6.57 dBi, and between 13.08 dB and 13.21 dB, respectively.

3.2.3 Antenna array

The antenna array (Fig. 3.3) consists of three identical antenna elements, arranged in such a way that the array exhibits 3-fold rotational symmetry, resulting in an angle $\alpha = 60°$ between the E-planes of subsequent antenna elements. Such a configuration reduces the dependency of the MIMO channel capacity on the angular position between the AP and MU array by exploiting polarization diversity. By means of full-wave electromagnetic simulations in CST Microwave Studio, the distance D between the array center and the center of each antenna element (Fig. 3.3) is selected to be 32.8 mm. This guarantees an isolation of at least 25 dB between antenna elements and a TARC below -10 dB over the entire frequency band of operation, as depicted in Fig. 3.6 and Fig. 3.7, respectively. It also leads to an inter-antenna element spacing S (Fig. 3.3) of at least one wavelength. Choosing a larger value for D may lead to a larger multiplexing gain in an ultra-short-range propagation scenario, as demonstrated in [10]. Yet, a higher D will result in a larger required surface by the antenna array, which is not desirable for the intended application.

To assess the MIMO performance of our proposed array in a conventional far-field multipath environment, the envelope correlation coefficient (ECC), mean effective gain (MEG) and multiplexing efficiency [25] were analyzed in a uniform far-field propagation environment, as in [26]. Simulations demonstrate a constant MEG ratio of 1 and an ECC well below 0.001 within the 5 GHz Wi-Fi band. Furthermore, the minimum multiplexing efficiency within the frequency band of operation amounts to -0.54 dB. Hence, our proposed antenna array is also very suitable for application in a conventional far-field MIMO channel.

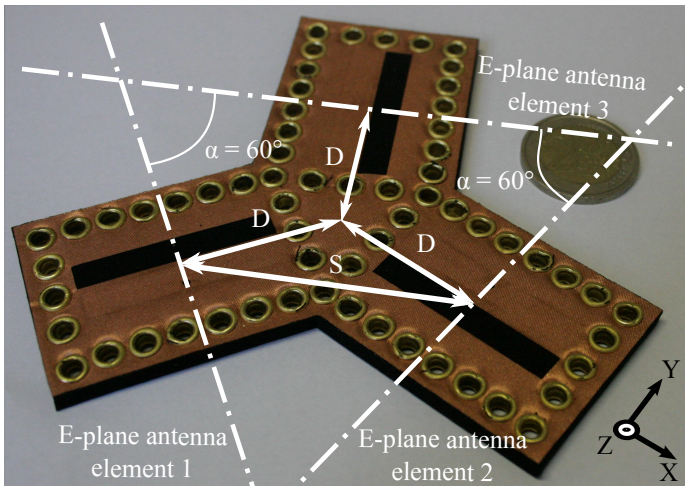

Figure 3.3: Prototype of the threefold rotationally symmetric SIW cavity-backed slot antenna array.

3.2.4 Antenna materials and fabrication procedure

To achieve a low-cost, stable and high-performance broadband design that facilitates recycling, a 3.94 mm-thick closed-cell expanded-rubber by Javaux [27] is adopted as antenna substrate. It is a low-weight, flame retardant foam material with a low-moisture regain that exhibits very good dimensional stability and is resistant to oils and solvents [27]. In addition, the rubber is free of CFCs and HCFCs and can easily be recycled, resulting in a green antenna array. At 5.5 GHz, it is found that 1.495 and 0.017 are good estimations for its dielectric permittivity (ϵ_r) and loss tangent (tanδ), respectively, according to the characterization procedure described in [28]. The slot and feed layer are constructed using a pure copper-coated polyester taffeta, characterized by a surface resistivity $R_s = 0.18\Omega/sq$ [29]. After structuring both conductive layers, according to the design layout depicted in Figs. 3.2 and 3.3, with a picosecond pulsed solid state laser, thermally activated adhesive sheets are used to laminate both conductive layers to the antenna substrate. The antenna cavity is then formed by four lateral rows of flat-flange brass tube eyelets, spaced closely enough to minimize radiation loss ($S_1/d < 2$ and $S_2/d < 2$) [19]. In this work, a manual eyelet press has been used to fix the tube eyelets at their correct locations and to guarantee good contact between both conductive layers. A fully automatic eyelet machine, or a computer numerically controlled (CNC) eyelet setting machine, could be used in an industrial mass production process [30].

3.2.5 Array integration

Two scenarios are considered for the integration of the proposed three-element antenna array within a desk. In the first scenario, the three-element antenna array is integrated inside the worktop (Fig. 3.4(a)). In the second integration scenario, the antenna array is integrated underneath the worktop (Fig. 3.4(b)). The worktop used in both scenarios consists of a 38 mm-thick, high density, moisture resistant particle board on which a 1 mm-thick Formica® high pressure laminate (HPL) is thermally bonded. The reason for selecting this material as an integration platform is twofold. First, such panels are commonly used to manufacture desktops because of their high wear resistance, durability and processability. Second, their ability to be used in humid environments, based on their high moisture resistance, guarantees stable antenna performance after integration inside or underneath such a worktop in realistic environments, with varying humidity levels [31]. The permittivities of the particle board and the HPL equal $\epsilon_r = 2.13$ and $\epsilon_r = 3.56$, respectively, according to the material characterization technique described in [32].

In the first integration scenario, a recess is milled out of the particle board with the exact shape of the antenna array. The depth of this recess was chosen $t_1 = 26$ mm, resulting in a stack of particle board with thickness $t_2 = 12$ mm and HPL of thickness $t_3 = 1$ mm, that covers the antenna array's slots (Fig. 3.4(a)). These dimensions are selected based on antenna measurements, to guarantee -10 dB impedance

matching in the [5.15 - 5.85] GHz band when integrated inside the worktop, in the meantime maintaining sufficient mechanical strength. After milling, the antenna array is mounted in the recess with nylon screws. The final step consists of gluing both HPL layers to the particle board.

In the second integration scenario, the array is mounted underneath the worktop, in parallel with its surface at a distance $T = 50$ mm (Fig. 3.4(b)). The array is fixed in this position by attaching it to an acrylic glass platform by means of nylon screws and using nylon rods to keep the plexiglass platform at its desired position.

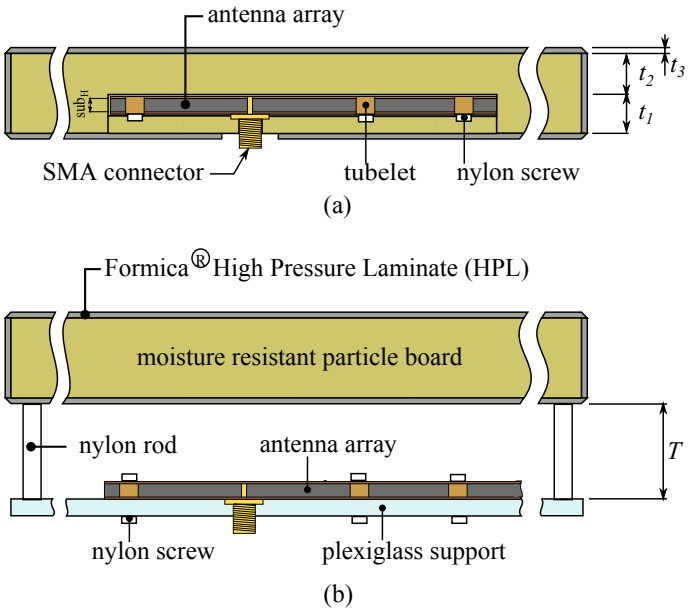

Figure 3.4: Cross-sectional view of the proposed three-element array integrated according to integration scenario 1 (a) and integration scenario 2 (b) .

3.3 System model and channel capacity for ultra-short-range MIMO communication

3.3.1 Channel model

Fig. 3.5 represents the ultra-short-range 3 x 3 MIMO channel that arises when the proposed array is used at both the AP and MU side in the scenario depicted in Fig. 3.1, making abstraction of the worktop shown in Fig. 3.4, for an arbitrary location and orientation of the array at the MU (array 2). A right-handed cartesian coordinate system is defined in Fig. 3.5 to unambiguously describe the MU array's location and orientation with respect to the AP array. Then, the location

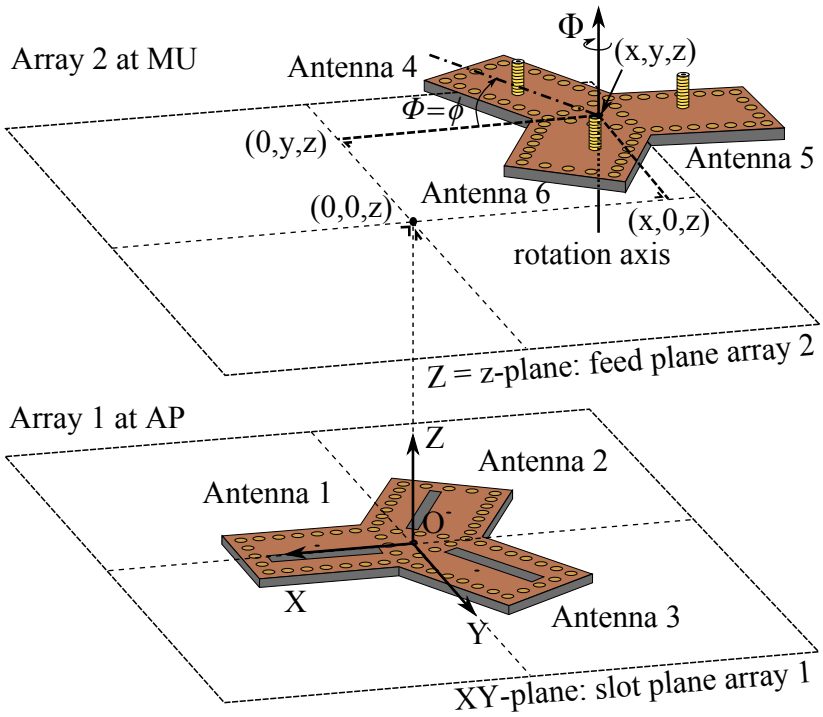

Figure 3.5: Ultra-short-range 3x3 MIMO channel model in case the proposed array is used at both sides of the wireless link, making abstraction of the worktop, for an arbitrary location (x, y, z) and orientation (Φ) of the MU array.

of the MU array is defined by its bottom plane center (x, y), whereas the angle Φ determines its orientation. The vertical distance z between both arrays depends on the integration scenario, and equals 19 mm for the first integration scenario and 96 mm for the second scenario. Note that, for measurement purposes, the array at the MU is separated from the worktop by a styrofoam spacer of 2 mm thickness. To predict the capacity of such an ultra-short-range, wideband MIMO channel, we subdivide the channel under study into K frequency-flat subchannels. Denoting by $\mathbf{H}_k(x, y, z, \Phi) \in \mathbb{C}^{N_r \times N_t}$ the transfer matrix of the k-th subchannel, the received signal in this subchannel is associated to the transmitted signal by

$$\mathbf{y}_k = \sqrt{\frac{E_S}{N_t}} \mathbf{H}_k(x, y, z, \Phi)\mathbf{s}_k + \mathbf{n}_k, \tag{3.1}$$

where $\mathbf{y}_k \in \mathbb{C}^{N_r \times 1}$ is the signal vector at the receiver, $\mathbf{s}_k \in \mathbb{C}^{N_t \times 1}$ is the signal vector at the transmitter, $\mathbf{n}_k \in \mathbb{C}^{N_r \times 1}$ is the complex additive white Gaussian noise (AWGN) vector and E_S is the total available average energy over a symbol period at the transmitter, which is chosen identical for all K subchannels. In this chapter,

N_t and N_r are both equal to three as they represent the number of transmit and receive antennas, respectively. Subchannel matrices $\mathbf{H}_k(x,y,z,\Phi)(k=1,2,...,K)$ are determined by taking the relevant S-parameters of the measured six port **S**-matrix, according to the convention adopted in Fig. 3.5. These measured channel matrices are then used to analyze the potential of ultra-short-range MIMO. For the ease of notation, $\mathbf{H}_k(x,y,z,\Phi)$ will be denoted $\mathbf{H}_k$ in the remainder:

$$\mathbf{H}_k = \begin{bmatrix} h_{k,11} & h_{k,12} & h_{k,13} \\ h_{k,21} & h_{k,22} & h_{k,23} \\ h_{k,31} & h_{k,32} & h_{k,33} \end{bmatrix} = \begin{bmatrix} S_{k,41} & S_{k,42} & S_{k,43} \\ S_{k,51} & S_{k,52} & S_{k,53} \\ S_{k,61} & S_{k,62} & S_{k,63} \end{bmatrix}. \tag{3.2}$$

3.3.2 Channel capacity and ellipticity

Assuming that the channel is unknown to the transmitter, but perfectly known by the receiver, and therefore applying uniform power allocation, the error-free spectral efficiency (in the remainder denoted as channel capacity) C_k in the k-th subchannel is given by [33]

$$C_k = \log_2 \det\left(\mathbf{I}_{N_r} + \frac{E_S}{N_t N_0}\mathbf{H}_k\mathbf{H}_k^H\right), \tag{3.3}$$

with N_0 representing the noise power. The eigenvalues $\lambda_{k,i}(i=1,2,...,r)$ of $\mathbf{H}_k\mathbf{H}_k^H$ represent the power gains of the $r=\min(N_t,N_r)$ crosstalk-free virtual data transmission links and provide an indication of the multiplexing gain. A purely diagonal channel with an uniform eigenvalue distribution yields the largest multiplexing gain [33]. In case of singular value dispersion, waterfilling [33], [34] may be applied to further increase channel capacity [35], provided that channel state information is also known by the transmitter.

The ellipticity of a MIMO channel $\log_2(\gamma_k)$ [36] provides an indication about the capacity gain that may be achieved by applying waterfilling. It is a negative value that indicates the channel capacity loss in bps/Hz, compared to a purely diagonal channel:

$$\log_2(\gamma_k) = r\log_2\left[\frac{\left(\prod_{i=1}^{r}\lambda_{k,i}\right)^{1/r}}{\frac{1}{r}\sum_{i=1}^{r}\lambda_{k,i}}\right]. \tag{3.4}$$

3.4 Simulation and measurement results

3.4.1 Antenna array performance

First, the antenna array's S-parameters are measured in an anechoic chamber to verify its stand-alone performance and to evaluate the effect of the worktop on the antenna array's performance for both integration scenarios (Fig. 3.4), without the MU array in its proximity.

As the proposed array exhibits 3-fold rotational symmetry, only the array's $|S_{11}|$, representing the reflection coefficient of an individual antenna element, and $|S_{21}|$, as a measure for the mutual coupling between antenna elements, are depicted in Fig. 3.6. The simulated and measured stand-alone reflection coefficients $|S_{11}|$ are in good agreement. The measured bandwidth, being 1.433 GHz or 25.7 %, is slightly larger than predicted by simulations, due to a slight upward shift of the highest hybrid mode. This deviation probably finds its origin in fabrication inaccuracies, and varations in the electromagnetic properties of the antenna substrate. Integrating the antenna array inside the worktop according to integration scenario 1 (Fig. 3.4(a)) causes both hybrid modes to merge into a single resonance peak. Yet, coverage of the entire 802.11ac band is still guaranteed. The array's $|S_{11}|$ after integration underneath the worktop according to scenario 2 (Fig. 3.4(b)), is in good agreement with the stand-alone measurement. Furthermore, Fig. 3.6 demonstrates a higher isolation between antenna elements in stand-alone, free-space conditions than predicted by simulation. More specifically, the minimum measured in-band isolation amounts to 33.55 dB, whereas simulations predicted a minimum in-band isolation of 28.88 dB. With respect to the stand-alone measurement, mutual coupling is reduced by integrating the array inside the worktop, as shown in Fig. 3.6, whereas mounting the array underneath the worktop results in an increase of mutual coupling within the desired band, due to reflections on the worktop's interface. Still, mutual coupling remains lower than -25 dB over the entire [5.15 - 5.85] GHz band for both integration scenarios, as imposed in Section 3.2.1.

Finally, the array's TARC is calculated based on simulated and measured S-parameters, by exciting the array with 1369 different combinations of its port excitation signals. The maximum TARC at each frequency is then plotted in Fig. 3.7, which clearly demonstrates that, even under worst-case excitation, the -10 dB TARC criterion remains fulfilled.

Hence, Figs. 3.6 and 3.7 prove that our proposed array allows integration into a worktop, as discussed in Section 3.2.5, with only a minor influence on its impedance matching, mutual coupling and TARC.

3.4.2 Ultra-short-range MIMO Performance

Second, the potential of the ultra-short-range 3 by 3 MIMO communication link, depicted in Fig. 3.5, is investigated in a real-life environment for both integration

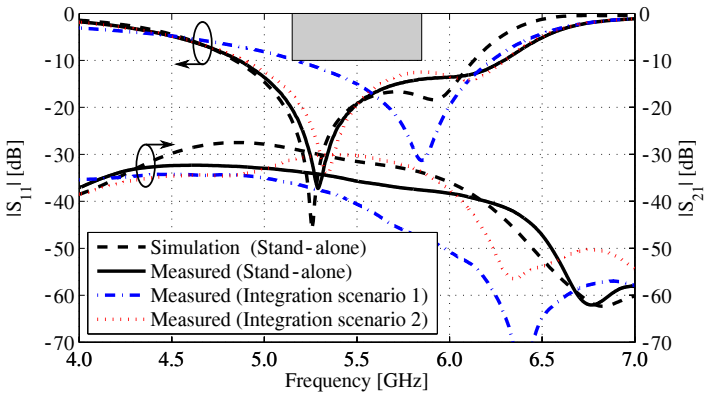

Figure 3.6: Return loss characteristic $|S_{11}|$ of an individual antenna element and the mutual coupling $|S_{21}|$ between subsequent antenna elements in free-space conditions.

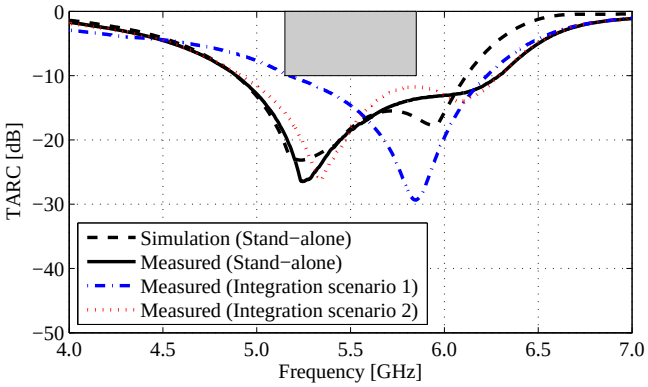

Figure 3.7: Total active reflection coefficient (TARC) of the three-element antenna array in free-space conditions.

scenarios. Therefore, ellipticity and channel capacity are analyzed for multiple well-considered locations and orientations of the MU array, placed on a worktop that is equipped with the AP array, either integrated according to integration scenario 1 (Fig. 3.4(a)) or according to integration scenario 2 (Fig. 3.4(b)). The worktop is placed in a 2.77 m by 3.34 m office room, with a height of 2.31 m, to emulate a realistic environment. Furthermore, the multiplexing gain that arises by exploiting ultra-short-range 3 by 3 MIMO, compared to the median of the nine corresponding SISO links, is investigated as well as the capacity gain that is obtained through waterfilling. Finally, the influence of the worktop on MIMO performance is assessed.

Measurement set-ups

Table 3.1 provides an overview of the three selected locations (x, y) of the MU array on the worktop. Location 1 corresponds to the z-axis being aligned with the MU array's rotation axis (Fig. 3.5), representing the case in which a mobile multimedia device is positioned perfectly above the AP array. Locations 2 and 3 correspond to the MU array being translated over a distance of 120 mm along the X- and Y-axis, respectively. These locations represent the cases where the mobile multimedia device is shifted away from its optimal position. At each of the three locations, subchannel matrices $\mathbf{H}_k$ are measured for two different orientations (Φ), depicted in Table 3.1, of the MU array. During the measurement process, subchannels with a bandwidth of 1 MHz are considered.

Table 3.1: Selected locations and orientations of the MU array (Fig. 3.5). The distance z between both arrays depends on the integration scenario and equals 19 mm for the first integration scenario and 96 mm for the second scenario.

Measurement setup		Location		Orientation
Location	Orientation	$x[mm]$	$y[mm]$	$\Phi[^\circ]$
1	(a)	0	0	0
	(b)	0	0	60
2	(a)	-120	0	0
	(b)	-120	0	60
3	(a)	0	-120	0
	(b)	0	-120	60

Bringing the MU array in proximity of the AP array, as shown in Fig. 3.5, influences the isolation between antenna elements within the same array and their matching. Yet, measurements demonstrate that the requirements stated in Section 3.2.1 are met for all setups denoted in Table 3.1, except for setups 1(a) and 1(b) in case of integration scenario 1. Still, for these two measurement setups, a return loss exceeding 6 dB is obtained within the entire 5 GHz Wi-Fi band, while the minimum isolation still exceeds 30 dB.

H-matrix and ellipticity analysis

First, the coupling between both arrays (Fig. 3.8) and the corresponding ellipticity (Fig. 3.9) are analyzed for each setup of the MU array and for both integration scenarios of the AP array, to assess the multiplexing potential of the ultra-short-range 3x3 MIMO link. When both arrays are perfectly aligned (setup 1(a)), the channel transfer matrices of both the first (Fig. 3.8 (a)) and second (Fig. 3.8 (b))

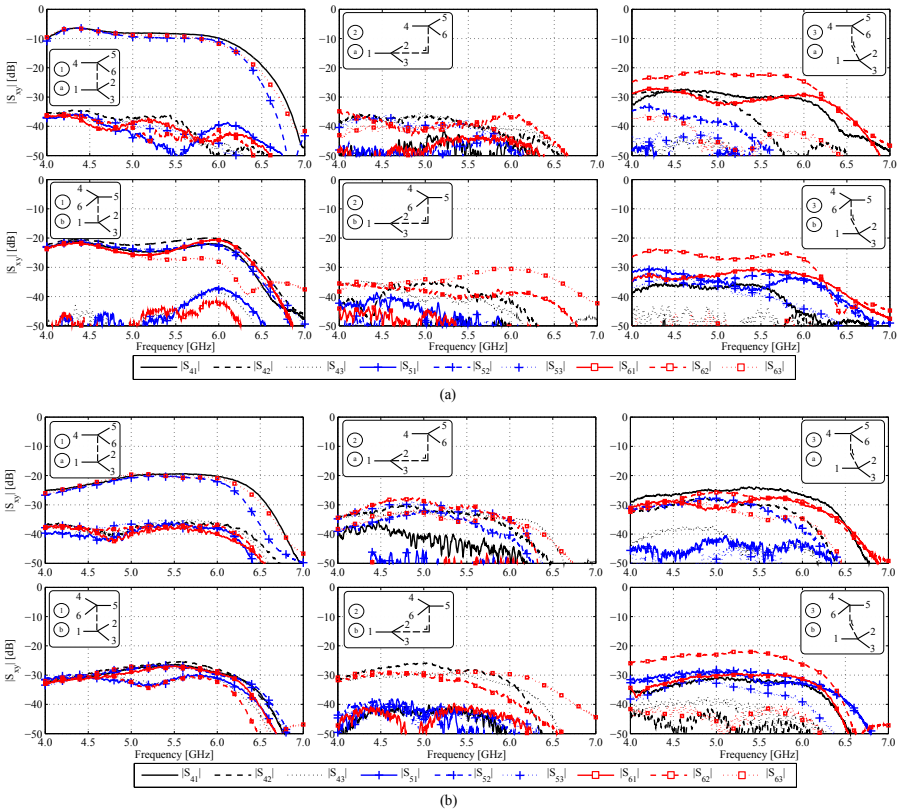

Figure 3.8: H-matrix coefficients (according to (3.2)), as a function of frequency, describing the coupling between the MU and AP array for all placements of the MU array depicted in Table 3.1. (a) Integration scenario 1. (b) Integration scenario 2.

integration scenario are characterized by three strong links (S_{41}, S_{52} and S_{63}) and six significantly weaker links (S_{42}, S_{43}, S_{51}, S_{53}, S_{61} and S_{62}). Hence, the ultra-short-range MIMO channel of setup 1(a) consists of three parallel data links with low crosstalk, guaranteeing strong decorrelation of the received signals. For both integration scenarios, this leads to a near-zero ellipticity within the 5 GHz Wi-Fi band (Fig. 3.9). When the MU array is placed according to setup 1(b), corresponding to the worst-case orientation of the MU array at its optimal location, the channel transfer matrices of both integration scenarios (Fig. 3.8) consist of six equally strong links (S_{41}, S_{42}, S_{52}, S_{53}, S_{61} and S_{63}) and three weaker links (S_{43}, S_{51} and S_{62}). Two subsequent antenna elements in the MU array (for example, antennas 4 and 5) now receive a very similar signal component, transmitted by the same antenna element of the AP array (for this example, antenna 2). This increases correlation between the received signals at the MU array and causes a

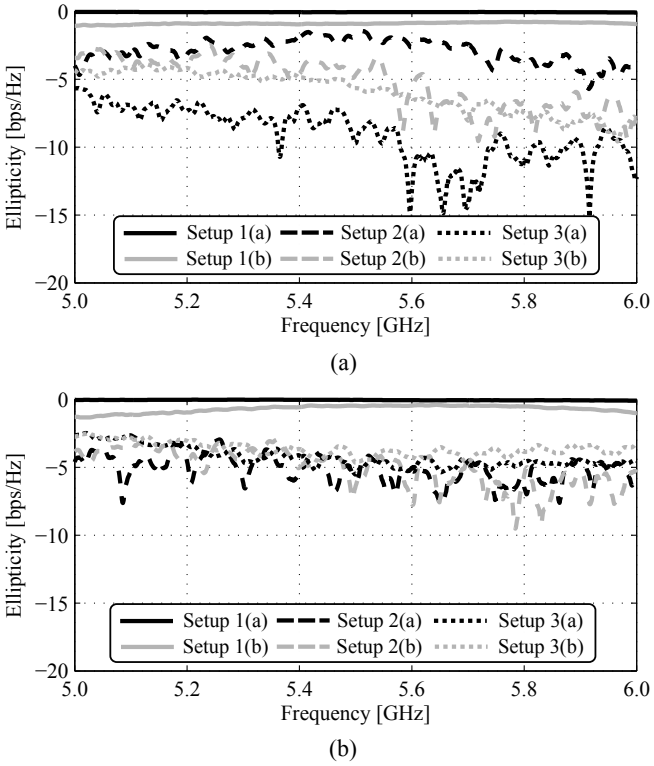

Figure 3.9: Ellipticity, as a function of frequency, describing the multiplexing potential of the ultra-short-range 3 x 3 MIMO channel for all placements of the MU array (Table 3.1). (a) Integration scenario 1. (b) Integration scenario 2.

slightly unequal power gain distribution. This effect translates into a slight ellipticity degradation with respect to setup 1(a) (Fig. 3.9). Yet, the channel can still be separated into three, quasi equally-strong, virtual transmission links. Hence, at the optimal location for the MU array, the proposed array fully exploits parallelism and minimizes the influence of the MU array's orientation on the multiplexing potential, as evinced in Fig. 3.9, and this for both integration scenarios.

Translation of the MU array with respect to location 1 causes a degradation of the ellipticity (Fig. 3.9), indicating increased singular value dispersion. This reduction in multiplexing capability of the ultra-short-range channel is due to the weaker links between elements at the most extreme positions in such a configuration (Fig. 3.8). For setup 2(b), the strongest channel coefficients are associated to antenna elements 2, 3, 4 and 6, whereas the coefficients corresponding to antenna elements 1 and 5 are significantly lower (Fig. 3.8). Similarly, for setup 2(a), antenna element 1 exhibits the lowest coupling with the antenna elements of the MU array. Antenna elements 3 and 5, and 3 and 4 contribute the least for setups

3(a) and 3(b), respectively. Hence, the strongest antenna links vary from setup to setup. Therefore, all antenna elements are necessary to minimize dependence of the multiplexing capability of the ultra-short-range channel on the orientation of the MU array. In this regard, integration scenario 2 is superior to the first integration scenario (Fig. 3.9).

MIMO Channel Capacity

The resulting aggregated MIMO channel capacity $\bar{C}_{\text{tot}}$, averaged over the 5 GHz Wi-Fi band, is depicted in Fig. 3.10 as a function of the SNR for all considered placements of the MU array and for both integration scenarios, in case the channel is known (and waterfilling is applied) or unknown to the transmitter. Fig. 3.10 shows that only very small capacity gains are obtained by applying waterfilling. Therefore, an ultra-short-range MIMO channel implemented with our three-element array does not require channel knowledge at the transmitter. This reduces latency and signal processing complexity, since no feedback is required.

The antenna array also yields a significant reduction in power consumption. To express the gain in SNR that is obtained by exploiting the multiplexing capabilities of the ultra-short-range 3 x 3 MIMO channel, the multiplexing gain $Gain_{\text{MUX}}$ is defined. It is calculated by comparing the SNR required by the ultra-short-range 3 x 3 MIMO channel (denoted as SNR_{MIMO}) to the SNR required by the median of the nine corresponding SISO links in order to guarantee $\bar{C}_{\text{tot}} = 14.375$ bps/Hz. This specific value for $\bar{C}_{\text{tot}}$ was selected as it is the maximum supported error-free spectral efficiency by a three-stream 802.11ac Wi-Fi access point with 160 MHz bandwidth [37]. Both the SNR_{MIMO} and the $Gain_{\text{MUX}}$ are depicted in Table 3.2, for all considered placements of the MU array and for both integration scenarios, in case the channel is unknown to the transmitter. Specifically, the ultra-short-range 3 x 3 MIMO channel, implemented with our three-element arrays, yields a $Gain_{\text{MUX}}$ up to 55.9 dB and up to 41.0 dB for the first and second integration scenario, respectively.

Next, the influence of the worktop on the MIMO channel capacity is assessed by analyzing the integration loss for both integration scenarios. The integration loss expresses the increase in SNR required to maintain $\bar{C}_{\text{tot}}$ at 14.375 bps/Hz, as a result of the presence of the worktop. Measurements show that the integration loss varies between 1.0 dB and 4.3 dB for integration scenario 1 and between 4.2 dB and 6.3 dB for integration scenario 2, depending on the placement of the MU array. In general, the integration loss is lower for integration scenario 1, because only a fraction of the thickness of the worktop is present between both arrays (Fig. 3.4).

Despite the excellent multiplexing performance of the array in both integration scenarios (Fig. 3.9 and Table 3.2), Fig. 3.10 and Table 3.2 demonstrate that the integration scenario has a significant influence on $\bar{C}_{\text{tot}}$ and its behavior when the MU array's placement is varied. The first integration scenario guarantees the best performance, provided that the MU array is perfectly aligned with the AP ar-

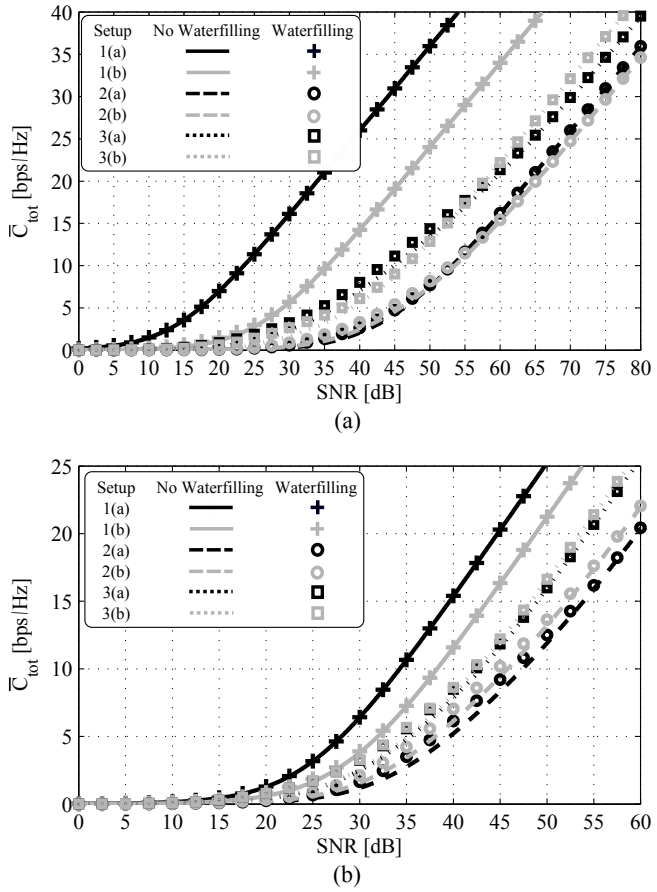

Figure 3.10: Aggregated MIMO channel capacity $\bar{C}_{\text{tot}}$, averaged over the 5 GHz Wi-Fi band, as a function of SNR, in case the channel is unknown (lines) and known (markers) by the transmitter, for all placements of the MU array (Table 3.1). (a) Integration scenario 1. (b) Integration scenario 2.

ray, whereas the second integration scenario guarantees more stable performance with respect to displacement of the MU array. This can be mainly attributed to the smaller z-distance in integration scenario 1 (Fig. 3.4). Obviously, this effect influences the total aggregated data throughput that can be provided to the MU, when the MU array's position and orientation are varied. In particular, an identical SNR of 40 dB in both integration scenarios guarantees a maximum aggregated datarate between 329 Mbps and 4.158 Gbps for the first integration scenario, and a maximum aggregated datarate between 834 Mbps and 2.464 Gbps for the second integration scenario, assuming full and exclusive use of the maximum 802.11ac subchannel bandwidth (= 160 MHz). In case the entire 5 GHz Wi-Fi bandwidth

Table 3.2: Main MIMO channel capacity performance metrics for the six measurement setups discussed in Table 3.1.

Setup	Integration scenario 1		Integration scenario 2	
	SNR_{MIMO} $[dB]$	$Gain_{\text{MUX}}$ $[dB]$	SNR_{MIMO} $[dB]$	$Gain_{\text{MUX}}$ $[dB]$
1(a)	28.2	55.9	39.0	41.0
1(b)	40.1	26.8	43.0	27.7
2(a)	58.1	25.7	53.1	24.9
2(b)	59.0	34.2	51.4	34.0
3(a)	51.4	31.7	48.2	26.2
3(b)	51.8	28.3	47.6	27.6

(= 700 MHz) is exclusively assigned to the MU and the SNR remains 40 dB, the maximum aggregated datarate varies between 1.439 Gbps and 18.193 Gbps for the first integration scenario and between 3.650 Gbps and 10.780 Gbps for the second integration scenario. Note that, in integration scenario 1, the smaller distance z and the lower integration loss guarantee a significantly higher maximum aggregated datarate at the optimum placement of the MU array (setup 1(a)), owing to the stronger coupling between the AP and MU array for that specific setup (Fig. 3.8).

Hence, the high and stable multiplexing gain offered by the ultra-short-range MIMO channel, implemented with our novel three-element arrays, allows reducing the transmit power to sufficiently low values [38], while guaranteeing data rates that are comparable to the data rates achieved by ethernet-connected devices (100 Mbps for 100base-T, 1 Gbps for 1000base-T, and 10 Gbps for 10 Gbase-T). In a real-life application, the distance z should be further optimized to obtain the best performance in the desired position for the MU (when AP and MU array are perfectly aligned), while guaranteeing sufficiently stable performance when the MU is shifted away from its optimal position. Alternatively, the optimal position for the MU may be indicated on the worktop. Then, the distance z can be minimized.

3.5 Conclusion

We have designed, fabricated and validated a novel three-element SIW cavity-backed slot antenna array for operation in the [5.15 - 5.85] GHz band, suitable for integration inside or underneath the worktop of a desk. The antenna topology and array geometry were carefully selected to set up a stable, high data rate ultra-short-range 3 x 3 MIMO wireless communication link with a mobile

user positioned on top of that worktop. The array was implemented in innovative antenna materials by means of the SIW technology to obtain a low-profile, low-cost, stable and high-performance broadband design that facilitates recycling. Two scenarios were considered for the integration of the three-element antenna array within a desk. In the first scenario, the array was integrated inside the worktop, whereas in the second integration scenario, the array was integrated underneath the worktop. Measurements prove that the antenna array maintains its excellent performance after integration, irrespective of the integration scenario, guaranteeing a bandwidth of at least 1.078 GHz and a minimum isolation between antenna elements of 30 dB within the entire [5.15 - 5.85] GHz band. Finally, the potential of ultra-short-range MIMO was investigated for both integration scenarios and for diverse relative orientations and positions of the MU, in case the channel is known to the transmitter and waterfilling is applied, and in case the channel is unknown by the transmitter. These measurements have revealed a high and stable multiplexing gain, which can be used to reduce power consumption and/or to increase the data rate, provided that the array is carefully integrated.

Acknowledgment

This work was supported in part by the iMinds IoT research program and in part by the Inter-University Attraction Poles Program initiated by the Belgian Science Policy Office.

References

[1] G. Kortuem, F. Kawsar, D. Fitton, and V. Sundramoorthy, "Smart objects as building blocks for the Internet of Things", *IEEE Internet Computing*, vol. 14, no. 1, pp. 44–51, Jan. 2010.

[2] C.-H. Lim, Y. Wan, N. Boon-Poh, and C.-M. See, "A Real-Time Indoor WiFi Localization System Utilizing Smart Antennas", *IEEE Trans. Consumer Electron.*, vol. 53, no. 2, pp. 618–622, 2007.

[3] K. Nishimori, N. Honma, T. Seki, and K. Hiraga, "On the Transmission Method for Short-Range MIMO Communication", *IEEE Trans. Veh. Technol.*, vol. 60, no. 3, pp. 1247–1251, Mar. 2011.

[4] H. Sundmaeker, P. Guillemin, P. Friess, and S. Woelffle, Eds., *Vision and challenges for realising the internet of things.* Luxembourg: Publications Office of the European Union, 2010.

[5] C. Hansen, "Wigig: Multi-gigabit Wireless Communications in the 60 GHz Band", *IEEE Wireless Communications*, vol. 18, no. 6, pp. 6–7, Dec. 2011.

[6] Y. Karasawa, "Innovative Antennas and Propagation Studies for MIMO Systems", *IEICE Transactions on Communications*, vol. E90-B, no. 9, pp. 2194–2202, Sep. 2007.

[7] B. Clerckx, C. Craeye, D. Vanhoenacker-Janvier, and C. Oestges, "Impact of Antenna Coupling on 2 x 2 MIMO Communications", *IEEE Trans. Veh. Technol.*, vol. 56, no. 3, pp. 1009–1018, 2007.

[8] M. Jensen and J. Wallace, "A Review of Antennas and Propagation for MIMO Wireless Communications", *IEEE Trans. Antennas Propagat.*, vol. 52, no. 11, pp. 2810–2824, 2004.

[9] N. Honma, K. Nishimori, T. Seki, and M. Mizoguchi, "Short range MIMO communication", in *Proc. of the 3th European Conference on Antennas and Propagation (EUCAP)*, Berlin, Germany, 23-27 March 2009, pp. 1763–1767.

[10] J.-S. Jiang and M. Ingram, "Spherical-wave model for short-range MIMO", *IEEE Transactions on Communications*, vol. 53, no. 9, pp. 1534–1541, Sep. 2005.

[11] F. Bohagen, P. Orten, and G. Oien, "Construction and capacity analysis of high-rank line-of-sight MIMO channels", in *Wireless Communications and Networking Conference, 2005 IEEE*, vol. 1, New Orleans, LA, USA, 13-17 March 2005, pp. 432–437.

[12] O. Caytan, S. Lemey, S. Agneessens, D. Vande Ginste, P. Demeester, C. Loss, R. Salvado, and H. Rogier, "Half-mode substrate-integrated-waveguide cavity-backed slot antenna on cork substrate", *Antennas Wirel. Propag. Lett.*, vol. 15, no. 99, pp. 162–165, May 2015.

[13] A. Georgiadis, A. Collado, S. Via, and C. Meneses, "Flexible hybrid solar/EM energy harvester for autonomous sensors", in *2011 IEEE MTT-S International Microwave Symposium*, Baltimore, MD, USA, 5-10 June 2011, pp. 1–4.

[14] S. Kim, A. Georgiadis, A. Collado, and M. M. Tentzeris, "An inkjet-printed solar-powered wireless beacon on paper for identification and wireless power transmission applications", *IEEE Trans. Microwave Theory Techn.*, vol. 60, no. 12, pp. 4178–4186, Dec. 2012.

[15] V. Lakafosis, A. Rida, R. Vyas, L. Yang, S. Nikolaou, and M. M. Tentzeris, "Progress Towards the First Wireless Sensor Networks Consisting of Inkjet-Printed, Paper-Based RFID-Enabled Sensor Tags", *Proc. IEEE*, vol. 98, no. 9, pp. 1601–1609, Sep. 2010.

[16] T. Kaufmann and C. Fumeaux, "Wearable textile half-mode substrate-integrated cavity antenna using embroidered vias", *IEEE Antennas Wirel. Propag. Lett.*, vol. 12, pp. 805–808, 2013.

[17] Federal Communications Commission, "Revision of Part 15 of the Commission's Rules to Permit Unlicensed National Information Infrastructure (U-NII) Devices in the 5 GHz Band, First Report and Order, ET Docket No. 13-49", released in April 1, 2014.

[18] G. Q. Luo, Z. F. Hu, L. X. Dong, and L. L. Sun, "Planar slot antenna backed by substrate integrated waveguide cavity", *IEEE Antennas Wirel. Propag. Lett.*, vol. 7, pp. 236–239, 2008.

[19] M. Bozzi, A. Georgiadis, and K. Wu, "Review of substrate-integrated waveguide circuits and antennas", *IET Microwaves, Antennas & Propagation*, vol. 5, no. 8, pp. 909–920, 2011.

[20] M. Bozzi and R. Moro, "Low-cost fabrication, eco-friendly materials, and easy integration: the new technological paradigm for the future wireless sensor networks", in *European Microwave Conference (EuMC)*, Nuremberg, Germany, Oct. 6-10, 2013, pp. 858–861.

[21] N. Gvozdenovic, W. Thompson, M. A. Beach, C. F. Mecklenbrauker, and G. Hilton, "Short range ultra-wideband multiple-input multiple-output channel measurements", in *2013 IEEE WCNC*, Shanghai, China, pp. 2575–2578.

[22] M. Manteghi and Y. Rahmat-Samii, "Multiport characteristics of a wide-band cavity backed annular patch antenna for multipolarization operations", *IEEE Trans. Antennas Propagat.*, vol. 53, no. 1, pp. 466–474, Jan. 2005.

[23] G. Q. Luo, Z. F. Hu, W. J. Li, X. H. Zhang, L. L. Sun, and J. F. Zheng, "Bandwidth-Enhanced Low-Profile Cavity-Backed Slot Antenna by Using Hybrid SIW Cavity Modes", *IEEE Trans. Antennas Propagat.*, vol. 60, no. 4, pp. 1698–1704, Apr. 2012.

[24] S. Lemey, F. Declercq, and H. Rogier, "Dual-band substrate integrated waveguide textile antenna with integrated solar harvester", *IEEE Antenn. Wireless Propag. Lett.*, vol. 13, no. 1, pp. 269–272, 2014.

[25] R. Tian, B. K. Lau, and Z. Ying, "Multiplexing Efficiency of MIMO Antennas", *IEEE Antennas Wireless Propag. Lett.*, vol. 10, pp. 183–186, 2011.

[26] M. Karaboikis, V. Papamichael, G. Tsachtsiris, C. Soras, and V. Makios, "Integrating Compact Printed Antennas Onto Small Diversity MIMO Terminals", *IEEE Trans. Antennas Propagat.*, vol. 56, no. 7, pp. 2067–2078, 2008.

[27] Javaux, "Fiche technique NBR41-42", Tech. Rep.

[28] F. Declercq, H. Rogier, and C. Hertleer, "Permittivity and loss tangent characterization for garment antennas based on a new matrix-pencil two-line method", *IEEE Trans. Antennas Propagat.*, vol. 56, no. 8, pp. 2548–2554, Aug. 2008.

[29] S. Agneessens and H. Rogier, "Compact Half Diamond Dual-Band Textile HMSIW On-Body Antenna", *IEEE Trans. Antennas Propagat.*, vol. 62, no. 5, pp. 2374–2381, 2014.

[30] S. Lemey, F. Declercq, and H. Rogier, "Textile antennas as hybrid energy-harvesting platforms", *Proc. IEEE*, vol. 102, no. 11, pp. 1833–1857, Nov. 2014.

[31] M. Scarpello, D. Vande Ginste, and H. Rogier, "Design of a low-cost steerable textile antenna array operating in varying relative humidity conditions.", *Microw. Opt. Technol. Lett.*, vol. 54, no. 1, pp. 40–44, Jan. 2012.

[32] M. Rossi, S. Agneessens, H. Rogier, and D. Vande Ginste, "Stochastic analysis of the impact of substrate compression on the performance of textile antennas", *IEEE Trans. Antennas Propagat.*, vol. 64, no. 6, p. 1, 2016.

[33] A. Paulraj, R. Nabar, and D. Gore, *Introduction to Space-Time Wireless Communications*. Cambridge University Press, 2003.

[34] T. M. Cover and J. Thomas, *Elements of Information Theory (Wiley Series in Telecommunications and Signal Processing)*. Wiley-Interscience, 1991.

[35] M. Qaraqe, Q. H. Abbasi, A. Alomainy, and E. Serpedin, "Experimental Evaluation of MIMO Capacity for Ultrawideband Body-Centric Wireless Propagation Channels", *IEEE Antennas and Wirel. Propag. Lett.*, vol. 13, pp. 495–498, 2014.

[36] J. Salo, P. Suvikunnas, H. El-Sallabi, and P. Vainikainen, "Ellipticity statistic as measure of MIMO multipath richness", *Electronics Letters*, vol. 42, no. 3, pp. 160–162, Feb. 2006.

[37] M. Gast, *802.11ac: A Survival Guide*, M. Blanchette, Ed. O'Reilly, 2013.

[38] L. Ward, "802.ac technology: introduction", Rohde&Schwarz, Tech. Rep., 2012.

PART II

Textile Antenna Systems for Body-Centric Wireless Communication

Smart-fabric interactive-textile (SFIT) systems offer exciting new possibilities in a wide range of application areas, provided that they exhibit sufficient robustness and autonomy to be reliably deployed. In this part of the dissertation, we focus on a holistic design approach to realize autonomous, reliable and unobtrusive SFIT systems, capable of setting up an energy-efficient and stable wireless body-centric communication link without the discomfort of frequent battery recharging. In our design approach, textile antenna design plays a vital role. In Chapter 4, a high-performance, ultra-wideband textile antenna is presented that exhibits excellent on-body performance. Chapters 5 and 6 describe how the functionality of such highly-efficient textile antennas can be further extended by reusing their surface as an integration platform for energy-harvesting and power management hardware. In Chapter 7, the antenna/harvester co-design strategy, proposed in Chapter 5 and further developed in Chapter 6, is combined with a state-of-the-art active textile antenna co-design procedure to obtain a novel holistic microwave system design paradigm. This novel strategy is based on a dedicated textile antenna design, serving as an integration platform for the energy-harvesting, power management, sensing, processing, and transceiver hardware. This approach guarantees extended operational autonomy by matching the power generation profile of the energy-harvesting transducers to the power consumption of the SFIT system.

4

SIW Textile Antennas as a Novel Technology for UWB RFID Tags

Sam Lemey and Hendrik Rogier

Published in the proceedings of the 2014 IEEE Conference on RFID Technology and Applications (RFID-TA)

★ ★ ★

A wearable ultra-wideband (UWB) textile antenna based on substrate integrated waveguide technology is presented for application in the next generation radio-frequency identification (RFID) systems operating in the low-duty cycle restricted [3.4-4.8] GHz UWB band. The design of a UWB antenna for application in smart textiles is very challenging. For end users, the antenna should be unobtrusively integrated and comfortable to wear. From a system point of view, good impedance matching and radiation characteristics over a very large bandwidth are of major importance, even under harsh operating conditions. Our approach consists of applying brass tube eyelets to implement a cavity-backed slot antenna in textile materials. A prototype was realized and measured. The measured return loss characteristic and radiation performance after bending and deploying the antenna on different human body parts prove that our antenna is extremely suited for on-body use. A -10 dB-bandwidth of 1.33 GHz, or 33%, was realized, in which the radiation pattern remains quasi invariable.

4.1 Introduction

Rapid developments in smart-fabric interactive-textile (SFIT) systems promise to revolutionize many aspects of a person's daily life. Potential applications are, amongst others, monitoring and localization of first responders during interventions and monitoring vital signs and position of patients in hospitals and home-care scenarios. For instance, [1] designed a wearable multiband active antenna for use in Global Positioning System (GPS) applications and demonstrated the possibility to track first responders in outdoor locations. Reference [2] showed that GPS users could expect positional accuracies within approximately 5 m in open sky settings. Moreover, solutions based solely on GPS are not optimal in indoor scenarios.

Recent developments in radio-frequency identification (RFID) systems paved the way to accurate submeter localization in indoor and confined areas [3], [4]. RFID systems consist of readers on the one hand, and tags applied to objects, on the other hand. The narrow band nature of first and second generation RFID systems, operating in the ultra-high-frequency (UHF) band and using standard continuous wave communication, makes them sensitive to narrowband and multiuser interference, vulnerable to multipath signal cancellation, and unsuitable for accurate localization [5]. Therefore, next generation RFID systems adopt the impulse radio ultra-wideband (IR-UWB) implementation to transmit (sub)nanosecond duration pulses. This enables them to provide both reliable identification [5] and high-accuracy localization of objects [3], [4]. Besides real-time localization at submeter level, these next generation RFID systems feature extremely low power consumption [6], low cost and small size. Hence, they are very suitable for integration into SFIT textile systems, to enable high-definition localization of persons in indoor locations or confined areas. Implementing multiple of judiciously positioned RFID tags could even allow reconstructing the position and orientation of the human body to enable augmented sensing, such as fall detection for the elderly. The U.S. Federal Communications Commission (FCC) has allocated a [3.1-10.6] GHz-block of radio spectrum for unlicensed UWB transmission at a maximum power spectral density of -41.3 dBm/MHz [7]. They defined an UWB signal as a signal with instantaneous spectral occupancy in excess of 500 MHz or a fractional bandwidth of 20% or more. The European Commission has issued an EC decision which states that UWB devices can use the [3.4-4.8] GHz and the [6.0-8.5] GHz band with the same maximum power spectral density as in the U.S., provided that signals in the lower frequency band meet a low duty cycle restriction [8].

Obviously, the ultra-wide bandwidth implies substantial different antenna topologies and propagation aspects as compared to narrow band systems, which makes practical antenna design more challenging [9]. Besides the fact that matching and efficient radiation should be ensured over an ultra-wide bandwidth, UWB antenna radiation patterns should be as constant as possible over the entire bandwidth to minimize direction-specific distortion of UWB waveforms [9]. Moreover, a wearable on-body antenna should exhibit robust impedance matching and radiation performance, independent of the wearer's morphology and of the antenna's posi-

tion on the body. This can be achieved by designing the antenna in such a way that it radiates away from the body. Since power is radiated in the desired directions instead of being absorbed by the user's body, such a design strategy also results in a safer and more power-efficient design. Finally, end users of SFIT systems impose stringent requirements in terms of wearability and comfort. Hence, each component should be low-profile, flexible and breathable, making textile antennas very suitable for unobtrusive integration in SFIT systems.

In this chapter, we present a robust wearable UWB textile cavity-backed slot antenna in substrate integrated waveguide (SIW) technology, for operation in the low duty cycle restricted [3.4-4.8] GHz band. More specifically, we design for a maximum -10 dB impedance bandwidth within this band, in the meantime maintaining robust and efficient operation, since [10] demonstrates a ranging error of only 1.63 cm when using an IR-UWB pulse with a 500 MHz bandwidth at a center frequency of 4.25 GHz and [11] stated that a larger bandwidth is beneficial for reducing the ranging error. Cavity-backed slot antennas have the potential to exhibit stable characteristics in the vicinity of the human body, since they only transmit/receive power in one hemisphere and reduce radiation leakage in the opposite hemisphere. By implementing the cavity with SIW technology, a low-profile single substrate antenna can be realized. Different textile SIW cavity-backed antennas were already realized by using conductive yarn [12] or tubular eyelets [13]. Yet, on the one hand, both designs are narrowband, as they rely on a single resonant frequency excitation. On the other hand, [14], [15] describe techniques to increase the impedance bandwidth. The latter technique is effectively exploited in [16] to realize a wideband textile SIW cavity-backed antenna with an impedance bandwidth of 409 MHz or 15.1%, thereby covering the 2.45 GHz Industrial, Scientific and Medical band as well as both up- and downlink of the 4G LTE band 7. [16] also demonstrates the potential to integrate electronic circuits below the antenna cavity and solar cells on top of the cavity beside the antenna slot. The antenna topology, its construction process and the measures taken to achieve a robust wearable UWB textile antenna are discussed in Section 4.2. The performance of the antenna in free space and when deployed on different parts of the human body is evaluated and documented in Section 4.3.

4.2 Antenna design and topology

4.2.1 Antenna design considerations

The most widely accepted definition of an UWB signal, formulated by the FCC, requires that the antenna exhibits a -10 dB bandwidth in excess of 500 MHz and/or a fractional bandwidth higher than 20%. Our main design goal is therefore to design a wearable textile antenna with UWB behavior in the low duty cycle restricted [3.4-4.8] GHz band. The deployment of a wearable antenna on the human body in conjunction with several detrimental conditions, such as crumpling, bending and moisture regain will cause a shift in bandwidth and resonant frequency [17] which

can be minimized by a suitable choice of antenna topology, antenna materials and implementation technology. Obviously, in all realistic deployment conditions, the antenna topology should also maintain its UWB behavior. These choices will be discussed in Section 4.2.2 and Section 4.2.3. Once a suitable topology is chosen, the antenna will be designed for maximum bandwidth, in combination with large radiation efficiency. Moreover, we aim for a stable and broad radiation pattern over the entire bandwidth, to minimize direction-specific distortion of the UWB waveforms, in the meantime maintaining a compact and low-profile structure.

4.2.2 Antenna design

The configuration of our proposed textile UWB SIW cavity-backed slot antenna is shown in Fig. 4.1. A cavity-backed slot antenna is selected because such a topology demonstrates an excellent isolation from its environment [14], making it not only extremely suitable for on-body deployment, but also for the integration of additional electronic hardware [16]. By deploying the antenna on the human body in such a way that the slot is oriented away from the body, the antenna mainly radiates in that hemisphere and backside radiation is minimized. Hence, a high front-to-back ratio (FTBR) can be obtained, resulting in a much safer and more efficient design, since absorption of radiation by the human body is minimal. In addition, a high suppression of unwanted surface waves can be achieved [18]. By selecting SIW technology for the implementation of the backed cavity, a simple low-profile and cost-effective single substrate design can be realized to allow unobtrusive integration in SFIT systems. To overcome the narrowband nature of such topologies, the bandwidth enhancement technique presented in [15] is applied to obtain a textile UWB SIW cavity-backed slot antenna.

The proposed design, depicted in Fig. 4.1, is based on a rectangular shaped SIW cavity which is split into two half-cavities (half-cavity A and B) by a non-resonant rectangular slot. By carefully determining the dimensions of the slot and both half parts of the cavity, two hybrid mode combinations are excited at two different, neighboring frequencies. The hybrid mode at the lowest resonance frequency consists of a combination of a weak TE_{110} and a strong TE_{120} mode, resulting in fields in both cavity parts which are out-of-phase. This results in a dominant field situated in half-cavity B. At the higher resonance frequency, a strong TE_{110} and a weak TE_{120} mode are combined. Then, the fields in both cavity parts are in phase, but exhibit a large difference in magnitude. The dominant field is now situated in half-cavity A. In both cases, the large electric field across the non-resonant slot will cause it to radiate. By selecting both resonance frequencies close enough to each other, both hybrid modes can be merged and the bandwidth can be increased to obtain an UWB antenna. Power is injected into/extracted from the SIW cavity by means of a 50 Ω grounded coplanar waveguide (GCPW) feed line, located in the feed plane at the center point of the largest SIW cavity wall (Fig. 4.1.c). For measurement convenience, a SMA connector is soldered at the end of a microstrip line that results from extending the inner conductor of the GCPW feed line.

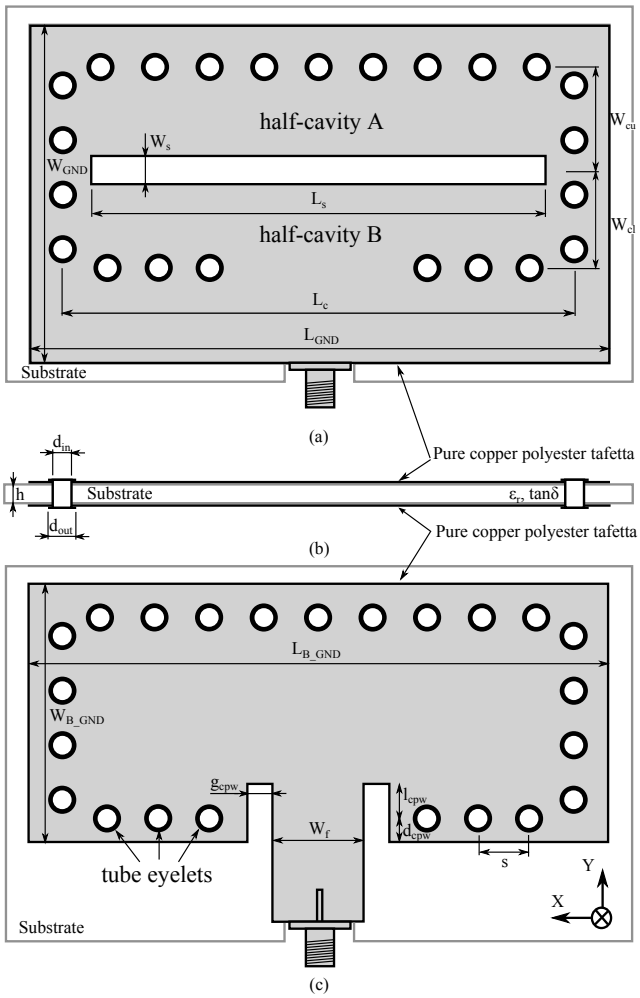

Figure 4.1: Topology of the textile UWB SIW cavity-backed slot. (a) Top view: slot plane. (b) Cross-sectional view. (c) Bottom view: feed plane.

The antenna was designed and optimized by using the transient solver of CST Microwave studio. During the design process, we take care that the return loss characteristic exceeds 10 dB well below 3.4 GHz and exceeds 13 dB in the region where both hybrid modes merge, to account for variations in material parameters, inaccuracies of the fabrication process and frequency de-tuning caused by bending, crumpling or proximity of the human body. Furthermore, simulations revealed out-of-band backside radiation at higher frequencies when g_{cpw} was too small and/or when d_{cpw} was chosen too large. The antenna dimensions after an extensive optimization process are given in Table 4.1.

Table 4.1: Antenna dimensions.

Parameter	Value [mm]	Parameter	Value [mm]	Parameter	Value [mm]
L_c	75.0	W_s	4.2	W_{GND}	49.5
W_{cu}	14.34	L_s	67.0	L_{GND}	85.0
W_{cl}	14.17	W_f	13.4	W_{B_GND}	38.0
d_{in}	4.0	g_{cpw}	3.7	L_{B_GND}	85.0
d_{out}	6.0	l_{cpw}	4.8	h	3.94
s	8.0	d_{cpw}	3.5		

4.2.3 Antenna materials and realization

The materials from which on-body antennas are assembled are of major importance to achieve flexible, light-weight and robust on-body devices. Hence, their selection should be done with the greatest care.

A 3.94-mm-thick closed-cell expanded rubber protective foam, possessing good chemical stability, low moisture regain, and good resistance against oils and solvents, is selected as antenna substrate. It exhibits a relative dielectric permittivity ϵ_r of 1.495 and loss tangent (tanδ) of 0.016 at 2.45 GHz [19]. However, a better agreement between measurements and simulations is achieved when a tanδ of 0.035 was used in simulations. The slot and feed plane are realized with a copper-coated polyester taffeta electro-textile, with a surface resistivity $R_S = 0.18\ \Omega$/sq [19]. After judicious alignment, both conductive layers are glued to the antenna substrate by means of thermally-activated adhesive sheets. Finally, flat flange brass tube eyelets are applied to form the antenna cavity (Fig. 4.1). Fig. 4.2 depicts a prototype of our UWB SIW textile antenna.

4.3 Antenna performance

First, the return loss characteristic of the antenna in free space conditions was verified in an anechoic room by means of Agilent's N5242A PNA-X Network Analyzer. The simulated and measured reflection coefficients $|S_{11}|$, depicted in Fig. 4.3, are in very good agreement. Simulations and measurements demonstrate good impedance matching to $Z_0 = 50\ \Omega$ from 3.33 GHz to 4.66 GHz, corresponding to a -10dB impedance bandwidth of 1.33 GHz and a fractional bandwidth of 33%. Hence, the antenna exhibits UWB behavior. Over the entire [3.4-4.8] GHz band, the return loss remains larger than 6 dB.

The same measurement setup, extended by an orbit/FR positioning system, was used to measure the free-space radiation patterns. Fig. 4.4 depicts the measured and simulated radiation patterns in the E- and H-plane of the antenna at 3.4 GHz,

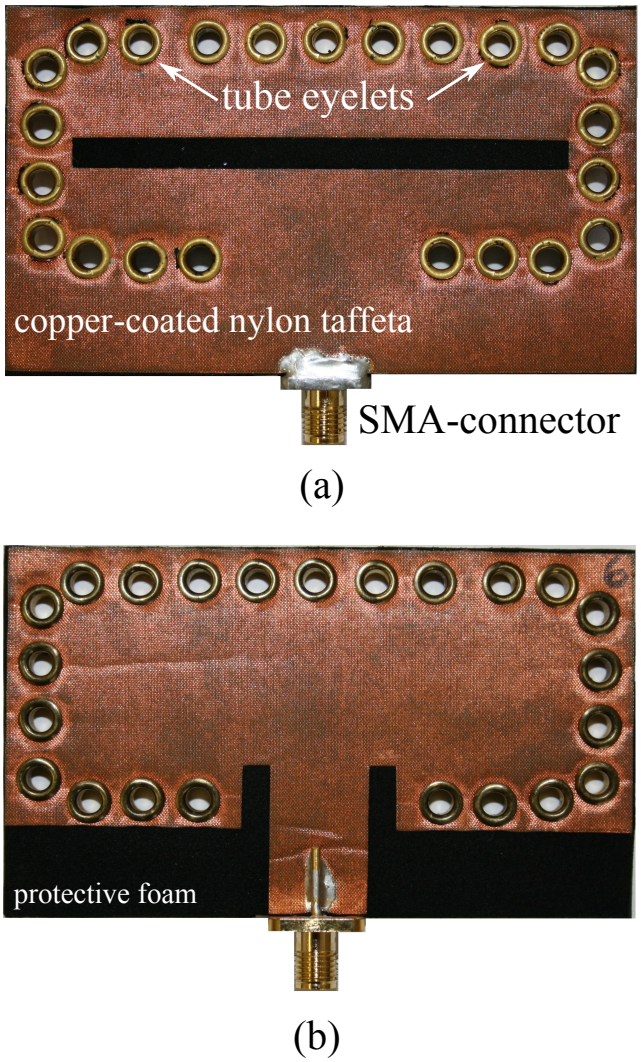

Figure 4.2: Prototype of the UWB SIW textile antenna. (a) Top view: slot plane. (b) Bottom view: feed plane.

3.85 GHz, and 4.3 GHz. Simulations predicted very similar radiation patterns over the entire bandwidth, which is advantageous for minimizing direction-specific distortion of UWB wave forms, and is proven by the measurements in Fig. 4.4. Simulated and measured antenna gain along broadside, FTBR, and 3dB-beamwidth in the E- and H-plane at the three earlier mentioned frequencies are described in Table 4.2. The measured gain along broadside is slightly higher than the simulated gain at 3.4 and 3.85 GHz, whereas the gain at 4.3 GHz is lower than simulated. A

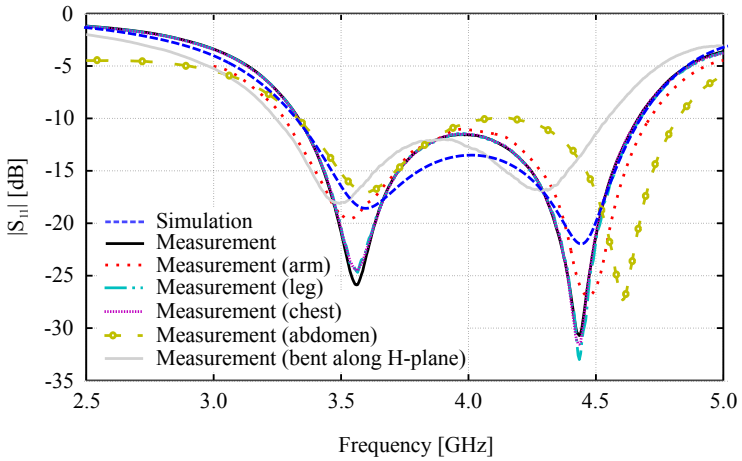

Figure 4.3: $|S_{11}|$ with respect to 50 Ω when the antenna is deployed under different conditions.

slightly larger backside radiation could be observed at all three frequencies. The measured 3dB-beamwidth along the H-plane is similar at each frequency. A narrower beam is observed compared to simulations, whereas the measured 3dB-beamwidth along the E-plane slightly increases with frequency. A broader beam is obtained compared to simulations. Generally speaking, we conclude that simulations and measurements agree very well.

Since textile on-body antennas will be worn in proximity of the body, their performance should also be extensively tested when deployed onto the human body and when bent, to be certain that they still perform in more realistic situations. Therefore, on-body $|S_{11}|$ measurements were performed and depicted in Fig. 4.3. The antenna was positioned on the arm, leg, chest and abdomen of an average height and weight male test person wearing a T-shirt and jeans. In case of deployment on the leg, the jeans served as spacer. In the other cases, the T-shirt was used as spacer. The antenna was positioned in such a way that bending is prevented as much as possible. The $|S_{11}|$ remains unchanged when deploying the antenna on the chest or leg, whereas a minor change can be noticed when the antenna is deployed on the arm. The curve corresponding to the measurement on the abdomen exhibits an increase in bandwidth (1.49 GHz) because of a shift in the highest resonance frequency.

Finally, the antenna was bent with a radius of 5 cm along its H-plane. Fig. 4.3 shows a decrease in both resonance frequencies and in return loss. However, the bandwidth reduces only to 1.30 GHz, demonstrating its robustness even under extreme bending.

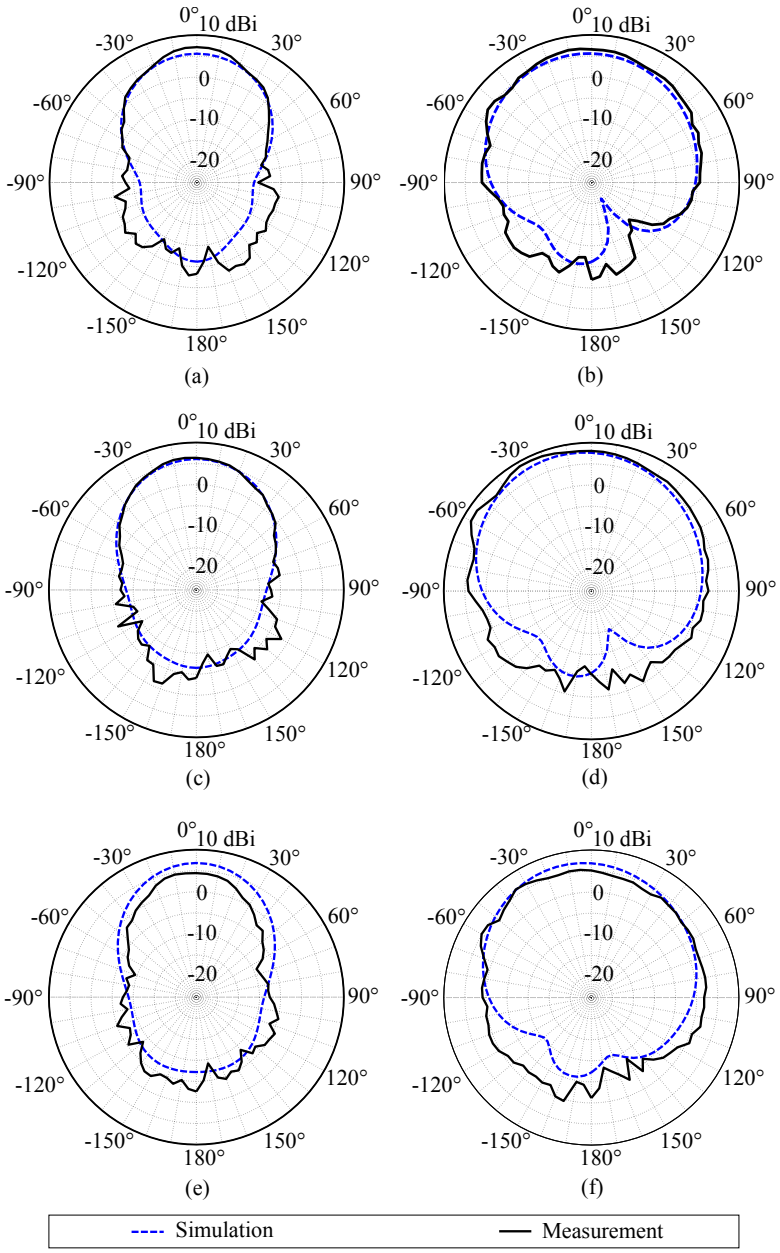

Figure 4.4: Measured and simulated radiation pattern [dBi] of the antenna at 3.4 GHz in the H-plane (a) and E-plane (b), at 3.85 GHz in the H-plane (c) and E-plane (d) and at 4.3 GHz in the H-plane (e) and E-plane (f).

Table 4.2: Measured (simulated) antenna characteristics

f	Gain	FTBR	3dB-beamwidth [°]	
[GHz]	[dBi]	[dB]	H-plane	E-plane
3.40	6.8 (5.9)	10.5 (11.6)	46 (60)	117 (111)
3.85	6.5 (6.1)	10.5 (12.6)	54 (63)	123 (108)
4.30	4.6 (6.3)	7.1 (12.3)	46 (60)	133 (101)

4.4 Conclusion

In this chapter, the design of a robust wearable ultra-wideband (UWB) textile cavity-backed slot antenna in substrate integrated waveguide (SIW) technology for operation in the low duty cycle restricted [3.4-4.8] GHz band was described. Our design relies on brass tube eyelets and textile materials to realize a conformal, light-weight and low profile cavity-backed slot antenna, which exhibits a -10dB impedance bandwidth of 1.33 GHz, or 33%, in which a quasi-invariable radiation pattern is maintained. Over the complete [3.4-4.8] GHz band, the return loss exceeds 6dB. Measurements performed on our prototype after bending and deploying the antenna on different positions of the human body prove its robust performance and very high isolation from the human body. Hence, the potential of exploiting SIW technology for realizing robust UWB wearable antennas is demonstrated.

Acknowledgment

Part of this work was supported by BELSPO through the IAP phase VII BESTCOM project.

References

[1] A. Dierck, H. Rogier, and F. Declercq, "A Wearable Active Antenna for Global Positioning System and Satellite Phone", *IEEE Trans. Antennas Propag.*, vol. 61, no. 2, pp. 532–538, Feb. 2013.

[2] M. Wing, A. Eklund, and L. Kellogg, "Consumer-grade Global Positioning System (GPS) Accuracy and Reliability", *J. Forest.*, vol. 103, no. 4, pp. 169–173, 2005.

[3] P. Meissner, E. Leitinger, M. Frohle, and K. Witrisal, "Accurate and Robust Indoor Localization Systems using Ultra-wideband Signals", in *European Navigation Conference (ENC)*, Vienna, Austria, 23-25 Apr. 2013.

[4] W. C. Chung and D. S. Ha, "An Accurate Ultra Wideband (UWB) Ranging for Precision Asset Location", in *IEEE Int. Conf. on Ultra Wideband Systems and Technologies*, Virginia, USA, 16-19 Nov. 2003, pp. 389–393.

[5] D. Dardari, R. D'Errico, C. Roblin, A. Sibille, and M. Z. Win, "Ultrawide Bandwidth RFID: The Next Generation?", *Proc. IEEE*, vol. 98, no. 9, pp. 1570–1582, Sept. 2010.

[6] Z. Li, W. Dehaene, and G. Gielen, "A 3-tier UWB-based indoor localization system for ultra-low-power sensor networks", *IEEE Trans. Wireless Commun.*, vol. 8, no. 6, pp. 2813–2818, 2009.

[7] Federal Communications Commission, "Revision of Part 15 of the Commission's Rules Regarding Ultra-Wideband Transmission Systems, First Rep. Order ET Docket 98-153", Adopted Feb. 14, 2002. Released Apr. 22, 2002.

[8] Electronic Communications Committee, "Specific UWB Applications in the bands 3.4-4.8 GHz and 6.8-8.5 GHz Location Tracking Applications for Emergency Services (LAES), Location Tracking Applications Type 2 (LT2) and Location Tracking and Sensor Applications for Automotive and Transportation Environments (LTA).", Oct. 2011.

[9] W. Q. Malik, C. J. Stevens, and D. J. Edwards, "Ultra-wideband antenna distortion compensation", *IEEE Trans. Antennas. Propag.*, vol. 56, no. 7, pp. 1900–1907, 2008.

[10] H. Zhan, J. Ayadi, J. Farserotu, and J.-Y. Le Boudec, "Impulse radio ultrawideband ranging based on maximum likelihood estimation", *IEEE Trans. Wirel. Commun.*, vol. 8, no. 12, pp. 805–808, Dec. 2009.

[11] D. Dardari, A. Conti, U. Ferner, A. Giorgetti, and M. Z. Win, "Ranging With Ultrawide Bandwidth Signals in Multipath Environments", *Proc. IEEE*, vol. 97, no. 2, pp. 404–426, Mar. 2009.

[12] T. Kaufmann and C. Fumeaux, "Wearable textile half-mode substrate-integrated cavity antenna using embroidered vias", *IEEE Antennas Wirel. Propag. Lett.*, vol. 12, pp. 805–808, 2013.

[13] R. Moro, S. Agneessens, H. Rogier, and M. Bozzi, "Wearable textile antenna in substrate integrated waveguide technology", *IET Electron. Lett.*, vol. 48, no. 16, pp. 985–987, Aug. 2012.

[14] W. Yang and J. Zhou, "Wideband Low-Profile Substrate Integrated Waveguide Cavity-Backed E-shaped Patch Antenna", *IEEE Antennas Wirel. Propag. Lett.*, vol. 12, pp. 143–146, 2013.

[15] G. Q. Luo, Z. F. Hu, W. J. Li, X. H. Zhang, L. L. Sun, and J. F. Zheng, "Bandwidth-Enhanced Low-Profile Cavity-Backed Slot Antenna by Using Hybrid SIW Cavity Modes", *IEEE Trans. Antennas Propagat.*, vol. 60, no. 4, pp. 1698–1704, Apr. 2012.

[16] S. Lemey, F. Declercq, and H. Rogier, "Dual-band substrate integrated waveguide textile antenna with integrated solar harvester", *IEEE Antenn. Wireless Propag. Lett.*, vol. 13, no. 1, pp. 269–272, 2014.

[17] A. Dierck, H. Rogier, and F. Declercq, "An Active Wearable Dual-band Antenna for GPS and Iridium Satellite Phone Deployed in a Rescue Worker Garment", in *IEEE Int. Conf. on RFID Technologies and Applications*, 4-5 Sept. 2013, pp. 1–5.

[18] G. Q. Luo, Z. F. Hu, L. X. Dong, and L. L. Sun, "Planar slot antenna backed by substrate integrated waveguide cavity", *IEEE Antennas Wirel. Propag. Lett.*, vol. 7, pp. 236–239, 2008.

[19] F. Declercq, I. Couckuyt, H. Rogier, and T. Dhaene, "Environmental High Frequency Characterization of Fabrics Based on a Novel Surrogate Modelling Antenna Technique", *IEEE Trans. Antennas Propagat.*, vol. 61, no. 10, pp. 5200–5213, Oct. 2013.

5

Dual-Band Substrate Integrated Waveguide Textile Antenna with Integrated Solar Harvester

Sam Lemey, Frederick Declercq and Hendrik Rogier

Published in the IEEE Antennas and Wireless Propagation Letters

★ ★ ★

A dual-band wearable textile antenna based on substrate integrated waveguide technology is presented for operation in the [2.4 - 2.4835] GHz Industrial, Scientific and Medical band and the [2.5 - 2.69] GHz 4G LTE band 7. The antenna features an integrated flexible solar harvesting system, consisting of a flexible solar cell, a power management system and energy storage. All these components are judiciously positioned on the antenna platform in order not to affect its radiation performance. The measured reflection coefficients and radiation characteristics after bending and deploying the antenna on a human body prove that the antenna is well suited for on-body use. A measured on-body antenna gain and radiation efficiency of 5.0 dBi and 89 % are realized. Measurements in a real-life situation have demonstrated the ability to scavenge a maximum of 53 mW by means of a single integrated flexible solar cell.

5.1 Introduction

Smart-fabric interactive-textile (SFIT) systems play a key role in critical professional applications such as monitoring rescue workers during interventions and

patients in hospitals and home-care. Therefore, they set up reliable wireless communication links between the mobile users and the control center. Obviously, end-users impose stringent requirements on wearable wireless communication systems, such as stable energy-efficient performance in harsh operating conditions, combined with wearability and comfort. In terms of antenna, a sufficiently broad radiation pattern, a high front-to-back ratio (FTBR), and large radiation efficiency are needed, besides flexibility and breathability. Moreover, to avoid heavy batteries and frequent recharging, low power consumption is called for. This makes 2.45-GHz Industrial, Scientific, and Medical (ISM) band textile antennas, implementing high-data-rate wireless audio/video communication links, ideal for SFIT systems, provided wireless local area network (WLAN) access points are available at the location of operation. In absence of this infrastructure, a 4G Long Term Evolution (LTE) wireless metropolitan area network (WMAN) may serve as an alternative.

While other components miniaturize continuously, the textile antenna's dimensions remain of the order of the wavelength to yield large radiation efficiency in proximity of the human body [1]. Professional garments offer a sufficiently large platform to integrate a textile antenna while active electronic circuitry, such as low noise amplifier and transceiver, may be directly integrated onto its feed plane [2]. In addition, to extend its autonomy, the system may be powered using energy harvesters [3], [4] by direct integration of solar cells on the antenna patch [5], [6].

Therefore, we present a novel dual-band wearable textile solar antenna for operation in the [2.4 - 2.4835]-GHz ISM band and the 4G LTE band 7 ([2.5 - 2.69] GHz). By implementing a cavity-backed slot antenna in substrate integrated waveguide (SIW) technology, high robustness against bending and stable characteristics in proximity of the human body are achieved. In addition, a flexible solar cell, a power management system (PMS), and microenergy cell (MEC) are easily integrated without affecting the antenna's radiation performance. Hence, the antenna surface serves simultaneously as efficient wireless communication, energy harvesting, and power management platform. To the best of the authors' knowledge, this is the first 2.45-GHz ISM/LTE band 7 dual-band wearable antenna with integrated solar harvester in literature.

Dual-band textile antennas for the bands covered by the proposed antenna have been described in literature before. Reference [7] presents a dual-band WiFi and 4G LTE textile antenna operating in the [2.4 - 2.69]-GHz and [5.1 - 5.875]-GHz bands. However, its gain is smaller than 2 dBi in the lower band. The absence of a ground plane between antenna and human body makes the antenna less suitable for on-body use. In contrast, [8] and [9] proposed different textile realizations of cavity-backed antennas based on the SIW technology. Such topologies are very suitable for on-body use [8]–[10]. Yet, both designs are narrowband due to the excitation of only one resonance frequency, although [11]–[13] outline techniques to enhance the impedance bandwidth.

5.2 Design of SIW cavity-backed slot antenna

We first design a wearable textile antenna with a return loss larger than 10 dB in the 2.45-GHz ISM band ([2.4-2.4835] GHz) and in the uplink and downlink of the 4G LTE band 7 ([2.50-2.57] and [2.62-2.69] GHz, respectively).

The geometrical configuration of the proposed SIW cavity-backed slot antenna is shown in Fig. 5.1. This topology realizes a very high isolation from its surroundings [12], making it suitable for body-worn applications and as platform for the integration of electronic hardware. In addition, an excellent suppression of unwanted surface waves, a large FTBR, and a high radiation efficiency (η_{rad}) are achieved [10] without the need for a large ground plane. SIW technology achieves a simple low-profile and cost-effective single substrate realization by means of tube eyelets, enabling easy routing of the solar cell's DC+ connection without affecting the antenna performance. The bandwidth enhancement technique presented in [13] was applied to realize good bandwidth performance even in the presence of material inhomogeneity, fabrication inaccuracy, and frequency detuning caused by bending or proximity of the human body.

A rectangular SIW cavity is split into two halves (parts A and B in Fig. 5.1(a)) by a nonresonant rectangular slot. The dimensions of the slot and both parts of the cavity were carefully chosen to simultaneously excite two hybrid modes, being two different combinations of the TE_{110} and the TE_{120} modes, at resonance frequencies close enough to yield a return loss larger than 10 dB in the frequency range of interest. The hybrid mode at the lowest resonance frequency is a combination of a strong TE_{120} and a weak TE_{110} mode. The fields in both cavity parts are out of phase, while the dominant field is situated in cavity part A. This results in radiation by the slot. The hybrid mode at the highest resonance frequency is a combination of a strong TE_{110} and a weak TE_{120} mode. The fields in both cavity parts are in phase, but exhibit a large difference in magnitude with the dominant field situated in cavity part B, generating radiation by the slot. A 50 Ω grounded coplanar waveguide (GCPW) feedline is designed in the bottom metal layer (Fig. 5.1(c)). In contrast to [8], impedance matching is realized without extending the GCPW feedline beyond the slot, providing more space to integrate electronic circuitry and improving shielding from the human body. Computer-aided optimization was performed using the transient solver of CST Microwave Studio, yielding the antenna dimensions given in Table 5.1.

The proposed antenna is fabricated using pure copper polyester Taffeta, with a surface resistivity $R_S = 0.18$ Ω/sq [14], as top and bottom layer. A 3.94-mm-thick closed-cell expanded rubber protective foam with $\epsilon_r = 1.495$ and $tan\delta = 0.016$ at 2.45 GHz serves as substrate [14]. After gluing the two conductive fabrics to the substrate with thermally activated adhesive sheets, the backed cavity is constructed by a row of equally spaced flat flange copper tube eyelets along each side of the cavity.

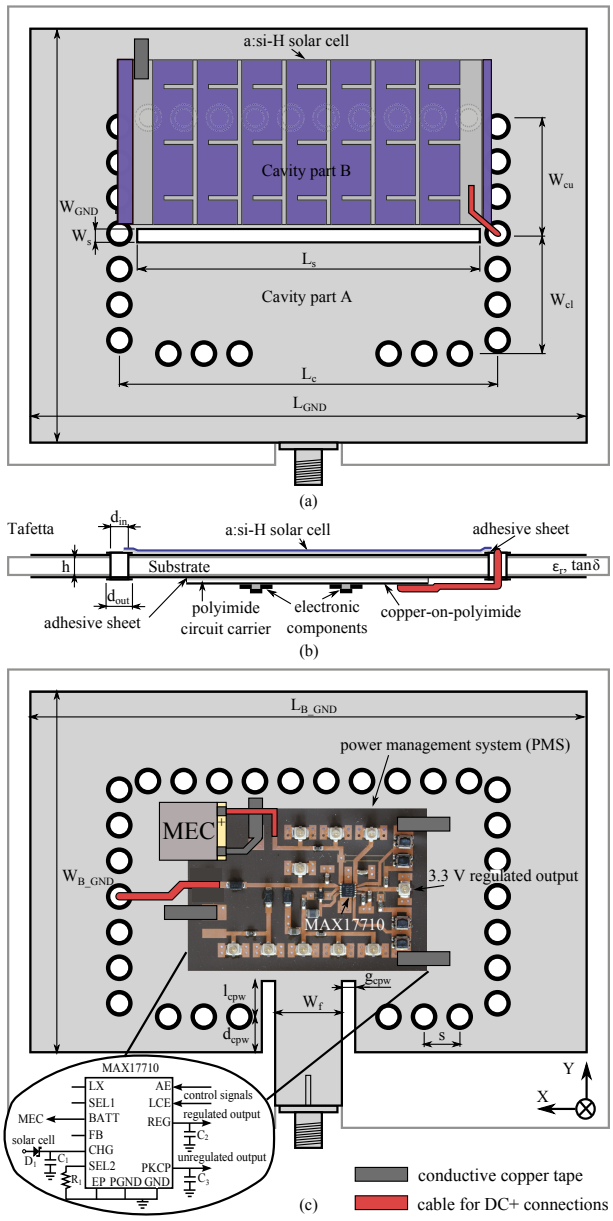

Figure 5.1: Dual-band textile SIW cavity-backed slot antenna with integrated energy-harvesting hardware. Inset: circuit representation of the PMS (D_1 = DFLS130L by Diodes Inc., $C_1 = 0.22\ \mu F$, $C_2 = 1\ \mu F$, $C_3 = 10\ \mu F$, $R_1 = 150\ \Omega$). (a) Top view. (b) Cross-sectional view. (c) Bottom view.

Table 5.1: Antenna dimensions.

Parameter	Value [mm]	Parameter	Value [mm]	Parameter	Value [mm]
L_c	84.5	W_s	3.9	W_{GND}	93
W_{cu}	26.2	L_s	76.5	L_{GND}	124.5
W_{cl}	26.8	W_f	15.5	W_{B_GND}	81
d_{in}	4	g_{cpw}	2.6	L_{B_GND}	124.5
d_{out}	6	l_{cpw}	8	h	3.94
s	8	d_{cpw}	7		

5.3 Integration of flexible solar energy harvester

The surface required by the antenna is then reused as a platform for solar energy harvesting and power management. Therefore, a flexible solar cell is integrated on top of the antenna. A PMS and an MEC are deployed on the antenna feed plane, as shown in Fig. 5.1(c). Only a single MEC and solar cell are applied here. Yet, depending on the application, more solar cells and energy storage devices may be added to the antenna.

5.3.1 Solar cell integration

The antenna provides a useful area of 11 280 mm^2 for solar cell integration, of which 84 x 37 mm^2 is effectively exploited by one SP4.2-37 ultra-thin and ultra-flexible PowerFilm thin film a-Si:H solar cell. The solar cell is positioned such that the radiating slot remains uncovered (Fig. 5.1(a)). The DC+ contact wire is routed through one of the tube eyelets to connect with the PMS (Fig. 5.1).

5.3.2 Power management circuit integration

The PMS is built around the MAX17710, a general-purpose energy-harvesting charger and protector IC by Maxim Integrated, as depicted in the inset of Fig. 5.1(c). The PMS controls the charging process of a 170-μm-thick Thinergy MEC-225 microenergy cell and generates a regulated output voltage to adequately power a wireless communication module. In addition, the PMS also protects the MEC against overcharge and overdischarge. The PMS is a linear harvesting system that allows a lower break-even threshold than maximum power point tracking [15]. Hence, solar energy harvesting is enabled in lower light intensity situations. The circuit is implemented on a flexible substrate consisting of one polyimide layer and two copper layers with a thickness of 25 and 9 μm, respectively. The PMS is

integrated directly underneath the antenna to achieve a compact module and to prevent antenna radiation from coupling into the circuitry. Moreover, only small electronic components (maximum footprint is 3 x 3 mm^2) are used, and these are distributed over a larger area than necessary to maintain the flexibility of the design. A nonconductive adhesive sheet is used to fix the solar cell to the slot plane. A similar sheet attaches the PMS and MEC to the feed plane without covering the feedline, as depicted in Fig. 5.1(c). Note that the implementation of the PMS depicted in Fig. 5.1(c) also contains additional test pins and push buttons for measurement purposes. Therefore, the dimensions of the PMS can be further reduced in the final application.

5.4 Simulation and measurement results

5.4.1 Antenna performance

First, the input matching of the antenna in free space was verified in an anechoic chamber by means of an Agilent N5242A PNA-X Network Analyzer. The measured and simulated reflection coefficients, shown in Fig. 5.2, are in good agreement. Impedance matching over the entire ISM band and both uplink and downlink of the 4G LTE band 7 is obtained with a measured bandwidth of 409 MHz. The measured and simulated radiation patterns in the E- and H-planes of the antenna at 2.45 GHz are shown in Fig. 5.3. Similar radiation patterns are obtained at 2.53 and 2.65 GHz. Measured and simulated antenna gain along broadside, FTBR, and η_{rad} at 2.45, 2.53, and 2.65 GHz are described in Table 5.2. Antenna radiation efficiencies were determined by measuring the 3D radiation patterns at each specific frequency. Compared to a similar antenna presented in [8], a significantly higher η_{rad} is obtained with our design. Second, an on-body $|S_{11}|$ measurement was performed by deploying the antenna on the chest of a person wearing a T-shirt. The corresponding curve in Fig. 5.2 exhibits a slight increase in bandwidth due to some additional losses because of body absorption. Yet, the radiation patterns in Fig. 5.3(b) demonstrate a similar gain along broadside as in free-space conditions, whereas proximity of the body results in lower backside radiation. Third, the $|S_{11}|$ and radiation patterns of the antenna with integrated solar harvesting system (SHS) were measured in free-space conditions. Figs. 5.2 and 5.3 prove that the integration of the solar cell, PMS, and MEC has a minor influence on antenna performance. Finally, the antenna was bent with a radius of 5 cm along H- and E-planes to simulate the antenna deployed on a human arm. Fig. 5.2 shows that the antenna remains matched over the frequency ranges of interest in both cases, demonstrating its robustness under extreme bending.

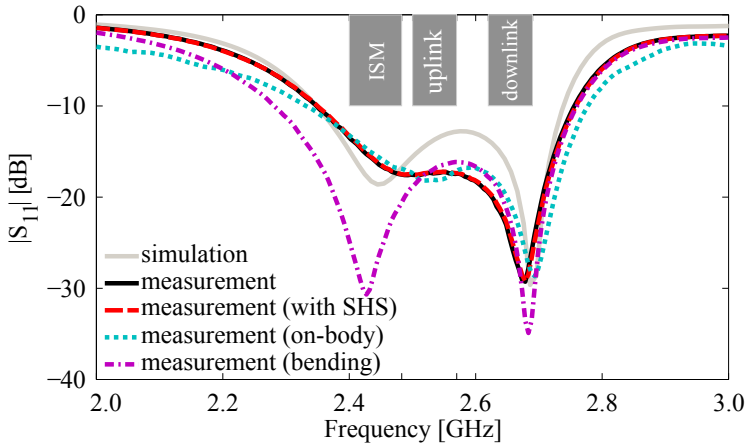

Figure 5.2: Magnitude of the reflection coefficient when the antenna is deployed in different conditions.

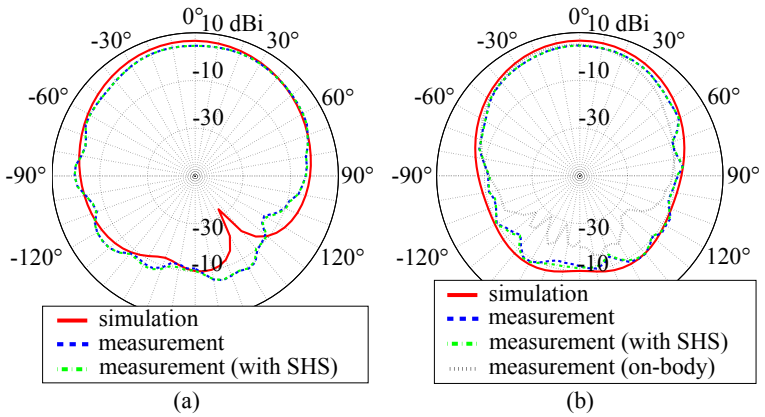

Figure 5.3: Measured and simulated radiation pattern [dBi] of the antenna at 2.45 GHz. (a) E-plane. (b) H-plane.

Table 5.2: Measured (simulated) antenna characteristics

	Gain [dBi]	FTBR [dB]	η_{rad} [%]
2.45 GHz	4.7 (6.6)	17.1 (16.7)	89 (83)
2.53 GHz	4.9 (6.5)	17.9 (15.1)	93 (83)
2.65 GHz	5.1 (6.1)	16.3 (13.6)	92 (75)

5.4.2 Energy harvesting performance in a real-life situation

The solar cell's maximum power point was measured to be 78.6 mW using a solar simulator (100 mW/cm^2). This illumination level corresponds to sunlight directly overhead on a turbidity-free sky. In a practical application, the power output of the solar cell will be lower due to overcast and skew incidence of the solar rays. Therefore, the following measurement setup was considered to characterize and validate our system in a real-life situation. A test person, wearing the proposed system on his chest, stood outside in an upright position in such a manner that the flexible solar cell is perpendicular to the earth surface and pointing in the direction of the sun. An adjustable constant current source (a current mirror, copying a stable and accurate reference current set by a trimmer and the Fluke Philips PM2811) was connected as a load (sink) to the regulated voltage output of the PMS. Then, the load current was swept from 1 to 15 mA, and the power delivered by the solar cell to the PMS was measured. Each specific load current was applied over a sufficiently long time interval to yield continuous load conditions. The measurement started at 2 p.m. local time in Ghent, Belgium (latitude: 51°2'46", longitude: 3°43'37"). The elevation angle of the sun was 51.45°, and the sky was turbidity-free. The scavenged power as a function of the continuous load current was measured and is depicted in Fig. 5.4. In this specific real-life case, the maximum harvested DC output power decreased to 53 mW, occurring at a continuous load current of 13 mA. Moreover, the SHS is able to sustain continuous load currents up to 14 mA. Furthermore, with the same measurement setup but with open-circuited regulated output and a fully discharged MEC (discharge current of 50 μA), it took 11 min and 30 s to charge the connected MEC to 50% of its nominal capacity. However, it took only 6 min to harvest the exact same amount of energy with two parallel connected initially fully discharged MECs. This can be attributed to a reduced total series resistance of the cells and a shifted operation point of the solar cell allowing an increased total charge current.

These measurements demonstrate good performance of the fully integrated SHS. Yet, depending on the application, an even better performance can be achieved by integrating more MECs and/or more flexible solar cells or tailoring the PMS to the power profile of the communication module.

5.5 Conclusion

A novel dual-band wearable textile antenna based on SIW technology for operation in the [2.4 - 2.4835]-GHz ISM band and the [2.5 - 2.69]-GHz 4G LTE band 7 was designed and validated. The design exhibits large radiation efficiency, high front-to-back ratio, and large bandwidth. Its high robustness against bending, low influence of human body, and compact flexible structure make the proposed antenna extremely suitable for wearable applications. The surface required by the antenna is reused for integration of a solar energy-harvesting and energy management sys-

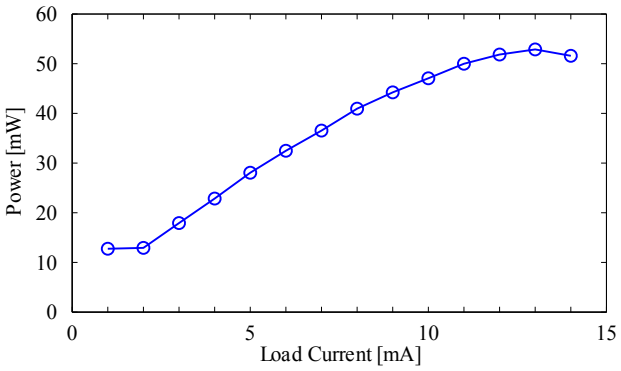

Figure 5.4: Power delivered by the solar cell to the PMS as a function of load current of the regulated output in the described real-life situation.

tem. This novel integration of both energy scavenging and power management hardware onto a wearable textile antenna allows for a more compact overall SFIT system and improves user comfort.

Acknowledgment

This work was supported in part by the Inter-University Attraction Poles Program initiated by the Belgian Science Policy Office.

References

[1] P. Vanveerdeghem, B. Jooris, P. Becue, P. Van Torre, H. Rogier, I. Moerman, and J. Knockaert, "Reducing power consumption in body-centric zigbee communication links by means of wearable textile antennas", in *Proc. 2nd Int. Workshop Meas.-Based Exp. Res. Methodol. Tools*, vol. 4, Dublin, Ireland, 7 May 2013, pp. 1–5.

[2] A. Dierck, H. Rogier, and F. Declercq, "A Wearable Active Antenna for Global Positioning System and Satellite Phone", *IEEE Trans. Antennas Propag.*, vol. 61, no. 2, pp. 532–538, Feb. 2013.

[3] V. Leonov, C. Van Hoof, and R. J. M. Vullers, "Thermoelectric and hybrid generators in wearable devices and clothes", in *Proc. 6th Int. Workshop Wearable Implantable Body Sensor Netw.*, Berkeley, SA, USA, 3-5 Jun. 2009, pp. 195–200.

[4] G. Orecchini, L. Yang, M Tentzeris, and L. Roselli, "Smart Shoe: An autonomous inkjet-printed RFID system scavenging walking energy", in *Proc. IEEE Int. Symp. Antennas and Propagation (APSURSI)*, Spokane, WA, USA, 3-8 Jul. 2011, pp. 1417–1420.

[5] F. Declercq, A. Georgiadis, and H. Rogier, "Wearable Aperture-Coupled Shorted Solar Patch Antenna for Remote Tracking and Monitoring Applications", in *Proc. 5th Eur. Conf. Antennas Propag. (EUCAP)*, Rome, Italy, 11-15 Apr. 2011, pp. 2992–2996.

[6] A. Collado and A. Georgiadis, "Conformal Hybrid Solar and Electromagnetic (EM) Energy Harvesting Rectenna", *IEEE Trans. Circuits Syst. I Reg. Papers*, vol. 60, no. 8, pp. 2225–2234, Aug. 2013.

[7] M. Mantash, S. Collardey, A.-C. Tarot, and A. Presse, "Dual-band WiFi and 4G LTE Textile Antenna", in *Proc. 7th EUCAP*, Gothenburg, Sweden, 8-12 Apr. 2013, pp. 422–425.

[8] R. Moro, S. Agneessens, H. Rogier, and M. Bozzi, "Wearable textile antenna in substrate integrated waveguide technology", *IET Electron. Lett.*, vol. 48, no. 16, pp. 985–987, Aug. 2012.

[9] T. Kaufmann and C. Fumeaux, "Wearable textile half-mode substrate-integrated cavity antenna using embroidered vias", *IEEE Antennas Wirel. Propag. Lett.*, vol. 12, pp. 805–808, 2013.

[10] G. Q. Luo, Z. F. Hu, L. X. Dong, and L. L. Sun, "Planar slot antenna backed by substrate integrated waveguide cavity", *IEEE Antennas Wirel. Propag. Lett.*, vol. 7, pp. 236–239, 2008.

[11] K. Gong, Z Chen, X. Qing, P. Chen, and W. Hong, "Substrate Integrated Waveguide Cavity-Backed Wide Slot Antenna for 60-GHz Bands", *IEEE Trans. Antennas Propag.*, vol. 60, no. 12, pp. 6023–6026, Dec. 2012.

[12] W. Yang and J. Zhou, "Wideband Low-Profile Substrate Integrated Waveguide Cavity-Backed E-shaped Patch Antenna", *IEEE Antennas Wirel. Propag. Lett.*, vol. 12, pp. 143–146, 2013.

[13] G. Q. Luo, Z. F. Hu, W. J. Li, X. H. Zhang, L. L. Sun, and J. F. Zheng, "Bandwidth-Enhanced Low-Profile Cavity-Backed Slot Antenna by Using Hybrid SIW Cavity Modes", *IEEE Trans. Antennas Propagat.*, vol. 60, no. 4, pp. 1698–1704, Apr. 2012.

[14] F. Declercq, I. Couckuyt, H. Rogier, and T. Dhaene, "Environmental High Frequency Characterization of Fabrics Based on a Novel Surrogate Modelling Antenna Technique", *IEEE Trans. Antennas Propagat.*, vol. 61, no. 10, pp. 5200–5213, Oct. 2013.

[15] Maxim Integrated, "MAX17710: Energy-harvesting charger and protector", datasheet, 2013.

6

Textile Antennas as Hybrid Energy-Harvesting Platforms

Sam Lemey, Frederick Declercq, and Hendrik Rogier

Published in the Proceedings of the IEEE

★ ★ ★

Smart-fabric interactive-textile systems offer exciting new possibilities, provided that they exhibit sufficient robustness and autonomy to be reliably deployed in critical applications. Textile multi-antenna systems, unobtrusively integrated in a professional garment, are key components of such systems, as they set up energy-efficient and stable wireless body-centric communication links. Yet, their functionality may be further extended by exploiting their surface as energy-harvesting platform. Different state-of-the-art energy harvesters are suitable for compact integration onto a textile antenna. We demonstrate this by integrating a power management system, together with multiple diverse scavenging transducers and a storage module, on a well-chosen textile antenna topology. We provide guidelines to ensure that the additional hardware does not affect the textile antenna's performance. Simultaneous scavenging from different energy sources significantly increases the autonomy of a wearable system, in the meanwhile reducing battery size.

6.1 Introduction

Smart-fabric interactive-textile (SFIT) systems have the potential to revolutionize many aspects of life. In critical professional applications, SFIT systems could enable monitoring, localization, and coordination of first responders or firefighters during rescue missions and interventions. Employing SFIT systems in healthcare applications will facilitate wireless monitoring of vital signs of patients in hospitals. Eventually, it will also enable remote monitoring of patients in home-care scenarios, resulting in a much higher comfort for the patient. In addition, elderly people could stay longer at home, which would partly resolve the future dilemma for healthcare services originating from rising life expectancy of the world's population. Each such SFIT system should be able to set up a reliable wireless communication link between the mobile user and a central control center. Beside this, each end user will impose stringent requirements on wearable wireless communication systems, such as stable energy-efficient performance in harsh operating conditions, as well as wearability and comfort. Fully flexible and breathable textile antennas, exhibiting a sufficiently broad radiation pattern, a high front-to-back ratio (FTBR) and large radiation efficiency, are the ideal solution for energy-efficient and reliable wireless communication in SFIT systems. Moreover, low and efficient power consumption forms an additional key requirement to avoid heavy batteries and frequent recharging.

In contrast to flexible batteries [1], [2], traditional rigid batteries are bulky [3] and uncomfortable to wear. Therefore, they are impractical for integration into wearable textile systems. Moreover, in critical applications, life-threatening situations may occur when the batteries of the wearable system run out of power and immediate battery replacement or recharging is impossible. As many physical quantities that are monitored by sensors in smart textiles change slowly, they can be measured and transmitted in bursts. Hence, a low duty cycle operation, yielding a low average power consumption, is suited [4]. Given the low average power requirement, smart textiles are prime candidates to be partly or even solely powered by energy-harvesting techniques, as in [5] and [6], resulting in a system with less or without bulky batteries. Alternatively, the lifetime of the battery may be extended, as energy is harvested at the location where the system is operating. As described in open literature, energy can be scavenged from different sources in the environment, such as solar [7] and radio-frequency (RF) energy [8], [9], or from the user's activities, generating body heat [10]–[12] or kinetic energy from walking [6], [13] or cycling [14]. However, an adequate power management module is necessary to convert the very small and highly fluctuating levels of energy into a form useful for powering smart textiles. In addition, in a wearable system, this module should be flexible, facilitating unobtrusive integration into the garment. Up to now, most researchers have focused on energy harvesting from a single energy source [6]–[8], [10]–[14]. Few of them have scavenged from two different power sources [15]–[18] or have used two different actuation techniques [19] to increase the amount of power or to achieve a higher continuity in energy scavenging.

As smart textile systems should be comfortable to wear, the textile antenna and, by extension, every component in the smart textile system, have to be low-profile, lightweight, and mechanically flexible. The textile antenna's dimensions must remain of the order of half a wavelength to realize sufficient gain and large antenna radiation efficiency in proximity of the human body [20]. Moreover, multiple well-positioned antennas will be necessary to avoid shadowing caused by the human body and/or to provide different services in distinct frequency bands. This, however, does not present a particular problem as a garment provides a sufficiently large integration platform, even for multiple antennas. In addition, the continuously decreasing size of sensor nodes and computational hardware enables the direct integration of active electronic circuitry, such as low-noise amplifiers and transceiver modules, onto the antenna feed plane [21]. Hence, a high level of integration can be achieved, avoiding long interconnections and reducing the risk of failure.

In this chapter, we reuse the antenna as an integration platform for energy-harvesting and power management hardware. To outline the state of the art and the future potential in terms of integrating a relevant transducer onto a textile antenna platform, we first review the four primary energy-harvesting sources. We also point out future opportunities, given some upcoming technologies. Next, we describe suitable antenna topologies for facilitating easy integration of energy-harvesting hardware. In addition, we outline the measures that should be taken to avoid a reduction in antenna performance. Finally, we demonstrate the integration of a flexible hybrid energy-scavenging system onto a wearable substrate integrated waveguide (SIW) cavity-backed textile slot antenna for efficient communication in the 2.45-GHz Industrial-Scientific-Medical (ISM) band. To enable energy harvesting from three different poorly regulated energy sources by means of three different actuation techniques, a flexible central power management system (CPMS), including energy storage, is placed on the antenna feed plane. The power management system is designed for linear solar energy harvesting, as in [22], and energy scavenging from artificial light by means of a boost converter. An ultralow-voltage step-up converter is added to this power management system, enabling energy scavenging by means of a thermoelectric generator (TEG), placed on the human skin. The design leverages operation at net thermal gradients lower than 1 K. The integration of the flexible CPMS and ultralow-voltage step-up converter, together with an energy-storage element, onto the wearable textile antenna results in a highly compact flexible module able to scavenge energy from energy-harvesting transducers (EH transducers) integrated onto the textile antenna, as well as from standalone EH transducers. This is demonstrated by the integration of two off-the-shelf flexible solar cells onto the wearable textile antenna, connected to the linear harvesting input and the boost converter input of the power management system, enabling energy harvesting from solar and artificial light, respectively. A standalone TEG, placed into direct contact with the human skin and connected to the input of the ultralow-voltage step-up converter, enables thermal body energy harvesting. The power available of these three different poorly regulated energy

sources is combined by the CPMS to charge the microenergy cell (MEC), in the meanwhile protecting the MEC and providing a regulated output voltage. This limits the size and weight of the battery and extends its life time.

To the authors' best knowledge, this is the first highly integrated wearable textile system which, on the one hand, combines the energy scavenged by a solar cell from artificial light in an indoor environment and the energy scavenged by a TEG from the heat emanated by the user's body, enabling energy scavenging in most indoor situations. On the other hand, a second solar cell, integrated on the same antenna, harvests an additional amount of energy in outdoor environments. This hybrid energy-harvesting approach leverages a higher total harvested energy and reduces the time, during which no energy can be harvested. Measurements were carried out to prove the quasi unaffected antenna performance, to characterize each subsystem, and to demonstrate the system's performance in real-life scenarios.

6.2 Energy harvesting in body-worn applications

The most limiting operational constraint of current wireless body area network (WBAN) systems is the limited system autonomy between subsequent battery recharges [23]. To this moment, batteries, in their various appearances, are the primary solution to power SFIT systems. Besides the obvious maintenance burden of recharging or replacing, batteries frequently dominate the size and cost of the SFIT system [24]. One potential solution consists of exploiting energy harvesting by extracting energy from ambient sources at the place where the SFIT is worn by the user. In critical applications, this could prevent life-threatening situations due to batteries of the wearable system running out of power during interventions. In these situations, there is typically neither time nor possibility of immediate battery replacement or recharging.

Energy harvesting, or energy scavenging, received a great deal of interest as a potential inexhaustible source for low-power devices. At this moment, most common energy-harvesting systems exploit four sources of energy, being light, electromagnetic radiation, thermal and motion energy. All have received a certain degree of attention, but the general conclusion after an extensive literature review is that the optimal energy-harvesting solution is highly application specific. Therefore, in this section, we review energy harvesting in the context of SFIT systems for rescue workers and for patients in home-care scenarios and hospitals. In particular, by a suitable choice of antenna topology, the textile antenna of the SFIT system may act as integration platform for the necessary energy-harvesting hardware, in the meantime maintaining its flexibility and wearability. As a starting point, we first describe the necessary energy-harvesting hardware.

6.2.1 Energy-harvesting hardware

To enable energy harvesting and to adequately power an SFIT system, the following three hardware blocks, depicted in the system level diagram, as shown in Fig. 6.1, should be implemented:

- an energy-harvesting transducer, which efficiently converts ambient energy into electrical energy;
- an energy storage device, which stores the harvested energy to increase the lifetime of the SFIT system and to overcome periods in which no energy is harvested;
- a power management system that optimally charges the energy storage device from the unregulated and discontinuous alternating current (AC) or direct current (DC) output of the transducer. It also generates a regulated DC voltage for adequately powering an SFIT system.

Each of these components can easily be integrated onto the textile antenna, provided that a suitable antenna topology is chosen and that the transducing mechanism allows this. These aspects are studied in more detail in Sections 6.2.2 - 6.2.5.

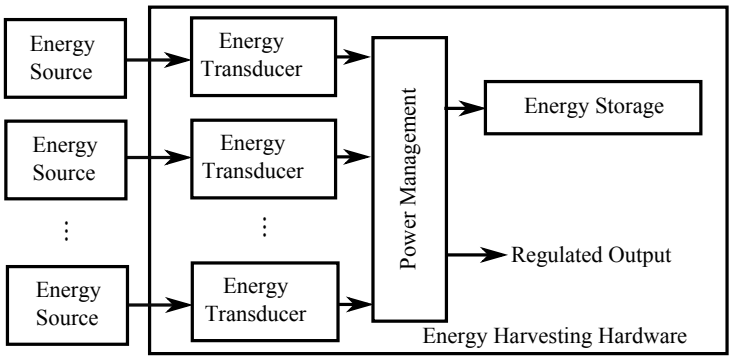

Figure 6.1: System level diagram of energy-harvesting hardware.

6.2.2 Light energy harvesting

Light energy harvesting generates electrical energy from ambient light, being natural sun light or artificial light, using photovoltaic (PV) cells as transducers. PV cells are the most mature and commercially exploited energy-harvesting solution [25]. The harvestable energy depends on the spectral composition, incident angle, and intensity of the light impinging on the PV cell, on the one hand, and the size, sensitivity, temperature, and type of the PV cell, on the other hand [26]. Availability of light is the key limitation of this energy-harvesting technique.

Table 6.1: Power densities of energy-harvesting sources.

Energy-harvesting source	Power density	Information source
Outdoor solar light	20-100 mW/cm^2	Open literature
Indoor solar light	3-128 μW/cm^2	[26]
RF scavenging	0.1 to 3.0 mW/m^2	[30], [31]
Thermal body energy	25 μW/cm^2	[32]
Piezoelectric shoe inserts	330 μW/cm^3	[3]

When using light energy harvesting, the most important consideration for choosing the optimum PV cell is the source of light energy that will be available for harvesting. The spectral composition of natural and artificial light differs. Even within the artificial light sources, there is a difference in spectral composition between incandescent bulbs, fluorescent light, and light-emitting diode (LED)-based lighting [26].

For instance, Matiko et al. [26] indicate that a-Si cells are the better choice for harvesting from white fluorescent and LED-based light sources, whereas c-Si solar cells are more suitable for harvesting from incandescent bulbs. In addition, for SFIT systems, the PV cell needs to be flexible for unobtrusive integration. Markus and Jürgen [27] provide an overview of flexible solar cell technologies and conclude that the development of flexible hydrogenated amorphous silicon (a-Si:H) solar cells on a flexible thin film polymer substrate enables low-cost, eco-friendly and reliable powering of an SFIT system. In [28], the first fiber-optic solar cell was created. This device could result in an even more unobtrusive SFIT integration in the near future by constructing woven fabric solar cells. Another promising integration strategy is the incorporation of polymeric PV cells into garments and textiles [29]. The performance is encouraging, yet stability issues still need to be resolved.

However, even with an optimum choice of PV cell, there will be a large, application-dependent spread in available power density, as depicted in Table 6.1. The power density in an indoor scenario will be much lower than the power density in an outdoor scenario. Moreover, in indoor scenarios, for example, for patients in home care or hospitals, the available light source and intensity will vary when moving from one room to another room [26].

However, in [33], indoor application of solar cells, for converting incident fluorescent light, was demonstrated with the aim of powering a wireless sensor network for biomedical sensing applications. A sensor node and two router nodes, connected to eight monocrystalline solar cells, placed at 1 cm distance from 34 W fluorescent lights, were satisfactorily tested for over 24 h. Despite the unpractical distance of 1 cm, they demonstrated the potential to power a biomedical application solely by indoor light. Standalone solar-powered wireless sensor nodes are already available. For instance, Infinite Power Solutions (Littleton, CO, USA)

developed a wireless environmental sensor energy-harvesting evaluation kit that includes an amorphous silicon solar panel, enabling efficient charging in low illumination conditions. It utilizes a MiWi RF protocol, by Microchip Technology Inc. (Chandler, AZ,USA), to transmit sensor data to a personal computer (PC) [34]. However, to the authors' best knowledge, each commercially available solution is currently rigid and does not reuse the surface of the antenna.

In critical professional applications, where rescue workers are active in both indoor and outdoor interventions, several design strategies may be adopted. In [22], a solar cell was applied with a broad spectrum and with its maximum power point close to the nominal voltage of the energy storage device. A power management chip was then chosen to implement linear harvesting. Hence, a lower break-even threshold is achieved than with maximum power point tracking (MPPT) [22]. This leverages light energy harvesting in lower light intensity situations. Another design strategy may consist in combining the energy scavenged by two different solar cells, with one optimized for indoor light energy harvesting and the other optimized for outdoor light energy harvesting. However, one should take care when using indoor solar cells in outdoor applications, as this may cause damage to the modules, typically designed for continuous use at illumination levels of the order of only a few 1000 lx [26].

In literature, a lot of solar antennas have been reported. A high level of integration may be realized by cutting slot structures in the amorphous silicon solar cells and applying the apertures as slot antennas [35] or by gluing the solar cells on top of a radiating patch [7]. Since the thickness of the solar cells is very small compared to the wavelength, the influence of the solar cell integration on antenna performance is negligible [7]. In [36], a planar PV dipole and a cylindrical loop PV antenna were designed for use in the [3.1-10.6]-GHz band. In case of the dipole, two parallel-connected solar cells were applied as the arms of the dipole antenna. They enable solar energy harvesting in outdoor situations via a boost converter using an MPPT algorithm to charge a supercapacitor. To implement the loop antenna, five flexible a-Si:H series-connected PV modules were used. They enable 360° indoor light energy harvesting via a DC-DC converter charging a thin film battery. Both configurations were used to supply power to a sensor, microprocessor, and radio transmitter, which transmits data packets every 8.5 s at a 10-kb/s data rate at a center frequency of 9.1 GHz. In that case, the autonomy of each system equals 9 h and 30 min and 2 h and 30 min, respectively. Yet, the aforementioned solutions are not suitable for integration in SFIT systems due to their rigid nature and the absence of a ground plane that isolates the antenna from the human body. Printing technologies and fabric solar cells are not yet robust and efficient enough. Therefore, flexible a-Si:H foil-based solar cells are commonly integrated onto textile antennas and serve as reliable and low-cost power supply for smart textiles [7], [27]. In [7], two such flexible solar cells were unobtrusively integrated onto a shorted patch antenna. These parallel-connected solar cells generate a maximum power of 114 mW, measured under ideal illumination conditions of 100 mW/cm^2, corresponding to a clear bright day and sunlight directly overhead. In [22], the wearable textile

antenna features an integrated flexible solar harvesting system, consisting of an a-Si:H flexible solar cell, a power management system, and an MEC. The solar cell provides 78.6 mW, measured under the same ideal illumination conditions. The specific integration of the solar cell and the choice of an antenna topology will be discussed in Section 6.3.

6.2.3 RF energy harvesting

Exploiting far-field RF energy to power an SFIT textile system is perhaps the most obvious solution if one wants to reuse the textile antenna for energy-harvesting purposes. Only a rectifier should be connected to the textile antenna's feed to turn the antenna into a rectenna, which converts incident RF radiation into DC power. However, the limited RF field levels produce very small amounts of harvested RF energy.

According to [37], GSM900 in Europe, GSM1800, and WiFi are the most interesting systems to be explored, because of their omnipresence and their frequency ranges resulting in reasonably small antennas. Table 6.1 depicts the total power density in the downlink band of GSM900 available within a range of 25-100 m from a base station. These data were gathered in the Cooperation in Science and Technology (COST) Action 244 bis "Biomedical Effects of Electromagnetic Fields" [30]. The power density levels, received from GSM1800 base stations, are up to 100 m in the same order of magnitude as those depicted in Table 6.1 [31], whereas power density levels in a wireless local area network (WLAN) are at least one order of magnitude lower than those depicted in Table 6.1. These low power level densities demonstrate the need for a large scavenging aperture. Another solution could be introducing an RF source dedicated to RF energy transport. Visser and Vullers [37] point out that no specific regulations are applicable for rectennas. Hence, such systems could operate in the license-free ISM bands. However, national and international restrictions apply on the allowed permitted power levels [37]. Potential health hazards caused by the RF radiation are another important issue to be dealt with. When one transmits in the license-free ISM frequency bands with a power level beneath the national and international transmit power restrictions, the exposure limits stated by the International Commission on Non-Ionizing Radiation Protection (ICNIRP) will not be exceeded if the test person is not too close to a transmit antenna.

Patients in home-care scenarios could exploit the omnipresent RF energy radiated by GSM900, GSM1800, and/or WiFi to power their SFIT system. In [38], a continuously wearable, battery-free wireless multichannel electrocardiography (ECG) telemetry device was presented, exploiting ultra-high-frequency (UHF) RF identification (RFID) techniques, that is potentially disposable, low cost, and suitable for integration in a flexible circuit. By exploiting RF energy harvesting, a battery is avoided. Wireless three- and five-channel ECGs are recorded on a human subject within a 1-m range. In addition, a dedicated source could be introduced to provide more power. In [39], a two-hop system for capsule endoscopy inspection was

proposed. Transmitters, integrated in the floor, transmit power to a power relay in a patient's jacket, which relays power to a capsule in the patient. Similar scenarios could be used for RF energy transport and harvesting in hospital scenarios, although the implementation may be more difficult or even impossible to realize due to interference with hospital equipment. Rescue workers in critical professional applications could exploit RF energy harvesting as well. However, in certain environments, such as basements, underground car parks, etc., the available RF power will be extremely small.

In literature, fully wearable textile rectennas were reported in [40] and [41]. In [40], a fully textile dual-band antenna for integration in clothes for operation in the GSM900 and GSM1800 bands was designed and realized. A five-stage Dickson voltage multiplier enables perpetual operation of an IRIS mote by a received RF power larger than -1 dBm. In addition, a TX91501 Powercast RF transmitter was applied as dedicated source. Then, the sensor nodes could be powered up to a distance of 3 m. In [41], a wearable, triple-band ring antenna was designed to harvest RF energy in the GSM900, GSM1800, and 2.45-GHz WiFi bands. A phone call with a GSM 900 mobile at 1 m distance of the rectenna resulted in a DC voltage of 600 mV during 3 s and an average received RF power of about 80 μW [42]. In [43], the antenna of [41] is equipped with a novel power management platform enabling autonomous operation and battery-less activation for RF energy power levels higher than -15 dBm. In [44], array configurations were investigated to enhance the RF power harvesting. The rectenna topology indicator (RTI) was introduced for performance comparison.

6.2.4 Thermal body energy harvesting

In case of thermal body energy harvesting, the thermal gradient existing between the human body and its environment is exploited. The efficiency, by which the heat generated by the human body can be recovered, is limited by the Carnot efficiency $\Delta T/T_h$ [3], with ΔT representing the thermal gradient between the human body and the ambient air, and T_h corresponding to the highest temperature of both. A body core temperature of 37°C and a room temperature of 18°C lead to a Carnot efficiency of 6.1%, dropping to 2.3% when the room temperature rises to 30°C, which implies a maximum recoverable power of only 2.7-7.3 W in case of normal office work [3]. In a practical application, it is not possible to harvest all of the heat radiated by the body. A harvesting area of 50 x 50 mm^2 on the human body, taking latent heat of vaporization into account and assuming an even heat dissipation over the body, yields only 2.9-8.1 mW of maximum recoverable power. Leonov and Vullers [32] state that a power density level of 25 μW/cm^2 (Table 6.1) is achievable with a 15-mm-thick TEG at an ambient temperature of 22°C.

A Peltier module, as depicted in Fig. 6.2, can be used to convert thermal body energy into electrical energy, based on Seebeck's effect [10]–[12], [15]. It operates as a TEG by placing its hot side to the human skin, whereas the cold side of the TEG is exposed to the ambient air. One TEG is composed of N_{th} thermoelectric couples

of *n*-type and *p*-type semiconductors, which are connected thermally in parallel and electrically in series to achieve a significant voltage at its terminals [10]–[12], [17], [45]. It is preferable to use a flexible TEG as in [11], [46], and [47], since such a TEG can be tightly attached to the human skin. Moreover, this TEG improves wearability compared to a solid TEG. Yet, at this moment, flexible TEGs exhibit a lower performance than solid TEGs. In addition, to the authors' best knowledge, they are still not available on the market. Many examples are reported where thermal body energy harvesting is applied to power wireless healthcare sensor networks. In [48], a prototype of a battery-free wireless two-channel electroencephalography (EEG) system was presented that is solely powered by a TEG. It could be worn as a headband and produces 2-2.5 mW. Leonov et al. [49] demonstrated the integration of a wireless ECG system in an office-style shirt. Therefore, 17 small TEG modules, with a thickness less than 6.5 mm, were distributed over the T-shirt, harvesting 0.8-1 mW of thermal energy, during sedentary activities, increasing to 3 mW when the user started walking in an indoor environment. In addition, Leonov et al. [50] showed that the textile has an insignificant impact on harvested energy. In [51], the use of small TEGs was explored to harvest energy from persons that perform intense physical and physiological operations in a short period of time, such as firefighters or first responders. TelosB sensor motes, transmitting temperature data every 250 ms to the base station at a data transmission rate of approximately 250 kb/s, were used to investigate the potential of thermal body energy harvesting. An optimal number of TEGs could extend the autonomy of the sensor node by 2-4 h of operation.

At this moment, however, no TEGs integrated onto textile antennas have been reported in literature. A potential solution could be gluing the cold side of a flexible TEG to a carbon fabric heat spreading layer [50] and using the textile antenna as heat sink, as in [52].

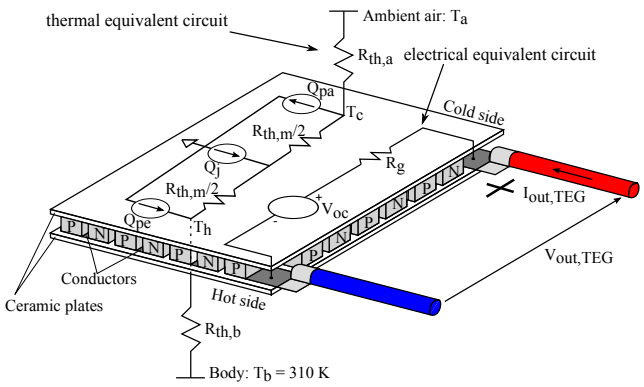

Figure 6.2: Combined electrical and thermal equivalent circuit and structure of the TEG.

6.2.5 Motion/vibration energy harvesting

According to [24], kinetic energy is generally the most versatile and ubiquitous ambient energy source. Kinetic energy is available as vibration and motion energy, whereby the latter is the most important usable form in an SFIT system. Motion-driven generators are used to convert motion energy into electric energy. They can be categorized in direct-force generators or inertial generators, of which the inertial generator provides more flexibility and allows a higher degree of miniaturization [24]. Both categories require a suitable electromechanical transducer in order to generate electrical power. Electromagnetic, electrostatic, and piezoelectric conversion are the main transduction techniques.

A comprehensive review of this energy-harvesting technique can be found in [24], including a comparison table for the effectiveness of published electromagnetic, electrostatic, and piezoelectric motion harvesters. As Mitcheson et al. [24] point out that power density reduces with device size and is strongly dependent on frequency, it is a serious challenge to design a miniature device, able to harvest useful power levels from low-frequency human movements.

In addition, the need of a direct applied force in case of a direct-force generator makes it almost impossible to integrate such a generator onto the textile antenna of the SFIT system. To the authors' best knowledge, no such systems have been reported in literature. However, Mitcheson et al. [24] mention that 78 mW could be harvested from the expansion of the chest, originating from breathing, by means of piezoelectric materials. The emergence of off-the-shelf piezoelectric generators (e.g., by Advanced Cerametrics (Lambertville, NJ, USA) [53]) using fiber composite materials for integration into clothing marks an important step for SFIT systems. Such a generator could potentially be integrated onto a textile antenna placed on the chest of the wearer. In [54], a single piezoelectric transducer was used to power a strain sensor, for application in structural and human health monitoring. Orecchini et al. [6] have integrated a piezoelectric pushbutton in a shoe in order to scavenge energy from the heel strike and to power an active RFID tag. In [55], an RF beacon was powered by means of a solar cell and a piezoelectric generator, to enhance the duty cycle from 2% (only piezoelectric generator) to 11% (hybrid energy harvesting). The need of movement in case of inertial generators makes them hard to integrate onto the textile antenna. Again, to the authors' best knowledge, no such systems have been reported in literature. However, since Mitcheson [56] has proposed several forms of vibration-driven microelectromechanical system (MEMS) microgenerators that exploit human body motion to produce power, some new opportunities have arisen. Several of these MEMS microgenerators could potentially be integrated onto the textile antenna which is placed on a moving part of the wearer, e.g., an arm, a leg, etc.

6.3 Antenna as integration platform

First, a textile antenna topology must be selected that exhibits high and stable radiation efficiency, both in proximity of the human body and in the presence of the energy-harvesting and power management hardware. A carefully designed textile antenna greatly improves the energy efficiency of the wireless communication system [20]. Indeed, the wireless communication module is the major power consumer in a WBAN [57]. As adduced in Section 6.2, the large surface required by the textile antenna may be reused as energy-harvesting and power management platform to extend the autonomy of the SFIT, in the meantime maintaining flexibility, wearability, and compactness. In this section, we describe different antenna topologies that facilitate easy integration of these additional hardware components, and outline the measures that should be taken to ensure that their integration does not affect the antenna performance.

6.3.1 Planar inverted-F antenna (PIFA) with aperture-coupled feeding

Fig. 6.3 shows an aperture-coupled shorted wearable solar patch antenna for communication in the [902-928]-MHz UHF band. By adopting the PIFA topology, a more compact antenna can be achieved compared to conventional $\lambda/2$ patch antennas. This topology allows the necessary connections to be routed from the antenna patch to the antenna feed plane along the PIFA's shorting wall without affecting the antenna radiation performance. In addition, the antenna patch provides sufficient space to deploy solar cells. This makes the proposed antenna very suitable for solar energy harvesting. An effective integration of two solar cells is demonstrated in Fig. 6.3.

Only the positive connection needs to be routed since the solar cells' cathode can be directly connected to the antenna patch, acting as a DC ground. The choice for aperture-coupled feed leads to a more robust and flexible design, by eliminating the physical feed connection between antenna patch and feed plane. In addition, this feeding technique enables a very compact integration of additional circuitry on the antenna feed plane, by reusing the antenna's ground plane and feed substrate as ground plane and substrate for the integrated active circuitry, respectively [21]. The large ground plane avoids the absorption of antenna radiation by the human body and minimizes the coupling between antenna radiation and contingent integrated electronic hardware.

A flexible polyurethane protective foam, used in professional garments, with a permittivity $\epsilon_r = 1.15$, a loss tangent $\tan\delta = 0.010$, and a thickness $h_1 = 11$ mm is adopted as antenna substrate. The feed substrate consists of two aramid textile layers, resulting in a total thickness $h_2 = 0.95$ mm, $\epsilon_r = 1.97$, and $\tan\delta = 0.020$. The antenna patch, shorting wall, and ground plane are constructed using Flectron from LessEMF, a copper-plated fabric, with a surface resistivity $R_s = 0.10\ \Omega/sq$,

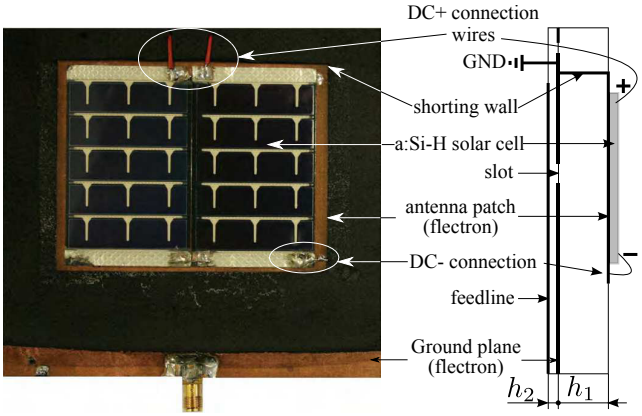

Figure 6.3: Wearable aperture-coupled shorted solar patch antenna for the [902-928]-MHz UHF band [7].

whereas the microstrip feed line is made out of copper foil. All layers are glued together with thermal adhesive sheets.

Measurements have shown that the integration of the flexible solar cells only has a minor influence on radiation pattern and reflection coefficients [7]. Placing the proposed solar antenna onto the chest of a test person results in an increased bandwidth (64 MHz instead of 48 MHz) and a reduced gain along broadside (1.6 dBi instead of 3 dBi). This is caused by additional losses due to the proximity of the human body.

6.3.2 Substrate integrated waveguide cavity-backed slot antenna

Fig. 6.4 depicts an SIW cavity-backed slot antenna with integrated solar harvester, for communication in the 2.45-GHz ISM band ([2.4-2.4835] GHz), and for uplink and downlink of the fourth-generation (4G) long term evolution (LTE) band 7 ([2.50-2.57] GHz and [2.62-2.69] GHz, respectively). A cavity-backed slot antenna was selected because of its high suppression of unwanted surface waves, large FTBR, and high radiation efficiency [58] without the need for a large ground plane. In addition, this topology exhibits a very high isolation from its surroundings [59], making it both suitable for body-worn applications and an ideal platform for integration of electronic hardware. SIW technology was adopted to achieve a simple low-profile and cost-effective single substrate realization by means of tube eyelets, enabling an easy routing of necessary connections from the antenna slot plane to the antenna feed plane without affecting the antenna performance.

The antenna provides sufficient space on its slot plane to deploy multiple solar cells, whereas an electronic circuit may be easily positioned on the feed plane surface.

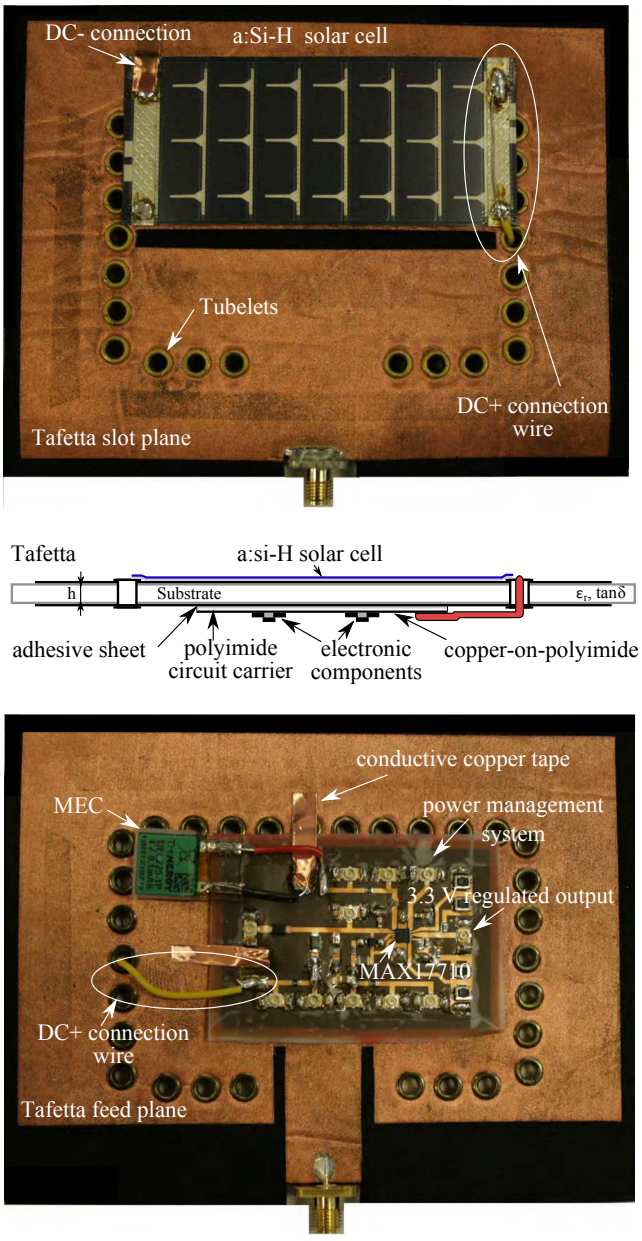

Figure 6.4: Dual-band SIW textile antenna with integrated solar harvester [22].

By integrating the electronic circuitry at the backside of the antenna, radiation is prevented from coupling to the circuitry. In particular, the textile antenna features

an integrated flexible solar harvesting system, consisting of an a-Si:H flexible solar cell, a flexible power management system, and an MEC. Again, only the anode of the solar cell has to be connected via a wire to the power management system, since the antenna cavity acts as DC ground.

A 3.94-mm-thick closed-cell expanded-rubber protective foam, typically applied in firefighter suits, with $\epsilon_r = 1.495$ and $\tan\delta = 0.016$, is adopted as antenna substrate. The slot and feed layer is constructed out of pure copper-coated polyester Taffeta fabric, characterized by a surface resistivity $R_s = 0.18\ \Omega$/sq. After patterning both conductive fabric layers according to the design layout, both layers are laminated to the substrate by means of thermally activated adhesive sheets, in the meantime judiciously maintaining accurate alignment of all layers. The textile antenna cavity is formed by four rows of equally spaced flat-flange brass tube eyelets, which are fixed in the antenna substrate at the correct locations by means of a manual eyelet press. This fabrication method ensures a good contact between feed and slot layers and preserves flexibility of the antenna topology. In an industrial mass production process, a fully automatic eyelet machine, or even a computer numerically controlled (CNC) eyelet setting machine, could be used to produce large quantities at a lower price. Flexibility of the power management system is achieved by implementing the circuit on a flexible substrate, consisting of one ultrathin polyimide layer and two copper layers with a total thickness of only 43 μm. In addition, only small electronic components are used. They are distributed over a larger area than necessary to maintain flexibility [22]. Furthermore, a nonconductive stretchable adhesive sheet was used to fix the solar cell to the slot plane, leaving the slot uncovered. A similar sheet was used to attach the power management system and MEC to the feed plane without covering the feed line, as shown in Fig. 6.4.

Measurements have demonstrated that the integration of the power management system, MEC and flexible solar cell does not have a significant influence on radiation pattern and reflection coefficients [22]. In addition, when deploying the proposed system on the chest of a user, the antenna performance is less affected compared to the antenna in Section 6.3.1. The bandwidth increases from 409 to 449 MHz and the gain along broadside increases from 4.7 to 5.0 dBi. Finally, Fig. 6.5 depicts the antenna when bent along the H-plane [Fig. 6.5(a)] and along the E-plane [Fig. 6.5(b)] with a radius of 5 cm, proving that such a structure can be easily bent, provided that earlier guidelines are followed. Lemey et al. [22] show that the antenna remains matched over the desired frequency ranges when the antenna is bent as depicted in Fig. 6.5, demonstrating its robustness and capability to be deployed on the human arm.

6.3.3 Rectenna design

The presence of the nonlinear rectifier circuit in a rectenna requires harmonic-balance/electromagnetic cosimulation, to predict the harvested power levels in practical operating conditions, and full-wave/circuit co-optimization during the

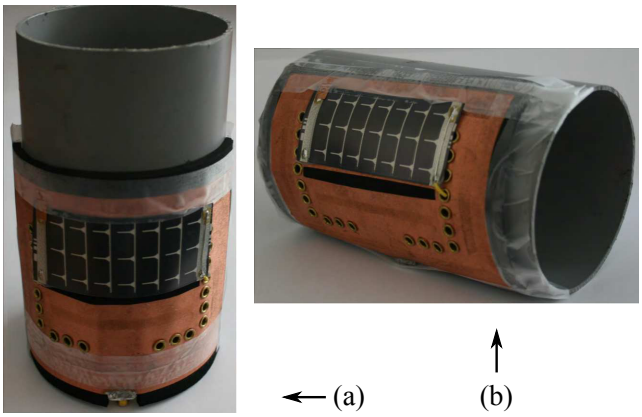

Figure 6.5: Dual-band SIW textile antenna [22], when bent with a radius of 5 cm. (a) Along the H-plane. (b) Along the E-plane.

design phase [42], [60]. In addition, a broad radiation pattern and circular polarization are of paramount importance as the position of the RF source(s) is (are) unknown. Circular polarization can be implemented by an appropriate single feed [61]. However, Dierck et al. [21] favor a two-port excitation to realize circular polarization, jointly optimizing port matching and decoupling to maximize antenna efficiency. Finally, multiband or ultra-wideband antenna operation is recommended to maximize the harvestable energy.

In [41], a triple-band ring rectenna was designed to enable RF energy harvesting in the GSM900, GSM1800, and 2.45-GHz ISM bands. Triple-band circular polarization is obtained by the excitation of couples of orthogonal TM_{11}, TM_{21}, and TM_{12} resonant modes on a slotted annular-ring antenna patch, by two H-shaped orthogonal slots in the ground plane. The slots inject electromagnetic energy from two feed lines fed by a compact, broadband divider, guaranteeing a 90° phase shift over the bands of interest. The aperture feeding technique leverages easy integration of the rectifier, matching network and broadband phase shifter/divider at the backside of the antenna. In addition, a power management system and energy storage could be integrated. However, the presented antenna topology is not suited for solar cell integration because of the multiple slots in the antenna patch, significantly reducing the useful surface area. Moreover, the antenna topology does not offer any possibility to connect the solar cell terminals to the potential power management system, without affecting the antenna performance.

A 4-mm-thick fabric pile (permittivity $\epsilon_r = 1.23$) forms the antenna substrate. For the antenna patch and ground plane, Global EMC UK Ltd.'s (Nottinghamshire, U.K.) shielding fabric ($R_s = 0.02\ \Omega$/sq) is chosen. Kapton, with $\epsilon_r = 3.4$ and $\tan\delta = 0.002$, is adopted for the 0.1-mm-thick feeding circuit substrate. Its size is limited to the area required for the feeding network. Thermoadhesive sheets

were used to bond each dielectric-conductive fabric interface, whereas conductive biadhesive is used to join the Kapton ground plane and the antenna ground plane. Furthermore, zero interaction with the test person's body is guaranteed by an additional conductive fabric layer, connected to the Kapton ground plane, at the bottom of the multilayer structure.

6.4 System architecture

6.4.1 Overview

To demonstrate the versatility of SIW cavity-backed slot antennas for integrating energy-harvesting and power management hardware, we select the wearable textile SIW cavity-backed slot antenna presented in [62] as a platform for our highly integrated flexible hybrid energy-harvesting textile antenna system. This wearable textile antenna, depicted in Fig. 6.6, was proposed for use in the 2.45-GHz ISM band. The surface, required by the antenna for efficient wireless communications, is then reused as the energy-harvesting and power management platform, by integrating a flexible power management module and suitable energy harvesters onto the textile antenna. An overview of the proposed system is depicted in Fig. 6.6. The power management module enables energy harvesting from light and thermal body energy, which may be considered the most reliable sources, following [15]. More specifically, the power management implements three different actuation techniques to enable energy harvesting from:

- natural solar light via solar cell 2, connected to the linear harvesting input (LHI);
- artificial light via solar cell 1, connected to the boost converter input (BCI);
- the user's body heat via a TEG, connected to the low power system (LPS), implementing a ultralow-voltage step-up converter.

The power management module combines the energy harvested from these three energy sources to charge an MEC and to provide a regulated output voltage. The combination of energy scavenged from diverse sources leverages a higher total scavenged power and reduces time, during which no energy can be scavenged. The most important dimensions of the proposed system are depicted in Fig. 6.6. More detailed dimensions of the antenna can be found in [62]. Copper tape is applied to connect the ground of the power management module and the solar cells to the antenna cavity, which acts as DC ground.

As illustrated in Fig. 6.6, all functional building blocks other than the TEG are integrated onto the wearable antenna, yielding a very high level of integration while maintaining a compact overall system. The TEG was not integrated onto the antenna since the optimal on-body position of a TEG for maximum energy recovery

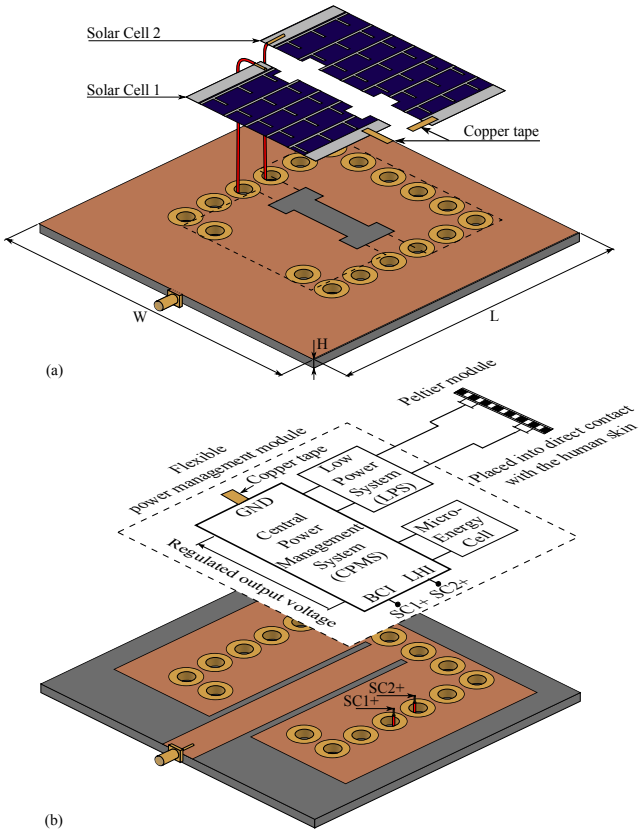

Figure 6.6: Wearable SIW cavity-backed textile slot antenna proposed in [62] ($W = 131.5$ mm, $L = 126.5$ mm, and $H = 4$ mm), with two a-Si:H solar cells glued on top, directly beside the antenna slot, and an energy-harvesting and power management module, integrated directly underneath the textile antenna, in block schematic representation. (a) Front. (b) Back.

does not always correspond to the ideal location for the antenna. In addition, this approach yields a high degree of freedom. For example, multiple TEGs, potentially stacked [12], may be used, or a heat sink may be added to increase the efficiency of the thermoelectric energy scavenging [12], [63]. Hence, even when it is not possible to integrate the EH transducer onto the antenna, the antenna can be reused for the integration of necessary power conditioning and management hardware.

In this chapter, an off-the-shelf TEG was chosen that is able to activate the LPS when placed onto the arm of a static wearer, in a room at a temperature of 18.9°C, without using a heat sink or stacking. In [10], a smaller TEG is applied at the expense of a large heat sink. Fig. 6.7 illustrates a typical layout of our system. A TEG is placed on the human arm and the antenna, with integrated power management

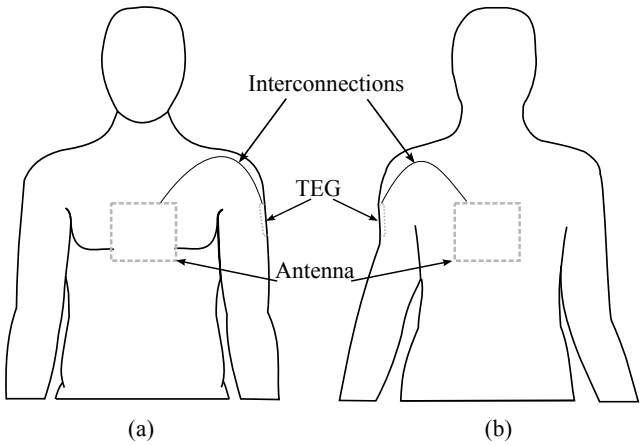

Figure 6.7: Typical system deployment: Antenna (a) on the front torso or (b) on the back torso, with one TEG placed on an arm without a heat sink.

module and solar cells, is positioned on the front (Fig. 6.7(a)) and/or on the back (Fig. 6.7(b)) of the torso.

6.4.2 Power management module

The complete power management module depicted in Fig. 6.6 consists of three essential functional blocks. The CPMS controls the two main functions of the energy-harvesting system, being the charging process of an MEC and the generation of a regulated output voltage. In addition, it also protects the MEC against overcharge and overdischarge. Second, the LPS upconverts the low voltages supplied by the TEG to a voltage level that is high enough for the CPMS to charge the MEC. Finally, a Thinergy MEC-225 [64] stores the harvested energy. These cells are ultrathin and combine the best properties of supercaps and batteries. The MEC stores and buffers the discontinuous flow of energy harvested by the TEG and the two solar cells. A uniform flow of energy is provided by the regulated output voltage pins. It can be used to adequately power a wireless communication module.

Central power management system (CPMS)

Fig. 6.8 shows a schematic representation of the CPMS. It is designed to charge an MEC from two high-voltage DC sources by means of linear harvesting and one low-voltage DC source via a boost converter. As in [22], the core of the CPMS is the MAX17710, an energy-harvesting charger and protector IC from Maxim Integrated (San Jose, CA, USA) [65]. In this work, solar cell 2 is connected to one of the LHIs, whereas solar cell 1 is connected to the BCI of the CPMS, to enable energy harvesting in low light intensity situations. Hence, in indoor environments, only

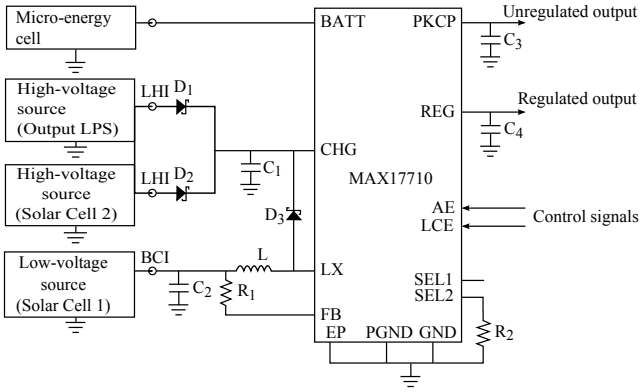

Figure 6.8: Circuit representation of the CPMS ($D_1 = D_2 =$ DFLS130L by Diodes Inc., $D_3 =$ ZLLS410TA by Diodes Inc., $C_1 = 0.22\ \mu F$, $C_2 = 47\ \mu F$, $C_3 = 10\ \mu F$, $C_4 = 1\ \mu F$, $R_1 = 300\ \mathrm{k}\Omega$, $R_2 = 150\ \Omega$, and $L = 1.5\ \mu H$.

solar cell 1 is able to scavenge energy. However, in outdoor situations, both solar cells charge the MEC, increasing the harvestable energy. The output of the LPS with one TEG connected is used as the other high-voltage source.

To achieve the highest possible efficiency, charging energy is transferred directly from the CHG pin to the MEC, whenever the voltage at the CHG pin exceeds the cell voltage. However, the MAX17710 limits the charge voltage by means of an internal linear regulator to prevent overcharging of the MEC. In addition, the voltage at the CHG pin is also limited by an internal shunt protection. Diodes D_1 and D_2 block reverse currents between the two high-voltage sources. If a solar module is connected to a high-voltage input, as in this paper, the series diodes also prevent the solar cell from draining the MEC in the absence of light. A Schottky diode with a very low leakage current was chosen to minimize the voltage drop and the leakage current from one source to the other. Charging the MEC from a low-voltage DC source is implemented by means of a boost regulator controller, which is only enabled when the source, connected to the BCI, provides more power than the boost converter consumes for operation. This is guaranteed by a proper selection of the harvest-source capacitor C_2. $C_1 = 0.22\ \mu F$, $C_2 = 47\ \mu F$, and $L = 1.5\ \mu H$ are dimensioned based on [65], in order to yield the highest possible efficiency for the IC to charge the MEC, making use of both high- and low-voltage sources while maintaining good stability.

By leaving SEL1 disconnected, the IC is configured to maintain the voltage on the REG pin at 3.3 V, by means of an internal low-dropout (LDO) linear regulator. The LDO supports two modes of operation based on the load on the REG pin and is configured by the control signals depicted in Fig. 6.8. Push buttons are used to generate the appropriate control signals. However, in practical applications, these control signals will be generated by a microcontroller, sensors, etc.

The low-current mode should be selected if the load is rather low, since it reduces the quiescent current drain from the MEC compared to the high-current mode. An internal undervoltage-lockout (UVLO) circuit provides overdischarge protection in both modes. An internal load switch block at the protected output of pack (PKCP) and a properly selected capacitor $C_3 = 10\ \mu F$ allows the circuit to support a much higher pulsed load, such as during startup, than supported by a standalone MEC in the same conditions.

Low power system

The LPS, shown in Fig. 6.9, is designed based on the LTC3108, an ultralow voltage step-up converter and power management IC from Linear Technology (Milpitas, CA, USA) [66]. This IC was also used in [67] for the purpose of thermal body energy harvesting. In this work, the power managing functionalities and the ability to power a microcontroller are unused, since these are already provided by the CPMS. Yet, the IC was chosen because of his low start-up voltage and high conversion efficiency as step-up converter.

An internal depletion mode N-channel metal-oxide-semiconductor field-effect transistor (MOSFET) and an external step-up transformer T with a transformer ratio of $1:100$ forms a resonant oscillator at a fixed resonance frequency, leveraging operation by ultralow input voltages. This is the most attractive solution for harvesting body heat, compared to modulating the duty cycle to implement MPPT [67]. To be able to charge the MEC in the absence of light, relying on a single TEG placed on the arm of a static wearer without heat sink, the start-up voltage is minimized by choosing the highest possible transformer ratio and an appropriate decoupling capacitor C_1, to minimize the input ripple. Low-cost and low-leakage capacitors and

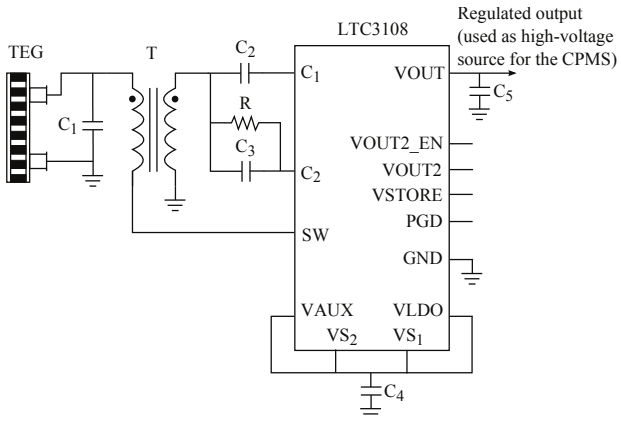

Figure 6.9: Circuit representation of the LPS ($C_1 = 220\ \mu F$, $C_2 = 1\ nF$, $C_3 = 330\ pF$, $C_4 = 1\ \mu F$, $C_5 = 47\ \mu F$, $R = 499\ \text{k}\Omega$, $T =$ LPR6235-752 SML by Coilcraft (Cumbernault, Scotland, U.K.)).

a bleeder resistor $R = 499$ kΩ, in parallel with C_3, to prevent squegging, complete the design [66]. The regulated output voltage VOUT is set to 5 V, by connecting VS1 and VS2 to VAUX.

The AC voltage produced on the secondary winding of the external step-up transformer T (Fig. 6.9) feeds the internal charge pump and rectifier circuit to charge C_4 and hence power the active circuits within the LTC3180 IC via the VAUX pin. If VAUX exceeds 2 V, the LTC3108 improves the conversion efficiency by using synchronous rectifiers in parallel with each of its internal diodes. Once VAUX exceeds 2.5 V, C_5 is charged until the programmed 5 V is reached.

6.5 Integration on the SIW cavity-backed slot antenna

6.5.1 Solar cell integration

A first step toward a high level of integration, in the meantime maintaining flexibility, consists of gluing two flexible solar cells on top of the antenna by means of stretchable nonconductive adhesive sheets, as illustrated in Fig. 6.6. Ultraflexible PowerFilm thin-film a-Si:H-solar cells are chosen because of their very thin profile. Moreover, as the thickness of the solar cell (200 μm) is much smaller than the wavelength at the frequency of operation, the integrated solar cells have a negligible influence on the antenna performance [7]. The antenna provides a useful area of 16 027 mm^2 for solar cell integration, of which 15% (being 64 x 37 mm^2) and 19% (being 84 x 37 mm^2) are effectively used for accommodating solar cell 1 [68] and solar cell 2 [69], respectively (Fig. 6.6). The effective aperture of solar cell 1 and solar cell 2 are 50 x 37 mm^2 (12%) and 70 x 37 mm^2 (16%), respectively. To prevent havoc of the MAX17710 IC when exposing the module to direct sunlight, it was necessary to choose a smaller solar cell with a lower open circuit voltage for solar cell 1. Since the transverse electric field across the slot is responsible for the antenna radiation [58], pieces of the solar cell were cut out of the solar cells and the solar cells were placed in such a position that the radiating slot remains uncovered, still yielding an effective solar cell area of 4260 mm^2 (or 27% of the available area). The positive polarity DC connection of each solar cell is routed through the eyelets that form the cavity (Fig. 6.6), to avoid that the wires influence the radiation characteristics of the antenna. The negative polarity DC connection of each solar cell is connected with copper tape to the antenna cavity, acting as DC ground.

6.5.2 Integration of the power management module

To maintain flexibility while maintaining a high level of integration and minimizing coupling between antenna radiation and the circuitry, the CPMS and the LPS were integrated directly underneath the SIW cavity-backed slot antenna and are depicted in Fig. 6.10. Both circuits were implemented on an etched Upisel BE1410

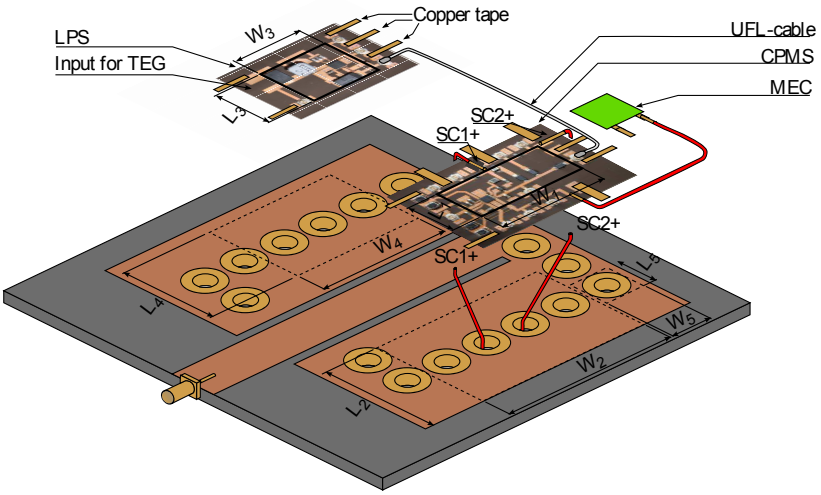

Figure 6.10: Backside of the SIW cavity-backed slot antenna with integrated CPMS ($W_1 = 33$ mm, $L_1 = 16$ mm, $W_2 = 55$ mm, and $L_2 = 37$ mm), LPS ($W_3 = L_3 = 22$ mm, $W_4 = 41$ mm, and $L_4 = 30$ mm), and MEC ($W_5 = L_5 = 12.7$ mm).

foil, being a flexible substrate consisting of one layer of polyimide with a thickness of 25 μm and two copper layers with a thickness of 9 μm, allowing a full copper ground plane at the backside of each circuit. Stretchable nonconductive adhesive sheets were used to fix both circuits to the wearable antenna, as depicted in Fig. 6.10, letting the feed line of the antenna uncovered. As in [22], only small electronic components are used. They are distributed over a larger area than necessary to maintain flexibility of the design. The wearable antenna, shown in Figs. 6.6 and 6.10, is realized by applying pure copper polyester Tafetta with surface resistivity $R_s = 0.18\ \Omega$/sq at 2.45 GHz, as top and bottom layers and using a protective foam, typically found in firefighter suits, as a substrate. The dielectric permittivity and loss tangent of the foam were measured to be $\epsilon_r = 1.575$ and $\tan\delta = 0.0238$, at 2.45 GHz [7]. Then, the procedure, as described in detail in Section 6.3.2, was used to fabricate the textile antenna. The CPMS and the LPS depicted in Fig. 6.10, with external dimensions W_2 x L_2 and W_4 x L_4, respectively, are equipped with additional test pins and push buttons for measurement purposes. In a real-life application, only the part of both systems without additional test pins and push buttons with dimensions W_1 x L_1 and W_3 x L_3 should be integrated. Moreover, in a future design, the backside of the antenna cavity could potentially be reused as GND for both LPS and CPMS, and unnecessary parts of the polyimide film, used as a substrate for LPS and CPMS, could be removed by a laser to obtain an even more flexible and breathable overall design. The signals generated by the buttons can be produced by, for example, a microprocessor or event detector. The MEC is integrated below the SIW cavity-backed slot antenna.

It is 170 μm thick and positioned on an eyelet, but separated by a nonconductive layer. Hence, flexibility of the overall system is maintained.

6.6 Thermoelectric generator: modeling and selection procedure

In [4], it was shown that choosing a TEG with the highest product of $V_{max}I_{max}$, with I_{max} the input current producing the maximum possible ΔT across the Peltier module and V_{max} the DC voltage delivering the maximum ΔT at the supplied I_{max}, generally provides the highest output power. Yet, this does not yield any information about the expected output voltage. Instead, in this paper, the combined thermal and electrical equivalent circuit of a TEG, depicted in Fig. 6.2, is used to predict the thermal body energy that can be harvested by a specific TEG. This allows selecting the most appropriate off-the-shelf TEG for given specifications.

The combined electrical and thermal equivalent circuit of a TEG, depicted in Fig. 6.2, is a combination of the models proposed in [12] and [45]. The system model proposed in [12] assumes that the human body and the environment are operating as sources with a constant temperature, independent from the TEG. The thermal resistance $R_{th,b}$ [KW^{-1}] represents the thermal conduction through the skin and human tissue between the body core, at a temperature of $37°C$, and the hot side of the TEG. $R_{th,a}$ [KW^{-1}] represents the radiation and natural convection of the cold side with ambient air. $R_{th,a}$ and $R_{th,b}$ are related to the heat transfer coefficients h_a [$\mathrm{Wm}^{-2}\mathrm{K}^{-1}$] and h_b [$\mathrm{Wm}^{-2}\mathrm{K}^{-1}$] [12]

$$R_{th,a} = \frac{1}{h_a wl} \tag{6.1}$$

$$R_{th,b} = \frac{1}{h_b wl} \tag{6.2}$$

with w and l representing the width and length of the TEG, respectively. The values of h_a and h_b, used in this work, are shown in Table 6.2. These values are within the ranges proposed in [12] and are determined by relying on measurements. We keep all these assumptions but base our model of the TEG on [45], as in [10]. Lineykin and Ben-Yaakov [45] propose a PSPICE compatible equivalent circuit of a thermoelectric cooler (TEC). This equivalent circuit of the TEG is preferred over the equivalent circuit presented in [12], as it describes four out of five energy-conversion processes that take place in a Peltier module, whereas Lossec et al. [12] only account for the Seebeck effect and the heat conduction through all of the N_{th} thermocouples, modeled by the thermal resistance $R_{th,m}$ [KW^{-1}] . The model adopted here also includes Joule heating, Peltier cooling, and Peltier heating of the TEG by means of the heat flows Q_j [W], Q_{pa} [W], and Q_{pe} [W], respectively. As for the electric circuit equivalent, the Seebeck effect gives rise to an open circuit

voltage $V_{oc} = \alpha(T_h - T_c)$, proportional to the difference in temperature between the TEG's hot side T_h and its cold side T_c, with α [VK^{-1}] being the Seebeck coefficient of all N_{th} thermocouples. The electrical resistance of the N_{th} thermocouples is represented by R_G.

Most of the manufacturers of thermoelectric modules do not provide the parameters needed for the SPICE model of the module. However, they do almost always specify I_{max}, V_{max} and the largest achievable temperature difference ΔT_{max} across a thermoelectric module for a given temperature T_h at the hot side. In [45], a methodology for extracting the parameters of the PSPICE-model from the TEC's datasheet is presented

$$\alpha = \frac{V_{max}}{T_h} \tag{6.3}$$

$$R_G = \frac{V_{max}}{I_{max}} \frac{T_h - \Delta T_{max}}{T_h} \tag{6.4}$$

$$R_{th,m} = \frac{\Delta T_{max}}{I_{max} V_{max}} \frac{2T_h}{T_h - \Delta T_{max}} \tag{6.5}$$

First, when selecting an appropriate TEG for a specific application, one should start by looking for TEGs with a semiconductor material that offers the best dimensionless figure of merit $Z\bar{T}$, with $\bar{T} = (T_h + T_c)/2$ denoting the average temperature encountered in the application. The efficiency of a TEG is optimal when $Z\bar{T}$ is maximized under the constraint that the ratio of the load resistance R_L to the internal resistance R_G is equal to $\sqrt{1 + Z\bar{T}}$ [12]. In the vicinity of 300 K, bismuth telluride (Bi_2Te_3) offers the best dimensionless figure of merit and has therefore been used in different human heat energy-harvesting applications in this temperature range [11], [12], [46]. Next, we calculate the different parameters pertaining to the model presented in Fig. 6.2, for a selection of off-the-shelf Bi_2Te_3 TEGs. Based on (6.1)-(6.5), we perform SPICE simulations to estimate the power, provided by the TEG when connected to the LPS, assuming a certain body and ambient air temperature. In this case, we rely on typical temperature values (Table 6.2) for body-heat-harvesting applications [12].

Table 6.2: Heat transfer coefficients and considered temperatures [12].

Quantity	Value
h_a [$Wm^{-2}K^{-1}$]	11
h_b [$Wm^{-2}K^{-1}$]	25
Ambient temperature T_a [°C]	18.9
Body core temperature T_b [°C]	37

Let us compare two TEGs, being the UT15,288,F2,5252 [70] (TEG1) and the UT6,24,F1,5555 [71] (TEG2) by Laird Technologies (Monchengladbach, Germany), whose specifications and calculated $V_{max}I_{max}$ products are given in Table 6.3. According to [4], the UT15,288,F2,5252 by Laird Technologies should be chosen, since it has the largest $V_{max}I_{max}$ product of the considered TEGs. However, the simulations, based on the model depicted in Fig. 6.2, favor the UT6,24,F1,5555 by Laird Technologies, which has a rather moderate $V_{max}I_{max}$ product. Table 6.4 depicts the calculated and simulated parameters of the two modules, based on the proposed model. The input voltage $V_{in} = V_{out,TEG}$ and current I_{in} = - $I_{out,TEG}$ of the LPS in the penultimate row of Table 6.4 and, hence, the power generated by the TEG in the last row of Table 6.4 are calculated by means of a SPICE simulation. Therefore, we load both TEGs by a fixed resistor of 2.5Ω to emulate the input impedance of the LPS. In reality, the input impedance of the LPS varies with input voltage. The resulting error is not very critical at this stage of the design process, as the procedure is only applied to differentiate between the different TEGs. Table 6.4 already clearly demonstrates that TEG2 outperforms TEG1.

Table 6.3: Specifications of the UltraTec Series UT15,288,F2,5252 and UT6,24,F1,5555.

	TEG1 [70]	TEG2 [71]
Series	UT15,288,F2,5252	UT6,24,F1,5555
Length l	52 mm	55 mm
Width w	52 mm	55 mm
V_{max}	36 V	29.8 V
I_{max}	15.4 A	6 A
ΔT_{max} @ T_h	68°C @ 25°C	74°C @ 25°C
$V_{max}.I_{max}$	554.4 W	178.8 W

Table 6.4: Simulated and calculated parameters of the UltraTec Series UT15,288,F2,5252 and the UltraTec Series UT6,24,F1,5555, based on the model in Fig. 6.2

	TEG1	TEG2
α [mV/K]	121	100
R_G [Ω]	1.80	3.73
$R_{th,m}$ [K/W]	0.318	1.101
$R_{th,a}$ [K/W]	33.6	30.1
$R_{th,b}$ [K/W]	14.8	13.2
ΔT_{net} [K]	0.12	0.45
V_{oc} [mV]	14.3	44.9
V_{in} [mV]	6.3	11.9
I_{in} [mV]	2.5	4.7
P_{out} [μW]	15.75	55.9

Our proposed methodology is used here to select an off-the-shelf TEG that is capable of charging the MEC via the designed LPS, without using a heat sink or a stack of TEGs, in order to minimize the form factor of the system and hence increasing the user's comfort. However, when flexible TEGs are available, the combined model in Fig. 6.2 cannot only be used to select the most appropriate flexible TEG for a specific real-life application, but also to simulate, for instance, the influence of using a carbon fabric heat spreading layer as in [50] and using a fabric heat sink (or reusing the conductive fabric parts of a textile antenna as heat sink, analogous to [52]).

6.7 Results and discussion

6.7.1 Influence of integration on the antenna performance

The excellent performance of the antenna in proximity of the human body and under bending was already demonstrated in [62]. In this section, the reflection coefficients and radiation pattern in the E- and H-plane of the antenna are measured: first, before integration of any energy-scavenging hardware, then, after solar cell integration and, finally, after circuitry integration. This approach allows us to verify the influence of the integration of the energy-scavenging hardware on antenna performance. The results are depicted in Figs. 6.11 and 6.12, respectively. In case of solar cell integration, both wires for connecting the anodes of the solar cells to the power management module were included in the measurement, as well as the copper tape for connecting both solar cells' cathodes to the antenna cavity. After integrating the circuitry and MEC, the required connections, as depicted in Fig. 6.10, were made and included in the measurement. The radiation patterns were measured in an anechoic chamber by means of an orbit/FR 3D positioning system and the N5242A PNA-X vector network analyzer from Agilent Technologies (Santa Clara, CA, USA). The measured bandwidth of the SIW textile slot antenna without any solar cells or hardware integrated is 330 MHz.

Fig. 6.11 shows a slightly larger bandwidth for the antenna with integrated energy-harvesting hardware, because of the additional losses due to presence of the power management module on the back of the textile slot antenna. The presence of only the solar cells does not affect the measured reflection coefficients much. Figs. 6.12(a) and (b) depict the free space gain of the antenna at 2450MHz in the E- and H-plane. The integration of the energy-harvesting hardware has a minimal influence on the radiation pattern of the antenna. A maximum gain in broadside of about 1.3 dBi is measured.

6.7.2 Influence of integration on solar cell DC properties

A solar simulator with an illumination of 100 mW/cm^2, corresponding to sunlight directly overhead and a turbidity-free sky, was used to obtain the DC P-V charac-

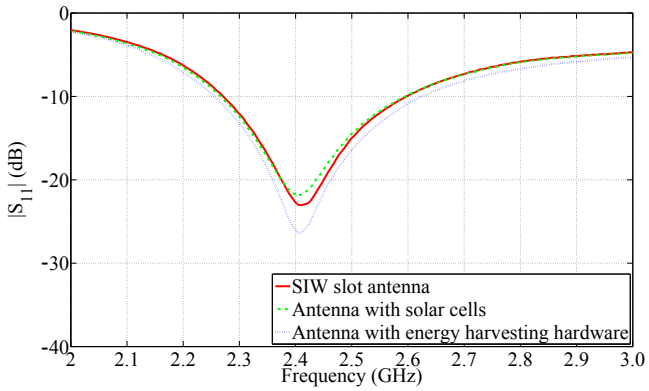

Figure 6.11: Measured reflection coefficients of the SIW cavity-backed slot antenna.

teristic from both solar cells before and after patterning the solar cell surface to fit the antenna slot contours. These DC P-V characteristics are depicted in Fig. 6.13. The modified solar cells produce a slightly lower power compared to the original ones due to the smaller effective solar cell area and a decreased shunt resistance. By removing parts of the solar cell to accommodate for the antenna slot, the maximum power delivered by solar cell 1 and solar cell 2 decreases from 56.9 to 52 mW and from 78.6 down to 68.9 mW, respectively. However, the reduced performance from solar cell 1 is negligible in indoor situations, since it will never be loaded in its maximum power point, but rather operates in lower power regions where the performance reduction is less significant. Since solar cell 2 is connected in series to a blocking diode, exhibiting a forward voltage of 400 mV, the maximum deliverable power by solar cell 2 decreases further to 62 mW. Moreover, in a practical application, the power output will be lower than in ideal test conditions, as there will be less sunlight available in actual conditions.

6.7.3 Performance of the energy-harvesting and power management module

Performance of the central power management system (CPMS)

On the one hand, measurements have shown that the CPMS is capable of charging the MEC from low-voltage sources that are able to produce at least 1.2 μW. However, first, the low-voltage DC source should be able to charge C_2 (Fig. 6.8) to a voltage level of 760 mV to activate the boost regulator of the CPMS. The boost circuit quits operating when the harvesting source is not capable of guaranteeing a voltage across C_2 (Fig. 6.8) higher than 354 mV. On the other hand, the CPMS is also able to charge the MEC from a high-voltage source, provided that the high-voltage source is able to deliver a higher voltage than the MEC. When charging

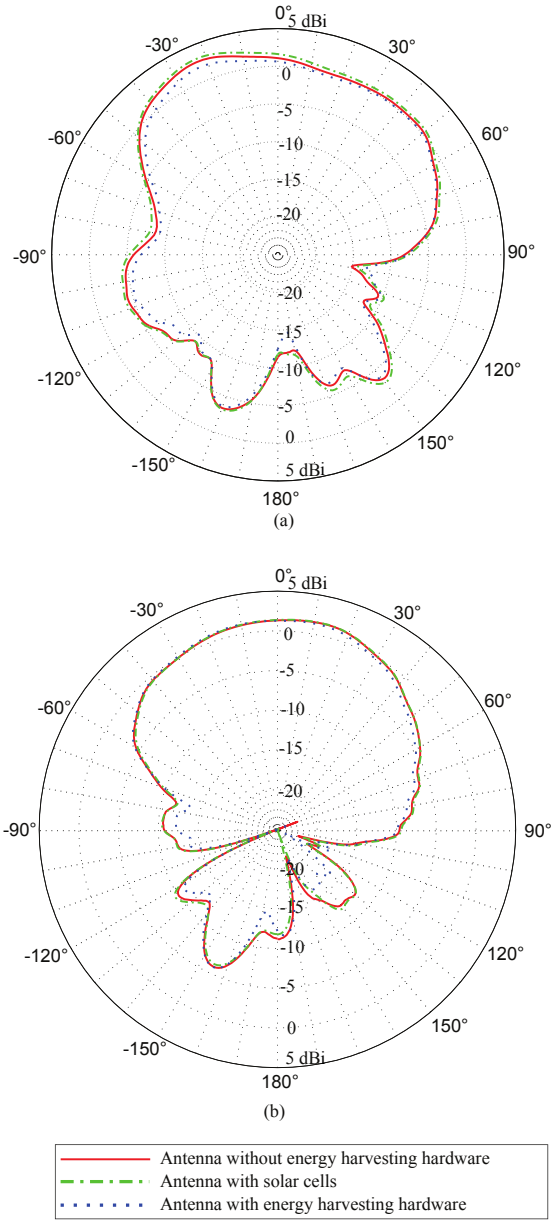

Figure 6.12: Measured radiation pattern of the SIW cavity-backed slot antenna at 2450 MHz. (a) In the E-plane. (b) In the H-plane.

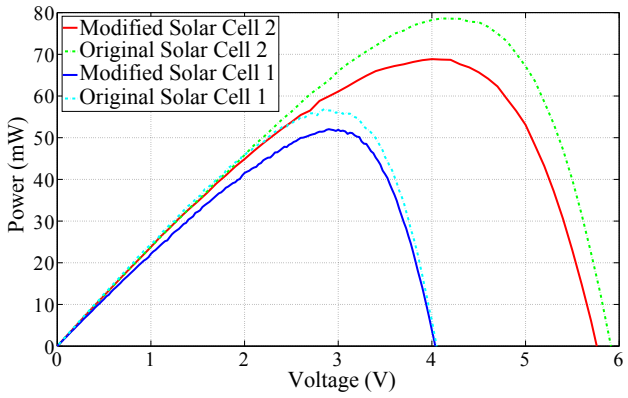

Figure 6.13: DC P-V characteristic of the original and modified solar cells.

from only one high-voltage source, that source should be able to deliver at least 4.1 V to activate the LDO. The LDO supports two modes of operation, based on the load connected to the REG pin of the CPMS. Measurements have shown a stable output voltage of 3.3 V up to 31 mA continuous load current in high-current mode, whereas in low-current mode, a stable output voltage is guaranteed up to at least 100 μA continuous load current. With only one MEC225-1P connected to the CPMS, a continuous load current in high-current mode can only be guaranteed if a high-voltage source is connected to the CPMS, delivering the difference in current between the load current and the current delivered by the MEC225-1P. By connecting multiple MECs, higher surge and continuous currents can be supported by the regulated output, even without a high-voltage source connected. A continuous load current up to 100 μA in low-current mode can be guaranteed without any source connected to the CPMS, on the condition that the MEC is sufficiently charged.

Performance of the low power system (LPS)

The measured input resistance of the LPS, as seen by the TEG, is depicted in Fig. 6.14, as a function of input voltage. Since measurements show that the LPS requires a minimum input voltage of 24.8 mV to charge C_5 to 5 V, we consider a range of input voltages from 25 to 500 mV. Up to 100 mV, an input resistance is observed that decreases with increasing input voltage. Beyond 100 mV, a quasi-constant input resistance of 2.5 Ω is found. Such behavior allows the LPS to adapt reasonably well to different off-the-shelf TEGs [4], hence also to both selected TEGs having an electrical resistance of 1.8 and 3.73 Ω, respectively. Another voltage-dependent input resistance can be achieved by choosing another transformer ratio [66].

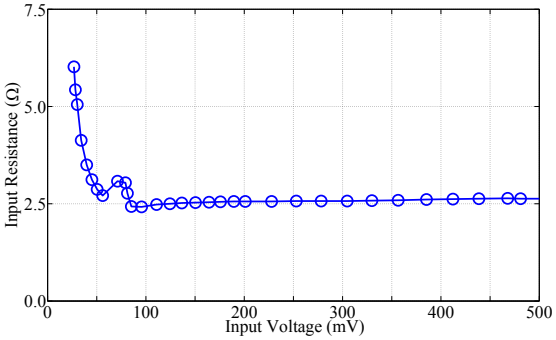

Figure 6.14: Input resistance of the LPS versus the input voltage with a 1 : 100 transformer ratio.

Figs. 6.15 and 6.16 depict the output voltage and the efficiency of the LPS, as a function of load resistance for different input voltage levels, respectively. Fig. 6.15 shows that as the input voltage increases, the point where the output voltage starts to deviate from 5 V shifts to a lower load resistance. Hence, a higher input voltage permits a higher load at the output. A maximum achievable efficiency of over 40% can be observed in Fig. 6.16 . Moreover, Fig. 6.16 shows that the maximum achievable efficiency is higher in the lower input voltage range and is reached in the load resistance region where the output voltage starts to deviate from the programmed 5 V. In general, a higher load resistance than the optimal resistance implies that more power is generated than required by the load. The excess current is then shunted to GND by an internal shunt regulator, hence decreasing the efficiency. A lower load resistance implies that more power is required by the load than generated by the source. As a result, the output voltage drops while the input power remains constant because of a constant input voltage and current, hence the decreasing efficiency. Measurements have shown that, when the LPS is connected to the CPMS (as in Fig. 6.6) and the MEC is charging, the output of the LPS is forced to voltages between 3.0 and 4.15 V, depending on the charge state of the MEC. Hence, during the charging process of the MEC, the LPS will experience a load resistance in the interval 100-192 kΩ for $V_{in} = 30$ mV, 25-44 kΩ for $V_{in} = 50$ mV, 10-16 kΩ for $V_{in} = 100$ mV, and 4.4-6.9 kΩ for $V_{in} = 250$ mV. Comparing these load resistance regions with Fig. 6.16 proves that, during the charging process of the MEC, the LPS operates in the regions where maximum efficiency is obtained, resulting in efficiencies in the interval 38%-41% for $V_{in} = 30$ mV, 40%-41% for $V_{in} = 50$ mV, 24%-26% for $V_{in} = 100$ mV, and 9%-10% for $V_{in} = 250$ mV. Once the MEC is fully charged, the output voltage of the LPS increases to 5 V and the excess current is shunted to GND by an internal regulator. However, such a scenario will not occur frequently in a well-designed SFIT system, in which the MEC is never fully charged because of a well-adapted energy-harvesting and consumption profile.

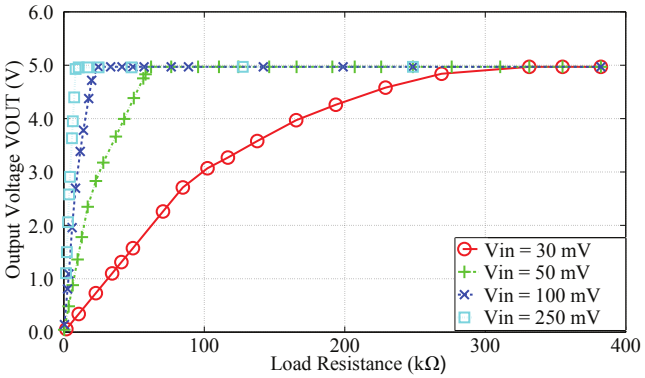

Figure 6.15: Output voltage of the LPS versus load resistance as a function of input voltage.

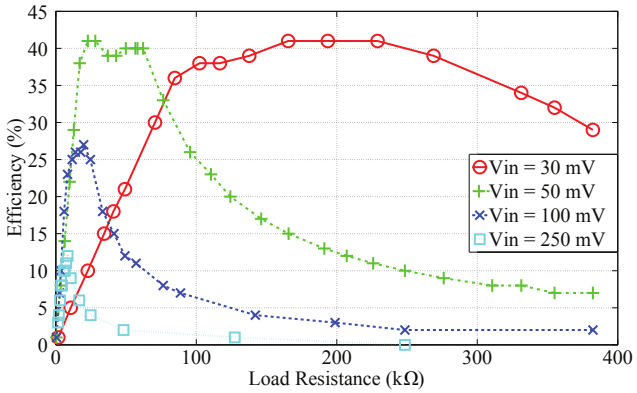

Figure 6.16: Efficiency of the LPS versus load resistance as a function of input voltage.

6.7.4 Performance of the TEGs

Figs. 6.17 and 6.18 prove that the TEG with the highest $V_{max}I_{max}$ product only should be selected when a constant thermal gradient across the TEG can be guaranteed, regardless of the chosen TEG. In that case, the TEG with the highest product of $V_{max}I_{max}$ will have the highest output power for the same thermal gradient. This is demonstrated in Fig. 6.17 , where the two selected TEGs are loaded by a variable resistance and the power delivered to the load as a function of the load resistance is shown. During measurements, a constant thermal gradient across the TEG of 1 K is maintained by placing the TEGs on a hot plate and cooling the cold side. An optimal power transfer is reached for a matched condition between the load resistor and the TEG's electrical resistance [4], [10], [12].

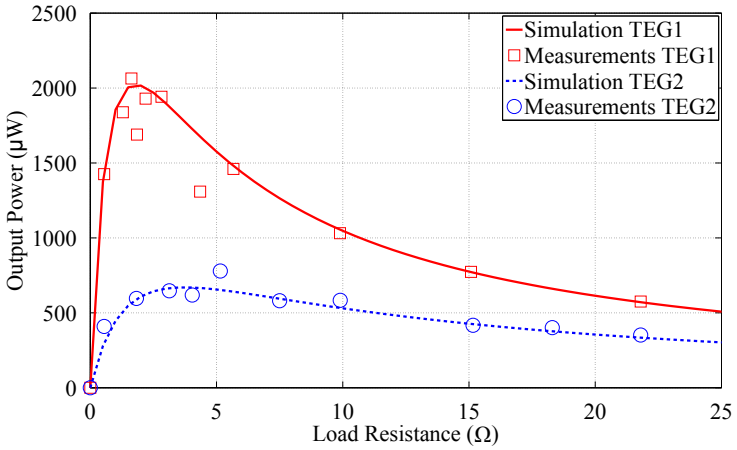

Figure 6.17: Output power generated by the selected TEGs, as a function of the load resistance, with a constant 1 K thermal gradient across the TEGs.

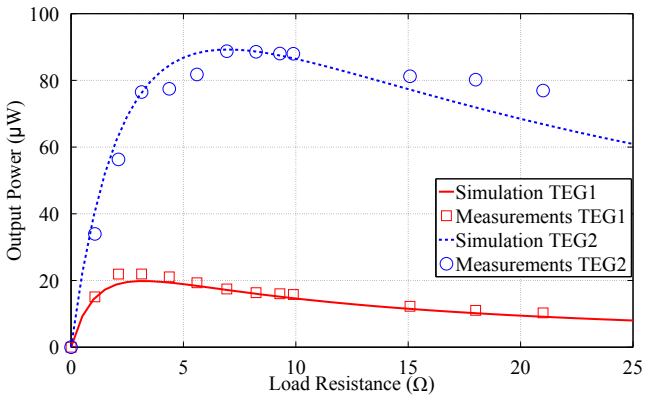

Figure 6.18: Output power generated by the selected TEGs, as a function of the load resistance, with the hot side of each TEG in contact with the hot plate at skin temperature ($33^{\circ}C$) and the cold side of the TEG exposed to the ambient air at $18.9^{\circ}C$.

Fig. 6.18 also shows the power delivered to a variable load resistance for both TEGs. The hot side of the TEG is now in direct contact with the hot plate at skin temperature ($33\ ^{\circ}C$) and the cold side of the TEG is exposed to the ambient air of $18.9\ ^{\circ}C$, emulating a TEG placed on a human arm as in Fig. 6.7. Fig. 6.18 shows that the TEG selected by our proposed combined model outperforms the TEG that should be selected if one uses the $V_{max}I_{max}$ product as a selection criterion. This is due to the presence of the product of $V_{max}I_{max}$ in the denominator of (6.5), resulting in a lower net thermal gradient across the TEG for a given overall

temperature difference and given size of the TEG, as shown in Table 6.4. Fig. 6.18 also shows that, for maximum power transfer, the load resistance differs from the source resistance, in contrast to [4], [10], and [12]. This is due to a varying open circuit voltage (Fig. 6.2) caused by a varying net thermal gradient across the TEG. The latter effect is attributed to the Peltier and Joule effect, which are different for each load resistance, as each load resistance results in a different current. Fig. 6.18 demonstrates the potential to recover more power than obtained in Table 6.4 by loading the TEG with the optimal impedance. The optimal load impedance for TEG1 and TEG2 equals 3.2 and 6.9 Ω, respectively. Fig. 6.14 shows the ability of the LPS to provide these input resistances.

Fig. 6.19 shows the open circuit voltage for both TEGs, as a function of the ambient air temperature. For this measurement, the TEGs were positioned on an arm, with the TEG making direct contact with the human skin. Again, we note that the second TEG outperforms the first TEG. For a decreasing ambient temperature, the open circuit output voltage increases. The measurements in Figs. 6.17-6.19 are obtained while the thermoelectric module remains stationary. Yet, in a practical application, the wearer of the thermoelectric module will move. In that case, Lossec et al. [12] have shown qualitatively that the open circuit output voltage will increase as a result of a decreased convective resistance $R_{th,a}$.

Nevertheless, the difference in temperature between the hot source and the cold source remains small, resulting in an even lower thermal gradient across the TEG because of its small $R_{th,m}$ with respect to the sum of $R_{th,a}$ and $R_{th,b}$, and, hence, leading to a low output voltage. In this respect, there is definitely room for future improvement. Indeed, to further maximize the harvested energy by the TEG, the TEG should also be thermally matched. This means that $R_{th,m}$ should equal the other thermal resistances along the path of heat flow from body core to the ambient

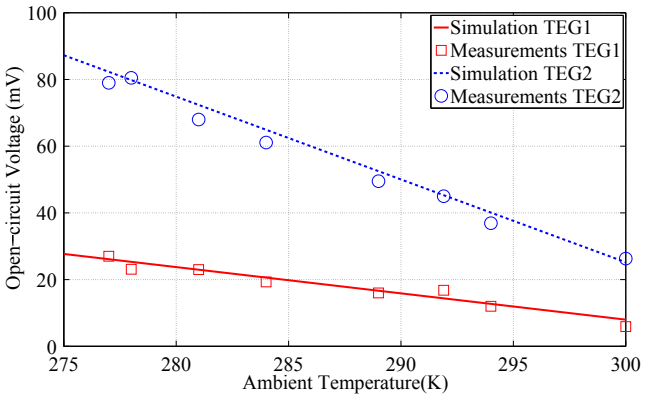

Figure 6.19: Open-circuit output voltage of both TEGs versus the ambient air temperature, with the hot side placed into direct contact with the arm of a static wearer.

air, or equivalently that, $R_{th,m} = R_{th,a} + R_{th,b}$ [63] (Fig. 6.2). However, Table 6.4 clearly demonstrates that the sum of $R_{th,a}$ and $R_{th,b}$ is much larger than $R_{th,m}$. It should be stressed that, in this chapter, we focused on selecting a single standalone, commercially available TEG that is capable of charging the MEC via the designed LPS. The small thermal gradient across the TEG, and, hence, the corresponding low output voltage, highlights the importance of using the LPS to efficiently convert the low-power source into a high-voltage source, which can then be connected to the CPMS.

In the short term, an increased harvested energy could be obtained by stacking multiple of such rigid off-the-shelf TEGs to increase $R_{th,m}$, as demonstrated in [12], or by using a rigid heat sink. In that case, $R_{th,a}$ (Fig. 6.2) represents the thermal resistance of the heat sink. By selecting an appropriate heat sink, $R_{th,a}$ can be reduced, resulting in a higher thermal gradient across the TEG. However, both solutions lead to larger aspect ratios, which are not suitable for body-worn applications. Therefore, future research, carried out to achieve thermal matching in body-worn scenarios, needs to be oriented toward a total solution, which consists of exploiting flexible and breathable TEGs covering a large surface of the human skin (reducing $R_{th,b}$) and using well-designed textile antennas (or other conductive fabric components) as heat sinks to reduce $R_{th,a}$. For instance, in [52], $R_{th,a}$ was decreased to values between 6 and 8 KW^{-1}, by using a rigid copper antenna as heat sink. But first, flexible TEGs should be further optimized to obtain higher conversion efficiencies. However, to date, TEGs based on flexible thermoelectric materials, such as organic semiconductors, are still impractical because of their low intrinsic electric carrier mobility [72]. Another approach, involving a flexible matrix with embedded discrete miniature thermoelectric chips, suffers from too much weight and a complex and expensive fabrication method [73]. From this point of view, Yadav et al. [73] propose a very promising design based on thin film thermoelectric junctions on flexible fibers, which could be woven into energy-harvesting fabrics and worn by the user. At this moment, Ni-Ag thin films are used, resulting in a maximum power of only 2 nW for seven couples at a $\Delta T = 6.6$ K. However, Yadav et al. [73] also state that evaporating thicker semiconductor films onto hollow, low thermal conductivity substrates offers an excellent opportunity to further improve thermal energy harvesting. Then, bismuth telluride could be used as thermoelectric material instead of Ni-Ag, since it still outperforms any other thermoelectric material in body-worn scenarios to this moment. However, Lossec et al. [12] propose to orient research, concerning new thermoelectric materials for body thermal energy harvesting, toward maximizing a newly introduced factor (instead of $Z\bar{T}$), being $Z_E = \alpha_0^2/(4\rho\lambda^2)$, with α_0, λ, and ρ being the Seebeck coefficient, the thermal conductivity, and electrical resistivity of the material, respectively. Perhaps this could lead to even better thermoelectric materials.

Since Figs. 6.17-6.19 show a good agreement between simulations and measurements, our proposed model can be used to evaluate different measures to obtain thermal matching and predict the amount of power that can be harvested in a certain scenario.

6.7.5 Performance of the proposed energy-harvesting and power management module in a real-life indoor environment

Since Tan and Panda [17] demonstrate higher recoverable power densities in an outdoor environment compared to indoor conditions, an indoor environment is considered to demonstrate the energy-harvesting potential of the proposed energy-harvesting system in minimum power density situations. Using the proposed system in an outdoor environment will increase the energy scavenging thanks to improved light conditions and convection of the cold side of the TEG due to wind. The measurements performed in this section demonstrate:

- the possibility to scavenge energy in most of the indoor conditions;
- an increase of scavenged energy by human motion/movement;
- cooperation between the TEG and the solar cell, connected to the boost converter.

Five carefully chosen scenarios are now studied to verify these claims. Before the start of each measurement, the MEC is discharged with a constant current of 50 μA at 25°C via the REG pin of the CPMS (Fig. 6.8), operating in high-current mode. This ensures a quasi-similar open circuit voltage of the MEC, slightly less than 3.9 V, at the start of each measurement. In addition, the LDO is turned off to reduce quiescent current.

Solar-cell-1-only scenario: A static wearer in an illuminated room at 25°C

In the first situation, measurements are performed in a 2.4-m high room with a steady temperature of 25°C, no air circulation and illuminated with fluorescent lamps mounted at the ceiling. A male test person with a height of 1 m 87 cm, wearing the energy-harvesting system on his back and the TEG on his left arm, is standing in an upright position. Measurements show that due to the high temperature, a lack of air circulation and movement of the wearer, the TEG is not able to provide a voltage high enough to enable the LPS and thus charge the MEC. Moreover, the maximum value of the open circuit voltage of solar cell 2 in the room amounts to only 2.1 V and, hence, does not suffice to charge the MEC. However, solar cell 1 is capable of scavenging energy from the artificial light sources. The power generated by solar cell 1, as a function of time and over a 40-min time interval, is depicted in Fig. 6.20. The generated power by solar cell 1 exhibits fluctuations around an average power level $\bar{P}_{\text{gen,SC1}}$ of 37 μW. However, measurement have shown that, over the 40-min time interval, an average power of $\bar{P}_{\text{cons,CPMS}} = 12.6\ \mu W$ has been consumed by the CPMS, resulting in an overall system efficiency $\bar{\eta}_{\text{system}}$ of 65.9%. 24.4 μW was delivered to the MEC ($\bar{P}_{\text{harv}}$) with

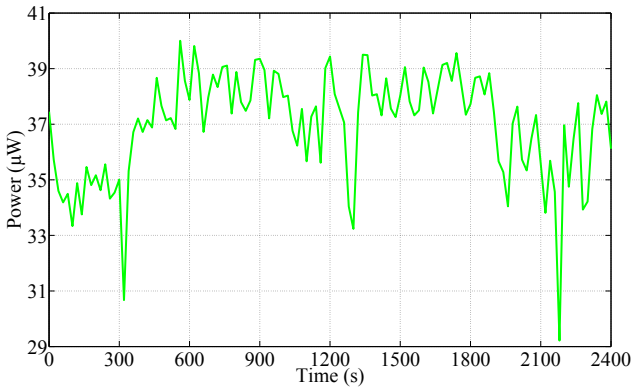

Figure 6.20: Power generated by solar cell 1 as a function of time in case of a static wearer in an illuminated room at 25°C.

an average charge current $\bar{I}_{\text{charge}}$ of 6.3 μA. Hence, we may conclude that the energy-harvesting system is able to scavenge energy from artificial light.

TEG-only scenario: A static wearer in a nonilluminated room at 15.5°C

The wearer sits in the same room as in the first situation and periodically stands up to stretch. Since the room is not illuminated in this case, none of the solar cells are able to recover energy. However, the room temperature is low enough, even in this static situation, to enable the LPS to charge the MEC via the CPMS. This is demonstrated in Fig. 6.21, which depicts the power delivered by the TEG to the LPS and the power delivered to the battery, as a function of time. The seven peaks in the power curves can be attributed to stretching of the user, whereas the minor fluctuations are due to minor movements of the wearer. It can be seen that the output and input power curves have the same shape. The efficiency of the overall system is shown in Fig. 6.22. Each input power peak in Fig. 6.21 corresponds to a small efficiency peak in Fig. 6.22, whereas even a small input power drop results in a big efficiency drop. The resulting charge current is also shown in Fig. 6.22. The curve has a very similar shape as the power delivered by the TEG to the LPS. Hence, the second scenario demonstrates the ability to charge the MEC in a nonilluminated room, solely by thermal energy recovered by a single TEG placed on the arm of a static wearer. During the 40-min interval, the TEG was able to generate an average power $\bar{P}_{\text{gen,TEG}}$ of 105 μW, of which $\bar{P}_{\text{cons,LPS}} =$ 66.8 μW was consumed by the LPS, and $\bar{P}_{\text{cons,CPMS}} = 2.5$ μW by the CPMS. Hence, $\bar{P}_{\text{harv}} = 35.7$ μW was delivered to the MEC, leading to an overall system efficiency $\bar{\eta}_{\text{system}}$ of 34.0% and an average charge current of $\bar{I}_{\text{charge}} = 9.2$ μA.

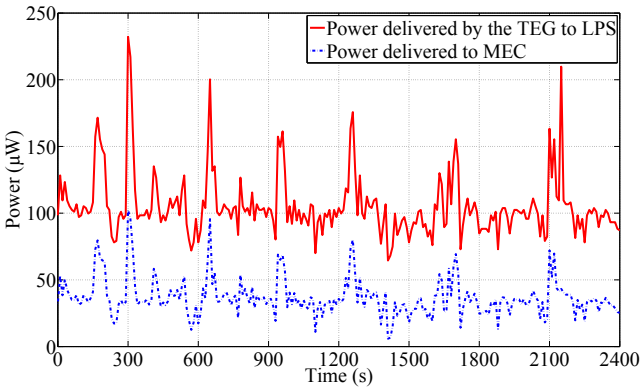

Figure 6.21: Power generated by the TEG and power delivered to the MEC as a function of time, in case of a static wearer in a nonilluminated room at 15.5°C.

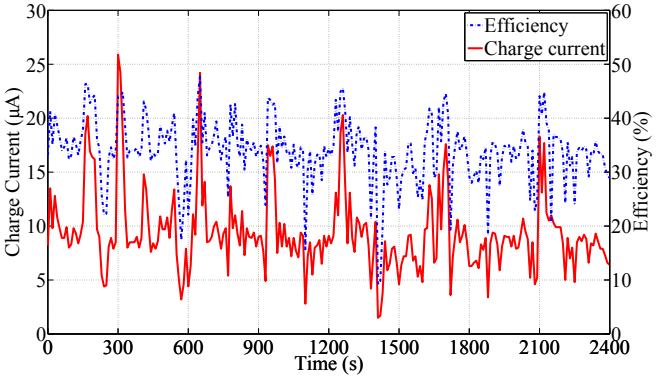

Figure 6.22: Efficiency of the LPS and charge current as a function of time, in case of a static wearer in a nonilluminated room at 15.5°C.

TEG-only scenario: A dynamic wearer in a nonilluminated room at 24°C

An increasing ambient temperature in the second scenario will result in a decrease of the open circuit output voltage of the TEG and, hence, in a lower operation point of the LPS. From a certain ambient air temperature, the output voltage of the TEG is not high enough to activate the LPS and the proposed energy-harvesting system cannot charge the MEC anymore in case the wearer remains static. However, it is still possible to charge the MEC in a nonilluminated room, at a higher temperature than the specific ambient air temperature mentioned earlier, with one single TEG and without a heat sink, provided the wearer starts to walk. To demonstrate this, the room in the second scenario is heated to a constant temperature of 24°C and

the lights remain dimmed. For a static user, the TEG then produces an open circuit voltage of 30 mV. Connecting the single TEG configuration to the LPS results in an input voltage of only 17.4 mV, which is not high enough to activate the LPS. The wearer then starts walking. Thanks to the increased convection, the input voltage increases to 27.4 mV. The TEG then generates $\bar{P}_{\text{gen,TEG}} = 138.7\ \mu W$, resulting in $\bar{P}_{\text{harv}} = 56.7\ \mu W$ delivered to the MEC. The difference in power is consumed by the LPS ($\bar{P}_{\text{cons,LPS}} = 79.5\ \mu W$) and the CPMS ($\bar{P}_{\text{cons,CPMS}} = 2.5\ \mu W$). Hence, this scenario is characterized by an overall system efficiency $\bar{\eta}_{\text{system}}$ of 40.9%, and an average charge current of $\bar{I}_{\text{charge}} = 14.4\ \mu A$.

Fourth scenario: A static wearer in an illuminated room at 15.5°C

To demonstrate the cooperation between the TEG and solar cell 1, the second scenario is considered but with the fluorescent lamps turned on and the test person standing. The power produced by the TEG and solar cell 1 is depicted in Fig. 6.23 as a function of time. The peaks in generated power by the TEG can be attributed to fast movements of the wearer, caused by stretching as in the second scenario. In the 40-min interval, the TEG and solar cell 1 generate a total average power $\bar{P}_{\text{gen,total}}$ of 145 μW, of which 111 μW is generated by the TEG ($\bar{P}_{\text{gen,TEG}}$) and 34 μW by solar cell 1 ($\bar{P}_{\text{gen,SC1}}$). However, not all of the power delivered by the TEG is used to charge the MEC, due to power consumption and dissipation in the LPS and the CPMS, as already depicted in Fig. 6.22. In fact, over the 40-min time interval, an average power of 69.6 μW was required by the LPS, whereas 11.6 μW was required by the CPMS. Eventually, an average power $\bar{P}_{\text{harv}}$ of 63.8 μW was delivered to the MEC, leading to an overall system efficiency $\bar{\eta}_{\text{system}}$ of 44.0%, and an average charge current of $\bar{I}_{\text{charge}}$ 16.3 μA.

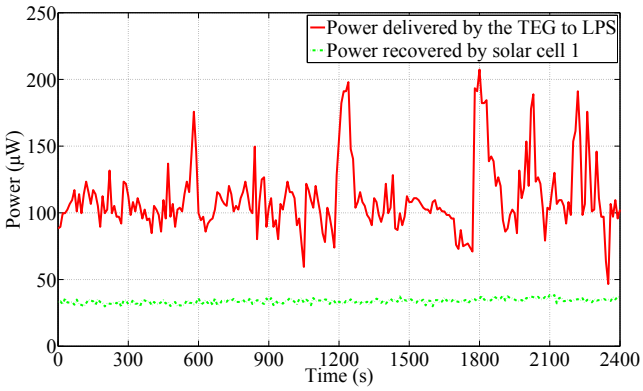

Figure 6.23: Power generated by the TEG and solar cell 1 as a function of time, in case of a static wearer in an illuminated room at 15.5°C.

Fifth scenario: A dynamic wearer in an illuminated room at 17.5°C

The same room as in the fourth scenario is considered, but now the ambient air temperature equals 17.5 $°C$ and the wearer is dynamic. Fig. 6.24 depicts the power generated by solar cell 1 and the TEG, as a function of time. The measurement starts with the test person sitting. This corresponds to 72 μW of generated power by the TEG and 9 μW effectively delivered by the LPS to the CPMS. Then, the wearer starts walking at normal pace, resulting in higher power generation by the TEG than in static conditions shown in Figs. 6.21 and 6.23. At certain times, the wearer takes a break. These breaks correspond to the drops in the instantaneously generated power by the TEG, to a level equal to or a bit larger than in the static scenario, shown in Figs. Figs. 6.21 and 6.23. One would expect a lower instantaneously generated power by the TEG due to the higher ambient temperature, but the breaks were kept short in duration. Hence, the instantaneous power did not have enough time to drop to the expected power level. Between 900 and 1940 s, the wearer is still walking, but at increased speed. This results in an average power generated by the TEG $\bar{P}_{\text{gen,TEG}}$ of 274 μW. This is more than double the power delivered in the fourth scenario, despite the fact that the wearer is not walking at a very fast pace, the four breaks he takes, and the ambient temperature of 17.5 $°C$. Again, not all of this power will be delivered to the MEC. The effectively delivered power by the LPS to the CPMS is also depicted in Fig. 24. It has the same shape as the curve representing the power generated by the TEG. The dynamic behavior of the wearer also has an influence on the power generated by solar cell 1. At certain times, a bad orientation of solar cell 1 results in a drop of generated power. However, the drops in generated power by solar cell 1 are very short since the wearer is walking. Hence, the influence of these drops on $\bar{P}_{\text{gen,SC1}}$ is negligible. On average, 36.9 μW of power was generated by solar cell 1, which is very similar to the average power obtained in the first scenario and results in a $\bar{P}_{\text{gen,total}}$ of 310.9 μW. Since 150 μW is required by the LPS and 12.6 μW is required by the CPMS in order to fulfill their tasks, $\bar{P}_{\text{harv}}$ amounts to 148.3 μW, resulting in an $\bar{\eta}_{\text{system}}$ of 47.7%, and an average charge current $\bar{I}_{\text{charge}}$ of 38.0 μA.

The most important quantities of each scenario, being the average power that was generated by each of the three EH transducers, the average power that is required by the LPS ($\bar{P}_{\text{cons,LPS}}$) and CPMS ($\bar{P}_{\text{cons,CPMS}}$), the average power that is effectively harvested and stored in the MEC ($\bar{P}_{\text{harv}}$), the average charge current of the MEC ($\bar{I}_{\text{charge}}$), and the efficiency of the flexible power management system ($\bar{\eta}_{\text{system}}$), that are observed over the considered 40-min time interval, are summarized in Table 6.5. $\bar{P}_{\text{cons,CPMS}}$ includes the power consumed by the boost converter and the power consumption caused by the quiescent current during harvesting. Since the LDO was turned off during measurements, no current was drawn from the cell in order to regulate the output voltage. Hence, this effect is not included in the system efficiencies depicted in Table 6.5. Turning on the LDO in high-current mode will cause a current of 725 nA to be drawn from the MEC, whereas turning on the LDO in low-current mode will result in a current of 150 nA to be drawn

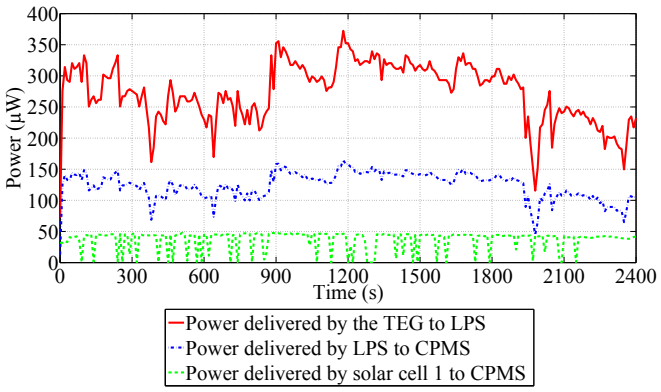

Figure 6.24: Power generated by the TEG and solar cell 1 as a function of time, in case of a dynamic wearer in an illuminated room at 17.5°C.

from the MEC [65]. Since solar cell 2 is selected to increase energy harvesting in an outdoor scenario, it does not output a voltage high enough to charge the MEC in an indoor scenario. Therefore, the generated power by solar cell 2 remains zero, as depicted in Table 6.5. The importance of solar cell 2 will be highlighted in Section 6.7.6. Furthermore, in each of the five indoor scenarios, the voltage across the MEC remained approximately 3.9 V (exhibiting a slight increase). This is inherent to the open circuit voltage characteristic of the MEC, which exhibits a quasi-constant value of 3.9 V in the region where the MEC is charged between 3% and 50% (or similarly, where the MEC is discharged between 50% and 97%) [64]. Also, the behavior of the charge current is similar for all indoor scenarios, being a charge current fluctuating around the average charge current, depicted for each scenario in Table 6.5, and following the fluctuations in generated power by the active EH transducer(s), as depicted in Figs. 6.20-6.24.

From Figs. 6.20-6.22 and Table 6.5, we conclude that, with the proposed energy-harvesting platform, it is possible to harvest energy in most of the indoor scenarios. This is confirmed by the measurements in the first three of the five scenarios mentioned earlier. Fig. 6.20 and Table 6.5 demonstrate the potential to recover energy in the presence of artificial light. However, in the absence of light, Fig. 6.21 and Table 6.5 show that the TEG is able to harvest energy. Yet, the energy recovered by the TEG is dependent on the room temperature. Hence, from a certain ambient temperature, it is no longer possible to harvest energy in the absence of light, in case of a static wearer. If this situation occurs, energy harvesting is still possible provided the wearer starts walking. This is demonstrated by the third scenario and clearly seen in Table 6.5. Moreover, Figs. 6.23 and 6.24 and Table 6.5 show that, in certain situations, it is possible to harvest energy from two different sources to increase the total harvested energy. The third and fifth scenarios demonstrate that more energy is recovered by the TEG when the wearer is walking than when he remains static, as indicated in Table 6.5.

Table 6.5: Summary of system performance for all indoor scenarios (Average power generated by Solar Cell 1 $\bar{P}_{\text{gen,SC1}}$, by Solar Cell 2 $\bar{P}_{\text{gen,SC2}}$, by the TEG $\bar{P}_{\text{gen,TEG}}$, and by all EH transducers $\bar{P}_{\text{gen,total}}$. Average power required by the LPS $\bar{P}_{\text{cons,LPS}}$ and CPMS $\bar{P}_{\text{cons,CPMS}}$. Average power that is effectively harvested and stored in the MEC $\bar{P}_{\text{harv}}$. Average charge current $\bar{I}_{\text{charge}}$, and overall efficiency of the power management system $\bar{\eta}_{\text{system}}$.).

Scenario	$\bar{P}_{\text{gen,SC1}}$ $[\mu W]$	$\bar{P}_{\text{gen,SC2}}$ $[\mu W]$	$\bar{P}_{\text{gen,TEG}}$ $[\mu W]$	$\bar{P}_{\text{gen,total}}$ $[\mu W]$	$\bar{P}_{\text{cons,LPS}}$ $[\mu W]$	$\bar{P}_{\text{cons,CPMS}}$ $[\mu W]$	$\bar{P}_{\text{harv}}$ $[\mu W]$	$\bar{I}_{\text{charge}}$ $[\mu A]$	$\bar{\eta}_{\text{system}}$ [%]
1	37.0	0.0	0.0	37.0	0.0	12.6	24.4	6.3	65.9
2	0.0	0.0	105.0	105.0	66.8	2.5	35.7	9.2	34.0
3	0.0	0.0	138.7	138.7	79.5	2.5	56.7	14.4	40.9
4	34.0	0.0	111.0	145.0	69.6	11.6	63.8	16.3	44.0
5	36.9	0.0	274.0	310.9	150.0	12.6	148.3	38.0	47.7

6.7.6 Performance of the proposed energy-harvesting and power management module in a real-life outdoor environment

Section 6.7.5 already demonstrated the energy harvesting potential of the proposed system in minimum power density situations, typical for indoor scenarios. It was also mentioned that employing the proposed system in an outdoor environment will increase the energy scavenging by solar cell 1 and the TEG, thanks to improved light conditions and increased convection of the cold side of the TEG, respectively. In addition, in outdoor scenarios, solar cell 2 will also be able to harvest energy, which was not the case in indoor scenarios. The energy-harvesting potential of solar cell 2 in a real-life outdoor environment is demonstrated in this section. Fig. 6.25 depicts the charge current of the MEC as a function of time in case the TEG and solar cell 1 are disconnected from the CPMS, so only solar cell 2 contributes to the charge current. The test person is standing in an upright position, with solar cell 2 on his chest perpendicular to the surface of Earth and pointed in the direction of the sun. The sky was turbidity-free. One notices a constant current during the first 15 min of the measurement, but then the current decreases. Due to the charge profile of the MEC, solar cell 2 is forced into operating points inferior to the maximum power point. Connecting more MECs in parallel will reduce series resistance of the cells, change the operation point of solar cell 2, and increase total charge current. In that case, more energy can be scavenged in the same time interval, as demonstrated in [22]. By loading the CPMS via the regulated output in a similar way as in [22], the solar cell can be forced into operating points delivering more power to the power management system. This is depicted in Fig. 6.26, which shows the power delivered by solar cell 2 to the CPMS as a function of load current of the regulated output. In this specific case, the maximum generated power, being 49 mW, occurs at a continuous load current of 13 mA. The maximum

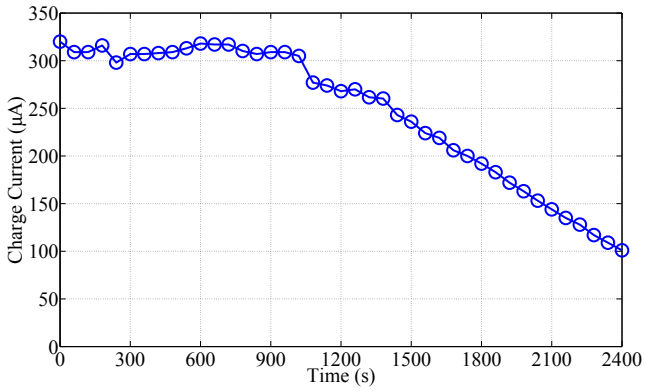

Figure 6.25: Charge current of MEC225-1p, as a function of time, in case of outdoor harvesting with only solar cell 2 connected and positioned in a vertical position pointed toward the sun.

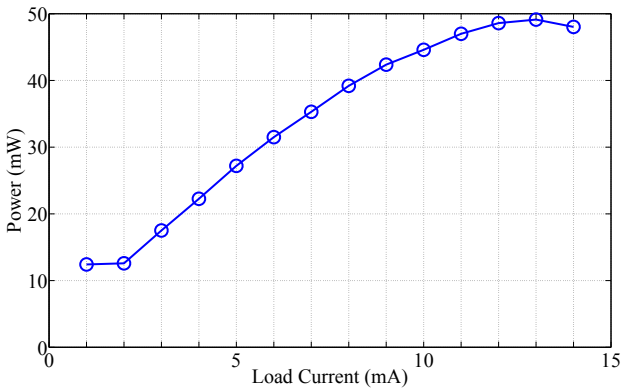

Figure 6.26: Power delivered by solar cell 2 to the CPMS, as a function of load current of the regulated output.

power point in Fig. 6.26 is lower than the one obtained in Fig. 6.13 due to a less ideal orientation of the solar cell. However, Fig. 6.26 also demonstrates that, even without an ideal orientation, the maximum generated power by solar cell 2 in this outdoor scenario is much higher than the maximum generated power achieved in the five indoor scenarios (Table 6.5), indicating the higher power densities in an outdoor environment and emphasizing the importance of including solar cell 2 in the design.

6.8 Conclusion

SFIT systems are able to set up wireless body sensor networks that implement augmented sensing for remote monitoring of vital signs and environmental conditions, wireless communication to enable remote interpretation, and actuation to trigger alarms. This enables them to improve quality of life of patients and elderly people by facilitating home care and independent living, in the meantime reducing healthcare costs for the society. Moreover, they reduce the risks, to which first responders are exposed during rescue missions and interventions, by leveraging improved disaster coordination through remote monitoring, localization, and control of the different team members. Autonomy, reliability, and user comfort are key requirements for these applications.

As the wireless communication module has a profound effect on the energy consumption of the SFIT system, special care should be taken to ensure its energy-efficient operation. As garments provide a sufficiently large integration platform, one or more high-efficiency and well-designed textile antennas may be integrated, to implement an energy-efficient and reliable wireless communication link. A low-power wireless communication module brings us a step closer to fully autonomous SFIT systems that are solely powered by energy-harvesting techniques, provided that the scavenging system can be unobtrusively integrated into a garment.

In this paper, we reviewed energy harvesting in the context of SFIT systems for rescue workers and for patients in home-care scenarios and hospitals. Specifically, a hybrid-antenna-harvester architecture was proposed that reuses the large surface required by the textile antenna(s) for efficient communication as an energy-harvesting and power management platform, to achieve a compact, highly integrated, and unobtrusive module. The integration of additional energy-harvesting and power management hardware may be realized on different textile antenna topologies, provided that the extra hardware does not affect antenna performance. We outlined the state of the art on energy harvesters that are suitable for such an integration process. Moreover, we discussed some upcoming harvesting technologies that offer great potential in combination with the textile antenna platform. Finally, a flexible hybrid energy-harvesting system that charges and protects MECs, and offers a regulated output, has been designed and effectively integrated onto a wearable textile substrate integrated waveguide antenna. The proposed flexible energy-harvesting system is capable of combining the energy harvested from three different energy sources, each with a different order of magnitude, to realize more continuous energy harvesting and larger amounts of scavenged energy. This extends battery lifetime or reduces battery size in the SFIT system. The performance of the proposed energy-harvesting system was analyzed in low-power-density scenarios to demonstrate the energy-harvesting potential in an indoor environment. The integration of a second solar cell increases the scavenged energy in outdoor environments. Excellent performance of the proposed system was obtained in different harvesting scenarios. However, depending on the application, an even better performance can be achieved by integrating more MECs and/or more flexible so-

lar cells, combining the energy from multiple diverse energy sources, tailoring the power management module to the power profile of the communication module and to the power profile of the energy-harvesting transducers.

Measurements have demonstrated that the integration of suitable energy-harvesting hardware onto a well-chosen wearable textile antenna has a negligible influence on the antenna performance. Hence, the surface required by the antenna in a smart textile system is effectively reused as energy-harvesting and power management platform. This novel integration of both energy scavenging and power management hardware onto a wearable textile antenna results in a more compact and more autonomous overall system, thereby improving the user's comfort.

References

[1] J. Yeo, S. G. Moon, and J. Y. Jung, "Design of Antennas for a Battery-Assisted RFID Tag with a Thin and Flexible Film Battery", *Microw. Opt. Technol. Lett.*, vol. 50, no. 2, pp. 494–498, Feb. 2008.

[2] H.-J. Yoo, J Yoo, and L. Yan, "Wireless fabric patch sensors for wearable healthcare", in *Proc. IEEE Conf. Eng. Med. Biol. Soc.,*, Buenos Aires, Argentina, 31 Aug. - 4 Sept. 2010, pp. 5254–5257.

[3] T. Starner, "Human-powered wearable computing", *IBM Syst. J.*, vol. 35, no. 3, pp. 618–629, 1996.

[4] D. Salerno, "Ultralow voltage energy harvester uses thermoelectric generator for battery-free wireless sensors", *LT J. Analog Innovat.*, vol. 20, pp. 1–11, Oct. 2010.

[5] A Rahman, N Rashid, A. Aziz, and G Witjaksono, "Design of autonomous micro-solar powered energy harvesting system for self-powered batteriesless wireless sensor mote", in *Proc. Electron. Goes Green*, Berlin, Germany, 9-12 Sept. 2012, pp. 1–4.

[6] G. Orecchini, L. Yang, M Tentzeris, and L. Roselli, "Smart Shoe: An autonomous inkjet-printed RFID system scavenging walking energy", in *Proc. IEEE Int. Symp. Antennas and Propagation (APSURSI)*, Spokane, WA, USA, 3-8 Jul. 2011, pp. 1417–1420.

[7] F. Declercq, A. Georgiadis, and H. Rogier, "Wearable Aperture-Coupled Shorted Solar Patch Antenna for Remote Tracking and Monitoring Applications", in *Proc. 5th Eur. Conf. Antennas Propag. (EUCAP)*, Rome, Italy, 11-15 Apr. 2011, pp. 2992–2996.

[8] G. Andia Vera, A. Georgiadis, A. Collado, and S. Via, "Design of a 2.45 GHz rectenna for electromagnetic (EM) energy scavenging", in *Proc. Radio Wireless Symp.*, New Orleans, LA, USA, 10-14 Jan. 2010, pp. 61–64.

[9] A. Nimo, D. Grgic, and L. M. Reindl, "Optimization of passive low power wireless electromagnetic energy harvesters", *Sensors*, vol. 12, no. 10, pp. 13 636–13 663, 2012.

[10] L. Mateu, C. Codrea, N. Lucas, M. Pollak, and P. Spies, "Human body energy harvesting thermogenerator for sensing applications", in *Proc. Int. Conf. Sensor Technol. Appl.*, Valencia, Spain, 14-20 Oct. 2007, pp. 366–372.

[11] L Francioso, C De Pascali, I Farella, C Martucci, P Creti, P Siciliano, and A Perrone, "Flexible Thermoelectric Generator for Wearable Biometric Sensors", in *Proc. IEEE Sensors*, Kona, HI, USA, 1-4 Nov. 2010, pp. 747–750.

[12] M. Lossec, B. Multon, H. Ahmed, and C. Goupil, "Thermoelectric generator placed on the human body: system modeling and energy conversion improvements", *Eur. Phys. J.*, vol. 52, no. 1, pp. 1–10, 2010.

[13] Y Minami and E Nakamachi, "Development of enhanced piezoelectric energy harvester induced by human motion", in *Proc. Annu. Int. Conf. IEEE Eng. Med. Biol. Soc.*, San Diego, CA, USA, 28 Aug. - 1 Sept. 2012, pp. 1627–1630.

[14] Y. Yang, J. Yeo, and S. Priya, "Harvesting energy from the counterbalancing (weaving) movement in bicycle riding", *Sensors*, vol. 12, no. 8, pp. 10 248–10 258, 2012.

[15] V. Leonov, C. Van Hoof, and R. J. M. Vullers, "Thermoelectric and hybrid generators in wearable devices and clothes", in *Proc. 6th Int. Workshop Wearable Implantable Body Sensor Netw.*, Berkeley, SA, USA, 3-5 Jun. 2009, pp. 195–200.

[16] H. Yu, Y. Li, Y. Shang, and B. Su, "Design and investigation of photovoltaic and thermoelectric hybrid power source for wireless sensor networks", in *Proc. 3rd IEEE Int. Conf. Nano/Micro Eng. Molecular Syst.*, Sanya, China, 6-9 Jan. 2008, pp. 196–201.

[17] Y. K. Tan and S. K. Panda, "Energy harvesting from hybrid indoor ambient light and thermal energy sources for enhanced performance of wireless sensor nodes", *IEEE Trans. Ind. Electron.*, vol. 58, no. 9, pp. 4424–4435, Sept. 2011.

[18] A. Collado and A. Georgiadis, "Conformal Hybrid Solar and Electromagnetic (EM) Energy Harvesting Rectenna", *IEEE Trans. Circuits Syst. I Reg. Papers*, vol. 60, no. 8, pp. 2225–2234, Aug. 2013.

[19] A. Khaligh, P. Zeng, X. Wu, and Y. Xu, "A hybrid energy scavenging topology for human-powered mobile electronics", in *Proc. 34th Annu. Conf. IEEE Ind. Electron.*, Orlando, FL, USA, 10-13 Nov. 2008, pp. 448–453.

[20] P. Vanveerdeghem, B. Jooris, P. Becue, P. Van Torre, H. Rogier, I. Moerman, and J. Knockaert, "Reducing power consumption in body-centric zigbee communication links by means of wearable textile antennas", in *Proc. 2nd Int. Workshop Meas.-Based Exp. Res. Methodol. Tools*, vol. 4, Dublin, Ireland, 7 May 2013, pp. 1–5.

[21] A. Dierck, H. Rogier, and F. Declercq, "A Wearable Active Antenna for Global Positioning System and Satellite Phone", *IEEE Trans. Antennas Propag.*, vol. 61, no. 2, pp. 532–538, Feb. 2013.

[22] S. Lemey, F. Declercq, and H. Rogier, "Dual-band substrate integrated waveguide textile antenna with integrated solar harvester", *IEEE Antenn. Wireless Propag. Lett.*, vol. 13, no. 1, pp. 269–272, 2014.

[23] M. A. Hanson, "Body Area Sensor Networks: Challenges and Opportunities", *Computer*, vol. 42, no. 1, pp. 58–65, 2009.

[24] P. Mitcheson, E. Yeatman, G. Rao, A. Holmes, and T. Green, "Energy harvesting from human and machine motion for wireless electronic devices", *Proc. IEEE*, vol. 96, no. 9, pp. 1457–1486, Sept. 2008.

[25] K. Sangani, "Power solar: the sun in your pocket", *Eng. Technol.*, vol. 2, no. 8, pp. 36–38, Aug. 2007.

[26] J. Matiko, N. Grabham, S. Beeby, and M. Tudor, "Review of the application of energy harvesting in buildings", *Meas. Sci. Technol.*, vol. 25, no. 1, pp. 1–25, 2014.

[27] B Markus and H Jurgen, "Flexible solar cells for clothing", *Mater. Today*, vol. 9, no. 6, pp. 42–50, 2006.

[28] R. He, T. D. Day, M. Krishnamurthi, J. R. Sparks, G. V. Sazio P. J., and J. V. Badding, "Silicon P-I-N junction fibers", *Adv. Mater.*, vol. 25, no. 10, pp. 1461–1467, 2013.

[29] A. Bedeloglu, B. Y. Demir A., and N. S. Sariciftci, "A flexible textile structure based on polymeric photovoltaics using transparent cathode", *Synt. Met.*, vol. 159, no. 19-20, pp. 2043–2048, Oct. 2009.

[30] U. Bergqvist, G. Friedrich, Y. Hamnerius, L. Martens, G. Neubauer, G. Thuroczy, E. Vogel, and J. Wiart, "Mobile telecommunication base stations–exposure to electromagnetic fields", Short Term Mission on Base Station Exposure, Cooperation in Science and Technology (COST) 244 bis, 2000.

[31] H. J. Visser, A. C. F. Reniers, and J. A. C. Theeuwes, "Ambient RF Energy Scavenging: GSM and WLAN Power Density Measurements", in *Proc. Eur. Microw. Conf.*, Amsterdam, The Netherlands, 27-31 Oct. 2008, pp. 721–724.

[32] V. Leonov and R. J. M. Vullers, "Wearable thermoelectric generators for body-powered devices", *J. Electron. Mater.*, vol. 38, no. 7, pp. 1491–1498, 2009.

[33] A. Hande, T. Polk, W. Walker, and D. Bhatia, "Indoor solar energy harvesting for sensor network router nodes", *Microprocess. Microsy.*, vol. 31, no. 6, pp. 420–432, 2007.

[34] Infinite Power Solutions, "Wireless environmental sensor energy harvesting evaluation kit", product brief, 2011.

[35] S. Shynu, M. Roo Ons, M. J. Ammann, S. McCormack, and B. Norton, "Dual Band a-Si:H Solar-Slot Antenna for 2.4/5.2 GHz WLAN Applications", in *Proc. 3rd Eur. Conf. Antennas and Propag.*, Berlin, Germany, 23-27 Mar. 2009, pp. 408–410.

[36] M. Danesh and J. Long, "Photovoltaic antennas for autonomous wireless systems", *EEE Trans. Circuits Syst. II, Exp. Briefs*, vol. 58, no. 12, pp. 807–811, Dec. 2011.

[37] H. Visser and R. J. Vullers, "RF energy harvesting and transport for wireless sensor network applications: Principles and requirement", *PRoc. IEEE*, vol. 1001, no. 6, pp. 1410–1423, Jun. 2013.

[38] J. Besnoff, T. Deyle, R. Harrison, and M. Reynolds, "Battery-free multichannel digital ECG biotelemetry using UHF RFID techniques", in *Proc. IEEE Int. Conf. RFID*, Penang, Malaysia, 30 Apr.- 2 May 2013, pp. 16–22.

[39] T. Sun, X. Xie, G. Li, Y. Gu, Y. Deng, and Z. Wang, "A two-hop wireless power transfer system with an efficiency-enhanced power receiver for motion-free capsule endoscopy inspection", *IEEE Trans. Biomed. Eng.*, vol. 59, no. 11, pp. 3247–3254, Nov. 2012.

[40] J. Tavares, N. Barreca, H. M. Saraiva, L. M. Borges, F. J. Velez, C. Loss, R. Salvado, P. Pinho, R. Goncalves, and N. Borges Carvalho, "Spectrum opportunities for electromagnetic energy harvesting from 350 MHz to 3 GHz", in *Proc. 7th Int. Symp. Med. Inf. Commun. Technol. (ISMICT)*, Tokyo, Japan: Institute of Electrical & Electronics Engineers (IEEE), 6-8 Mar. 2013, pp. 126–130.

[41] D. Masotti, A. Costanzo, and S. Adami, "Design and realization of a wearable multi-frequency RF energy harvesting system", in *Proc. 5th Eur. Conf. Antennas Propag. (EUCAP)*, Rome, Italy, 11-15 Apr. 2011, pp. 517–520.

[42] A. Costanzo, D. Masotti, and M. Del Prete, "Wireless power supplying flexible and wearable systems", in *Proc. 7th Eur. Conf. Antennas Propag. (EUCAP)*, Gothenburg, Sweden, 8-12 Apr. 2013, pp. 2843–2846.

[43] M. Dini, M. Filippi, A. Constanzo, A. Romani, M. Tartagni, M. Del Prete, and D. Masotti, "A fully-autonomous integrated RF energy harvesting system for wearable applications", in *In Proc. Eur. Microw. Conf. (EuMC)*, Nuremberg, Germany, 6-10 Oct. 2013, pp. 987–990.

[44] U. Olgun, C.-C. Chen, and J. L. Volakis, "Investigation of Rectenna Array Configurations for Enhanced RF Power Harvesting", *IEEE Antenn. Wireless Propag. Lett.*, vol. 10, pp. 262–265, Apr. 2011.

[45] S. Lineykin and S. Ben-Yaakov, "Analysis of Thermoelectric Coolers by a SPICE-Compatible Equivalent-Circuit Model", *IEEE Power Electron. Lett.*, vol. 3, no. 2, pp. 63–66, Jun. 2005.

[46] E. Schwyter, W. Glatz, L. Durrer, and C. Hierold, "Flexible Micro Thermoelectric Generator Based on Electroplated Bi2+xTe3-x", in *Proc. Symp. Design Test Integr. Packag.*, Nice, France, 9-11 Apr. 2008, pp. 46–48.

[47] S. Jo, M. Kim, M. Kim, and Y. Kim, "Flexible thermoelectric generator for human body heat energy harvesting", *Electron. Lett.*, vol. 48, no. 16, pp. 1015–1017, 2012.

[48] V. Leonov, T. Torfs, C. Van Hoof, and R. Vullers, "Wearable self-powered wireless devices with thermoelectric energy scavengers", in *Proc. 2nd Eur. Conf. Smart Syst. Integr.*, Barcelona, Spain, 9-10 Apr. 2008, pp. 1–8.

[49] V. Leonov, T. Torfs, C. Van Hoof, and R. J. M. Vullers, "Smart wireless sensors integrated in clothing: an electrocardiography system in a shirt powered using human body heat", *Sensors Transducers J.*, vol. 107, no. 8, pp. 165–176, 2009.

[50] V. Leonov, R. J. M Vullers, and C. . Van Hoof, "Thermoelectric generator hidden in a shirt with a fabric radiator", in *Proc. 9th Eur. Conf. Thermoelectr.*, Thessaloniki, Greece, 28-30 Sep. 2011, pp. 556–559.

[51] A. Jamthe and D. P. Agrawal, "Approaches for energy harvesting and power management in wireless healthcare sensor networks", *Int. J. Comput. Commun. Eng*, vol. 2, no. 2, pp. 596–600, Sept. 2013.

[52] A. Alnukari, P. Guillemet, Y. Scudeller, and S. Toutain, "Active heatsink antenna for radio-frequency transmitter", *IEEE Trans. Adv. Packag.*, vol. 33, no. 1, pp. 139–146, Feb. 2010.

[53] Advanced Cerametrics Inc., "Power generation of a piezoelectric fiber composite bimorph (PFCB-W14)", datasheet.

[54] N. G. Elvin, A. A. Elvin, and M. Spector, "A self-powered mechanical strain energy sensor", *Smart Mater. Struct.*, vol. 10, no. 2, pp. 293–299, 2001.

[55] S. Roundy, B. Otis, Y.-H. Chee, J. M. Rabaey, and P. Wright, "A 1.9 GHz RF transmit beacon using environmentally scavenged energy", in *Dig. IEEE Int. Symp. Low Power Electr. Devices*, Seoul, Korea, 2003, pp. 1–6.

[56] P. Mitcheson, T. Green, E. Yeatman, and A. Holmes, "Architectures for vibration-driven micropower generators", *J. Microelectromech. Syst.*, vol. 13, no. 3, pp. 429–440, Jun. 2004.

[57] L. Huang, V. Pop, R. De Francisco, R. Vullers, G. Dolmans, H. De Groot, and K. Imamura, "Ultra low power wireless and energy harvesting technologies: An ideal combination", in *Proc. IEEE Int. Conf. Commun. Syst.*, Singapore, 17-19 Nov. 2010, pp. 295–300.

[58] G. Q. Luo, Z. F. Hu, L. X. Dong, and L. L. Sun, "Planar slot antenna backed by substrate integrated waveguide cavity", *IEEE Antennas Wirel. Propag. Lett.*, vol. 7, pp. 236–239, 2008.

[59] W. Yang and J. Zhou, "Wideband Low-Profile Substrate Integrated Waveguide Cavity-Backed E-shaped Patch Antenna", *IEEE Antennas Wirel. Propag. Lett.*, vol. 12, pp. 143–146, 2013.

[60] A. Georgiadis, G. Vera Andia, and A. Collado, "Rectenna design and optimization using reciprocity theory and harmonic balance analysis for electromagnetic (EM) energy harvesting", *IEEE Antenn. Wireless Propag. Lett.*, vol. 9, pp. 444–446, 2010.

[61] M. Klemm, I. Locher, and G. Troster, "A novel circularly polarized textile antenna for wearable applications", in *Proc. 7th Eur. Conf. Wirel. Tech.*, Amsterdam, The Netherlands, 11-12 Oct. 2004, pp. 285–288.

[62] R. Moro, S. Agneessens, H. Rogier, and M. Bozzi, "Wearable textile antenna in substrate integrated waveguide technology", *IET Electron. Lett.*, vol. 48, no. 16, pp. 985–987, Aug. 2012.

[63] P. Mitcheson, "Energy harvesting for human wearable and implantable biosensors", in *Proc. IEEE Conf. Eng. Med. Biol. Soc.*, Buenos Aires, Argentina, 31 Aug. - 4 Sept. 2010, pp. 3432–3436.

[64] Infinite Power Solutions, "Thinergy MEC225: Solid-state, flexible, rechargeable thin-film micro-energy cell", datasheet, 2012.

[65] Maxim Integrated, "MAX17710: Energy-harvesting charger and protector", datasheet, 2013.

[66] Linear Technology Coorporation, "LTC3108 ultultra voltage step-up converter and power manager", datasheet, 2009.

[67] C. J. Udalagama, "Electrical energy generation from body heat", in *Proc. IEEE Int. Conf. Sustain. Energy Technol. (ICSET)*, Kandy, Sri Lanka, 6-9 Dec. 2010, pp. 1–5.

[68] PowerFilm, "PowerFilm Solar Cell: SP3-37 Flexible Solar Panel", datasheet, 2009. [Online].

[69] ——, "PowerFilm Solar Cell: SP4.2-37 Flexible Solar Panel", datasheet, 2009.

[70] Laird Technologies, "UltraTECTM series UT15,288,F2,5252 Thermoelectric module", *Datasheet, 2009.*,

[71] ——, "UltraTECTM series UT6,24,F1,5555 Thermoelectric module", datasheet, 2011.

[72] A. I. Casian, "Thermoelectrics Handbook: Macro to Nano", D. M. Rowe, Ed. London, U.K.: CRC Press, 2006.

[73] A. Yadav, K. Pipe, and M. Shtein, "Fiber-based flexible thermoelectric power generator", *J. Power Sources*, vol. 175, no. 2, pp. 909–913, 2008.

7

Wearable, Flexible, Light-Weight Modular RFID Tag with Integrated Energy Harvester

Sam Lemey, Sam Agneessens, Patrick Van Torre, Kristof Baes, Jan Vanfleteren, and Hendrik Rogier

Published in the IEEE Transactions on Microwave Theory and Techniques

★ ★ ★

A novel wearable radio-frequency identification (RFID) tag with sensing, processing, and decision-taking capability is presented for operation in the 2.45-GHz RFID super high frequency (SHF) band. The tag is powered by an integrated light harvester, with a flexible battery serving as energy buffer. The proposed active tag features excellent wearability, very high read range, enhanced functionality, flexible interfacing with diverse low-power sensors, and extended system autonomy through an innovative holistic microwave system design paradigm that takes antenna design into consideration from the very early stages. Specifically, a dedicated textile shorted circular patch antenna with monopolar radiation pattern is designed and optimized for highly-efficient and stable operation within the frequency band of operation. In the process, the textile antenna's functionality is augmented by reusing its surface as an integration platform for light-energy-harvesting, sensing, processing, and transceiver hardware, without sacrificing antenna performance or the wearer's comfort. The RFID tag is validated by measuring its stand-alone and on-body characteristics in free-space conditions. Moreover, measurements in a real-world scenario demonstrate an indoor read range up to 23 m in non-line-of-sight indoor propagation conditions, enabling interrogation by a reader situated in another room. In addition, the RFID platform only consumes 168.3 μW, when sensing and processing are performed every 60 s.

7.1 Introduction

In the near future, it is expected that the Internet of Things (IoT) paradigm will step out of its infancy [1], [2], fueled by the adaptation of a variety of key-enabling technologies such as Radio-Frequency Identification (RFID) [3], wireless sensor networks (WSN) [4], [5] and wireless power transfer (WPT) [6], [7]. The integration into the internet of everyday objects, devices, and garments equipped with sensing, processing, and wireless communication capabilities will revolutionize many aspects of everyone's daily life [8]. Smart-fabric interactive-textile (SFIT) systems, in which unobtrusive integration of electronic components increases functionality of the garment [9], [10], play an important role within the vision of the IoT [8]. They will experience a significant growth in diverse application areas in the coming years [11], such as critical professional applications [12]–[14], healthcare [2], [15], [16] and sports [17]. Yet, to accelerate the pervasive deployment of the IoT, it is necessary to combine the potential of diverse, complementary, key-enabling technologies [18]–[22].

Several research efforts in the past few years have pushed passive RFID beyond simple barcode replacement to enhanced RFID tags. These combine the potential of WSN and RFID technology to implement identification, sensing, arbitrary processing, data logging, and actuation functionality [22]–[26]. Integrating such an enhanced RFID/WSN tag within a garment will leverage pervasive quantification of the wearer's interaction with its environment by wirelessly communicating

physical information about the wearer and his/her environment to the internet via a question-and-reply protocol. This, however, introduces novel, stringent design requirements. First, the enhanced RFID tag functionality and larger operating range make system autonomy one of the major critical design constraints [21], [23]. Powering enhanced RFID tags exclusively by RF energy transmitted by RFID readers restricts data logging, sensing and computational operations to the coverage range of the RFID reader [23], [27]. Reliability, functionality and operation range may be increased [9], [23] by combining an antenna with high radiation efficiency and tailored radiation pattern [9], [28] with energy harvesters relying on ambient sources, such as vibration [29], kinetic [17], solar [23], [30], or RF energy [26]. Second, enhanced RFID tags for body-worn applications must be low-profile, light-weight and mechanically flexible, allowing unobtrusive integration [28]. Moreover, the tag should maintain its performance in proximity of the human body and under harsh operating conditions [31]. Finally, unwanted absorption of radiation by the human body should be minimized to prevent potential health threats [32].

In this chapter, we introduce an innovative holistic RFID tag design paradigm for body-worn applications that takes antenna design into consideration from the very early stages. Adopting this paradigm leverages a new highly-integrated, compact, low-profile RFID tag that combines excellent wearability with very high read range, enhanced functionality, and extended system autonomy. This active RFID tag is flexible, compact, low-profile, light-weight and modular. It is equipped with sensing, processing, and decision-taking capability. The tag operates in the 2.45-GHz RFID super high frequency (SHF) band and envisions communication with a smart floor/ceiling [18], [33]. In this scenario, one or multiple RFID readers are integrated into the ceiling/floor of the building in which the wearer is walking around. Embedded software implements a novel protocol that logs sensor data to support the decision-taking process implemented on the node, in the meantime reducing energy consumption. An integrated light energy harvester further increases system autonomy, whereas an integrated flexible battery allows the tag to remain fully operative in the absence of light.

Current literature features a plethora of passive (battery-less) wearable, flexible RFID tags, based on novel implementation/manufacturing technologies, such as conductive thread embroidery on textile substrates [34], [35], substrate integrated waveguide technology on textile [31], and inkjet-printing with conductive ink [17]. In contrast, the tag described here possesses more functionality and a much larger communication range compared to these passive RFIDs. The wearable RFID tag that is the most closely related to our proposed RFID platform in terms of functionality is the one proposed in [28]. However, as the tag in [28] is exclusively powered by the RFID reader, a read range of only 4 m is achieved, provided that the RFID reader transmits at a 30 dBm power level. In contrast, our tag features an indoor read range up to 23 m when three brick walls are in between both link ends and enables communication with a reader at an overhead floor, through a reinforced concrete floor. Therefore, our tag only consumes 168.3 μW

of power, when sensing and processing are performed every 60 s, yielding a system autonomy of 138 days in complete absence of light, provided that the battery was fully charged. Hence, our design significantly reduces the required amount of RFID readers to cover an entire building.

The remainder of this chapter is organized as follows. Section 7.2 describes the design and fabrication of our wearable, light-energy-harvesting assisted RFID based sensing, processing, and decision-taking platform. First, the design approach and system architecture are outlined. Next, we elaborate on the implementation of each subsystem (including the novel textile antenna). Finally, the fabrication of the RFID tag is discussed. In Section 7.3, experimental results as well as practical measurements are presented to validate simulation results and to demonstrate our platform's performance in terms of energy-harvesting potential, power consumption, communication distance, and antenna performance. Section 7.4 concludes this chapter.

7.2 Wearable, light energy-harvesting RFID based sensing platform design

7.2.1 Design considerations and requirements

The wearable RFID tag must not affect the comfort of the wearer under any circumstance. This does not only require a low-profile, flexible and light-weight design, enabling unobtrusive integration, but also demands energy-efficient operation to avoid the discomfort of (frequent) battery recharging. Furthermore, a robust, stable and long-range wireless communication link is desired to provide the wearer with the highest possible freedom of movement, without being out of read range. To meet these stringent requirements, a holistic microwave system design paradigm is adopted, in which antenna design is taken into consideration from the very early stages. Indeed, as the antenna performs a vital task within the wireless tag, an inappropriate design of this component will inadvertently lead to short communication range, poor energy efficiency (quickly draining batteries) and discomfort to the user [28].

7.2.2 System architecture

Fig. 7.1 shows a block diagram of the light-energy-harvesting RFID based sensing platform that fulfills the requirements stated in Section 7.2.1. Fig. 7.1 also illustrates our design approach. A circular patch antenna, designed to operate with maximum total efficiency in the 2.45 GHz RFID SHF band, serves as an integration platform for a flexible photovoltaic (PV) module, with the power management system (including energy storage) and sensing, processing and transceiver hardware integrated on its feed plane. This topology, implemented in appropriate materials, yields a wearable, highly-integrated, and low-profile antenna, realizing

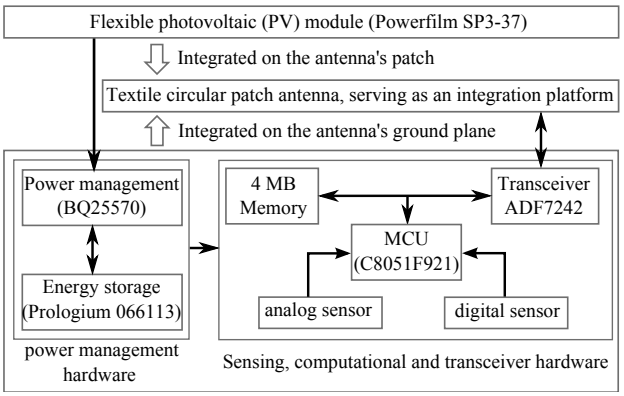

Figure 7.1: Block diagram of the wearable, light-energy-harvesting RFID based sensing platform.

a robust, efficient, and long-range wireless communication link. The implementation of each block, as well as the component selection, is discussed into more detail in Sections 7.2.3 to 7.2.5. The fabrication of the entire system is described in Section 7.2.6.

7.2.3 Textile antenna design and fabrication

A mobile user prefers a compact antenna for inconspicuous integration, whereas an antenna engineer will opt for larger dimensions (in the order of half a wavelength) to obtain better overall performance. A good design must reconcile these two conflicting demands to achieve optimal system performance with manageable dimensions. In addition, as our design is envisioned for communication with a smart floor/ceiling, in which an interrogator is located at either low or high elevation angles, an antenna with a radiation pattern where these angles of arrival are well-received is required. This rules out conventional patch antennas, a popular choice for body-worn applications as their main direction of radiation is orthogonal to the user and not directed towards the floor or ceiling. Yet, high body-antenna isolation should be pursued to prevent antenna detuning caused by the presence of the human body. Finally, the adopted antenna topology and implementation technology must enable straightforward integration of carefully-selected active low-power electronics (transceiver, microcontroller, etc.) that implement the desired functionality (such as logging sensor data, processing, and decision-taking), and appropriate energy harvesters which further increase system autonomy, without performance degradation or discomfort for the wearer. From the RFID designer's point of view, a large antenna can provide interesting possibilities, as its area may be reused to integrate the complete system [36], [37].

To this end, a low-profile topology implemented in low-cost, light-weight, and flexible textile materials is selected, based on [38]. The topology consists of a

circular patch with four shorting vias, connecting the patch to the ground plane. The antenna is fed by a probe in the center. Fig. 7.2 depicts the tag's geometry. The shorting posts enable the excitation of the TM_{22} mode, which gives the antenna a monopole-like radiation pattern, allowing reliable communication between a body-worn node and an interrogator located in a smart floor/ceiling.

The most important parameters for antenna optimization are the position of the shorting posts (R_s) and the radius of the patch (R_p). The size of the patch has a significant influence on the resonance frequency, while the position of the shorting posts can be adjusted to improve the matching to 50 Ω (Fig. 7.3). Furthermore, Fig. 7.4 depicts the simulated radiation pattern at 2.45 GHz, when the patch is deployed in the center of a ground plane of size $W_{GND} = L_{GND} = 113$ mm, and for the ground plane dimensions depicted in the caption of Fig. 7.2. Observe that, by shrinking the width of the ground plane, while keeping the length sufficiently large, the antenna can be made more compact, without reducing sensitivity in the direction of the floor and ceiling (i.e in the YZ-plane ($\varphi = 90°$)).

System integration can be improved by carefully selecting the fabrication materials. A low-cost protective textile foam ($\epsilon_r = 1.42$ and $\tan\delta = 0.016$ at 2.45 GHz, $H_{SUB} = 3.94$ mm [39]) is used as antenna substrate to achieve sufficient bandwidth, while guaranteeing a low-profile, flexible and light-weight antenna design. The conductive patch and ground plane are fabricated from conductive textile materials (surface resistivity $R_s = 0.18\ \Omega/sq$ [39]), which are laminated to the dielectric antenna substrate by means of thermally-activated glue. Hollow, brass eyelets realize the shorting connections between ground plane and antenna patch. They are manually fixed with a hand press. Antenna optimization is performed by full-wave electromagnetic simulations in CST Microwave Studio. The final dimensions can be found in the caption of Fig. 7.2. The simulated performance of the antenna, in terms of impedance matching and radiation pattern, is shown in Fig. 7.7 and Fig. 7.8, respectively.

As radiation originates only from the radiating edge of the patch, a low-profile object can be placed on the patch without altering the antenna's operation. Furthermore, the eyelets applied to make the shorting connection between the patch and the ground plane, are hollow, which makes it possible to rout wires from the front side of the tag (top of the antenna patch) to the backside (behind the ground plane). Hence, the topology allows for easily integration of a PV module on top of the patch. It can easily be connected to a power management circuit, placed underneath the antenna.

The directional nature of the radiation pattern is another asset of this topology. The ground plane directs all radiation towards one hemisphere and shields the other side from the radiating parts. Thereby, it enables the placement of electronics behind the ground plane, where they are not exposed to the radiated electromagnetic fields of the antenna. Additionally, the antenna is not influenced by the presence of the electronics or a human body in its near field, resulting in robust and reliable performance.

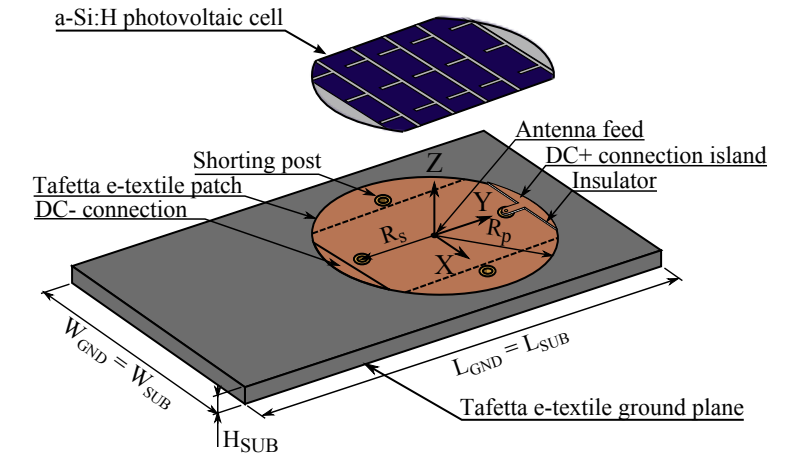

(a)

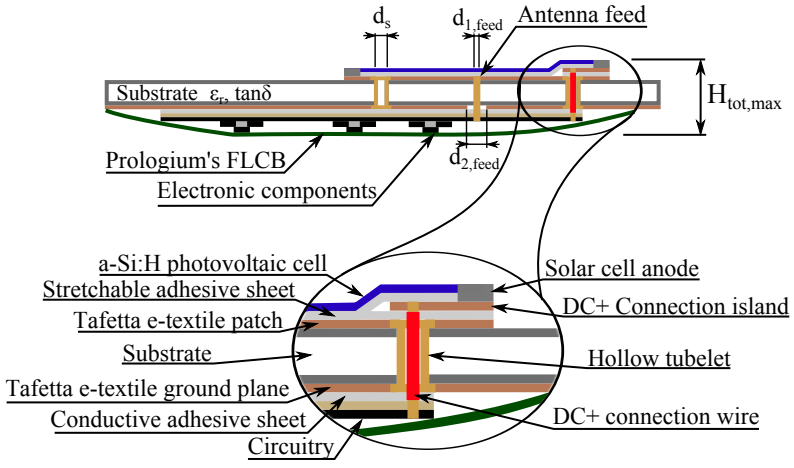

(b)

Figure 7.2: Wearable, light energy-harvesting RFID based sensing platform, consisting of a circular patch antenna with four shorting tubelet posts, on which a flexible a-Si:H PV module is integrated onto its antenna patch and power management, sensing, processing, and transceiver hardware are integrated onto its ground plane (R_s = 19.75 mm, d_s = 2 mm, R_p = 27.5 mm, $d_{1,feed}$ = 1.3 mm, $d_{2,feed}$ = 4.6 mm, H_{SUB} = 3.94 mm, $W_{GND} = W_{SUB}$ = 66 mm, $L_{GND} = L_{SUB}$ = 113 mm, $H_{tot,max}$ = 6.6 mm). (a) Top 3D view. (b) Cross-sectional view with enlarged inset.

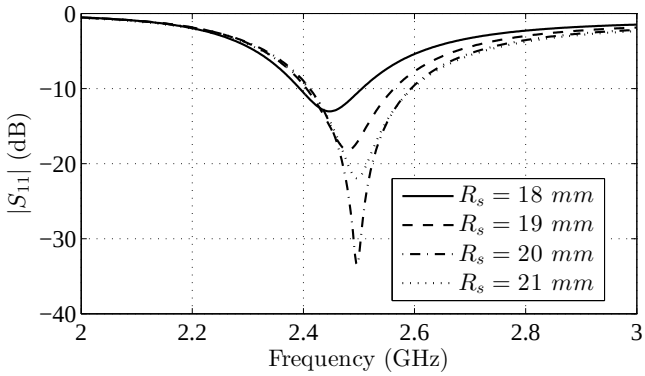

Figure 7.3: Effect of the position of the shorting posts (R_s) on the antenna's reflection coefficient.

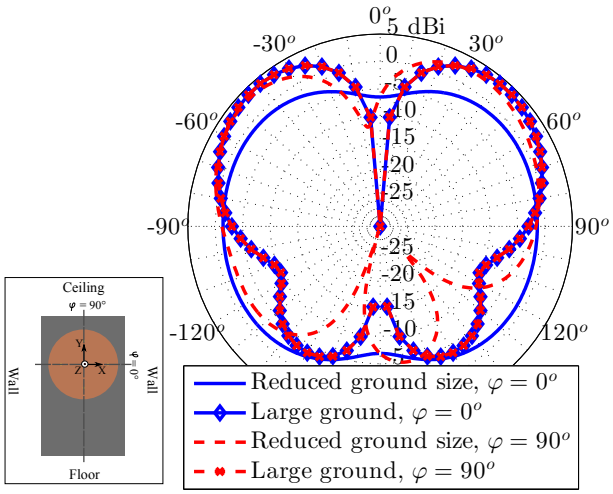

Figure 7.4: Effect of ground plane size on the antenna's radiation pattern.

7.2.4 Sensing, computational and transceiver hardware

As shown in Fig. 7.1, the advanced low-power C8051F921 microcontroller by Silicon Laboratories is selected to form the heart of the sensing, processing, and transceiver hardware. The lowest-power sleep mode is employed in this design. The microcontroller contains a SmaRTClock, which is a real-time clock performing cyclic wake-up from sleep mode. According to the specifications, the microcontroller chip consumes less than 1 μA of supply current in sleep mode, with the

SmaRTClock running. Different sensors may be connected to this microcontroller through analog as well as digital inputs. The device is programmed in the C language and contains all the software to control the wireless transceiver together with the sensors. Moreover, it implements the node's low-power algorithm.

An Analog Devices ADF7242 transceiver is applied for communication in IEEE802.15.4 mode [40]. The wireless transceiver exchanges data with the microcontroller over a Serial Peripheral Interface (SPI). Also the ADF7242 can be configured in a low-power sleep mode, reducing its supply current to less than 1 μA, provided that all oscillators are shut down. The ADF7242 transceiver's RF output port, characterized by a complex chip impedance Z_{chip} = (74.3 - 10.7 j) Ω at 2.45 GHz, is conjugate matched to the 50 Ω antenna feed via a Johansson Technology 2450BM14E0007 balun.

A 1 MB Microchip 25AA1024 serial EEPROM memory is also included for nonvolatile data storage. Sensor measurements can be logged here and a history of measurements can be requested at the time of interrogation. The EEPROM memory can also be put in a deep power-down mode, such that it consumes a little over 1 μA of supply current when it is not operational.

Employing a state-of-the-art transceiver component allows reliable communication over a long range [41]. The microcontroller provides plenty of sensor connectivity and can be conveniently configured to process sensor data in real time. Digital sensors can be connected via a SPI or I^2C bus. Analog sensors can also be directly connected, as the microcontroller contains a 10-bit Analog to Digital Converter (ADC). Local processing of the sensor data for unit conversions, filtering or statistical processing is possible, providing a reduction in the amount of data to be transmitted. A large nonvolatile storage capacity is available for measurement data.

Since all selected components provide a low-power mode, a very low average supply current is achieved, enabling extended battery-supported operation.

7.2.5 Energy-harvesting and power management hardware

Powerfilm's ultrathin (200 μm) and ultraflexible SP3-37 hydrogenated amorphous silicon (a-Si:H) PV ambient light energy harvesting transducer [23], positioned on top of the antenna, is connected to the power management subsystem, located on the node's feed plane. This particular PV module is selected because of four multidisciplinary reasons. First, the SP3-37 harvester exhibits a broad spectral response, not only enabling energy harvesting from solar light, but also from the most frequently available light sources in an indoor environment [9], [23]. More specifically, the SP3-37 PV module is characterized by a maximum output voltage of 3.0 V at 22 mA under full sunlight (107 527 Lux) and a maximum output voltage of 2.5 V at 100 μA under typical office lighting (330 Lux) [23]. Second, its flex-

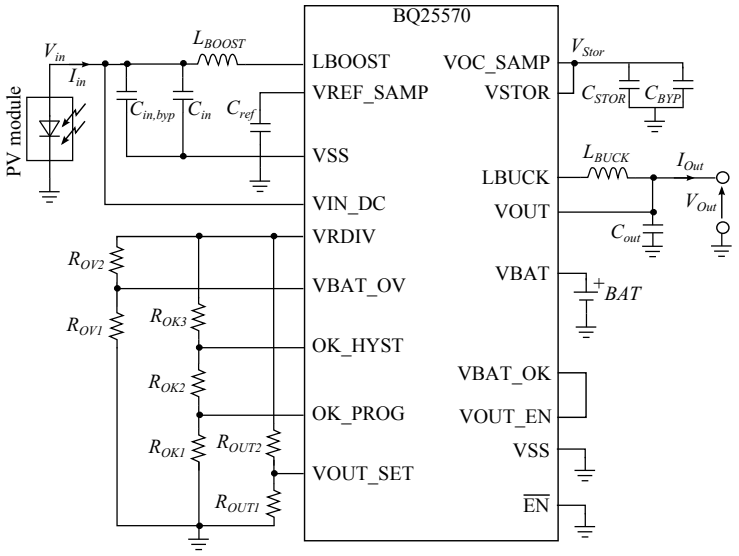

Figure 7.5: Circuit schematic of the energy-harvesting and power management hardware ($C_{in,byp} = 100$ nF, $C_{in} = 4.7$ μF, $C_{ref} = 10$ nF, $C_{STOR} = 4.7$ μF, $C_{BYP} = 100$ nF, $C_{out} = 44$ μF, $L_{BOOST} = 22$ μH, $L_{BUCK} = 10$ μH, $R_{OV1} = 5.62$ MΩ, $R_{OV2} = 7.32$ MΩ, $R_{OK1} = 3.83$ MΩ, $R_{OK2} = 7.5$ MΩ, $R_{OK3} = 680$ kΩ , $R_{OUT1} = 4.64$ MΩ and $R_{OUT2} = 8.25$ MΩ).

ible and ultrathin structure permits a conformal and low-profile integration [42]. Third, the SP3-37 is manufactured through a low-cost roll-to-roll printing process, making it compatible with current RFID production processes [23]. Finally, the harvester's relatively small size, and the ease of patterning the solar cell's surface to fit the antenna patch contours, facilitate the integration procedure.

For a given PV module at a specific temperature, the instantaneous generated power depends on the spectral composition, incident angle, and intensity of the light impinging on the PV module [9]. This requires a power management system that converts the highly fluctuating, and often small, levels of harvested light energy into a form useful for adequately powering the node. To this end, the Texas Instruments bq25570, an integrated energy-harvesting nano-power management system (Fig. 7.5), is applied. This integrated circuit (IC) implements two highly efficient conversion stages. The first stage encompasses a pulse-frequency modulated (PFM) boost converter charger, with maximum power point tracking (MPPT) capability, to efficiently store the energy generated by the energy-harvesting transducer in a suitable energy storage device. During the charging process, the energy storage component is protected from overcharging by disabling the boost converter once the voltage at VBAT (Fig. 7.5) exceeds 4.18 V, set by selecting the proper values for R_{OV1} and R_{OV2}. As the PV module's maximum output power fluctuates in ambient light conditions, the fractional open circuit (FOC) algorithm is adopted

to optimize power transfer from the PV unit to the energy storage device. This means that the bq25570 periodically (every 16 seconds) samples the open circuit input voltage of the PV module, by disabling the boost converter for 256 ms, and determines the maximum power point (MPP) during that particular time interval. In this work, the boost converter is configured to subsequently load the light energy-harvesting transducer until its voltage drops to 80% of the sampled open circuit voltage. This periodic update continually maximizes power delivery in real time, based on the harvesting conditions. The second conversion stage consists of a highly efficient, nano-power PFM buck converter, providing a regulated power supply to the sensing, processing and transceiver hardware. In this work, the buck converter/output regulator is set by means of R_{OUT1} and R_{OUT2} to provide a regulated output voltage of 3.36 V. Yet, to prevent overdischarging, the output voltage is disabled when VBAT (Fig. 7.5) drops below 3.60 V. It is only turned back on after the VBAT voltage exceeds 3.82 V. Both voltage levels are set by means of the voltage divider formed by R_{OK1}, R_{OK2} and R_{OK3}. The other passive components are dimensioned to obtain the highest possible efficiency for both conversion stages of the IC.

The availability of ambient light will often be sporadic or time-varying, thereby necessitating some type of energy storage element. Such a storage element will not only ensure that the required power is available when needed by the node, but will also handle peak currents that cannot directly be delivered by the PV module. The single cell version of Prologium's 066113 Flexible Printed Circuit Lithium Ceramic Battery (FLCB) is selected as the node's energy storage element. This FLCB cell is only 380 μm thick and covers an area of 113 mm x 66 mm. It exhibits a nominal capacity of 170 mAh and allows a maximum discharge current of 120 mA. The FLCB technology is selected because it exhibits favorable electrical properties, such as high energy density and good pulse discharge. Moreover, it can be manufactured through a roll to roll printing production process, reducing manufacturing cost. Furhermore, its ability to dynamically bend and/or twist, without reducing cycle life nor electrical performance, in combination with its ultrathin (380 μm) profile, facilitates integration on the textile antenna without significantly increasing its overall thickness or significantly reducing the overall conformality. In addition, the FLCB technology does not exhibit leakage, catch fire or explode after physical abuse (nail penetration, excessive vibrations, drop test, ...), after thermal test conditions up to 250°C or after electrical abuse (overcharging, reverse charging, and short circuiting), demonstrating its ability to be safely worn on the human body, even in harsh environments.

7.2.6 Integration procedure

Once the textile antenna is fabricated according to Section 7.2.3, the flexible PV module is glued on top of the antenna patch by means of stretchable, nonconductive adhesive sheets, as illustrated in Fig. 7.2. To maintain the antenna's excellent performance after solar cell integration, the PV module is patterned to fit the an-

tenna patch contours and placed in such a way that the radiating edge remains uncovered. Furthermore, the PV module is modified to facilitate the connection of its DC-terminals from its bottom side. The negative DC terminal of the PV module is directly connected to the antenna patch, acting as a DC ground. The positive DC terminal is connected to a DC connection island, fabricated out of pure copper-coated e-textile and isolated from the antenna patch by means of a non-conductive adhesive sheet, as depicted in the enlarged inset shown in Fig. 7.2(b). The DC connection island is connected to the power management system via a wire routed through one of the hollow tubelets. These measures not only reduce the number and length of interconnecting wires, but also prevent that interconnections influence the radiation characteristics of the antenna, resulting in a more robust design and improved comfort for the user.

Next, we integrate the processing, power management and transceiver hardware. These components are implemented on a compact, low-profile, polyimide flexible circuit board (FCB), as in [9], [39], [41]. To maintain flexibility, small electronic components were selected and distributed over a sufficiently large area to allow for small bending radii. Furthermore, special care was taken to avoid vias, whenever possible, and to position components on only one side of the FCB. This leads to a circuit bottom layer that almost entirely consists of a copper ground plane. The FCB is then integrated onto the antenna's feed plane by means of a conductive adhesive sheet, bonding the antenna ground plane with the circuit ground plane, as shown in Fig. 7.2(b). This approach allows using the antenna as a common DC ground and yields excellent shielding between the antenna patch and the active circuitry, owing to the ground plane.

As the antenna's ground plane is slightly larger than Prologium's 066113 FLCB, integration of the FLCB at the antenna's backside, as shown in Fig. 7.2(b), will not affect the antenna's radiation performance. Moreover, its ultrathin profile only adds 380 μm to the total thickness of the entire stack. The FLCB's cathode is directly connected to the antenna's ground plane, acting as a common DC-ground, whereas its anode is connected to the power management subcircuit. A prototype of our wearable, light-energy harvesting assisted RFID based sensing platform is depicted in Fig. 7.6. The figure shows that we have connected a HDC1000 low power humidity and temperature sensor by Texas instruments, implemented on a FR4 printed circuit board (PCB), via the I^2C bus, as a proof of principle. In a future design, this sensor may be directly implemented on the FCB as well. The sensor was selected as temperature and humidity are key parameters in diverse medical environments, for instance to assess the integrity of drugs or to detect the arise of an epidemic source producing fever rush [2].

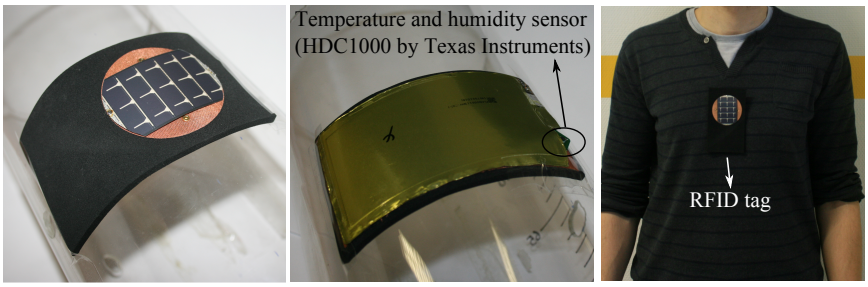

Figure 7.6: Prototype of the wearable, RFID tag with integrated light harvester (top) and flexible battery (bottom). (a) Top view: bending diameter = 15 cm. (b) Bottom view: bending diameter = 15 cm. (c) On-body deployment.

7.3 Measurement results

7.3.1 Textile antenna performance

To validate the antenna performance and the integration procedure, the antenna's figures of merit are measured under different operating conditions. First, the antenna performance is analyzed before and after the integration of the additional light-energy-harvesting, power management, sensing, processing, and transceiver hardware. Afterwards, the antenna performance is measured when deployed on the human body. All measurements are conducted in an anechoic room, where external interferers are absent.

Impedance matching to a 50 Ω source is validated by means of an Agilent PNA-X vector network analyzer. The antenna should have good impedance matching ($|S_{11}|$ < -10 dB) around the 2.45 GHz center frequency, irrespective of the operating condition. Comparison of the measured reflection coefficients in Fig. 7.7, demonstrates stable results for all different conditions with an impedance bandwidth of more than 150 MHz or 6.1%. In addition, a good agreement with the simulated curve is observed.

The gain pattern and how it is affected by the different operating conditions are also evaluated. Fig. 7.8 shows the simulated and measured radiation patterns for the $\varphi = 0°$ and $\varphi = 90°$ cross-sections. It is seen that the antenna exhibits a monopolar radiation pattern with most of the radiation directed towards the ceiling and the floor ($\varphi = 90°$). In contrast, due to the smaller ground plane size, there is less radiation towards the walls ($\varphi = 0°$), with a gain difference of approximately 4 dB. In the stand-alone scenario, a measured maximum gain of 3.3 dBi at the direction $(\theta, \varphi) = (-40°, 90°)$, a 3dB-beamwidth of more than 50° and a total efficiency of 66% is obtained.

Fig. 7.9 shows the radiation pattern at 2.45 GHz before and after integration of the

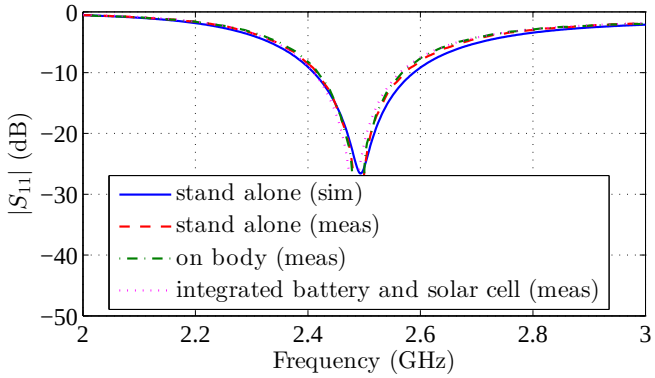

Figure 7.7: Reflection coefficients of the textile antenna, under free-space conditions, to validate the integration procedure and its on-body performance.

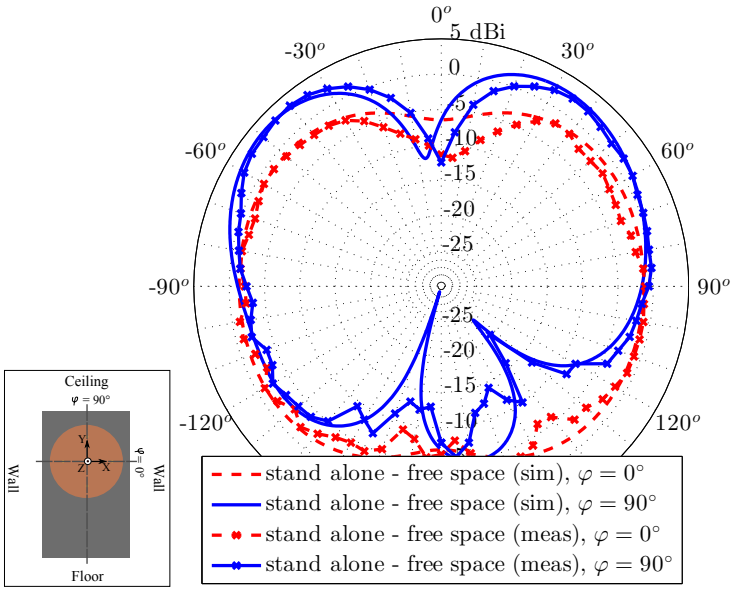

Figure 7.8: Simulated and measured radiation pattern of the stand-alone textile antenna at 2.45 GHz.

light-energy-harvesting, power management, sensing, processing and transceiver hardware. When integrating the solar cell on top and the flexible battery behind the antenna, the radiation pattern remains stable, with a maximal measured gain of

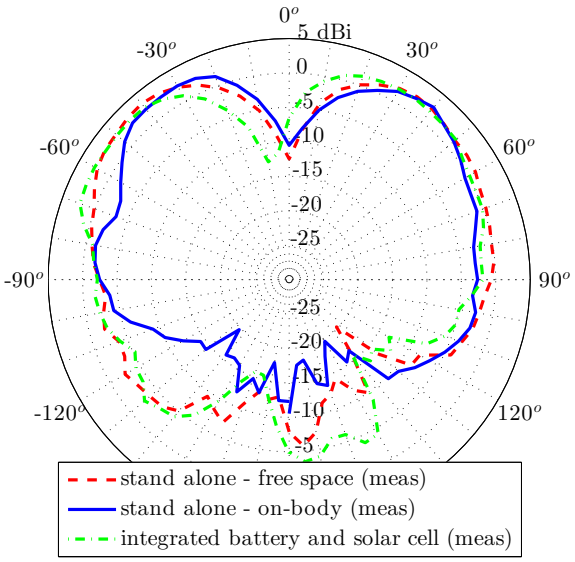

Figure 7.9: Measured radiation pattern of the textile antenna at 2.45 GHz, under free-space conditions, to validate the integration procedure and its on-body performance.

2.7 dBi and an efficiency of 65%. It is noted that the integrated radiation pattern is slightly rotated w.r.t the stand-alone and on-body cases, which is caused by a small alignment error during measurement. Despite this, it can clearly be seen that the shape and absolute values of the patterns remain very stable. The design also performs well in the on-body scenario (Fig. 7.9). The presence of the human body only has a slight influence on the pattern: the direction of maximal gain corresponds to $(\theta, \varphi) = (-20°, 90°)$ with a value of 2.5 dBi and more than 50° 3 dB-beamwidth.

These measurements validate that the antenna remains very stable under the different operating conditions, both in terms of impedance matching and radiation performance.

7.3.2 Light energy-harvesting potential

A Keithley 236 source meter and a solar simulator, with a standardized illumination level of 100 mW/cm^2, were used to measure the DC P-V characteristic of the SP3-37 PV module before and after patterning its surface to fit the antenna patch contour. Fig. 7.10 depicts both curves and shows that the maximum power generated by the PV module reduces from 56.9 mW downto 50.1 mW by modifying its

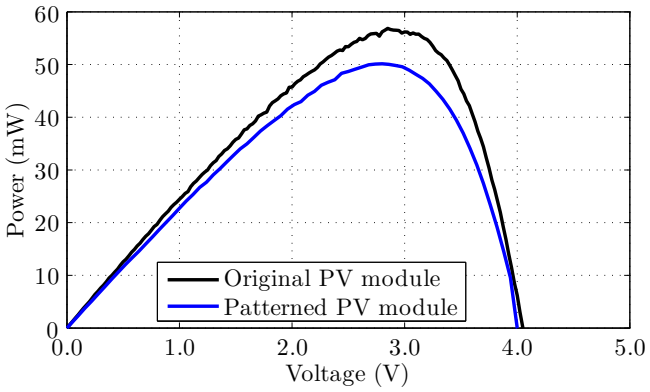

Figure 7.10: DC P-V characteristic of the flexible solar cell, before and after patterning.

surface. This decrease can be attributed to a smaller effective light aperture and shunt resistance after modification.

The boost converter/charger stage of the power management hardware is designed to minimize the required input voltage and power. This enables ambient light energy harvesting in near minimum lighting requirements. For indoor environments, the Occupational Safety and Health Administration specificies these conditions as 150 Lux for a warehouse, 330 Lux for an office and 650 Lux for a supermarket environment [23]. Measurements have demonstrated that the boost charger allows harvesting ambient light energy as long as the PV module is capable of generating a voltage and power level exceeding 110 mV and 6 μW, respectively. This is the case when the patterned PV harvester is illuminated by white LED light at an illumination level higher than 330 Lux, and when illuminated by fluorescent light at an illumination level exceeding 150 Lux.

Next, two Keithley 2400 source meters and a Fluke 45 multimeter were applied to accurately characterize the boost charger and buck regulator efficiency. The boost charger efficiency is depicted in Fig. 7.11, as a function of input current (I_{in}), for different input voltage levels (V_{in}) and V_{Stor} fixed to 3.9 V (Fig. 7.5). Fig. 7.11 demonstrates that the boost charger stage operates more efficiently for larger values of the input voltage. A maximum achievable efficiency of over 90% can be observed in Fig. 7.11. Yet, even for $V_{in} = 0.25$ V, the boost charger efficiency exceeds 70% for input currents larger than 200 μA.

Fig. 7.12 depicts the buck converter/regulator efficiency, as a function of output current (I_{Out}), for a regulated output voltage (V_{Out}) of 3.36V and V_{stor} fixed to 3.9 V (Fig. 7.5). Fig. 7.12 prove that the buck converter regulator is able to guarantee an efficiency higher than 75% from an output current as low as 3.8 μA to output currents exceeding 100 mA.

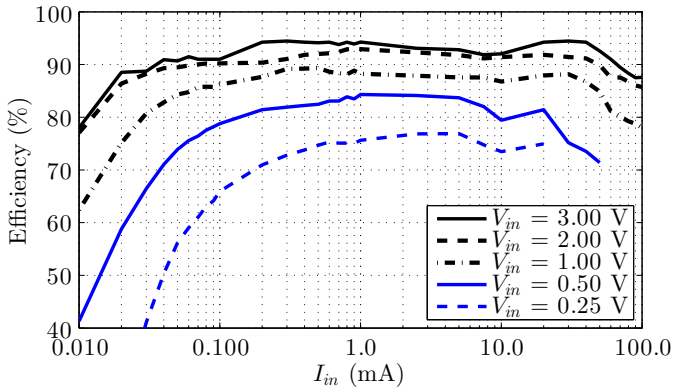

Figure 7.11: Boost charger efficiency as a function of input current (I_{in}) for different input voltage (V_{in}) levels and V_{Stor} fixed to 3.9 V (Fig. 7.5).

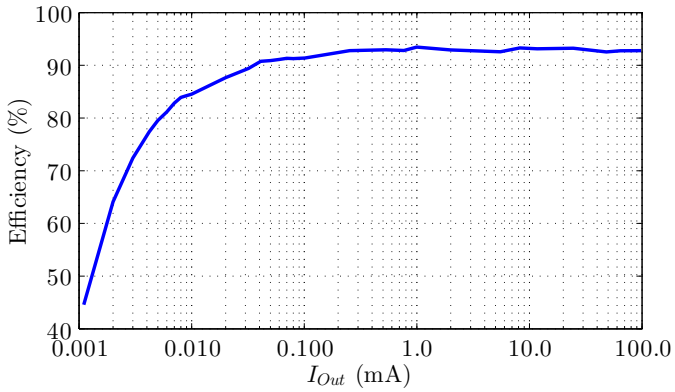

Figure 7.12: Buck regulator efficiency as a function of output current (I_{Out}) for V_{Out} regulated to 3.36 V and V_{stor} fixed to 3.9 V (Fig. 7.5).

7.3.3 Read range

The read range of the RFID sensor system is large enough to enable reading from another room, or another floor in a building. The indoor range has been tested to be up to 23 m in non line-of-sight indoor propagation conditions. Interrogation of nodes, or garments with integrated nodes, which are stored in a standard metal office closet is also possible. A standard closet does not provide enough attenuation to block the communication between the RFID node and the interrogator.

The measurement of the received signal strength (dBm) is performed for the ADF7242 transceiver chip deployed on the RFID node as well as on the interrogator. According to specifications, the minimum required received signal strength to successfully decode IEEE802.15.4 packets is −95 dBm. Table 7.1 lists a number of measured received signal levels in practical conditions. Fig. 7.13 depicts the mea-

surement setup and a floor plan of the real-life environment, with all practical test locations annotated. Line-of-Sight (LoS) measurements are performed within the same room, whereas Non Line-of-Sight (NLoS) conditions imply communication between rooms in the same building. The building is composed of a steel structure with reinforced concrete floors and solid brick walls. At 13 and 23 m, two and three brick walls are in between both link ends, respectively. Communication from the overhead floor is also included, through the reinforced concrete floor. Two measurements of this type are included, one with the RFID node directly overhead on the upper floor, and one with the node 10 m further away from this position.

Table 7.1: Received signal level for different reading scenarios

Transmitter location	Received signal level (dBm)
LoS 1 m	−39.4
LoS 2 m	−41.2
NLoS 5 m	−55.5
NLoS 13 m	−70.4
NLoS 23 m	−85.8
NLoS 1 floor up, overhead	−64.2
NLoS 1 floor up, 10 m off	−75.5

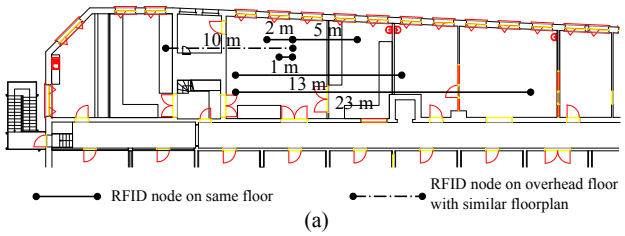

(a)

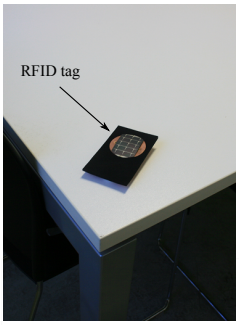

(b)

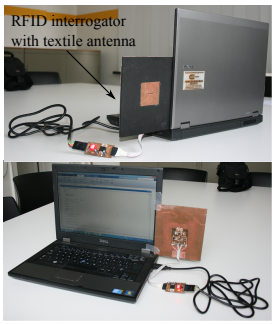

(c)

Figure 7.13: Read range measurement setup. (a) Floorplan with all reading scenarios annotated (Table 7.1). (b) RFID tag. (c) RFID interrogator with textile antenna [41].

7.3.4 Current consumption profile

The average current consumption of the RFID node is controlled by adjusting the amount of time the system is in sleep mode, as in this state, a current of only 8 μA is consumed. Compared to the leakage current of the battery, which is approximately 40 μA, this is a very low power consumption. However, when the node switches to its active state, the current consumption increases up to 35 mA, although this maximum current is only drawn during a period of 5 ms each time the node wakes up.

The current for different operation modes was measured by a Tektronix MSO2014B Mixed Signal Oscilloscope, with a 1 Ω resistor in series with the power supply ground. In Fig. 7.14, the current is displayed during receive mode. During the power-up event, the microcontroller first awakens from sleep mode, causing a current of 5 mA, then the ADF7242 transceiver chip is also awoken from its sleep mode. Some initialization time is necessary for the transceiver before actual packets can be received. As soon as the transceiver operates in receive (RX) mode, a current of 35 mA is consumed. During this mode, the transceiver keeps waiting for a valid packet. However, a time-out is implemented in the software to allow the system to return to sleep mode after a while if no packet is received.

The measured average current consumption during the active period $T_{Active} = 8$ ms is $I_{Active} = 22.45$ mA, yielding for an average current consumption of the system for a wake-up period T_{Sleep}:

$$I_{Avg} = \frac{T_{Active} \cdot I_{Active} + T_{Sleep} \cdot I_{Sleep}}{T_{Sleep} + T_{Active}}, \tag{7.1}$$

with $I_{Sleep} = 8$ μA.

A number of practical values are listed in Table 7.2. In addition, Table 7.2 depicts the system autonomy when complete absence of light is assumed and for two different battery types, being the integrated 170 mAh FLCB battery and a state-of-the-art 5 mm-thick 120 mAh lithium-ion coin cell battery (MULTICOMP LIR2450). In both cases, the battery's leakage current is taken into account, being 40 μA for the FLCB and 11 μA for the coin cell. Note that the coin cell's smaller leakage current yields a higher system autonomy at higher values for the sleep time. Yet, the FLCB is preferred in our design because of its mechanical flexibility and its thinner profile.

A protocol waking up the system every 10 seconds consumes an average supply current of 26 μA, guaranteeing a high system autonomy. In this mode, the system is standing by for interrogation and will answer within maximally 10 seconds. Of course, the interrogating device should rapidly transmit subsequent packets in order to be sure that the node is able to effectively receive a packet during its active receive state of 5 ms duration. If the received packet contains the node's serial number, the node will immediately respond by transmitting a reply packet.

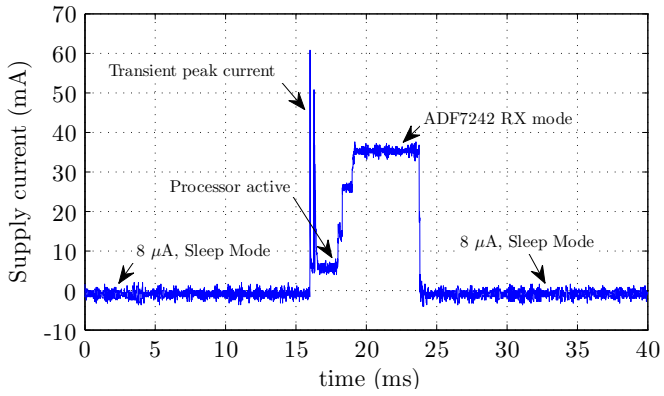

Figure 7.14: Current consumption during receive mode (sleep current was measured by a Fluke 45 multimeter).

Table 7.2: Average current consumption and system autonomy for different sleep periods and for two battery types

Sleep Time (s)	Average Supply Current (μA)	System autonomy (days)	
		FLCB	Coin cell
1	186	31	25
2	97	51	46
5	44	84	90
10	26	107	134
60	11	138	226

We prefer to use a protocol where the sleep period is automatically adjusted when interrogation of other nodes is detected. Receiving a packet intended for interrogation of another node indeed means a higher probability of interrogation in the near future, in which case it is interesting to temporarily reduce the sleep time to one second, in order to allow faster subsequent interrogation of multiple nodes.

Fig. 7.15 shows the current consumption during interrogation of the node. First, the node wakes up from sleep mode, and switches to RX mode, similar to the event shown in the previous Fig. 7.14. However, a packet containing the node's serial number is now received, indicating proper interrogation. After the packet is received, the node returns from RX mode, performing further processing and SPI communication between the processor and transceiver, requiring 12 *mA* of current. Finally, the node responds by transmitting a packet containing sensor data, consuming 27 *mA*.

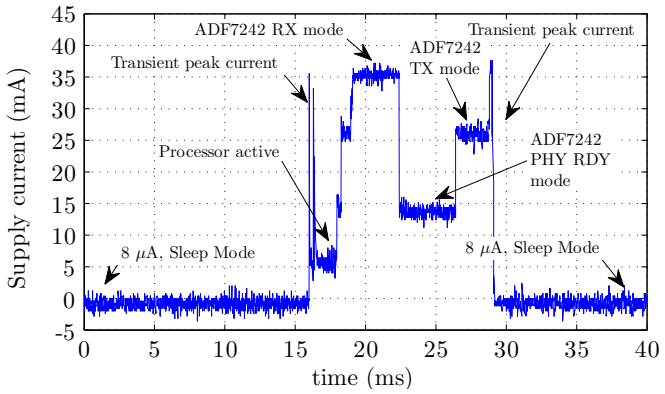

Figure 7.15: Current consumption when the node is interrogated (sleep current was measured by a Fluke 45 multimeter).

7.4 Conclusion

We have discussed the design, realization, and validation of a wearable, light energy-harvesting assisted sensing, processing, and decision-taking RFID tag for operation in the 2.45-GHz RFID SHF band. To the authors' best knowledge, this is the first tag in literature that combines excellent wearability with enhanced functionality, very high read range and extended system autonomy, through a newly introduced holistic microwave system design paradigm, in which antenna design is taken into account from the early beginning. In addition, the tag features flexible interfacing with a wide variety of digital and analog low power sensors, such as accelerometers, light sensors, gas sensors, and temperature sensors. This enables us to adapt our design to a plethora of real-life applications by introducing the appropriate sensor(s). Furthermore, the enhanced RFID node is capable of taking decisions, through processing of logged or real-time sensor data, even in absence of an RFID reader. However, the increased functionality and read range comes at an increased cost and power consumption of the RFID node compared to passive RFID tags, exclusively powered by an RFID reader. Yet, in our design, dedicated embedded software minimizes energy consumption, while system autonomy is further increased by integration of a flexible maximum-power-point-tracking light-energy-harvester. In addition, the higher cost of an individual RFID node does not necessarily lead to a higher cost of the overall system, as the excellent read range of our proposed RFID tag reduces the amount of RFID readers that are needed to cover a specific area. Hence, our design is a step forward in realizing the IoT paradigm. It is particularly suited for unobtrusive integration within a garment, leveraging pervasive quantification of the wearer's interaction with his/her environment, by wirelessly communicating physical information about the wearer and his/her nearby environment to the internet via a question-and-reply protocol.

Acknowledgment

The authors would like to thank Dr. Samira Khelifi from Solar cells Lab, Department of Electronics and Information Systems (ELIS), Gent University, for her valuable help with the PV module measurements, and Dr. Peter Vanveerdeghem for his support in FCB assembly. This work was supported in part by the Inter-University Attraction Poles Program initiated by the Belgian Science Policy Office, by the iMinds IoT research program and by the Research Foundation Flanders (FWO-Vlaanderen).

References

[1] J. Gubbi, R. Buyya, S. Marusic, and M. Palaniswami, "Internet of Things (IoT): A vision, architectural elements, and future directions", *Future Gener. Comp. Sy.*, vol. 29, no. 7, pp. 1645–1660, Sep. 2013.

[2] S. Amendola, R. Lodato, S. Manzari, C. Occhiuzzi, and G. Marrocco, "RFID Technology for IoT-Based Personal Healthcare in Smart Spaces", *IEEE Internet Things J.*, vol. 1, no. 2, pp. 144–152, Apr 2014.

[3] E. Welbourne, L. Battle, G. Cole, K. Gould, K. Rector, S. Raymer, M. Balazinska, and G. Borriello, "Building the Internet of Things Using RFID: The RFID Ecosystem Experience", *IEEE Internet Comput.*, vol. 13, no. 3, pp. 48–55, May 2009.

[4] M. T. Lazarescu, "Design of a WSN Platform for Long-Term Environmental Monitoring for IoT Applications", *IEEE J. Emerg. Sel. Topics Circuits Syst.*, vol. 3, no. 1, pp. 45–54, Mar 2013.

[5] Q. Chi, H. Yan, C. Zhang, Z. Pang, and L. D. Xu, "A Reconfigurable Smart Sensor Interface for Industrial WSN in IoT Environment", *IEEE Trans. Ind. Inf.*, vol. 10, no. 2, pp. 1417–1425, May 2014.

[6] A. Costanzo and D. Masotti, "Wirelessly powering: An enabling technology for zero-power sensors, IoT and D2D communication", in *Microwave Symposium (IMS), 2015 IEEE MTT-S International*, Phoenix, AZ, USA, 17-22 May 2015, pp. 1–4.

[7] N. Borges Carvalho, A. Georgiadis, A. Costanzo, H. Rogier, A. Collado, J. A. Garcia, S. Lucyszyn, P. Mezzanotte, J. Kracek, and D. Masotti, "Wireless Power Transmission: R&D Activities Within Europe", *IEEE Trans. Microwave Theory Techn.*, vol. 62, no. 4, pp. 1031–1045, 2014.

[8] H. Sundmaeker, P. Guillemin, P. Friess, and S. Woelffle, Eds., *Vision and challenges for realising the internet of things.* Luxembourg: Publications Office of the European Union, 2010.

[9] S. Lemey, F. Declercq, and H. Rogier, "Textile antennas as hybrid energy-harvesting platforms", *Proc. IEEE*, vol. 102, no. 11, pp. 1833–1857, Nov. 2014.

[10] A. Dierck, S. Agneessens, F. Declercq, B. Spinnewyn, G.-J. Stockman, P. Van Torre, L. Vallozzi, D. Vande Ginste, J. Vanfleteren, T. Vervust, and H. Rogier, "Active Textile Antennas in Professional Garments for Sensing, Localisation and Communication", *International Journal of Microwave and Wireless Technologies*, vol. 6, no. 3-4, pp. 331–341, 2014.

[11] Markets and Markets, "Wearable electronics and technology market by applications (consumer, healthcare, enterprise), products (eyewear, wristwear, footwear), form factors and geography - analysis & forecast to 2014 - 2020", Tech. Rep., September 2014.

[12] S. Agneessens, P. Van Torre, F. Declercq, B. Spinnewyn, G.-J. Stockman, H. Rogier, and D. Vande Ginste, "Design of a wearable, low-cost, through-wall doppler radar system", *Int. J Antennas Propag*, vol. 2012, pp. 1–9, 2012.

[13] L. Vallozzi, P. Van Torre, C. Hertleer, H. Rogier, M. Moeneclaey, and J. Verhaevert, "Wireless communication for firefighters using dual-polarized textile antennas integrated in their garment", *IEEE Trans. Antennas Propag.*, vol. 58, no. 4, pp. 1357–1368, Apr. 2010.

[14] P. Van Torre, L. Vallozzi, C. Hertleer, H. Rogier, M. Moeneclaey, and J. Verhaevert, "Indoor Off-Body Wireless MIMO Communication With Dual Polarized Textile Antennas", *IEEE Trans. Antennas Propag.*, vol. 59, no. 2, pp. 631–642, Feb 2011.

[15] S. Agneessens, P. Van Torre, E. Tanghe, G. Vermeeren, W. Joseph, and H. Rogier, "On-body wearable repeater as a data link relay for in-body wireless implants", *IEEE Antenn. Wireless Propag. Lett.*, vol. 11, pp. 1714–1717, 2012.

[16] S. Park and S. Jayaraman, "Smart textile-based wearable biomedical systems: a transition plan for research to reality", *IEEE Trans. Inform. Technol. Biomed.*, vol. 14, no. 1, pp. 86–92, Jan 2010.

[17] G. Orecchini, L. Yang, M Tentzeris, and L. Roselli, "Smart Shoe: An autonomous inkjet-printed RFID system scavenging walking energy", in *Proc. IEEE Int. Symp. Antennas and Propagation (APSURSI)*, Spokane, WA, USA, 3-8 Jul. 2011, pp. 1417–1420.

[18] L. Roselli, F. Alimenti, G. Orecchini, C. Mariotti, P. Mezzanotte, and M. Virili, "WPT, RFID and energy harvesting: Concurrent technologies for the future networked society", in *Microwave Conference Proceedings (APMC), 2013 Asia-Pacific*, Seoul, Republic of Korea, 5-8 Nov. 2013.

[19] L. Roselli, N. Borges Carvalho, F. Alimenti, P. Mezzanotte, G. Orecchini, M. Virili, C. Mariotti, R. Goncalves, and P. Pinho, "Smart Surfaces: Large Area Electronics Systems for Internet of Things Enabled by Energy Harvesting", *Proc. IEEE*, vol. 102, no. 11, pp. 1723–1746, 2014.

[20] M. Bozzi and R. Moro, "Low-cost fabrication, eco-friendly materials, and easy integration: the new technological paradigm for the future wireless sensor networks", in *European Microwave Conference (EuMC)*, Nuremberg, Germany, Oct. 6-10, 2013, pp. 858–861.

[21] S. Kim, C. Mariotti, F. Alimenti, P. Mezzanotte, A. Georgiadis, A. Collado, L. Roselli, and M. M. Tentzeris, "No Battery Required: Perpetual RFID-Enabled Wireless Sensors for Cognitive Intelligence Applications", *IEEE Microw. Mag.*, vol. 14, no. 5, pp. 66–77, Jul 2013.

[22] S. Kim, R. Vyas, J. Bito, K. Niotaki, A. Collado, A. Georgiadis, and M. M. Tentzeris, "Ambient RF Energy-Harvesting Technologies for Self-Sustainable Standalone Wireless Sensor Platforms", *Proc. IEEE*, vol. 102, no. 11, pp. 1649–1666, Nov. 2014.

[23] A. P. Sample, J. Braun, A. Parks, and J. R. Smith, "Photovoltaic enhanced UHF RFID tag antennas for dual purpose energy harvesting", in *IEEE International conference on RFID*, Orlando, FL, USA, 12-14 Apr. 2011, pp. 146–153.

[24] H. Liu, M. Bolic, A. Nayak, and I. Stojmenovic, "Taxonomy and Challenges of the Integration of RFID and Wireless Sensor Networks", *IEEE Network*, vol. 22, no. 6, pp. 26–35, Nov 2008.

[25] D. De Donno, L. Catarinucci, and L. Tarricone, "Ramses: RFID Augmented Module for Smart Environmental Sensing", *IEEE Trans. Instrum. Meas.*, vol. 63, no. 7, pp. 1701–1708, Jul 2014.

[26] R. Colella, L. Tarricone, and L. Catarinucci, "Spartacus: Self-Powered Augmented RFID Tag for Autonomous Computing and Ubiquitous Sensing", *IEEE Trans. Antennas Propag.*, vol. 63, no. 5, pp. 2272–2281, May 2015.

[27] D. De Donno, L. Catarinucci, and L. Tarricone, "A Battery-Assisted Sensor-Enhanced RFID Tag Enabling Heterogeneous Wireless Sensor Networks", *IEEE Sensors J.*, vol. 14, no. 4, pp. 1048–1055, Apr 2014.

[28] T. Kaufmann and C. Fumeaux, "Wearable textile half-mode substrate-integrated cavity antenna using embroidered vias", *IEEE Antennas Wirel. Propag. Lett.*, vol. 12, pp. 805–808, 2013.

[29] A. Hande, R. Bridgelall, and B. Zoghi, "Vibration Energy Harvesting for Disaster Asset Monitoring Using Active RFID Tags", *Proc. IEEE*, vol. 98, no. 9, pp. 1620–1628, Sept. 2010.

[30] T.-H. Tsai, B.-Y. Shiu, and B.-H. Song, "A Self-Sustaining Integrated CMOS Regulator for Solar and HF RFID Energy Harvesting Systems", *IEEE J. Emerg. Sel. Topics Power Electron.*, vol. 2, no. 3, pp. 434–442, Sep 2014.

[31] S. Lemey and H. Rogier, "SIW textile antennas as a novel technology for UWB RFID tags", in *2014 IEEE RFID-TA*, Tampere, Finland, Sept. 8-9, 2014, pp. 256–260.

[32] S. Agneessens, S. Lemey, T. Vervust, and H. Rogier, "Wearable, small, and robust: the circular quarter-mode textile antenna", *IEEE Antenn. Wireless Propag. Lett.*, vol. 14, pp. 1482–1485, 2015.

[33] O. Caytan, S. Lemey, S. Agneessens, D. Vande Ginste, P. Demeester, C. Loss, R. Salvado, and H. Rogier, "Half-mode substrate-integrated-waveguide cavity-backed slot antenna on cork substrate", *Antennas Wirel. Propag. Lett.*, vol. 15, no. 99, pp. 162–165, May 2015.

[34] M. Hasani, A. Vena, L. Sydanheimo, L. Ukkonen, and M. M. Tentzeris, "Implementation of a Dual-Interrogation-Mode Embroidered RFID-Enabled Strain Sensor", *IEEE Antenn. Wireless Propag. Lett.*, vol. 12, pp. 1272–1275, 2013.

[35] M. Hasani, A. Vena, L. Sydanheimo, M. M. Tentzeris, and L. Ukkonen, "A Novel Enhanced-Performance Flexible RFID-Enabled Embroidered Wireless Integrated Module for Sensing Applications", *IEEE Trans. Compon., Packag. Manufact. Technol.*, vol. 5, no. 9, pp. 1244–1252, Sep 2015.

[36] F. Declercq, A. Georgiadis, and H. Rogier, "Wearable Aperture-Coupled Shorted Solar Patch Antenna for Remote Tracking and Monitoring Applications", in *Proc. 5th Eur. Conf. Antennas Propag. (EUCAP)*, Rome, Italy, 11-15 Apr. 2011, pp. 2992–2996.

[37] A. Georgiadis and A. Collado, "Improving range of passive RFID tags utilizing energy harvesting and high efficiency class-E oscillators", in *Antennas and Propagation (EUCAP), 2012 6th European Conference on*, Prague, Czech Republic, 26-30 March 2012, pp. 3455–3458.

[38] J. Tak, J. Choi, and S. Lee, "All-textile higher order mode circular patch antenna for on-body to on-body communications", *IET Microwaves, Antennas & Propagation*, vol. 9, no. 6, pp. 576–584, Apr. 2015.

[39] S. Lemey, F. Declercq, and H. Rogier, "Dual-band substrate integrated waveguide textile antenna with integrated solar harvester", *IEEE Antenn. Wireless Propag. Lett.*, vol. 13, no. 1, pp. 269–272, 2014.

[40] *IEEE Standard for local and metropolitan area Networks 802.15.4-2011*, Institute of Electrical and Electronics Engineers (IEEE), Std., Rev. of IEEE Std 802.15.4-2006, 5 Sept. 2011.

[41] P. Vanveerdeghem, H. Rogier, J. Knockaert, P. Van Torre, and C. Stevens, "Flexible dual-diversity wearable wireless node integrated on a dual-polarised textile patch antenna", *IET Science, Measurement & Technology*, vol. 8, no. 6, pp. 452–458, Nov. 2014.

[42] A. Collado and A. Georgiadis, "Conformal Hybrid Solar and Electromagnetic (EM) Energy Harvesting Rectenna", *IEEE Trans. Circuits Syst. I Reg. Papers*, vol. 60, no. 8, pp. 2225–2234, Aug. 2013.

Conclusions and future work

Conclusions

In the near future, it is expected that smart systems, seamlessly integrated into everyday consumer products, will change the way we experience and interact with our environment. In this vision of the Internet of Things, in which man and machine are in perfect symbiosis, smart surface technology plays an important role. The most widely-known smart surface concept, smart-fabric interactive-textiles, augments the user's capabilities through inconspicuous integration of functionality in his or her garment, whereas other novel smart surface related concepts, such as smart floors, smart wall papers, and smart ceilings, guarantee seamless interaction between man and infrastructure. This technology will leverage numerous application areas, ranging from healthcare to critical rescue missions.

This Ph.D. dissertation has focused on two main aspects related to the Internet of Things paradigm. First, innovations are proposed in antenna system design to enable seamless and robust integration within smart floors, ceilings and desk configurations. Special attention was devoted to combine compact dimensions with ultra-wideband performance. Second, autonomous SFIT systems are pursued with textile antennas as key enablers for high performance operation. Now, special care was taken to reconcile robustness, user comfort and high performance.

The first part of this work presented a new class of high-performance low-cost antenna designs that guarantee stable performance and invisible integration in an IoT environment. They rely on the Substrate Integrated Waveguide technology to implement cavity-backed slot antenna topologies on unconventional, yet innovative, substrate materials. Ultra-wideband performance was obtained by exciting two hybrid modes, while a very compact design is realized by exploiting the symmetry of the electromagnetic field distributions. The potential of this new generation of antennas was demonstrated by two novel antenna designs for dedicated applications. First, a three-fold rotationally symmetric antenna array was proposed. The specific topology guarantees excellent MIMO performance, whereas the substrate selection allows seamless integration into furniture. The second design enables invisible integration in cork floors and walls by exploiting the readily available cork material as substrate. The compactness, integrability, and stable, high performance over an ultra-wide bandwidth of both designs in diverse operating conditions, make them ideal candidates for demanding IoT applications. In a next step, the potential of this new class of antenna designs was exploited to bring the 'smart desk' concept to a higher level. In particular, we have embedded the ultra-wideband three-element antenna array in the worktop

of a desk with the idea of setting up a stable, high-speed ultra-short-range 3 x 3 MIMO wireless communication link with a laptop or tablet positioned on top of that worktop. We have demonstrated that the multiplexing gain provided by the ultra-short-range 3 x 3 MIMO channel, established by our dedicated arrays, allows to significantly reduce transmit power, while guaranteeing data rates that are comparable to those established by current-generation ethernet-connected devices. In fact, this research paves the way to provide full-speed internet at each seat of a meeting room or to come up with a user-friendly alternative for a wired docking station. Fulfillment of the conflicting demands of such an application would not have been possible with current-generation, off-the-shelf antennas.

The second part of this dissertation was devoted to two major issues of current generation SFIT systems, being reliability and autonomy. Our approach was twofold. On the one hand, we focused on the textile antenna component within the SFIT, as this is a vital component to guarantee excellent signal quality, long communication range, high-data rate communication, low power consumption (and high operational autonomy), and a high comfort to the user. On the other hand, we have examined the opportunities of energy-harvesting techniques to further increase system autonomy, reliability and user comfort. To unite the advantages of both key-enabling technologies, while avoiding reciprocal detrimental effects, we have introduced a novel comprehensive antenna/harvester co-design paradigm. As a starting point, we have applied the expertise acquired in the first part of this thesis to this research field. An ultra-wideband textile antenna was realized that boasts excellent performance and high body-antenna isolation. Then, the design was slightly modified to obtain a wearable textile antenna system that operates in two distinct bands, enhancing compatibility with the highly heterogeneous IoT environment, and that features enhanced system autonomy by compact integration of a photovoltaic (PV) module, power management system and an energy storage device. In the next step, operational autonomy was further increased by applying the co-design procedure to integrate a flexible hybrid energy harvester, enabling simultaneous energy harvesting from three different ambient energy sources, on a suitable textile antenna platform. Measurements in five indoor and outdoor scenarios evinced the potential of such a hybrid energy harvesting approach, and stressed its necessity in applications where environmental conditions quickly change. Finally, we have proposed a novel holistic microwave system design paradigm, in which our antenna/harvester co-design was combined with an already existing active textile antenna co-design procedure. Based on this novel strategy, an autonomous wearable radio-frequency identification (RFID) tag for operation in the 2.45-GHz RFID super high frequency (SHF) band was presented. A novel circular patch antenna, designed to exhibit maximum total efficiency in the 2.45 GHz RFID SHF band, serves as an integration platform for a flexible PV module, a dedicated power management system (including energy storage) and sensing, processing and transceiver hardware. The holistic design approach leverages unprecedented performance by not only relying on the textile antenna to obtain peak performance, but also by exploiting its topology to avoid lossy and

fragile interconnections, thereby enhancing signal integrity and robustness. Moreover, it allows tailoring the power management system to the power consumption profile of the wireless communication module and to the power generation profile of the application-specific energy-harvesting transducer(s).

Future work

The research performed in this dissertation forms a solid basis for future work. Yet, many improvements and progress can still be made.

Part I: Antenna systems for integration in smart floors, ceilings and desk configurations

Novel designs were proposed that take advantage of the potential of the SIW implementation technology. Yet, many other interesting research directions remain unexplored. In particular, special attention should be devoted to the high-frequency interconnection between these novel antenna designs and the RF front-end. In this respect, it would be interesting to further exploit the SIW technology to design and seamlessly embed complete RF systems, such as radio front-ends and radar systems, in smart surface systems.

Furthermore, we already explored one of the many new perspectives offered by this new generation of compact, ultra-wideband antenna systems that envision application in smart floors, ceilings and furniture. However, to fully realize this novel vision of a 'smart desk', many research efforts are still required. For instance, it would be interesting to examine the influence of the HMSIW miniaturization technique on the stability, reliability and speed of such an ultra-short-range MIMO wireless communication link. The optimum amount of antennas at each link end is another interesting research question. Furthermore, interference between two such setups should also be subjected to an extensive analysis. Last, but certainly not least, an RF front-end and communication protocol should be developed that are capable of fully exploiting the potential of such an ultra-short-range MIMO channel. Another interesting application area of these novel designs could be found in the very intriguing problem of precise indoor localization. Their ability of providing a quasi-invariable radiation pattern over a very large bandwidth in the challenging IoT environment make them very good candidates to be used as part of fixed ultra-wideband anchors embedded in the floors or ceilings of a building.

Finally, both designs operate in the [5.15 - 5.85] GHz frequency band. However, in the near future, it is expected that the tremendous increase in number of wireless devices, and the corresponding increase in data traffic, will force us to leave this lower, crowded frequency spectrum. The globally unlicensed 60 GHz band offers a promising alternative. Obviously, this brings along additional challenges for smart surface related systems as interconnections become more susceptible to unwanted interference, losses increase and fabrication tolerances play a more important role.

Hence, many challenges need to be tackled in order to realize this shift to higher frequencies.

Part II: Textile antenna systems for body-centric wireless communication

In this part of the dissertation, the utmost care was taken to guarantee sufficient flexibility of the entire textile antenna system. All electronic systems were implemented on a flexible and ultra-thin polyimide substrate, vias were avoided as much as possible and small electronic components were selected and distributed over a larger area than necessary. Yet, multiple novel techniques have the potential to enhance flexibility even further. First, dedicated chip design, instead of exploiting commercially available chips, could be used to minimize the amount of electronic components. Furthermore, the Ultra Thin Chip Package (UTCP) technology, in which a thinned silicon die (typically with a thickness below 30 μm) is encapsulated in an organic PCB substrate, could be exploited to maximize flexibility (and robustness) even further. Combining the latter with the technique of laser trimming unnecessary parts of the substrate is another interesting research area to improve both flexibility and breathability.

Upcoming energy-harvesting technologies also offer interesting new opportunities. In this work, we used flexible a-Si:H foil-based solar cells to scavenge light energy and rigid peltier modules to harvest energy from the wearer's body heat. Recently, fiber-optic solar cells were presented, which could be used to construct woven fabric solar cells. Another promising research area in the field of light energy harvesting is the incorporation of polymeric PV cells into garments and textiles. The results are encouraging, certainly in terms of wearability, but stability and efficiency issues still need to be resolved. Furthermore, a lot of research efforts are currently devoted to the realization of flexible and breathable peltier modules. These could be used to cover a larger surface of the human body in an unobtrusive way, leveraging substantially higher amounts of scavenged energy. Another interesting research direction within this field is the exploitation of textile antennas (or other conductive fabric parts) as heat sinks to increase operational autonomy even further. The emergence of off-the-shelf piezoelectric generators using fiber composite materials for seamless integration into garments marks another important step for SFIT systems. Such a generator could be integrated onto a textile antenna system deployed on the chest of the wearer. Then, energy could also be extracted from the breathing process of the wearer.

Furthermore, a vast amount of attention should be devoted to the fabrication procedure of textile antenna systems. During this research, several working prototypes were realized through a mix of experience, in-house knowledge, and a lot of patience. The currently exploited techniques are mature for research-related purposes and small-scale productions, but not for large scale production, which is necessary to reach a high market penetration.

Finally, it would be very interesting to apply the insights gained in this part on the smart surface related systems in the first part.